



**Joachim Hornegger, Ernst W. Mayr, Sergey Schookin,
Hubertus Feußner, Nassir Navab, Yuri V. Gulyaev,
Kurt Höller, Victor Ganzha (Eds.)**

3rd Russian-Bavarian Conference on Bio-Medical Engineering

Proceedings of the
3rd Russian-Bavarian Conference on Bio-Medical Engineering
at Friedrich-Alexander-Universität Erlangen-Nuremberg
and Fraunhofer Institute for Integrated Circuits IIS
Erlangen, Bavaria, July 2/3, 2007

Friedrich-Alexander-Universität
Erlangen-Nürnberg

TF TECHNISCHE FAKULTÄT



Volume Editors:

Joachim Hornegger
Kurt Höller
Erlangen, Germany

Sergey Schookin
Yuri Gulyaev
Moscow, Russia

Ernst Mayr
Hubertus Feußner
Nassir Navab
Victor Ganzha
Munich, Germany

Copyright 2007
All rights reserved

Printed in Erlangen, Germany

ISBN 3-921713-33-X

Preface

Interdisciplinary research is commonly considered as a key driver for innovation, and for that reason it is of highest importance to provide a platform for scientific exchange of researchers from diverse disciplines. The Russian-Bavarian Conference on Bio-Medical Engineering was established for researchers from Russia and Bavaria that are working on the application of engineering methods to solve medical problems. The major focus of this conference series is on the implementation of an interdisciplinary dialog and an innovative environment. The 3rd Russian-Bavarian Conference includes this time submissions that cover a broad variety of research topics at the frontiers of bio-medical engineering. Medical experts and engineers discuss challenging topics that range from Bioinformatics through Life Science Electronics to new surgery techniques like NOTES.

The proceedings summarize the scientific contributions of the conference and include most of the presented details. We hope that the proceedings will also reflect the inspiring atmosphere of the conference and the high motivation of its participants.

The success of the 3rd Russian Bavarian Conference is the success of many people that helped us to organize the meeting. At this point we want to thank all the restless people who contributed to the organization of the conference and the Fraunhofer IIS which was an excellent host.

July 2007

Joachim Hornegger
Conference Chair
RBC Biomed07

Organization

3rd Russian-Bavarian Conference on Bio-Medical Engineering 2007 is organized by the Institute of Pattern Recognition, Friedrich-Alexander-University Erlangen-Nuremberg and Fraunhofer Institute for Integrated Circuits IIS, Erlangen.

Conference Committee

General Chair

- Prof. Joachim Hornegger
*Head of the Institute of Pattern Recognition,
Friedrich-Alexander-University Erlangen-Nuremberg*
- Prof. Ernst W. Mayr
*Head of the Chair for Efficient Algorithms and Head of Bioinformatics Curriculum,
Technische Universität München*
- Prof. Sergey Schookin
*Head of Biomedical Techniques Department,
Bauman Moscow State Technical University*
- Prof. Hubertus Feußner
*Clinical Head of the Workgroup for Minimally Invasive Therapy and Intervention
MITI,
Klinikum Rechts der Isar*
- Prof. Nassir Navab
*Head of the Chair for Computer Aided Medical Procedures,
Technische Universität München*
- Prof. Yuri V. Gulyaev
*Director Academician RAS, Radio Electronics Institute
Russian Academy of Sciences*

Organizing Chair

- Kurt Höller
*Institute of Pattern Recognition,
Friedrich-Alexander-University Erlangen-Nuremberg*

– Dr. Victor Ganzha
Coordinator for the Bavaria-Russia Co-operation,
Technische Universität München

Session Chairs

Bauernschmitt, Robert
Buchholz, Rainer
Burlakov, Robert
Feußner, Hubertus
Greiner, Günther
Guggenbichler, J.Peter
Hahn, Eckhart G.
Hornegger, Joachim
Kuwert, Torsten
Leonov, Boris
Lerch, Reinhard
Leugering, Günter
Masloboev, Yuri
Mayr, Ernst
Medvedev, Oleg

Naraykin, Oleg
Navab, Nassir
Niemann, Heinrich
Pustovoyt, Vladimir
Schookin, Sergey
Selishchev, Sergey
Spiridonov, Igor
Tereshchenko, Sergey
Thull, Roger
Victorov, Vladimir
Weigand, Christian
Wessel, Niels
Wittenberg, Thomas

IV

Sponsoring Institution

Fraunhofer Institute for Integrated Circuits IIS

Table of Contents

Editorial	I
Advanced Imaging and Instrumentation for Surgery	1
Current status of the use of medical robots in Germany, Austria and Switzerland <i>F. Härtl, K.Höller, S. Beller, and H. Feussner</i>	2
Bioinformatics	4
Protein adsorption on nanostructured implant surfaces: A model calculation for the prediction of preferred adsorption sites	6
<i>P. Elter and R. Thull</i>	
Medical data extraction from legacy databases - case study	12
<i>Tomasz Adamusiak and Rafal Pawliczak</i>	
VisualMind Framework for Brain-Computer Interface development	15
<i>D.V. Karlovskiy and V.A. Konyshv</i>	
Usage of Hidden Markov Models for automatic sleep stages classification	19
<i>L.G. Doroshenkov and V.A. Konyshv</i>	
Cardiovascular Biosignal Analysis	23
Portable monitor for registration of ballistocardiographic signals	25
<i>Yu.P. Masloboev, A.A. Ohritsky, D.A. Prilutsky, and S.V. Selishchev</i>	
Mitral Valve Surgery Impedes Recovery of Cardiovascular Autonomic Function <i>B. Retzlaff, N. Wessel, H. Malberg, G. Brockmann, C. Uhl, R. Lange, and R. Bauernschmitt</i>	32
Blood Pressure Estimation based on Pulse Transit Time and Compensation of Vertical Position	38
<i>Christian Douniama, Robert Couronné</i>	
Automatic Extraction of quasi-Synchronous Views from Rotational Angiographic Sequence without ECG-Data	42
<i>Sahla Bouattour and Dietrich Paulus</i>	
Fast Recursive Data-driven Multi-resolution Feature Extraction For Physiological Signal Classification	47
<i>Florian Hönig, Anton Batliner, and Elmar Nöth</i>	

Analysis of cardiovascular dynamics: new approach for predicting of pre-eclampsia	53
<i>H. Malberg, R. Bauernschmitt, and N. Wessel</i>	
Imaging of Biomechanics of Heart Movements by Using Multichannel System for Precardiac Rheography	57
<i>Y.E. Kirpichenko and D.P. Timohin</i>	
Investigation of Graphic Methods for Rhythmocardiogram Phase Portraits Analysis	62
<i>Aliaksei I. Maistrou</i>	
Clinical Applications of Advanced Technology	69
Design of mechatronic drives for implantable systems of left ventricle assist device and artificial heart	71
<i>V.V. Morozov, A.V. Zhdanov, and E.A. Novikova</i>	
Real-time Shaping of the Embedded Waveform for External Defibrillation	77
<i>B. B. Gorbunov, A. N. Gusev, and S. V. Selishchev</i>	
Ultrasonic Peeling	81
<i>V. M. Gorshkova</i>	
Computer Aided Medical Procedures	86
Registration-free Laparoscope Superimposition for Intra-Operative Planning of Liver Resection	88
<i>Marco Feuerstein, Thomas Mussack, Sandro M. Heining, Nassir Navab</i>	
Semi-automatival Validation of SPECT/CT Scanners	93
<i>Jingfeng Han, Christian Bennewitz, Joachim Hornegger, and Torsten Kuwert</i>	
Adding navigation to radio-guided surgery: new possibilities, new problems, new solutions	96
<i>Thomas Wendler, Jörg Traub, Alexander Hartl, Tobias Lasser, Maria Burian, Andreas Buck, Farhad Daghighian, Markus Schwaiger, Sibylle I. Ziegler, and Nassir Navab</i>	
Imaging in Diagnosis and Therapy	100
The Model of Proportional Scattering Medium for Optical Tomographical Imaging of Biological Tissues	102
<i>Sergey Tereshchenko</i>	
Image Based Time Series Synchronization for Periodically Moving Targets	106
<i>Christian Schaller, Ali Khamene, and Joachim Hornegger</i>	

Quantitative Measurement of Kidney and Cyst Sizes in Patients with Autosomal Dominant Polycystic Kidney Disease (ADPKD)	111
<i>V. Daum, H. Helbig, R. Zeltner, R. Janka, K.-U. Eckardt and J. Hornegger</i>	
A Boosting Approach for Multiple Sclerosis Lesion Segmentation in Multi-Spectral 3D MRI	116
<i>Michael Wels, Martin Huber, and Joachim Hornegger</i>	
Image Compression Algorithm Based on Encoding of Tree-Arranged Wavelet Coefficients	121
<i>Sergei V. Umnyashkin, Dmitri M. Koplovich, Andrei S. Pokrovskiy, and Andrei A. Alexandrov</i>	
Appearance-based Approach to Extract an Age-related Biomarker from Retinal Images	127
<i>Rüdiger Bock, Jörg Meier, László G. Nyúl, Simone Wärntges, Georg Michelson, and Joachim Hornegger</i>	
Stent Structure-Graph Based Mapping	132
<i>Benjamin Keck, M. Prümmer, and Arun Ganguly Rebecca Fahrig</i>	
Life Science Electronics	137
Smartphone-based Mobile Solutions for Health Control in Humans	139
<i>Alexander V. Kobelev, Igor K. Sergeev, and Sergey I. Schookin</i>	
Integrated Measurement Circuits with Low Power Consumption for ECG-Application	143
<i>Hans Hauer, Edward Ryabov, and Slawa Efimov</i>	
Mathematical Methods for Medical Engineering	147
Solving direct and indirect tasks of tissue modelling in the precardiac area	149
<i>Y.E. Kirpichenko and D.P. Timohin</i>	
Nonlinear Diffusion Noise Reduction in CT Using Correlation Analysis	155
<i>M. Mayer, A. Borsdorf, H. Köstler, J. Hornegger, and U. Rüde</i>	
The Computer Modeling of Normal and Pathological Tissue Growth using Cellular Automata Conception	160
<i>E. M. Arkushina and V. V. Kotin</i>	
Numerical Method to Solve Inverse Problem for Horizontally Layered Model of Precardiac Tissues	167
<i>Alexander V. Kobelev, Sergey I. Schookin, and Igor K. Sergeev</i>	
Implementation of Adaptive Filters for Biomedical Applications	169
<i>Jennifer Baraniak, Johann Hauer, Norbert Schuhmann, and Günter Leugering</i>	

Medical Communication and Sensor Systems	173
Application of the Radar Technology in Medicine for Remote Monitoring of Human's Breath and Pulse	175
<i>A. Bugaev, V. Chapursky, S. Ivashov, V. Razevig, A. Sheyko, I. Vasilyev, and T. Bechtel</i>	
Generic Medical Data Persistence with the VITAL Framework	181
<i>Matthias Struck, Svetoslav Pramatarov, and Christian Weigand</i>	
A Fall Detection System Based On A Wireless Zigbee Sensor Network	186
<i>C. Hofmann and S. Feilner</i>	
Multi-channel electrical impedance system: hardware, architecture, topology ...	190
<i>I.K. Sergeev and A.V. Kobelev</i>	
Features of Brain Hemodynamics Rresearch at the Multichannel Rheoencephalography and Electroencephalography	198
<i>E. M. Astapenko, P. V. Luzhnov, and L. A. Shamkina</i>	
Effect of Respiratory Gases Composition on Duration of Forced Expiratory Tracheal Noises	204
<i>Alexander I. D'yachenko, Vladimir I. Korenbaum, Elena V. Kir'yanova, Irina A. Pochekutova, Yury A. Shulagin, and Antonina A. Osipova</i>	
Micro- and Nanotechnology in Bio-Medical Engineering	206
Prevention of implant associated nosocomial infections by impregnation of biomaterials with activated nanocrystalline silver	208
<i>J. Peter Guggenbichler</i>	
Paradontitis: Therapy and prevention with a nano-silver containing toothpaste - Experimental and clinical data	212
<i>W. Wanninger and JP Guggenbichler</i>	
Laser irradiation application for creating volumetric nanocomposits for medical purposes	218
<i>Podgaetsky V.M., Sàvransky V.A., Selishchev S.V., Simunin M.M., Titkova D.A.</i>	
MUSTOF-Endoscopy for Natural Orifice Transluminal Endoscopic Surgery	221
An Innovative, Safe and Sterile Sigmoid Access for NOTES (ISSA)	223
<i>D. Wilhelm, J. Penne, S. v. Delius, A. Meining, J. Hornegger, and H. Feussner</i>	

Auto-Gain Approach for Use with Time-Of-Flight Examination in Minimally Invasive Surgery	227
<i>P. Ritt, K. Höller, J. Penne, A. Schneider, J. Hornegger, and H. Feussner</i>	
Photorealistic 3-D Surface Reconstructions Using TOF Cameras	233
<i>Jochen Penne, Kurt Höller, Dirk Wilhelm, Hubertus Feußner, and Joachim Hornegger</i>	
Author Index	241

Advanced Imaging and Instrumentation for Surgery

Current status of the use of medical robots in Germany, Austria and Switzerland

F. Härtl¹, K. Höller², S. Beller³, and H. Feußner¹

- ¹ Chirurgische Klinik und Poliklinik, Klinikum rechts der Isar der TU München,
² Lehrstuhl für Mustererkennung, Universität Erlangen-Nürnberg
³ Klinik für Chirurgie und Chirurgische Onkologie, Charité Campus Buch, Berlin,

Abstract. The high expectations on medical robots in the beginning of the 90's were not achieved by the current systems so far, because of the high costs, limited flexibility and limited range of applications. Particularly in Germany there seems to be low use of telemanipulation systems in clinical routine. We were interested in the reality of the current status of the use of medical robots in Germany, Austria and Switzerland. For that, we designed a short questionnaire sent by e-mail to about 980 surgical hospitals, asking for the use of medical robots, the kind of robots and pros and cons of the use. The results of the survey will be presented.

1 Introduction

Contrary to optimistic prognoses mechatronic systems still play a minor role in surgery. Nevertheless, after a few years of depression there seems to be a growing interest on the area of robotic surgery. The aim of this study was to assess reality of the current use of medical robots in Germany, Austria and Switzerland.

2 Material and Methods

A questionnaire was designed, asking for the use of robotic systems in experimental and clinical routine, in the past or actually. In case of not using such a device or using it not any longer, we asked for the detailed reasons. If robotic systems were in use, we asked for the type and the indications and kind of interventions it is used for. Further we asked for a precise description of the pros and cons of the used systems. Finally it was collected if there are any activities in research.

The questionnaires were sent by e-mail to about 980 hospitals in Germany, Austria and Switzerland.

3 Results

89 of the 980 questionnaires were returned. In $n = 67$ cases there was no use of robotic systems (75,3%). In $n = 6$ cases (6,7%) an experimental use of robotic systems was reported, using the AESOP and daVinci system in one case respectively, or using a self-made prototype in the other four cases. $N = 19$ (21,3%) hospitals reported the use

of robotic systems in clinical routine, using the AESOP system in $n = 7$ (7,9%) cases, the daVinci system in $n = 7$ (7,9%) cases and $n = 5$ (5,6%) cases with use of other systems. The use of robotic devices was discontinued in $n = 6$ cases (6,7%), concerning the AESOP system in $n = 5$ cases (5,6%) and the Robodoc system in $n = 1$ case (1,1%) (Fig. 1). The average use per year was 20 cases with a range from 2 to 74.

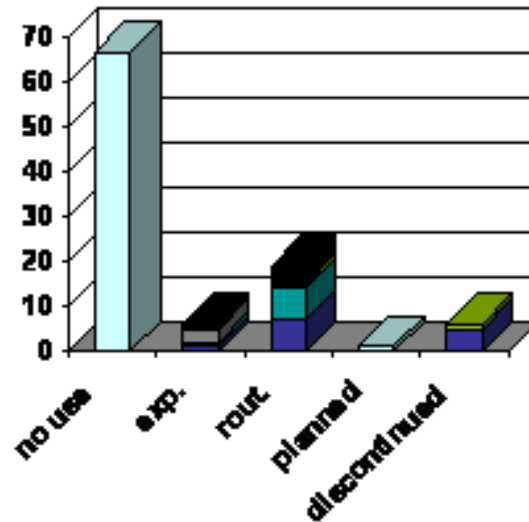


Fig. 1: The use of robotic systems in Germany, Austria and Switzerland

As reason for no application or discontinued application of robotic systems first of all the high costs were mentioned in 50 % of all answers (Fig. 2), followed by lack of true indications in 41 %. The education of untrained surgeons is the reason of about 13 % of the hospitals. 8 % of the hospitals can't see any benefit in the outcome of the operations using a robotic system and respectively 4 % mentioned the limited range of application and the reserved public opinion as criteria.

Those who use camera-guiding systems like AESOP or Endoassist, mentioned as positive arguments the stable visual field, the lack of exhaustion and the reduction of staff. They criticize the uncomfortable handling, the high operating costs and the prolonged operating time.

The users of master-slave systems like daVinci point out as advantages the 3D-visualisation, the precise movements and the ergonomic position of the surgeon at the console. On the other hand they criticize the high purchase and current costs, the long time for installation, the huge dimensions and weight and the reduced operating field.

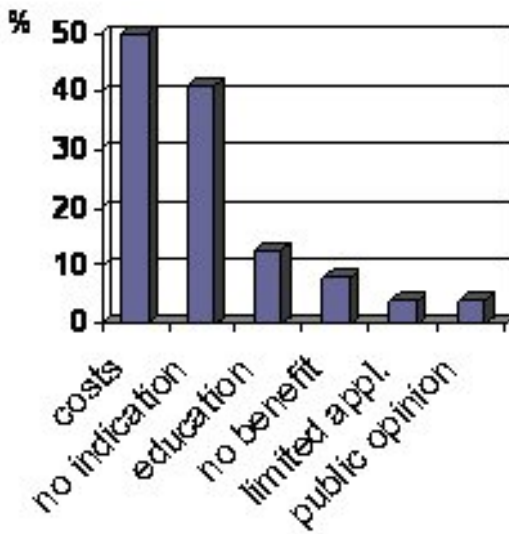


Fig. 2: Reason for no application or discontinued application of robotic systems

4 Conclusion

Telemanipulation systems are used in all surgical sections. However, clinical importance is low since no “killer applications” exists.

For surgical purposes a system is preferable, which can assist the surgeon in several different ways, which does not obstruct visibility in the operation-field which is as compact as possible, which is easily mountable and removable in clinical routine and can furthermore be controlled intuitively by the surgeon.

Bioinformatics

Protein adsorption on nanostructured implant surfaces: A model calculation for the prediction of preferred adsorption sites

P. Elter¹ and R. Thull²

¹ Lehrstuhl für Funktionswerkstoffe der Medizin und der Zahnheilkunde

² Universität Würzburg

1 Introduction

Adsorption of proteins at a solid-liquid interface is an important phenomenon in biology and highly relevant for the design of biocompatible materials. It is well-known that protein adsorption is one of the first events which take place when a foreign material comes into contact with a living body and is believed to be a key factor in controlling subsequent cellular adhesion. In the last years several studies were performed, in which protein adsorption on nano-patterned adsorbents was investigated and a dependence on the topography was determined. For example an increased adsorption of FActin at stripes and edges was observed on nanostructured titanium with structure heights of 12 nm and proteins were aligned parallel to the nanostructure [1]. Moreover, the range in which proteins are “sensitive” to structures of a certain size is usually very small and hence, a detailed knowledge of their effect on the adsorption is required.

In this article the influence of a topographical nanostructure with sharp edges and spikes is investigated by a theoretical model combining Brownian Dynamics (BD) and the Finite Differences (FD) method. The theoretical description of an adsorption process on three-dimensional rough or porous nanostructures is more complex than for a planar surface: The influence of edges and spikes on the local electric field has to be considered and it may be assumed that preferred sites of adsorption are formed. An increased adsorption rate at certain places will also affect the local neighborhood in the adsorption steps following at later times, due to protein-protein interactions. Thus, it stands to reason that a theoretical prediction is required to include protein-protein and protein-nanostructure interactions as well as a calculation of the individual motion trajectory of each single protein.

2 Materials and Methods

In a BDSimulation, the displacement of each particle i is derived from the forces acting on it. The new particle position after a small time step Δt will be considered as initial position for the next step. Thus, the gradual computation of many time steps results in the motion trajectory of a protein. The algorithm for updating particle positions [2] is given by

$$\xi_i(t + \Delta t) = \xi_i(t) + \frac{D_0}{k_B T} \mathbf{F}_i(t) \Delta t + \chi_i(\Delta t), \quad (1)$$

where $\xi_i(t)$ is the position of particle i at time t , D_0 is the lateral diffusion coefficient for free diffusion, k_B the Boltzmann constant and T the temperature of the system. Hydrodynamic interactions are neglected in this model. The shift of the protein positions is primarily determined by two factors: a systematic net force \mathbf{F}_i , which is calculated from the mutual interactions of the proteins along with the particle-nanostructure interactions, and a stochastic displacement χ_i . The latter has a Gaussian distribution, a variance-covariance according to the lateral diffusion coefficient and no correlations to the systematic force.

Interactions are based on the DLVO (Derjaguin, Landau, Verwey, Overbeek) theory and account for electrostatic and dispersion forces. While protein-protein interactions can be expressed analytically by the classical DLVO theory [5], protein-nanostructure interactions need to be described numerically, due to the arbitrary shape of the adsorbent. The electrostatic interactions of the numerical part were calculated from a solution of the Poisson-Boltzmann equation by an FD multigrid solution [3]

$$\nabla(\varepsilon_0\varepsilon_r(\mathbf{x})\nabla\phi) = -\varphi - \sum_{\nu} q_{\nu}e_0 \cdot c_{\nu}N_A \cdot \exp\left(-\frac{q_{\nu}e_0 \cdot \phi}{k_B T}\right) \quad (2)$$

and the dispersion interactions were obtained from a numerical integration of Hamaker's equation [4]

$$U = -\frac{A}{\pi^2} \int_{V_1} dv_1 \int_{V_2} dv_2 \frac{1}{r^6} \quad (3)$$

on a fine sub-grid. In the equations ϕ is the electrostatic potential (in Volt), φ the partial charge distribution belonging to the nanostructure, N_A the Avogadro's number, k_B the Boltzmann constant and T the temperature of the system. Moreover, dv_1 and dv_2 designate the volume elements from the integrals over the total particle volume V_1 and V_2 , respectively. r denotes the distance between dv_1 and dv_2 and A is the Hamaker constant. The analytic solution for the electrostatic part of the protein-protein interactions is given by [5]

$$U_{i,j}^{EL}(r) = \frac{q_{prot}^2 e_0^2}{4\pi\varepsilon_r\varepsilon_0} \left[\frac{\exp(\kappa \cdot a)}{1 + \kappa \cdot a} \right]^2 \frac{\exp(-\kappa \cdot r)}{r}, \quad (4)$$

where $\kappa^2 = (e_0^2 N_A \sum_{\nu} c_{\nu} q_{\nu}^2) / (\varepsilon_r \varepsilon_0 \cdot k_B T)$ is the inverse Debye-Length, a the radius of the protein sphere, $r > 2a$ the distance between two proteins, ε_0 the permittivity of free space, ε_r the relative dielectric constant, e_0 the electron charge and q_{prot} the net charge of a protein. Moreover, each ion sort ν of the electrolyte is parameterized by its concentration c_{ν} and its charge q_{ν} . The Hamaker equation for the dispersion part can be explicitly integrated for two spheres [4]

$$U_{i,j}^{DISP} = -\frac{A}{6} \left\{ \frac{2a^2}{r_{i,j}^2 - (2a)^2} + \frac{2a^2}{r_{i,j}^2} + \ln \frac{r_{i,j}^2 - (2a)^2}{r_{i,j}^2} \right\}. \quad (5)$$

Short-range repulsion as known from the Lennard-Jones potential is implicitly defined by the algorithm: each time a particular displacement leads to an overlap with another

protein or the nanostructure, it is reduced until the overlap disappears. The sequence, in which this is examined, is changed every time step, in order to reduce the effect of unwanted correlations. Additionally a protein is flagged as immobilized, as soon as it grazes the surface of the nanostructure (no surface diffusion).

The following model parameters are used for the calculation:

Table 1: Model parameters

Parameter	Value
Protein	Lysozyme
Type	Globular / sphere
Radius	1.5 nm
Net charge	+8 [6]
pH	7
A(Protein-Protein)	$2.0 \cdot 10^{-20}$ J [7]
A(Protein-Surface)	$1.0 \cdot 10^{-20}$ J [7]
Protein concentration	200 $\mu\text{g/ml}$
Surface Potential	$\phi_0 = -0.1$ V (Mica) [8]
Electrolyte	NaCl
ϵ_r	81 / 6
FD-Grid	128^3
Integration sub-grid	729 points / FD-Element

3 Results and Discussion

An oppositely charged nano-cube with an edge-length of 16 nm was chosen as model system, because it was expected that the adsorption at edges plays a major role for such small structures. In this setup all protein-nanostructure interactions are attractive while the protein-protein interaction consists of an attractive dispersion and a repulsive electrostatic part. The resulting pair potentials (without short-range repulsion) for the Lysozyme-Lysozyme interaction are shown in Fig.1. The short distances are dominated by the attractive dispersion interactions while the farther regions are more influenced by the electrostatic repulsion. The latter form a kind of barrier, whose height depends on the electrolyte concentration. At high sodium chloride concentrations, the height of the barrier is low, due to the screening effect of the electrolyte, while to lower salt concentration this barrier increases.

Fig.2 displays the adsorbed proteins at the nano-cube in the final state for three different electrolyte concentrations. The proteins are preferentially adsorbed near the edges of the cube at low salt concentrations, which is mainly due to two different effects: first, the local electric field is higher near the edges and corners than in the center of a surface. Moreover, a point that is located at a corner or an edge can be reached by more proteins of the surrounding neighborhood than a point on a surface and already possesses a higher probability of adsorption due to geometry. Since the charged

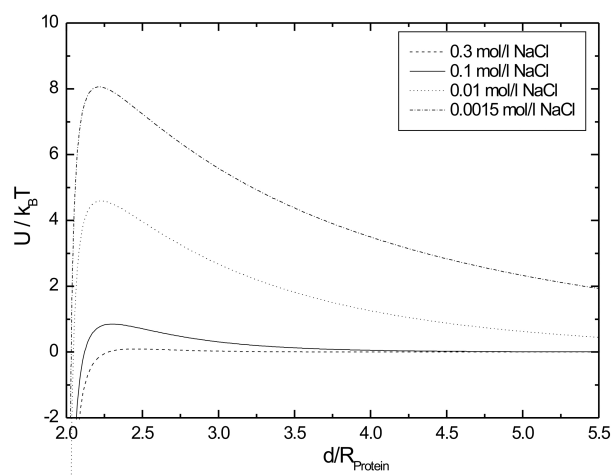


Fig. 1: Pair potential of the Lysozyme-Lysozyme interaction for different salt concentrations

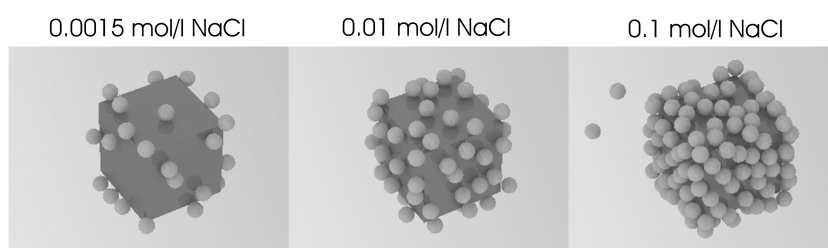


Fig. 2: Final state of the adsorption process on a 16 nm^3 nano cube for different salt concentrations

protein spheres repel each other, a higher adsorption rate at the edges leads to a lower surface coverage of the nearby planar surfaces at low salt concentrations. Only a few proteins manage to cross the repulsive barrier of the previously adsorbed proteins and reach regions where the attractive interaction of the nanostructure outweighs. At higher salt concentrations the adsorption process begins in exactly the same way. However, adsorption can be continued at later time steps, due to the higher screening effect of the electrolyte and also the surfaces are covered. At an NaCl concentration of 0.1 mol/l almost a closest packing is reached as already assumed on the basis of the surface coverage graph. A slight increase of the protein density at the corners of the cube is still determined. With all accomplished calculations the surface coverage never exceeds a monolayer, but proteins may extend into space at the edges and corners of the cube. Hence, the mechanism of protein adsorption is governed by two different stages: in the first part preferential places are occupied, which are determined by the electrical field near the surface and the size of the surrounding liquid volume. The dispersion forces have only a small influence on the selection of the adsorption sites in this model, due to their short range and fast raising character. If a protein reaches the regions near the surface of the nano-cube, where dispersion forces play a role, it is usually adsorbed in the immediate vicinity. In the second part of the mechanism, also more unfavorable sites are occupied. The significance of this part is determined by the electrolyte concentration and the prevailing charge ratios.

4 Conclusion

In this study a model for the prediction of preferred protein adsorption sites was developed by a combination of the Finite Differences Method and Brownian Dynamics. An increased adsorption rate along the edges of a $(16 \text{ nm})^3$ model cube is reached under consideration of electrostatic and dispersion interactions. If the cube comes into contact with a protein/electrolyte solution, obviously first the favourable positions at the edges are occupied. At later times also the surfaces of the cube are covered, if the salt concentration is sufficient to screen the repelling protein-protein electrostatic interaction.

References

1. C. Galli, M. C. Coen, R. Hauert, V. L. Katanaev, M. P. Wymann, P. Gröning, L. Schlapbach: Protein adsorption on topographically nanostructured titanium. *Surf. Sci.* **474** (2001) L180-L184
2. D. L. Ermak: A computer simulation of charged particles in solution. I. Technique and equilibrium properties. *J. Chem. Phys.* **62** (1975) 4189-4196
3. W. H. Press, B. P. Flannery, S. A. Teukolsky, and W. T. Vetterling: *Numerical Recipes in C*. Cambridge University Press (1993)
4. H. C. Hamaker: The London - Van Der Waals Attraction Between Spherical Particles *Physica* **4** (1937) 1058-1072
5. E. J. W. Verwey, J.T.G. Overbeek: *Theory of the Stability of Lyophobic Colloids* Elsevier Amsterdam (1948)

6. C. Tanford, R. Roxby:
Interpretation of Protein Titration Curves. Application to Lysozyme
Biochemistry **11** (1972) 2192-2198
7. M. R. Oberholzer, N. J. Wagner, A. M. Lenhoff:
Grand canonical Brownian dynamics simulation of colloidal adsorption.
J. Chem. Phys. **107** (1997) 9157-9167
8. O. J. Rojas, M. Ernstsson, R. D. Neumann, P. M. Claesson:
Effect of Polyelectrolyte Charge Density on the Adsorption and Desorption Behavior of Mica.
Langmuir **18** (2002) 1604-1612

Medical data extraction from legacy databases - case study

Tomasz Adamusiak¹ and Rafal Pawliczak¹

Department of Immunopathology, Faculty of Postgraduate Medical Education, Medical University of Lodz, Poland, tomasz.adamusiak@gmail.com

Abstract. Here we present extracting relevant medical information from a free text database. The documentation included individual records of 19694 patients treated at the Center for Diagnosing and Treatment of Asthma and Allergy, Medical University of Lodz between years 1995 and 2006. The database was based on legacy engine with no export feature and fragmentary documentation. The aim of the study was to data mine relevant clinical data for asthmatic patients 12-months prior and 36 months after the index date. Index event was defined as adding montelukast or salmeterol to present therapy or excluding salmeterol from therapy. The results of this retrospective observational study were in agreement with previous results on this particular topic.

1 Introduction

In 2002, the English National Health Service (NHS) began the process of transforming its health-care system with information technology. The experts assess the costs have already doubled reaching \$24 billion and for some the project is sleepwalking toward disaster. Nevertheless wide adoption of databases in medicine is of paramount significance. It is not only the matter of cutting down administrative inefficiencies in health-care but also saving lives having all the crucial patients information always at hand. Beyond the single Electronic Health Record lies the true big picture however. That is the ability to query the whole population of patients' data for treatment-outcomes relationships on a truly Evidence-Based Medicine basis. This could also mean detecting dangerous drugs interactions, undetectable at the moment without large targeted randomized clinical trials.

The aim of the study was to data mine relevant clinical data for asthmatic patients 12-months prior and 36 months after the index date. Index event was defined as adding montelukast or salmeterol to present therapy or excluding salmeterol from therapy.

2 Methods

The documentation included individual records of 19694 of patients treated at the Center for Diagnosing and Treatment of Asthma and Allergy, Medical University of Lodz between years 1995 and 2006. It amounted to about 70 thousand pages of clinical data collected in a textual database. Each entry was personally input by a doctor working at

the Centre during patients' visits and consisted of an interview, physical examination, laboratory results and prescribed drugs. All fields were unstructured text only.

We began by importing the records into a Microsoft Access database. This was achieved through a VBA routine that was tailored against the available documentation and reverse engineering of the database rudimentary relational model. The database maker was no longer reachable and original company ceased to exist.

The relevant entity extraction was linguistic based and employed heuristic rules and shallow parsing techniques on specific parts of the text around certain keywords. It was inspired by the works of Friedman et al. and their MedLEE extraction system. The aim was not only to extract some basic symptoms like daytime dyspnea or wheeze but also prescribed doses, occurrence of certain events (for instance asthma related hospitalizations) and pulmonary function tests values. It was crucial for the scientific relevance of acquired data that all entities are recalled. This, however, resulted in a high percentage (30%) of data being misclassified.

This first fully automated query resulted in a preliminary set narrowed down to about 250 records that met the stringent inclusion criteria. These were then manually checked for errors of automation on case by case basis and the study query was repeated resulting in the final set of 189 patients and their respective results for all the periods assessed as schematically shown in the figure 1.

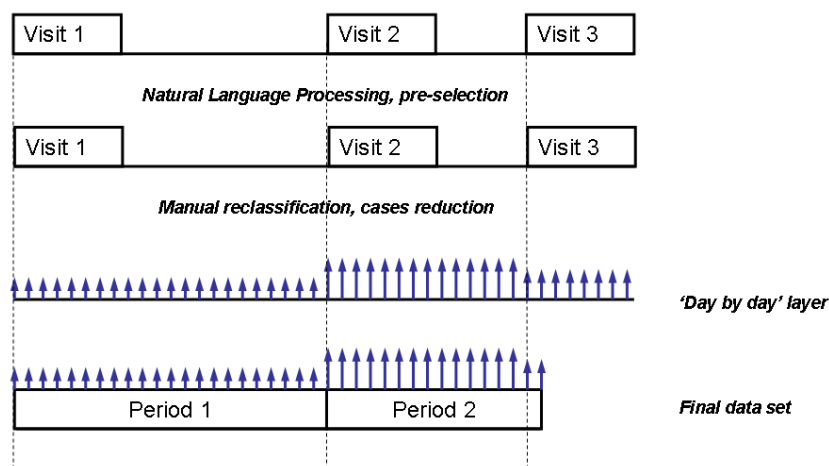


Fig. 1: Schematic of the final dataset creation

3 Results

Because the fields were text only and actually no strict rules were imposed on filling in the data, we found it difficult to automate the process of extracting information. The

key problems identified were: spanning the information over more than one field, typos, ambiguous abbreviations, shorthand and hyphenation. To account for discrepancy between visit date and outcomes that occurred days or months earlier, we found that a separate layer must be created that stores the events on a day by day basis. This allowed for instance to precisely compute the average prescribed daily doses (exposure).

During the observation period of ten years spirometry equipment was modernized, which resulted in a different reference range for the pulmonary function tests. That is why we found it more reasonable to extract the equivalents expressed in percentage of the predicted value. As the time factor was involved, over the years there were also subtle changes in therapy guidelines and also some proprietary drug forms have left the market. This all had to be taken under consideration.

Overall we found the acquired data valid. Repeated Measures ANOVA used to statistically analyze the results showed two already known trends in asthma. These were the presence of synergy between salmeterol and inhaled corticosteroids and montelukast positive influence on allergic rhinitis. The results were valuable as no observational study in asthma of such length was published before.

4 Conclusions

We concluded that extracting relevant medical information from legacy databases is possible, but the measures taken may be unfeasible on a larger scale due to time and resources involved. Also textual sources although offering far greater flexibility are not particularly well suited for automated data extraction.

Future ease of exporting data should always be considered when deciding how to store biomedical data. This is unfortunately rarely the case, as cheaper Database Management Systems are chosen over more expensive solutions built to last.

References

1. Leroy G, Chen H, Martinez JD.: A shallow parser based on closed-class words to capture relations in biomedical text. *J Biomed Inform.* (2003) 36(3):145-58.
2. Friedman C, Shagina L, Lussier Y, Hripcsak G.: Automated encoding of clinical documents based on natural language processing. *J Am Med Inform Assoc.* (2004) 11(5):392-402. Epub 2004 Jun 7.
3. Long-acting beta2-agonists versus anti-leukotrienes as add-on therapy to inhaled corticosteroids for chronic asthma. *Cochrane Database Syst Rev.* (2005) Jan 25;(1):CD003137.

VisualMind Framework for Brain-Computer Interface development

D.V. Karlovskiy¹ and V.A. Konyshv²

¹ Department of Biomedical Systems, Moscow State Institute of Electronics Technology (Technical University), Email: karlovskiy@yandex.ru

² Neurobotics Ltd., Email: vladimir@neurobotics.ru

1 Introduction

Any mental thought or movement planning and execution are accomplished by specific neuronal activity which is reflected on biopotentials recorded on scalp by means of electroencephalography. At present several systems, called Brain-Computer Interface (BCI), were created capable to differentiate temporal-spatial patterns of scalp biopotentials and to translate them to commands for controlling a computer and other electromechanical devices, e.g. mobile robots.

Such interface can be used in clinics by people with poor or lost neuromuscular control and by healthy person. For example, BCI user will be able to direct cursor to particular area on computer monitor, type messages or browse the Internet.

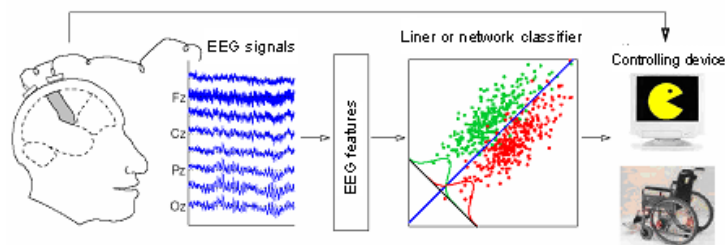


Fig. 1: Schematic view of BCI system components

Classical definition of BCI was formulated by Wolpaw (2002): “A BCI is a communication system in which messages or commands that an individual sends to the external world do not pass through the brain’s normal output pathways of peripheral nerves and muscles.”

Despite of the fact that BCI-system reliable provides only one dimensional control and, as a result, only binary decision tree it allowed to develop the impressive range of applications:

- Text typing;

- Internet browsing;
- Games (teletennis and Pacman);
- Prosthesis or robot control.

BCI systems can be classified by several criteria:

- Invasive (or implantable) and non-invasive;
- Synchronous and asynchronous;
- Universal or individual classificatory parameters setup;
- Offline and online operation;
- Type of used potentials.

2 Visualmind Framework

The most of contemporary EEG registration and analysis systems can't be used for BCI realization. Some of them lack the real time analysis; others lack flexibility of signal processing routines. That leads us to decision to create universal VisualMind framework which is organized as a set of independent program modules incapsulating different EEG processing algorithms and 2D/3D visualization. At design step, a framework user can select various analysis and visualization methods and then create the overall processing pipeline by inter connecting their inputs and output in a way of Simulink. During execution phase the framework will process the incoming EEG data fed to the pipeline.

For framework development we have selected .NET environment and C# programming language. That allowed us to develop quickly the distributed application which supports graph creation, their storage in XML format, data exchange through TCP/IP protocol, virtual scene and objects creation and control via Direct3D technology, registration equipment control.

This system was used for experiments with various BCI approaches as well as a standard EEG application. BCI application based on P300 cognitive component of evoked potentials is presented below.

To register P300 component an oddball stimulation paradigm is used. During such experiments two types of stimuli are used – frequent non-target and non-frequent target. Their proportion is typically set as 80 and 20%. Subject should count every appearance of target stimuli. Target stimulus is also referred as a relevant stimulus. After presentation of such stimulus a small positive deflection at 300 ms after stimuli onset will appear. It is called P300 component, lasts 300-400 ms and has amplitude 5-15 μV . Maximum amplitude is registered under Pz electrode. The smaller probability or percentage of target stimuli appearance, the bigger P300 amplitude is observed. Several averages is required to extract the component from background EEG activity which usually has amplitude 50-100 μV .

Based on this neurophysiological facts we have built several BCI modules to enter text in real time. It's stimulation window is shown below:

32 letters of Russian alphabet together with additional symbols and commands were presented on screen in front of subject as a virtual keyboard. Subject should fix his/her attention on the symbols to be entered. Stimulation is done as a repetitive intensification

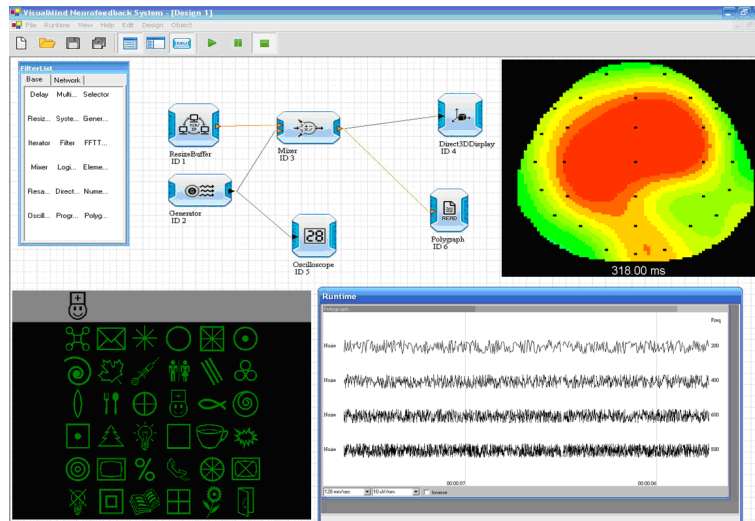


Fig. 2: VisualMind framework main window during execution

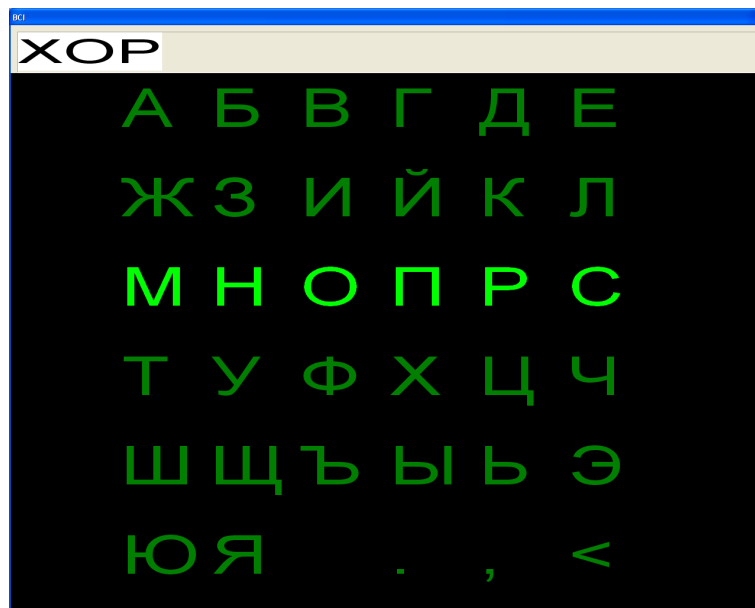


Fig. 3: VisualMind Stimulation window

of rows and columns in random order. As a row or column are flashed randomly the probability that intensity of the letter selected by subject will change is equal 16.7%. Probability for non-target stimuli is equal 83.3%. That ratio is optimal for recording the P300 component.

Usually only 15 averages were used to detect P300 component. After letter is identified, it appears at upper string of stimulation window. Using that module our subjects were able to enter short words and names. It takes around 90 seconds to enter a single letter, if interstimulus interval is set as 1000 msec.

Our current work on P300 BCI is related to built better classifier and to shorten interstimulus interval down to 125 msec. In that case single letter will be entered in 12-15 seconds. Other development is directed to usage icons instead of letters. The system is intended for disabled person communication with hospital staff.

References

1. Allison B. P3 or not P3: Toward a Better P300 BCI. PhD Thesis. 2004; UCSD
2. Farwell LA, Donchin E. Talking off the top of your head: towards mental prosthesis utilizing event-related brain potentials. *Electroenceph. Clin. Neurophysiol.* 1988; 70: 510-523
3. Millán J.del R, Renkens F, Mouriño J, Gerstner W. Noninvasive Brain-Actuated Control of a Mobile Robot by Human EEG. *IEEE Trans. Biomed. Eng.* 2004; 51(6): 1026-1033
4. Pfurtscheller G, Neuper C, Flotzinger D, Pregenzer M. EEG-based discrimination between imagination of right and left hand movement. *Electroenceph. Clin. Neurophysiol.* 1997; 103: 642-651
5. Pfurtscheller G, Zalaudek K, Neuper C. Event-related beta synchronization after wrist, finger and thumb movement. *Electroenceph. Clin. Neurophysiol.* 1998; 109: 154-160
6. Pfurtscheller G, Neuper C, Müller GR, Obermaier B, Krausz G, Schlögl A, Scherer R, Graimann B, Keinrath C, Skliris D, Wörtz M, Supp G, Schrank C. Graz-BCI: State of the Art and Clinical Applications. *IEEE Trans. Rehab. Eng.* 2003; 11(2): 177-180
7. Wolpaw JR, Birbaumer N, McFarland DJ, Pfurtscheller G, Vaughan TM. Brain-computer interfaces for communication and control. *Clinical Neurophysiol.* 2002; 113: 767-791

Usage of Hidden Markov Models for automatic sleep stages classification

L.G. Doroshenkov¹ and V.A. Konyshv²

¹ Department of Biomedical Systems, Moscow State Institute of Electronics Technology (Technical University), Email: leonid216@mail.ru

² Neurobotics Ltd., Email: vladimir@neurobotics.ru

1 Introduction

Brain activity level is determined by wake-sleep cycle. Sleep is organized as a sequence of several stages. Their cyclic organization proves the existence of the special regulatory system. This work is devoted to development of the algorithm for automatic sleep stages determination and following study of brain bioelectric activity during healthy sleep.

The most popular and widely used system for sleep classification was developed by Rechtschaffen and Kales (R&K) in 1968 [7]. The system allowed to standardize the criteria for sleep stages discrimination and thus provided the possibility to compare results of experiments from different laboratories and hospitals. According to that method, the whole EEG record is firstly divided on segments lasting 20-30 seconds and then for each segment main amplitude and spectrum parameters for standard EEG rhythms are calculated. By analyzing those values a human expert, e.g. somnologist, makes a decision about membership of analyzed segment to particular sleep stage.

Obviously, it is very hard and time consuming to use that method for analysis of whole night sleep recording which sometimes lasts as long as 8-10 hours. In spite of tremendous number of research in the field of automatic sleep stage classification [3, 5, and 8], still manual sleep staging systems are more popular than automatic ones.

For objective sleep studying we have used the polysomnography method which comprised on electroencephalography (EEG), electrooculography (EOG) and electromyography (EMG) registration. Then amplitude and frequency features were calculated and fed to neural net classifier based on Hidden Markov Models (HMM) [1]. That allowed us to identify sleep stages and phases and to build their sequence known as a hypnogram.

The results of that classification were validated by comparison with classification made by human expert who had utilized R&K rules. We have demonstrated that HMM can be used for sleep staging based only on 2 bipolar EEG channels (Fpz-Cz and Pz-Oz) with the quality sufficient for usage in real diagnostic process.

2 Sleep structure

Two different phases are discriminated during a sleep – slow wave sleep (SWS) and fast sleep (FS) [1]. In turn, slow wave sleep phase is divided on several stages. Each stage has different EEG picture and reflects difference in sleep depth:

Stage I, or drowsy stage, is characterized by gradual replacement of 8-12 Hz alpha-rhythm with low frequency oscillations like 4-7 Hz low amplitude theta-rhythm and some delta activity as well as low voltage high frequency beta activity. EEG can be described as a flat desynchronized signal with polymorphic low voltage components. Usually that stage lasts from 1 to 7 minutes. Slow waves appear mostly at the stage end. Their amplitude is below $75 \mu\text{V}$.

Stage II is characterized by appearance of sleep spindles. Spindles duration is 0.5-3 seconds and amplitude is around $50 \mu\text{V}$. Also in that stage K-complexes appear. They look as biphasic potentials frequently followed by sleep spindles. Their amplitude is maximal at vertex and duration is not less than 0.5 seconds. These complexes emerge spontaneously or as a response on sensory stimuli.

Stage III is characterized by increasing the delta activity with amplitude higher than $75 \mu\text{V}$. This activity occupies from 20 to 50% of all segment duration.

Stage IV is defined then amplitude of delta waves exceeds $75 \mu\text{V}$ and the waves occupy more than 50% of the segment duration.

Fast sleep phase is characterized by abrupt decrease of EEG amplitude with appearance of specific saw-tooth like signals, low voltage fast activity and rare alpha activity. Fast eye movement can be recorded by EOG channels and overall muscle tonus is decreased as registered by EMG channel. This phase is also referred as Rapid Eye Movement (REM) phase or paradoxical sleep.

In natural conditions a sleep starts by slow wave phase ranging from shallow sleep stage 1 to deepest stages 3 or 4 and then is replaced suddenly by fast sleep phase. That forms a single sleep cycle which lasts 90-120 minutes. During a whole night 4-5 such cycles can be observed for healthy persons. The duration of fast sleep is minimal at the sleep onset but gradually increases toward morning. In contrary, the duration of deep sleep (stages 3 and 4) is maximal at the 2nd and 3rd sleep cycle and diminishes toward the sleep end.

3 Method

For automatic sleep stage classification we have used signals from two EEG channels. Records were cut on 30 seconds segments. To extract and evaluate delta, theta, alpha and beta rhythms each segment was windowed by Hamming window and then filtered in correspondent frequency range by FFT-based band pass filter.

After filtration rhythm indexes and amplitudes were calculated. The amplitude was calculated as a difference between adjacent maximum and minimum. To define rhythm index we set a threshold. If amplitude of some signal portion exceeds the threshold, then that part was considered as containing the rhythm and its duration was added to index calculation. Additionally, we set upper threshold to eliminate movement artifact from calculations.

Alpha rhythm characteristics were defined from signal registered on Pz-Oz bipolar lead. To calculate features of other rhythms we have used Fpz-Cz bipolar lead.

Classification was made by utilizing HMM [6]. HMM represents a finite state machine which changes its state at a discrete time. Transitions between states are random with some fixed probabilities [4].

Calculated set of EEG features was used for initialization and training of HMM. Baum-Welch algorithm was employed for training. Following cluster analysis reveals the groups of similar elements, number of groups was set equal to number of stages to be identified. Cluster centers were stored in the model and used later to label observations.

Trained model was used for further classification by utilizing Viterbi algorithm which inputs a set of signal characteristics for all EEG segments. Resulting sequence of state changes is considered as a sequence of sleep stages.

As a last step, we have filtered obtained stages sequence by median filter to eliminate short-term transients. Such transients are related to non stationary EEG portions which have features from two different sleep stages. Value averaging for 2-3 minutes helps to clean up the graphics and to reveal better the sleep structure. Based on this post-filtration the hypnogram finally was plot.

4 Results

The algorithm was tested on 15 records containing several EEG channels, as well as EOG and EMG data. All records were scored by human expert according to R&K system [9]. To verify our algorithm the output of automatic evaluation was compared with expert scoring.

Upper portion of the figure 1 depicts the hypnogram built on the basis of HMM automatic classification. The picture lower part shows the hypnogram built by somnologist. Correlation between these two graphics is equal 0.7924.

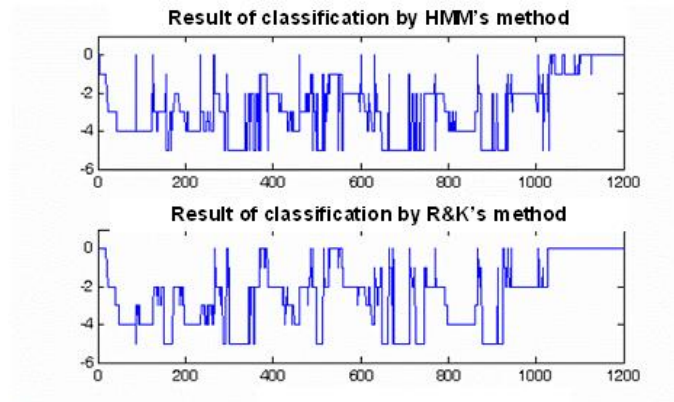


Fig. 1: Result of sleep stage classification without filtering

Both hypnograms expose some noisy behavior. To clean them up median filters with various length were applied. The effective filter order was determined experimentally and varied for different records.

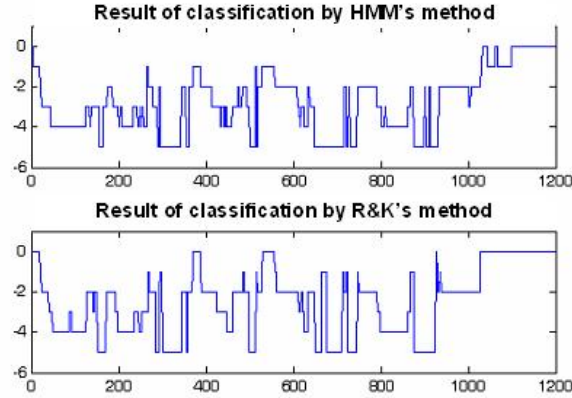


Fig. 2: Hypnograms after filtering by fifth order median filter

After filtration the correlation coefficient increased up to 0.8461. Classification results after filtering are shown in picture 2. Results for all records are summarized in table 1.

Table 1: Compare two classification methods: R&K and HMM (the table presents normalize coefficient of coincidence in every sleep stage)

		HMM					
		W	1	2	3	4	REM
R&K	W	0.5104	0.4730	0.0041	0	0	0.0124
	1	0	0.0484	0.4839	0	0	0.4677
	2	0	0	0.6862	0.2857	0.0077	0.0204
	3	0	0.0217	0	0.6413	0.3370	0
	4	0	0	0	0.0846	0.9154	0
	REM	0	0.0094	0.0472	0.0802	0	0.8632

Maximum coincidence between human and machine scoring is seen for stage 4 of deep sleep and equals 92%. REM stage is also matched with high accuracy (86% cases). The lowest classification precision was found for stage 1 and equaled 5%. In most cases this stage is classified either as stage 2 (48%) or REM sleep (47%).

Thus our algorithm can identify with high precision all key sleep stages such as REM, wakefulness and deep sleep. Further discrimination of slow wave stages is done with lower precision which is related to similarity between rhythm parameters for those stages [2].

5 Summary

The most important feature of our approach is that classification algorithm is trained without supervision. As a result, we don't need to create training set and can easily apply this method to different EEG records. Parameter calculation is performed individually for every subject. In contrast to traditional human scoring additional EOG and EMG channels are not required.

Automatic sleep analysis is more faster than manual scoring. Machine processing of 8 hours record takes less than 1 minute but it might take several hours for expert to evaluate the same record. Automatic analysis is objective because classification results are not tied with any subjective experience of human expert.

This system can be used in hospitals for sleep disturbance diagnosis as well as for fundamental sleep research.

Future work is related with the usage of additional polysomnograph channels to improve the diagnosis in clinics and with the development of portable Holter-EEG device which will allow to record sleep in natural environment outside research laboratory or hospitals.

References

1. Flexer, A., Sykacek, P., et al., "Using Hidden Markov Models to build an automatic, continuous and probabilistic sleep stager", IEEE Computer Society [IEEE-INNS-ENNS International Joint Conference on Neural Networks], 2000, Vol. III, pp. 627-631.
2. Flexer, A., Gruber, G., and Dorffner, G., "Improvements on Continuous Unsupervised Sleep Staging", Neural Networks for Signal Processing XII, Proceedings of NNSP 2002, Institute of Electrical and Electronics Engineers, Inc., New York, NY, pp. 687-695, 2002.
3. Malinowska U., Durka P.J., Blinowska K.J., Szelenberger W., Wakarow A., "Micro- and Macrostructure of Sleep EEG", IEEE Eng. Med. Biol. Mag., Vol 25, no. 4, pp. 26-31, 2006.
4. Novak D., Al-Ani T., Hamam Y., Lhotska L., "Electroencephalogram processing using Hidden Markov Models", 5th EUROSIM Congress on Modelling and Simulation, September 06-10, 2004, Paris.
5. Oropesa, E., Cycon, H. L., and Jobert, M., "Sleep Staging Classification using Wavelet Transform and Neural Network", Technical Report TR-99-008, International Computer Science Institute, Berkeley, California, pp. 6, March 30, 1999.
6. Pickup L. "Machine Learning Approaches for Brain-Computer Interfacing", Technical Report PARG-02-01, Pattern Analysis & Machine Learning Research Group in the Department of Engineering Science of the University of Oxford, pp. 49, 2002.
7. Rechtschaffen A., Kales A.A. A Manual of Standardized Terminology, Techniques and Scoring System for Sleep Stages of Human Subjects. Washington DC: U.S. Government Print. Office, Nat. Inst. Help Publ., 1968.
8. Shimada, T., Shiina, T., and Saito, Y., "Sleep Stage Diagnosis System with Neural Network Analysis", Proc. of the 20th Ann'l Int'l Conf. of the IEEE Engineering in Medicine and Biology Society, Hong Kong, China, no. 4, pp. 2074-2077, 1998.
9. International database PhysioNet <http://www.physionet.org/>

Cardiovascular Biosignal Analysis

Portable monitor for registration of ballistocardiographic signals

Yu.P. Masloboev¹, A.A. Ohritsky¹, D.A. Prilutsky¹, and S.V. Selishchev¹

Moscow Institute of Electronic Technology (Technical University)

1 Introduction

The basic function of the heart consists in the maintenance of necessary minute and systolic volumes of the blood by means of maintaining an appropriate pressure in the vascular system at the corresponding velocity of the blood flow. This function is usually referred to as the *pumping ability*, inasmuch as the cardiac muscle acts as two pumps creating necessary velocities of the blood flow and necessary pressure levels in the aorta and pulmonary artery (kinetic and hydrostatic effects). Cardiac efficiency of the heart with respect to maintaining the flow of the blood in the vascular system is the basic parameter of the functional condition of the myocardium. As a result of the cardiac contractions transforming energy into external work of the heart, a certain systolic volume and a certain blood velocity is maintained.

For practical purposes it is most convenient to estimate the external work of the heart with the help of the ballistocardiography (BCG) method [1]. According to this method micromovements of the human body are registered. The micromovements accompanying each cardiac contraction as a result of part of the energy of the blood circulation through the surrounding tissues and a skeleton being transformation to the body owing to the effect of "recoil". Ballistocardiogram is registered with the help of sensors attached to the body of a person lying on the back.

In BCG estimation it is important to take into account the influence of breath on the form and amplitude of the signal. This is due to the fact that at inhale and exhale there are opposite changes in the hemodynamics of the left and right heart. Usually, the respiratory fluctuations of the amplitude of the BCG complexes do not exceed 30-40 %, but in case of disruption of functional, energy and haemodynamic relations between the factors of inflow and expulsion of blood, respiratory fluctuations of the BCG amplitude increase [2].

Estimation of BCG records is a procedure of an expert character and is qualitative to a considerable extent. Expert BCG estimation is carried out in two directions: 1) Analysis of the peak amplitude that characterizes the conditional level of external work of the heart; 2) Analysis of changes in the amplitude and the form of BCG-complexes caused by breathing.

The method of seismocardiography (SCG) consists of registration of accelerations taken from the chest surface, caused by heart contractions. In the received records alongside with defining the phases of the cardiac cycle it is also important to measure the amplitude of the oscillatory cycle. The beginning of this cycle corresponds to the beginning of the phase of isometric ventricular contraction. The amplitude of the

cycle correlates with the maximum chamber pressure, thus reflecting the total cardiac work, i.e. characterizing the energy that is generated by the cardiac muscle at each contraction. By means of comparing the total cardiac work (SCG) with its external work (BCG) we can define the efficiency of the heart, i.e. the efficiency of the energy put out on maintaining the blood flow through the vessel.

Year by year mathematical analysis of cardiac rhythm is being used more and more extensively in clinical practice as a method of estimating the condition of different parts of the vegetative regulation system. In this study we present a portable monitor for registration of ballistocardiographic signals, constructed on the basis of Sigma-Delta ADC (analog-to-digital converter), as well as different approaches to processing signals of BCG and SCG with the help of neural-network algorithms.

2 Monitor for registration of ballistocardiographic signals

Monitor for registration of ballistocardiographic signals (MRB) is a device designed for acquisition of biological signals and the software for their processing on a personal computer. Registration of micromovements of the body is carried out by a built-in accelerometer sensor. The sensor consists of a thin steel disk with a piezoceramic structure in the center. The disk is weighted with a copper load on the back side. Fluctuation of the load affecting the steel disk causes polarization the piezoceramic structure. Electric potential arising from polarization varies in proportion to deviation of the pressure from its value in the initial position. The signals of the sensor after the analog-digital conversion are stored in the built-in memory of the device, or, if the device is switched to the monitoring mode, are displayed on the screen of the computer. Analog-to-digital converter (ADC) is the key element of the MRB. Characteristics of the ADC to a great extent determine the extraction quality of the valid signal against external disturbance. Analog-to-digital conversion is carried out by the microcircuit chip AD7714 manufactured by Analog Devices (USA). The microcircuit chip is a low-frequency high resolution sigma-delta ADC. Alongside with the analog-to-digital converter the device also contains built-in multiplexers, amplifiers with programmable coefficient of amplification and analog buffer-amplifiers.

Data transmission to the computer is carried out by means of a universal serial bus (USB). Management of the device is realized with the help of a built-in microcontroller.

The operation of the device is managed by a RISC microcontroller ATmega8515 manufactured by Atmel (USA). The signal of seismo / ballisto cardiograms is stored in non-volatile solid-state memory NAND such as KM29U128 manufactured by Samsung, storage space – 16 Mb. For more effective utilization of memory a lossless algorithm of signal compression is applied.

Here we apply a modified algorithm of differential adaptive coding. The algorithm is based on the fact that most part of time the signal is varying insignificantly within the limits of the proximate samples. It allows us to draw the conclusion that it will be more effective to store the difference between the amplitudes of the neighboring samples than its absolute value.

The microcontroller tracks out the condition of the button of event generation, providing synchronization of the time of the event occurrence and the stream of registered

data. In order to indicate the condition of the device two light-emitting diodes and a generator of sound signals are provided.

The monitor of biomechanical activity allows to register signals of micromovements of the body, caused by cardiac contractions, breathing and motion activity within the set period of time, the maximal duration of which is not less than 8 hours. Registered signals are stored in the built-in memory of the device, or, in the monitoring mode, are displayed on the screen of the computer.

There is only one battery used as a power source – galvanic element of standard size AA.

MRB can be used for registration of both ballistocardiograms and seismocardiograms. In order to register a ballistocardiogram the device should be attached to a special bed located on a special suspension bracket. This way it will register the movements of the body of the patient, caused by the emission of blood in the course of the cardiac activity. To register a seismocardiogram the device should be placed on the patient's chest, for example, in a special pocket of the vest. Thus it will be registering the movements of the chest.

Basic technical specifications of the MBA :

- Range of registered accelerations 0.001-0.1 m/s² ;
- Frequency range – 0-260 Hz.

Total energy consumption of the BMA makes up no more than 5,6 ìÀ . This guarantees operating capability of the device attached to a standard power source within the prescribed period of time (not less than 8 hours).

The MRB switches off automatically in case the built-in signal recording memory is exhausted, and there is no data exchange to a computer. To prevent the accidental disconnection of the device during an experiment, it is impossible to switch off the MRB with the control button, the device can be switched off only from the computer. If it is necessary to initialize the MRB, the adaptor plug should be inserted into a socket on the bottom side storage bank.

When the signal is being registered, the patient can mark the event himself. A special sound signal is designed to confirm that the mark has been made. This can be either a mark registering a change of the patient's condition, or the node point when the functional tests are carried out etc. When the seismo / ballisto cardiogram is reviewed, the tagged events are synchronized with the signal.

3 Algorithms of BCG and SCG analysis

Our next objective is the development of the software for processing the signals taken from the accelerometer sensor. The sensor signal is a complex function of the parameters of the cardiac rhythm, respiratory movements, motion activity, as well as with the parameters of cardiocycle. Accordingly, in order to allocate each of the listed parameters it is necessary to choose the most adequate mathematical method. Inasmuch as the connections between the form of the signal received from the gauge and calculated parameters are unknown in advance (especially regarding the parameters of motion activity and cardiocycle), it is reasonable apply methods based on self-training algorithms.

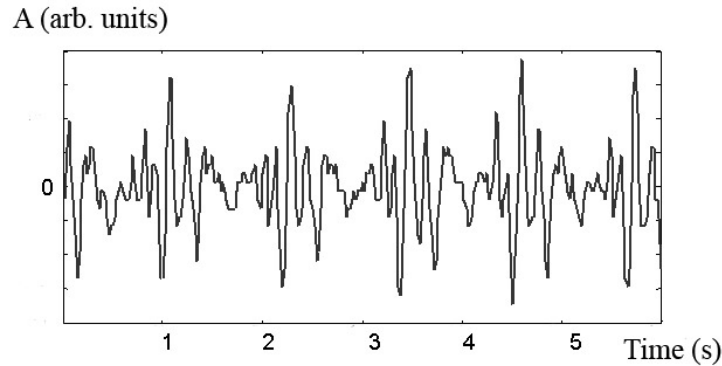


Fig. 1: The typical record of ballistocardiogram.

As such a method we suggest to use the algorithms of self-training artificial neural networks.

Analysis of the MRB signal must be carried out in two directions:

1. Analysis of periodic components of the signal carried out in order to allocate cyclic parameters, such as cardiac rhythm frequency and respiratory rhythm frequency.
2. Analysis of non-cyclic components of the signal carried out in order to such parameters, as those of the cardiocycle and motion activity.

For each of the directions it is necessary to choose a mathematical method, allowing to obtain the necessary information in an optimal manner.

The typical signal from the accelerometer sensor in the seismocardiogram registration mode is shown on Figure 1. The gauge was fixed on the patient's chest with the help of a special belt. The signal was registered in a motionless condition.

The diagram shows repeating cycles, each of which is the reflection of a separate cardiocomplex. The frequency of cycles is equal to the pulse rate. Thus, the pulse rate can be calculated on the basis of the Fourier spectrum of the signal. The same refers to the frequency of respiratory movements. However, the signal amplitude on the frequency of respiratory movements is much less than the signal amplitude on the pulse rate, therefore there may be the necessity of additional processing of the signal in order to suppress the noise. Thus, spectral analysis of the sensor signal can be accepted as the basis for the software for the analysis of periodic parameters. To increase the accuracy of the pulse rate measurements and that of the respiratory rhythm we shall require methods of noise abatement and, probably, methods of the correlation analysis.

Alongside with periodic components the MRB signal also comprises non-cyclic components caused by involuntary movements of the examinee, as well as components arising from the movement of the heart during a single cycle of cardiac activity.

Involuntary movements of the examinee are characterized by an increased signal amplitude and can be singled out from the signal by means of amplitude discrimination. In Figure 1 the surges caused by involuntary movements can be well seen.

Thus, the calculation of the quantity of involuntary movements, as well as the analysis of relative amplitudes of these movements can be performed on the basis of the amplitude analysis of the surges of the signal with accurate time correlation. Besides, involuntary movements can be accurately correlated with cardiac activity and respiratory phases.

4 Application of neural-network algorithms

From the point of view cardiovascular system condition diagnostics of special interest is the opportunity to receive information about the parameters of each cardiocycle by analyzing separate fragments of the gauge-accelerator readings. Here we have in mind the analysis of cycles of the signal associated with cardiac activity (see Figure. 1). Each signal cycle is the response of a cardiac muscles contraction and therefore contains information about the parameters of this cardiocomplex. To extract this information it is necessary to know the details of the transmission of motions from the heart to the gauge, which does not seem possible today. However, there are algorithms that can help to solve this problem. In the present study we suggest that neural-network algorithms should be applied with the purpose of extraction of the information about the parameters of separate cycles from the acceleration sensor signal.

Let us briefly consider two ways of neural-network algorithms application for the analysis of the signal. The first way is to use unidirectional neural network [3] for extraction of the parameters of the ballistogram. The second variant resorts to self-organizing Kohonen network [4] for classification of separate fragments into several classes, each of which should correspond to a concrete deviation of the parameters of cardiac activity from the norm.

Neural network consists of the several layers, interconnected in such a manner that the output signal of one layer, multiplied by weight-coefficient matrix, comes to the input of the layer next to it. Each neuron of the layer performs the elementary processing of the signal, which consists in summing-up input signals, adding the shift parameter and transformation of the signal with the help of the activation function.

In order the neural network can solve a specific task, i.e. extract the parameters of a certain signal when it is applied to the input, it is necessary to train the network. The training of the network consists in selecting weight coefficients and shifts. To perform the training we shall need to have a certain number of input vectors and the correct values of the output parameters corresponding to them – the training array. The procedure of network training consists of the following steps. A certain vector from the training array is applied to the network entry point. The output vector value received at the network output is compared to the correct value of the output vector from the training array. Then the correction of weight-coefficients and shifts is performed to reduce the difference between the network output and correct (reference) value. This procedure shall be repeated a number of times to cover all the values of the training array. Such training procedure is called *supervised training* or *training with a teacher*. After the training the values of the weight-coefficients and shifts shall be fixed and the network it is ready for operation – by applying an input vector to the entry point we shall receive correct values of output parameters on the output.

As input values to be applied to the network entry it is possible to use either the signal itself (its values at the discretization points) or a certain set of the signal parameters (for example, values of amplitudes, time intervals or spectral coefficients). To choose the input representation of the signal further research is required. As output network values we shall use a set of basic parameters of the ballistogram. To draw up a training array it is necessary to carry out a number of experiments on simultaneous measurement of the signal of the accelerometer sensor and ECG registration.

The above described approach to the analysis of the accelerometer sensor signal is considered to be quite promising, however, it will require further research focused on building-up the training array, optimization of neural network architecture, selection of the representation form of the input data, optimization of the training procedure.

The second approach to neural-network algorithms is based upon the application of the self-organizing Kohonen networks.

Kohonen networks essentially differ from all the other types of networks. While all other networks are intended for the objectives of the supervised training, Kohonen networks are designed for unguided training.

In the process of supervised training, the observations, working out training data, apart from the input variables also contain the corresponding output values, and the network must reconstruct the projection by translating the first into the second. In case of unguided training, the training data contain only the values of input variables.

In Kohonen network the so-called competing function of activation is often used, which is not valid for each separate neuron – but it is applicable to the whole layer. As a result on of this activation function zero value is assigned to the outputs of all the neurons, except for the neuron with the maximum distance, and the value 1 is assigned to the neuron output with the minimum distance (the winner neuron). Thus, the output vector \mathbf{a} has only one element equal to 1, and the other are equal to 0.

The Kohonen layer classifies input vectors in groups on the basis of their similarity. This is achieved with the help of such exact adjustment of the weights of the Kohonen layer that the closely-spaced input vectors activate on and the same neuron of this layer. Kohonen's training is a self-training, performed without reference values of the outputs (training without a teacher). Therefore, it is difficult (and not necessary) to predict, which Kohonen neuron exactly will be activated for the set input vector. It is only necessary to guarantee that as a result of the training the non-similar input vectors are separated.

Thus, as a result of self-training the Kohonen network acquires the "skill" to group input data into several classes.

As applied to the analysis of gauge-accelerator signals the Kohonen network can be used in the following way. As the input data of the network we will use the same data as was used for the unidirectional network (for example, values of amplitudes, time intervals or spectral coefficients). These data will be used for the training of the network. During training the network acquired the ability to group the input data into several classes (according to the number of neurons in the Kohonen layer). Each class will correspond to a certain condition of the examinee. For example, in case the data in split into two classes, one class will corresponds to the normal condition, the other – to the pathological. Thus, by consistently applying input signal to the entry point of the

network, at an output we shall receive the characteristics of the examinee's conditions (norm / pathology).

For the realization of this algorithm it is also necessary to carry out additional research focused on optimization of network parameters, choosing the quantity of classes and, probably, a certain modification of the network by way of adding a supplementary layer.

5 Conclusion

The small-sized monitor of biomechanical cardiac activity can be used for monitoring cardiovascular system condition both in clinic, and in actual practice.

In order to perform the analysis of cardiocycle parameters and obtain necessary the information about the parameters of the ballistocardiogram we suggest that neural-network algorithms of signal processing should be used. In particular – unidirectional neural networks and the self-organizing Kohonen networks.

References

1. Kiessling C.E., Preliminary appraisal of the prognostic value of ballistocardiography, *Biblioteca Cardiologica*, vol. 26, 292-295, 1970
2. Polo O., Tafti M., Hamalainen K., Vahtoranta K., Alibanka J., Respiratory variation of the ballistocardiogram during increased respiratory load and voluntary central apnoea, *Eur. Respir. Journal*, pp. 257-262, Vol. 5, 1992
3. Osovskii, C., *Neural Networks for Information Processing*, Moscow: Finansy i statistika, 2002
4. Kohonen T. 1988. *Self-organization and associative memory*. 2d ed. New-York, Springer-Verlag.

Mitral Valve Surgery Impedes Recovery of Cardiovascular Autonomic Function

B. Retzlaff¹, N. Wessel², H. Malberg³, G. Brockmann¹, C. Uhl¹, R. Lange¹, and R. Bauernschmitt¹ *

¹ German Heart Center Munich, Lazarettstr. 36, D-80636 München,

² University of Potsdam,

³ University of Karlsruhe
retzlaff@dhm.mhn.de

Abstract. Baroreflex Sensivity (BRS) and heart rate variability (HRV) have significant influence on the patients' prognosis after cardiovascular events. The following study was performed to assess the differences in the postoperative recovery of the autonomic regulation after mitral valve (MV) surgery and aortic valve (AV) surgery with heart-lung machine. 43 consecutive male patients were enrolled in a prospective study; 26 underwent isolated aortic valve surgery and 17 isolated mitral valve surgery. Blood pressure, ECG and respiratory rate were recorded the day before, 24h after surgery and one week after surgery. BRS was calculated according to the Dual Sequence Method, time and frequency parameters of HRV were calculated using standard methods. There were no major differences between the two groups in the preoperative values. At 24 h a comparable depression of HRV and BRS in both groups was observed, while at 7 days there was partial recovery in AV-patients, which was absent in MV-patients: p (AV vs. MV) $<0,001$. While the response of the autonomic system to surgery is similar in AV- and MV-patients, there obviously is a decreased ability to recover in MV-patients, probably attributing to traumatic lesions of the autonomic nervous system by opening the atria. Ongoing research is required for further clarification of the pathophysiology of this phenomenon and to establish strategies to restore autonomic function.

1 Introduction

The well-known depression of cardiovascular autonomic function following cardiac surgery is related to a variety of reasons like anaesthesia and the use of the heart-lung-machine [1,2]. The role of direct surgical trauma to the autonomic nerves (AN) is still unclear. The following study was performed comparing patients with isolated aortic valve replacement (AV, the surgical trauma to AN is considered to be low) or isolated mitral valve surgery (MV, high surgical trauma to AN is expected). With regard to the hypothesis that there is a traumatic lesion of the cardiovascular autonomic nervous system by opening the atria we observe the postoperative recovery of AV- and MV-patients.

* This study was supported by grants from the Deutsche Forschungsgemeinschaft (DFG BA 1581/4-1, BR 1303/8-1, KU 837/20-1).

2 Methods

43 consecutive male patients were analysed. 26 of them underwent aortic valve surgery and 17 of them mitral valve surgery. The mean age of AV-patients was 63 +/- 13 years and the mean age of MV-patients 59 +/- 12 years. Patients with concomitant coronary heart disease were excluded for the known effects of atherosclerosis. Perioperative medication was standardized.

Anaesthesia was standardized; induction was performed with sufentanil and midazolam. For maintaining narcosis, a continuous infusion of propofol was given; muscle relaxation was achieved by pancuronium. Central venous pressure and pulmonary artery pressure were monitored by a Swan-Ganz catheter, arterial pressure by cannulation of the radial artery. All operations were carried out with cardiopulmonary bypass (CPB) in mild hypothermia (32-34°C) and pulsatile perfusion mode, cold crystalloid cardioplegia or blood cardioplegia (isolated bypass surgery) was used for cardiac arrest. After declamping, most of the patients needed one countershock to terminate ventricular fibrillation.

After 10-min equilibrations to the environment, non-invasive blood pressure signals were collected from the radial artery by a tonometer (Colin Medical Instruments) at 1000 Hz. Data were channelled into a bed-side laptop after A/D-conversion and stored for analysis. Simultaneously, breathing excursions and a standard ECG were monitored. Data were sampled for a 30-min period the day before surgery, 24h and seven days after surgery on the ICU. Care was taken to perform the measurements during the same time of the day in each patient. From the recorded data the beat-to-beat intervals as well as the beat-to-beat systolic and diastolic values were extracted; premature beats, artifacts and noise were excluded using an adaptive filter considering the instantaneous variability.

Baroreflex sensitivity (BRS): Dual Sequence Method (DSM)

Using the DSM, the most relevant parameters for estimating the spontaneous baroreflex (BR) are the slopes as a measure of sensitivity. The DSM is based on standard sequence methods with several modifications: Two kinds of BBI responses were analyzed: bradycardic (an increase in systolic blood pressure (SBP)) that causes an increase in the following beat-to-beat-intervals (BBI) and tachycardic fluctuations (a decrease in SBP causes a decrease in BBI). Both types of fluctuations were analyzed both in a synchronous and in a 3-interbeat-shifted mode. The bradycardic fluctuations primarily represent the vagal spontaneous BR analysis of the tachycardic fluctuations represent the delayed responses of heart rate (shift 3) assigned to the beginning slower sympathetic regulation. The following parameter groups are calculated by DSM: (1) the total numbers of slopes in different sectors within 30 min; (2) the percentage of the slopes in relation to the total number of slopes in the different sectors; (3) the numbers of bradycardic and tachycardic slopes; (4) the shift operation from the first (sync mode) to the third (shift 3 mode) heartbeat triple; and (5) the average slopes of all fluctuations. DSM parameters are defined as described by Malberg et al [4].

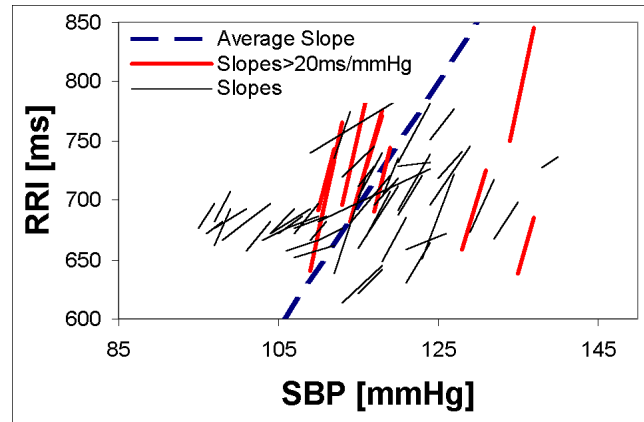


Fig. 1: Schematic representation of the two main baroreflex parameters estimated by the Dual Sequence Method: the average slope (dotted line) of all baroreflex sequences as well as the total number of baroreflex slopes above 20 ms/mmHg (thick lines). The thin lines symbolize all baroreflex slopes below 20 ms/mmHg.

Heart rate variability (HRV)

Respecting the suggestions by the Task Force HRV [3], the following standard parameters are calculated from the time series: MeanNN (mean value of normal beat-to-beat intervals): Is inversely related to mean heart rate. sdNN (standard deviation of intervals between two normal R-peaks): Gives an impression of the overall circulatory variability. Rmssd (root mean square of successive RR-intervals): Higher values indicate higher vagal activity. Shannon (the Shannon entropy of the histogram): Quantification of RR-interval distribution. Apart from the time-domain parameters mentioned above, the HRV analysis focused on high-frequency components (HF, 0.15-0.4 Hz, high values indicate vagal activity) and low-frequency components (LF, 0.04-0.15 Hz, high values indicate sympathetic activity). The following ratios were considered: LFn – the normalized low frequency ($LFn = LF / (LF + HF)$), HP/P - the to the total power P normalized high frequency as well as LP/P - the P-normalized low frequency.

Nonlinear dynamics

New parameters can be derived from methods of nonlinear dynamics, which describe complex processes and their interrelations. These methods provide additional information about the state and temporal changes in the autonomic tonus. Several new measures of non-linear dynamics in order to distinguish different types of heart rate dynamics as proposed by Kurths were used. The concept of symbolic dynamics is based on a coarse-graining of dynamics. The difference between the current value (BBI or systolic blood pressure) and the mean value of the whole series is transformed into an alphabet of four symbols (0; 1; 2; 3). Symbols '0' and '2' reflect low deviation (decrease or increase) from mean value, whereas '1' and '3' reflect a stronger deviation (decrease or increase

over a predefined limit, for details see Voss et al.). Subsequently, the symbol string is transformed to 'words' of three successive symbols explaining the nonlinear properties and thus the complexity of the system.

The Renyi entropy calculated from the distributions of words ('fwrenyi025' - $a = 0.25$) is a suitable measure for the complexity in the time series ('a' represents a threshold parameter). Higher values of entropy refer to higher complexity in the corresponding time series and lower values to lower ones. A high percentage of words consisting only of the symbols '0' and '2' ('wpsum02') reflects decreased HRV. The parameter 'Forbidden words (FW)' reflects the number of words which never or very rarely occur. A high number of forbidden words are typical for regular behaviour, while in highly complex time series, only very few forbidden words are found.

3 Results

There were no major differences among the two groups preoperatively. At 24h after surgery, both groups showed a comparable depression of HRV and BRS. One week after surgery, however, marked differences were present: SDNN 15+/-6 (MV) vs. 42+/-33 (AV); $p < 0.001$ (Fig. 1).

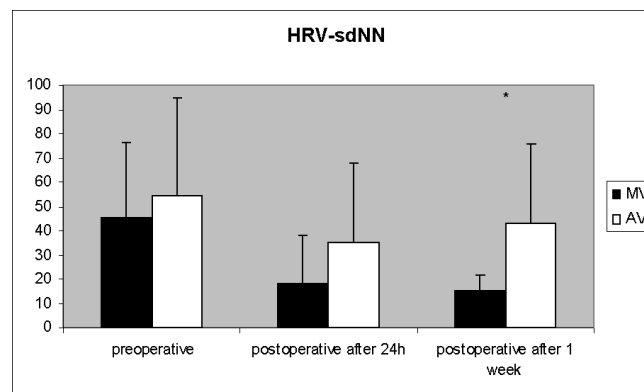


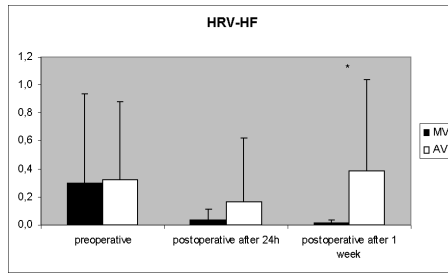
Fig. 2: HRV-sdNN, heart rate variability - standard deviation of beat to beat intervals

Similar kinetics were found for the High- and Low-Frequency components of HRV (HF 0.01+/-0.02 (MV) vs. 0.38+/- 0.64 (AV); $p < 0.02$ (Fig. 3)).

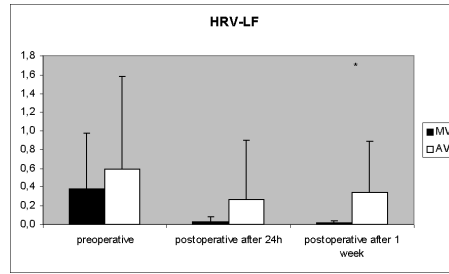
Regarding the nonlinear parameters, there was a significant depression present already 24h after surgery with mitral patients more suppressed than aortic patients, these alterations being even more distinct after one week (Fig. 3).

The baroreflex was impacted in a similar way for both the number and strength of regulations (BRS bradycardic) 4.5+/-1.2 (MV) vs. 7.3+/-2.7 (AV); $p < 0.001$ (Fig. 5).

For the tachycardic part of the baroreflex, however, the differences among aortic and mitral patients failed significance after one week ($p < 0.08$, data not shown).



(a) high frequency (indicator for parasympathetic regulation)fig2



(b) low frequency (indicator for sympathetic regulation)fig3

Fig. 3: HRV, high frequency (HF) and low frequency (LF)

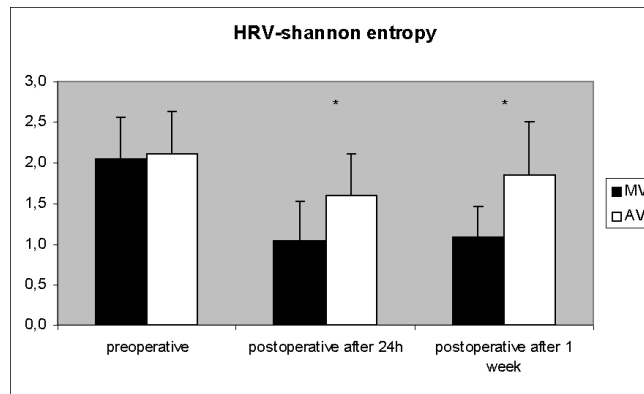
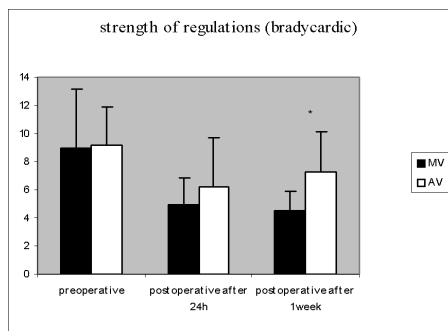
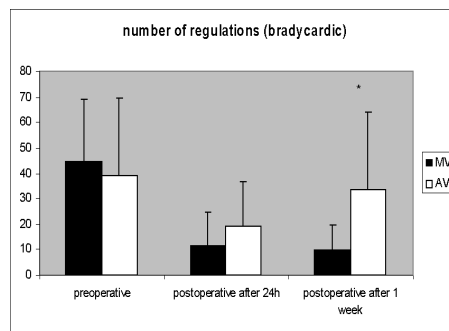


Fig. 4: HRV, Shannon-entropy



(a) BRS, strength of bradycardic regulations-fig5



(b) BRS, number of bradycardic regulations-fig6

Fig. 5: BRS, Baroreflex Sensivity

4 Discussion and conclusions

The last decade witnessed a strong increase in basic knowledge of the cardiovascular autonomic system. However, as far as alterations in the cardiac patient and in patients undergoing open heart surgery are concerned, we are still at the very start.

Meanwhile it is well known, that cardiac surgery leads to an early depression of autonomic function, and that there is potential for recovery after a certain time frame. The mechanisms for both phenomena are quite unclear, so the aim of the present study was to shed light on the precise role of direct surgical trauma. In contrast to earlier studies, where different preoperative conditions and different surgical procedures were mixed up, we focussed on patients with isolated aortic valve disease and isolated mitral valve disease, thus excluding the well known influences of atherosclerosis on cardiovascular autonomic function. On the other hand, the operative procedures done in these patients offer two entirely distinct entities of surgical trauma: while for aortic valve replacement the heart is left more or less untouched and the valve is approached by an incision in the anterior aspect of the ascending aorta only, in mitral valve operations, both the caval veins are extensively dissected, and the heart is opened by an incision right posterior to the interatrial groove, where an abundance of autonomic nerve endings are supposed to be.

The similar depression in both groups observed at 24h may reflect the effects of standardized anesthesia and perioperative treatment being comparable in all patients. While AV-patients showed a clear tendency to recover after one week, no recovery was recorded in MV-patients. In our opinion, this is a strong indicator of higher surgical trauma to AN, if the atria are dissected. Recovery of autonomic fibres is possible, even in heart transplant patients, as described earlier, so the next step will be investigating time and frequency parameters and baroreflex sensitivity after six months to give evidence of the hypothesis of direct surgical trauma.

Summarizing, we were able to demonstrate for the first time, that direct surgical trauma can be one of the major mechanisms leading to depression of cardiovascular autonomic function. The diversity of results in earlier studies may be caused by the case-mix of patients, comprising different initial conditions as well as different extents of trauma.

References

1. C. A. Brown, L. A. Wolfe, S. Hains, G. Ropchan, J. Parlow. Spontaneous baroreflex sensitivity after coronary artery bypass graft surgery as a function of gender and age. *Can. J. Physiol. Pharmacol.* 2003;(9): 894–902.
2. R. Bauernschmitt, H. Malberg, N. Wessel, B. Kopp, E. U. Schirmbeck EU, R. Lange. Impairment of cardiovascular autonomic control in patients early after cardiac surgery. *Eur J Cardiothorac Surg* 2004;25(3):320-326.
3. H. Malberg, R. Bauernschmitt, U. Meyerfeldt, A. Schirdewan, N. Wessel. Short-term heart rate turbulence analysis versus variability and baroreceptor sensitivity in patients with dilated cardiomyopathy. *Z Kardiol* 2003;92(7):547-557.
4. Heart rate variability Standards of measurement, physiological interpretation, and clinical use. Task Force of The European Society of Cardiology and The North American Society of Pacing and Electrophysiology. *European Heart Journal* 1996;17: 354–381.

Blood Pressure Estimation based on Pulse Transit Time and Compensation of Vertical Position

Dipl.-Inform. Med. Christian Douniama and Dipl.-Ing. Robert Couronné
christian.douniama@iis.fraunhofer.de

Fraunhofer Institute for Integrated Circuits, Germany
Am Wolfsmantel 33 – 91058 Erlangen
+49 (9131) 776-7349

Abstract. A chronically high blood pressure (BP) may lead to arteriosclerosis and consequently is a risk factor for apoplectic stroke and cardiac infarction – the main death causes in industrial countries. Hence, blood pressure recently has become one of the most relevant parameters for the assessment of a patients' health status. For the purpose of a continuous monitoring of cardiovascular patients, we have investigated a non-invasive and continuous (beat-by-beat) blood pressure estimation model, which is not based on the occlusion of arteries (like i.e. the auscultatory or the oscillometric method), but on the so called pulse transit time (PTT). In two studies, on the one hand we have evaluated the assumed linear relationship between pulse transit time and blood pressure and on the other hand we have examined the correlation between heart-rate and pulse transit time respectively the influence of the measuring arm position on the measured PTT.

1 Introduction

Blood pressure (BP) measurements have become one of the most relevant and cost effective methods for the assessment of a patients' health status. Since a chronically high BP may lead to arteriosclerosis and consequently is a risk factor for apoplectic stroke and cardiac infarction – the main death causes in industrial countries – a continuous monitoring of cardiovascular patients is highly recommended. Besides conventional techniques (like i.e. the auscultatory or the oscillometric method), another continuous and non-invasive, model-based approach to determine blood pressure values exists, which is not based on the occlusion of arteries but on the so called pulse wave transit time (PTT) [1]. A pulse wave in this context is defined as a pulse pressure wave, which is caused by the contraction of the heart and which is propagating through the vascular system from the heart to the periphery. Due to the vascular systems' properties (arterial diameter, vascular wall elasticity, blood viscosity and damping) there is a strong dependency between the transit time of the pulse wave (from the heart to a peripheral site) and its pressure, which is the arterial blood pressure (BP). The PTT is calculated as the temporal difference between the R-peak in an electrocardiogram (ECG) and the front slope of the following pulse wave measured by a finger photoplethysmograph (PPG) (see **figure 42**). In this way, one is able to form a beat-by-beat blood pressure estimation on the basis of pulse wave transit time.

To evaluate the approach and the correlation between PTT and BP (which is assumed linear by many publications [2, 3, 4]), and to investigate the influence of additional parameters (in this case *heart-rate* and the *vertical arm-position* wearing the finger PPG in relation to the heart), two separate studies [5] have been carried out.

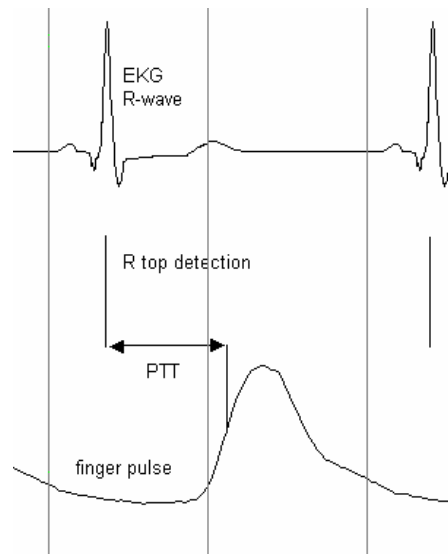


Fig. 1: The definition of pulse wave transit time

2 Evaluation of PTT/BP Model

The purpose of the first study, with 15 healthy volunteers (10 males and 5 females of ages 23 – 56), was to evaluate the assumed linear PTT/BP model.

Here, the test subjects' blood pressure (and so the pulse wave transit time) was steadily altered by an ergometric exercise of about one hour. During this time, the PTT as well as the corresponding reference BP were measured every 1 – 2 minutes. For the calculation of the beat-by-beat transit times an ECG with a sampling frequency (f_s) of 1 kHz and a finger PPG with $f_s = 200$ Hz synchronously were recorded. The corresponding reference blood pressure was measured with an auscultatory cuff. Furthermore, the ECG signal served as the source for heart rate (HR) calculation.

3 Examination of PPG-Position/PTT Relationship

The purpose of the second study, with six healthy male volunteers (of ages 26 – 31), was to investigate the relationship between the vertical position (relative to the heart)

of the arm wearing the finger PPG and the pulse wave transit time. For gravity reasons, the mentioned position has a significant impact on the PTT.

Here, the test subjects have changed the finger PPG sensors' vertical position every two minutes by raising the according arm (which was the left) from “beneath heart-level” (arm down) to “heart-level” to “above heart-level” (arm up). For every arm-level the PTT was determined by averaging the corresponding recorded transit times. The calculation of the pulse transit times was realized as explained above.

4 Results of Measurements

In our first study, we have observed a strong correlation between PTT and systolic blood pressure with a mean correlation coefficient of $r = 0.83$ (range: 0.61 – 0.98). In comparison, the correlation between PTT and diastolic blood pressure with mean $r = 0.36$ (range: 0.01 – 0.53) was rather weak (see figure 42). The blood pressure estimation error standard deviation in our study was in the interval 5.8 – 8.3 mmHg for systolic BP and in 5.9 – 6.7 mmHg for diastolic BP. Besides, there was also a very strong correlation between heart-rate and pulse transit time with mean $r = 0.95$ (range: 0.92 – 0.96). In our second study, as expected we have observed very significant differences in pulse transit time at different finger PPG sensor positions (see figure 42). There was a mean PTT difference (i) of 25 ms (STD: 17 ms) between “heart-level” and “beneath heart-level” and (ii) of 85 ms (STD: 53 ms) between “heart-level” and “above heart-level”.

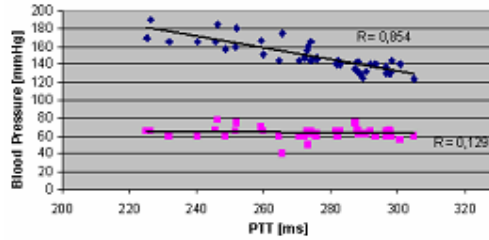


Fig. 2: Correlation between PTT and systolic BP (above) / diastolic BP (below)

5 Discussion

In our investigations the correlation between pulse transit time and (at least) systolic blood pressure could be confirmed. So, with respect to a certain error (5.8 – 8.3 mmHg) the linear model turned out to be an appropriate estimator for systolic BP.

To improve accuracy and reliability of the method, heart-rate has to be integrated in future model developments, since next to the PTT it was proved high correlation to the systolic blood pressure.

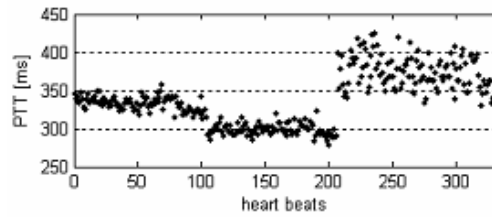


Fig. 3: PTT at different arm-levels: “heart-level (HL)” (left); “beneath HL” (middle); “above HL” (right)

In order to avoid severe blood pressure estimation errors, it is recommended to detect or better compensate PTT changes caused by a vertical finger PPG sensor displacement, because gravity effects in this case falsify the quantitative relationship between PTT and BP.

Due to the small number of subjects these results are preliminary and have to be confirmed by studies with representative number of persons or even patients. To achieve the reliability and accuracy in blood pressure estimation sufficient for medical use additional studies have to be conducted. Especially the variance of blood pressure values over days and weeks for one person, the variance within day profiles, sex and age specialities and the influence of drug delivery should be subject to investigations.

References

1. Continuous Blood Pressure Determination during Exercise ECG Recording, D. Barschdorff, M. Erig, *Journal of Biomedical Engineering* 43, pp. 34 – 39 (1998)
2. Pulse Transit Time as an Indicator of Arterial Blood Pressure, L. A. Geddes, M. H. Voelz, C. F. Babbs, J. D. Bourland, W. A. Tacker, *Psychophysiology* 18, pp. 71 – 74 (1980)
3. Clinical Evaluation of Continuous Noninvasive Blood Pressure Monitoring: Accuracy and Tracking Capabilities, C. C. Young, J. B. Mark, W. White, A. DeBree, J. S. Vender, A. Fleming, *Journal of Clinical Monitoring* 11, pp. 245 – 252 (1995)
4. Pulse Transit Time Changes Observed with Different Limb Positions, J. Y. A Foo, S. J. Wilson, G. R. Williams, M.-A. Harris, D. M. Cooper, *Physiological Measurement* 26, pp. 1093 – 1102 (2005)
5. <http://www.sensave.de/>

Automatic Extraction of quasi-Synchronous Views from Rotational Angiographic Sequence without ECG-Data

Sahla Bouattour and Dietrich Paulus

Institute of Computational Visualistics, University of Koblenz-Landau, Germany
bouattour@uni-koblenz.de
<http://www.uni-koblenz.de/agas>

Abstract. In this contribution we present an automatic method to extract quasi-synchronous views from a sequence of monoplane rotational coronary angiograms. Based on the work of Blondel et al. we build the image of horizontal integrals, which contains information about the vertical motion of the coronary tree. The maxima of this motion correspond to end-diastole states. We extract a curve of vertical motion and perform a spectral analysis to extract local maxima. We perform a spatial analysis to detect irregularities in the cardiac cycle, in order to extract just the regular views. Finally we present experiments on several angiographic sequences and compare the results to available electrocardiogram (ECG-) signal.

1 Introduction

3D centerline reconstruction of coronary vessels from rotational angiography sequences mostly involves ECG-data to detect synchronous views [1,2]. Of interest are the end-diastolic states, since the heart has the minimal motion in this state. Several problems arise with the usage of ECG data: Firstly, the assignment of heart states from the ECG-signal is not an easy task and can be unprecise. Secondly, examined patients can have coronary diseases therefore the ECG-data is misleading. Thirdly, the next generation of C-arms does not offer the triggering with this signal. Finally there is a delay between the electrical state observed in the ECG-signal and the mechanical state observed in the angiograms [3]. Therefore, there is a need to develop methods for automatic extraction of *mechanically* synchronous views directly from the image sequence.

Based on the idea of Blondel [3], synchronous views can be extracted from a rotational monoplane angiographic sequence by analyzing the curve of vertical motion (CVM). Each image is preprocessed to enhance only the vessels. The *horizontal integrals* are then computed: For each row the sum over all columns is calculated. This integration marginalizes the horizontal motion and captures the vertical one. All these vectors (for each frame) are concatenated to get an image of horizontal integrals. The end-diastolic views are the maxima of the motion observed. To extract them a reference frame should be specified and the distances between the horizontal integrals of the reference image and the rest of the sequence are computed to get a one-dimensional CVM. Synchronous views are determined by computing the periode using the auto-correlation function of the curve. This method assumes a preprocessing, which completely eliminates the background and just preserves the vessels. It also assumes a certain regularity in the cardiac cycle and depends on the chosen reference image. In this contribution we present a new method, which try to overcome these limitations.

2 Method

We preprocess a whole sequence with an operator that enhances the vessels and reduces the background [4]. Scales that enhance especially big vessels are used. Those are mostly located at the beginning of the coronary tree and are bound in their motion. We build the image of horizontal integrals as described in [3]. The CVM is approximated by the *curve of maxima* along each column (red curve). Figure 1 visualizes these steps.

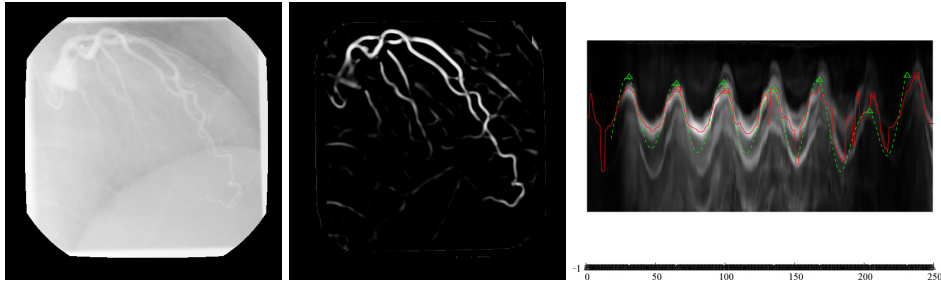


Fig. 1: From left to right: original image. Preprocessed image. The image of horizontal integrals.

Spectral Smoothing: The CVM is denoted by a set of points $v = v_0, \dots, v_{N-1}$ of length N , the number of frames in the sequence used to compute the image of horizontal integrals. This is a finite discrete signal, which is mostly corrupted by noise and irregularities. Performing a Fourier transform would only deliver useful information if the signal is periodic or regular. Computing the power spectral density requires stationarity of the signal. Those are in most sequences not available. So we propose to perform a local spectral analysis using the short time Fourier transform (STFT). We aim to transform the signal v into a smoother one, having similar developing and preserving the maxima. The (finite) STFT can identify not only the frequency content of a signal, but also how that content evolves over time:

$$\text{FSTFT}(n, k) = \sum_{\tau=0}^{T-1} v_{\tau} \gamma_{\tau-n}^* \exp\left(-j \frac{2\pi}{T} k \tau\right), \quad k = 0, \dots, T-1, \quad (1)$$

where γ_n^* is the complex conjugate of a *window* function, having a short time duration, T represents some power of two containing the product of the signal and the window function which is zero-padded to the desired length T . Since we are dealing with a pseudo-sinusoidal noisy signal we propose to take the dominant period of the signal as the width of the window $W = P_D$, where $P_D = \frac{N}{|k_{\max}|}$ and k_{\max} is the index of frequency of highest amplitude among the Fourier coefficients of the Fourier transformed signal v . This choice has the advantage that we are able at some locations (at maxima) to recover a stationary signal with a complete single dominant period of the original signal. Several typical window functions, that approximate the ideal but infinite

Gaussian window, can be used. By applying a moderate one like the *Hann* window at position v_i we smooth the signal around v_i until vanishing at borders while preserving the value at v_i . At each position v_i the area under the square of the magnitude of this local product can be considered as a measure for the local variation at v_i . According to the Parseval's theorem [5] this area is equal to the area under the energy spectral density curve, that is $E(i) = \sum_{k=1}^N |\text{FSTFT}(i, k)|^2$. We recover thus from the STFT-spectrogram a 1D-curve: *the curve of local energy* (CLE green in fig. 1). the CLE is smoother, more robust to noise and outliers and coincide with the original signal in the maxima.

Automatic Detection of Irregularities: This is a two-step approach. First the extrema of the input signal are extracted, by looking for points where the first order derivative vanishes. The first derivative disappears if its values are less or equal to the threshold T_{deriv} . The set of candidates is filtered to thin valleys of extrema and to through away points which are not consecutive minimum-maximum-minimum or maximum-minimum-maximum triplets. Second spatial features are computed and compared to decide for the regularity of the maxima. The ascending and descending double-amplitudes as well as the left and right half-periodes are computed for each triplet of extrema. Only extrema whose left and right values of periode and amplitude do not deviate a lot from the dominant periode and dominant amplitude are considered as regular. Four thresholds ($T_{A_{low/up}}$ for the amplitude, $T_{P_{low/up}}$ for the periode) have to be set to tune the sensitivity to this deviations.

3 Validation and Discussion

We applied the method on eight monoplane rotational angiographic sequences acquired using a Siemens AXIOM Artis system over an angular range of ca. 200° . Four of them visualize the left coronary artery tree (LCT), the rest show the right tree (RCT). For all sequences the ECG-table was available as a relative percentage for each view of the cardiac cycle measured between two subsequent R peaks. We applied our method once on the CVM ($T_{deriv} = 0$) and once on the CLE ($T_{deriv} = 0.01$) setting $T = 256$, $T_{A_{low}} = T_{P_{low}} = 0.25$ and $T_{A_{up}} = T_{P_{up}} = 0.75$. The resulting curves are shown in fig. 2 and fig. 3. Due to the smoothing of the energy-curve, we additionally adjusted the extracted maxima by looking in the original signal within a window of 5 bothsides around the detected maxima.

We inspected the sequences visually and extracted manually end-diastole views from the ECG-table. These are views which show the vessels completely filled before starting contraction. We chosed one reference image having this property and determined the views having nearest ECG-states to its state. These states are rarely the same due to the different frequencies of acquisition and heart beat. For each sequences we got six to seven ECG-states, which represent the ground truth. In order to quantitatively judge the method, we classified the results to maxima that were detected and do correspond to an end-diastole state (F1). We tolerated hierby once one view and once two views of deviation. Maxima that were automatically detected but do not coorespond to end-diatole are false positive (F2). End-diatole views, which were not detected automatically represent the false negative (F3). Two sequences with RCT were not considered

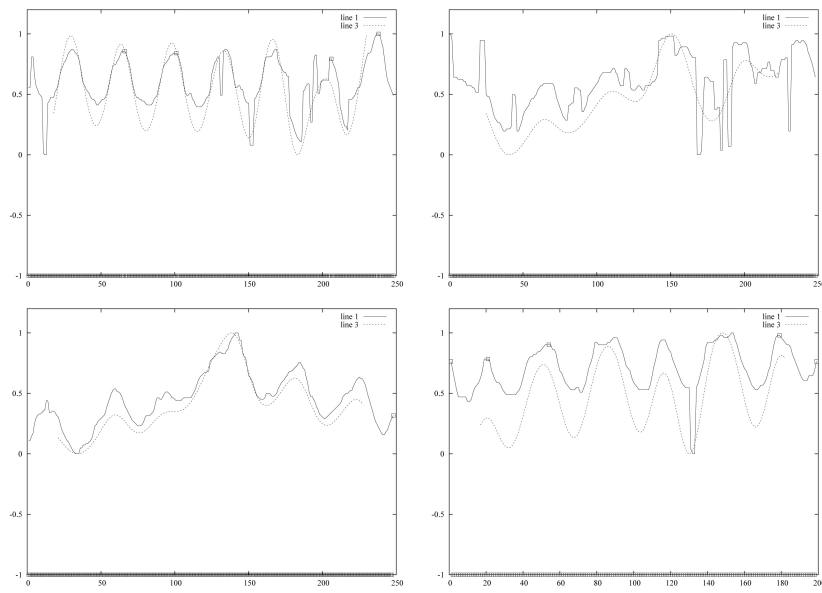


Fig. 2: Resulting maxima-CVM (continuousline) and CLE (dotted); automatically extracted maxima for seq. with LCT

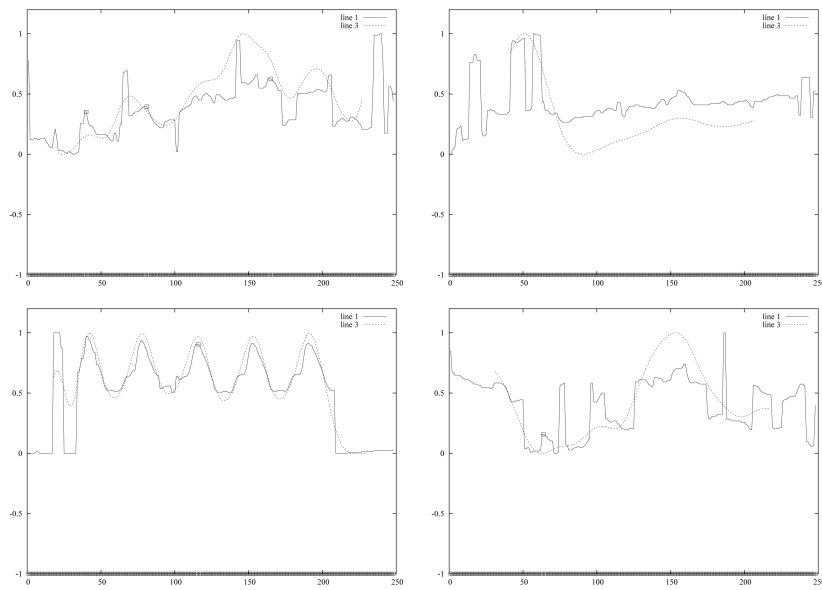


Fig. 3: Same caption as fig. 2 for seq. with RCT

in the statistics, since signals were very corrupted. Table 1 summarizes the statistics for all sequences.

		Four seq. with LCT (25 ECG-states)			Two seq. with RCT (13 ECG-states)		
Tolerance		original	local energy	adjusted	maxima	local energy	adjusted
F1	1 view	20 %	36 %	48 %	23.08 %	15.38 %	30.77 %
	2 views	24 %	48 %	68 %	30.77 %	30.77 %	30.77 %
F2	1 view	12 %	36 %	24 %	7.69 %	30.77 %	15.38 %
	2 views	8 %	24 %	4 %	0 %	15.38 %	15.38 %
F3	1/2 views	68 %	28 %	28 %	69,23 %	53.85 %	53.85 %

Table 1: Evaluation of automatic extraction of quasi-synchronous states in all considered sequences

Discussion: The curve of maxima is mostly very noisy and show many local maxima, valleys of maxima and discontinuities. The local energy transform operates like an overall smoothing, which -in several cases- avoids falling into local maxima. Most of time, more end-diastole states were correctly detected based on the local-energy curve (table 1, F1). Nevertheless the adjustment to the original signal revealed as advantageous, especially when allowing a deviation of two-views. Indeed up to 68% were then correctly detected ((table 1, F2). This tendency is better observed in sequences with LCT. Problems with the RCT can be explained by by the fact that the RCT moves rather horizontally, or their vertical motion overlap with C-arm rotation. Both cases hamper the detection of maxima. It has to be checked with an expert, whether this could be a pathological behavior. In general the more regular a signal is, the better is the automatic extraction. The detection of irregularities sometimes discards states, which are at end-diastole according to the ECG-signal. This occur either at the beginning and the end of an energy curve (correspond to half of the window size of STFT), or where there is an irregularity in fact. We believe that discarding irregularities is eventhough advantageous for further processing.

Future work will concentrate on a better extraction of a starting curve, e.g by considering continuous maxima. Furthermore the deviation from the correct end-diastole state by one or two views has to be investigated wrt. 3D Model reconstruction.

References

1. Morales, C.C.: 3D Reconstruction of the coronary tree using biplane snakes. PhD thesis (2002)
2. Movassaghi, B., Rasche, V., Viergever, M., Niessen, W.: A method for the determination of 3d vascular position and structure by the interaction in one single x-ray projection. In: SPIE - Medical Imaging. (2004)
3. Blondel, C.: Modelisation 3D et 3D+t des arteres coronaires a partir de sequences rotationnelles de projections rayons X. PhD thesis (2004)
4. Bouattour, S., Paulus, D.: Vessel enhancement in 2d angiographic images. In: FIMH proceedings. (2007) 41–50
5. Luecke, H.: Signalübertragung. Springer Verlag (1985)

Fast Recursive Data-driven Multi-resolution Feature Extraction For Physiological Signal Classification

Florian Hönig, Anton Batliner, and Elmar Nöth *

University of Erlangen-Nuremberg,
Institute of Pattern Recognition (Informatik 5),
Martensstraße 3, 91058 Erlangen, Germany
hoenig@informatik.uni-erlangen.de

Abstract. This study presents a new approach to feature extraction for real-time classification of physiological signals. By using multiple resolutions for the analysis of the signal, the stability of large analysis windows is combined with the capability of small windows to reflect quick changes. A large number of generic features is extracted from each signal for each resolution. These are calculated recursively for each sample which makes them very efficient in terms of computation time; a version with low memory requirements is also provided. A labelled dataset is utilised to convert the generic features into task- and signal-specific features by means of a data-driven transform. The performance of the approach is evaluated on a database containing different stress levels collected in a simulated driving context. A recognition rate of 89.8 % is achieved for online, user-independent classification of stress.

Key words: Biosignals, Recursive Calculation, Online Stress Recognition

1 Introduction

Research on Human-Computer-Interaction has recently turned a strong focus on the affective state of the user. Knowledge of this affective user state could lead to more pleasant, safer and more effective user interfaces [1]. For example, an in-car infotainment system as the one developed in the SmartWeb [2] project could respond to a stressed user state by retaining non-vital information in order not to further increase the user's cognitive load.

Affective states are known to have bodily correlates, which can be measured with suitable sensors. Most of the resulting *physiological signals*, e.g. skin conductivity or heart rate, are not under voluntary control and hence not subject to masking like e.g. speech and gesture. Physiological signals are therefore a valuable source of information for affective user state. Several studies have shown the feasibility of recognising affective states using physiological signals [3] [4].

* This work was funded by the EC within HUMAINE (IST-2002-507422) and by the German Federal Ministry of Education and Research (BMBF) within SmartWeb (Grant 01 IMD 01 F). The responsibility for the content lies with the authors.

2 Physiological Signal Processing

A number of problems arise when trying to recognise the affective user state with physiological signals. First, there is a large intra- and interpersonal *variability* of the signals. For a reliable classification, it seems therefore advisable to use large analysis windows in order to smooth out some of the variability. Another difficulty are *artefacts* in the physiological signals produced by motion, pressure, etc. which can render a signal useless for whole passages. Signal analysis and classification should therefore be able to cope with a dynamically varying number of input channels. For many conceivable applications of user state classification, at least a near *real-time* capability is required. On the one hand, this means that the feature extraction must be fast enough for a high classification frequency (i. e. small analysis step size) also for the above-mentioned large analysis windows; on the other hand it means that large analysis windows alone do not suffice because they can hardly provide the information necessary for a quickly reacting classification system.

Our approach seeks to address these issues. It is assumed that some detection algorithm for pronounced artefacts is available that marks passages in each signal which are probably corrupted as unusable. Furthermore, we discuss the case of online classification which means that all analysis windows are causal, i. e. using only samples from the past.

For the present study, six physiological signals are used: electrocardiogram (ECG), electromyogram measured at the neck (EMG), skin conductivity between index and middle finger (SC), skin temperature at the little finger (Temp), blood volume pulse at the ring finger (BVP) and abdominal respiration (Resp). Before computing the features, four additional signals are derived from the actually recorded signals: The heart rate acquired from the ECG channel (HR-ECG) and from the BVP channel (HR-BVP), the lag between ECG and BVP (Lag), which can be regarded as a surrogate parameter of the systolic blood pressure, and the respiration rate (Resp-rate). This has the considerable advantage that no signal-specific algorithms have to be included into the feature extraction. Furthermore, it makes sense to treat these parameters separately with respect to artefact detection. For example, if the heart rate computed from the BVP cannot be used, there might still be useful information in the raw BVP signal.

3 Feature Extraction and Classification

In order to deal with a variable number of input channels, feature extraction is performed separately for each signal. First, it is decided whether the signal is corrupted. Currently, this artefact detection is only a simple rule disqualifying signals with unplugged sensors or physically implausible values for the derived signals. Then, multiple analysis windows of different length (1, 5, 20 and 60 seconds) are extracted. Signals containing a sample marked as corrupted in any of the analysis windows are excluded from further processing for the current point in time. This multi-resolution approach aims at combining the stability of large analysis windows and the capability of small windows to reflect quick changes which is needed for real-time classification.

No attempt was made to design special features for each of the recorded and derived signals or the different window lengths. Instead, a large number of multi-purpose

features like mean, standard deviation or slope is extracted from each of these analysis windows. A labelled dataset is then utilised to create features specialised to the set of states to be recognised and signal at hand by means of a data-driven transform, the Fisher linear discriminant analysis (LDA): the generic features from all analysis windows of a signal are stacked into a single feature vector which is then projected into a lower-dimensional space.

Two different feature sets are provided. The *moving features* are computed recursively for each new sample and thus have a constant computational complexity with respect to the length and step size of the analysis windows. A ring-buffer is used to store the necessary sample history. In effect, these features can be computed very quickly even for the large required window sizes and are well-suited for a possible implementation on limited hardware. The recursive calculation is illustrated by the update rule for the mean value μ_n of a window containing w samples at the n -th sample x_n : $\mu_n = \mu_{n-1} - x_{n-w}/w + x_n/w$. If floating point numbers are used, and unless w is small, errors due to the numerical instability of adding and subtracting small values accumulate and render the result useless with time. This can be solved by periodically providing a mean value calculated anew; substituting the recursively calculated value every w samples results in a reasonable degree of numerical stability and only increases the computational effort by a constant factor of about 2. With similar techniques, also mean values as would result from a triangle- and bell-shaped window can be computed recursively, e. g. $\mu_n^{\text{tri}} = \mu_{n-1}^{\text{tri}} - m_{n-w_1}/w_1 + m_n/w_1$, $m_n = m_{n-1} - x_{n-w_2}/w_2 + x_n/w_2$, $w_1 = \lfloor w/2 \rfloor$, $w_2 = w - w_1$. Further recursively computed features are e. g. the slope of the regression line, a smoothed derivative, energy, variance, mean absolute or squared rise, fall and change and approximations of minimum, maximum, median and the amplitude. The variance $\sigma_n^2 = e_n - \mu_n^2$, $e_n = e_{n-1} - x_{n-w}^2/w + x_n^2/w$ is given as another example. Furthermore, the square, the square root or the absolute value of the computed features is added where applicable, e. g. the absolute value of the slope or the square root of the variance, yielding the standard deviation. In total, 50 moving features are calculated for each analysis window.

The *sliding features* drop the need for a sample history, resulting in a memory requirement independent of the window length. This is favourable for a possible implementation on hardware with small memory. The recursive calculation is illustrated by the update rule for the sliding mean $\mu_{\alpha,n}$ with a parameter $\alpha < 1$: $\mu_{\alpha,n} = \alpha \cdot \mu_{\alpha,n-1} + (1 - \alpha) \cdot x_n = (1 - \alpha) \sum_{i=0}^{\infty} \alpha^i x_{n-i}$, i. e. $\mu_{\alpha,n}$ is the mean value of the signal multiplied with an exponentially decaying window function. The parameter α determines how quickly the window function approaches zero. The standard deviation is used to characterise this by assigning a nominal window length $w = 2\sqrt{3}/(1 - \alpha)$ which is the length of a rectangular window that has the same standard deviation as the exponential window. This rectangular window contains approx. 97% of the mass of the exponential window. Depending on the desired length of the analysis window, α is computed from the nominal window length. Due to the fact that the window function never actually reaches zero, large outlier values of a signal can corrupt the mean value for a long time. Therefore, $\mu_{\alpha,n}$ is periodically substituted by a value that would result if the exponentially decaying window function was set to zero after 99% of its mass. Again, the computational effort is only increased by a constant

factor of about 2. With similar techniques, “sliding” equivalents of most of the moving features can be calculated, e.g. the mean value over a decaying bell-shaped window, $\mu_{\alpha,n}^{\text{bell}} = (a-1)^2 / (\epsilon(1-a-\epsilon)) \cdot \mu_{\alpha+\epsilon,n} - (1-a)/\epsilon \cdot \mu_{\alpha,n}$, and a sliding smoothed derivative, $\delta_{\alpha,n} = (\alpha-1)^3 / (2/\epsilon^2) \cdot (\mu_{\alpha,n} - 2\mu_{\alpha+\epsilon,n} + \mu_{\alpha+2\epsilon,n})$ with $\epsilon \rightarrow 0$ (for practical purposes, $\epsilon = (1.0 - \alpha)/100$ suffices). In total, 44 sliding features are calculated for each analysis window.

The final feature vectors of each valid signal resulting from the LDA transformation of the generic features are scored with a Gaussian Mixture Model consisting of 10 mixture components. The resulting probabilities are, assuming statistical independence between the different physiological signals, combined by multiplication, yielding a final score for each class.

4 Experiments and Results

We evaluate our approach on the DRIVAWORK (Driving under Varying Workload) database which contains audio, video and physiological recordings of different stress levels in a simulated driving context. The six above-mentioned physiological signals have been digitised at 256/2048 Hz with the Mind Media NeXus-10 device. Relaxed and stressed states are elicited by giving the participant different tasks; subjective and objective measures support the effectiveness of this approach. The structured design of the experiment can be used to obtain a preliminary “ground truth”; a fine-grained manual annotation of the perceived stress level is currently being conducted. The database contains recordings of 24 participants and amounts to 15 hours or 1.1 GB of physiological data alone.

We investigate the task of user-independent, online classification of a relaxed or stressed user state using a subset of the Drivawork dataset: due to the fact that the actual user state is unknown, the classification accuracy is only evaluated during the most unambiguous segments. For those 3.4 hours, it is assumed that the affective state of the person is the one intended by the experimental design. Classification is done with a frequency of 1 Hz, so the number of used feature vectors is about 15600. Note that the chosen online classification task is more difficult than the task of discriminating previously defined, relatively large segments in an offline manner as studied e.g. in [4] in the following sense: the context of 60 seconds available to the classification module is relatively small, in addition, it is only taken from the past. So, a considerable fraction (28 %) of the feature vectors is computed from intervals that are not completely contained within the unambiguous segments. However, the task is still artificially simplified by the fact that the studied segments are well separated.

All evaluations are done using person-independent 10-fold cross validation, i. e. each pair of train and test set is disjoint with respect to the participants. The class-wise averaged recognition rates are reported. Table 1 lists the results obtained using different input features, for the individual signals as well as for the combination of all signals. Using the moving features from a single analysis window of length 60 seconds, recognition rates between 48.5 % (Resp-rate) and 80.5 % (ECG) were obtained for the single signals. The combination of all signals yielded an accuracy of 88.1 %. Using the multi-resolution approach with the four analysis windows of 1, 5, 20 and 60 seconds length (i. e. a total of 200 generic features) was better than using only the single window of

Table 1: Class-wise averaged recognition rates in % for recognising stress using single channels or the combination of all signals. For feature extraction, either one analysis window of length 60 seconds (“single”) or multiple windows of length 1, 5, 20 and 60 seconds (“multi”) are used. The used feature set per analysis window is either the moving or sliding set or both (“All”).

<i>Features</i>	<i>ECG</i>	<i>EMG</i>	<i>SC</i>	<i>Temp</i>	<i>BVP</i>	<i>Resp</i>	<i>HR-ECG</i>	<i>HR-BVP</i>	<i>HR-Lag</i>	<i>Resp-rate</i>	<i>Comb.</i>
Moving single	80.5	67.4	64.7	77.1	76.3	75.6	66.3	68.9	54.3	48.5	88.1
Moving multi	83.8	67.6	71.4	76.0	79.5	77.5	68.2	69.6	54.7	49.1	89.8
Sliding single	80.9	73.0	72.4	76.4	77.7	79.5	67.8	68.7	54.7	50.5	89.6
Sliding multi	84.2	71.3	75.2	76.9	78.4	79.8	67.6	68.7	55.9	50.6	89.5
All multi	84.3	72.6	75.0	77.3	78.7	80.1	67.7	69.5	56.0	49.2	88.8

60 seconds in all but one case. Again, ECG was the best single channel with 83.8 % recognition rate. For the combination of all signals, 89.8 % resulted in this case. The sliding feature behaved similarly; however, the gain from the multi-resolution approach is not so marked. For the combination even a slight decrease from 89.6 % to 89.5 % was observed. Combining moving and sliding features (i.e. using a total of 376 generic features) gave an additional gain only in some cases, but not for the combination. Simulating user adaption by normalising the mean and variance of all features per participant (before estimating the LDA transform), the best recognition rate was obtained for the moving features from multiple resolutions. Here, an accuracy of 96.0 % resulted (not contained in the table).

5 Conclusion

This study presents a unified and efficient approach to feature extraction and classification for physiological signals. No signal- or task-specific knowledge is used to define the features; instead, a labelled dataset is utilised by means of a data-driven transform to convert a large number of generic features into specialised features. The approach is evaluated on the task of online, person-independent classification of relax vs. stress. The results of up to 89.8 % are quite satisfactory and prove that the approach works well. Further research will be devoted to the evaluation of the real-time capability of the system in terms of a reaction speed to user state transitions. It is expected that the multiple analysis windows will be especially useful in this respect. Further studies will investigate a sophisticated artefact detection, recursively calculated spectral features and an un-supervised adaption to the user.

References

1. Nass, C., Jonsson, I.M., Harris, H., Reaves, B., Endo, J., Brave, S., Takayama, L.: Improving automotive safety by pairing driver emotion and car voice emotion. In: CHI '05 extended abstracts on Human factors in computing systems, New York, NY, USA, ACM Press (2005) 1973–1976

2. Reithinger, N., Herzog, G., Blocher, A.: Smartweb - mobile broadband access to the semantic web. *KI Zeitschrift* (2) (2007) 30–33
3. Picard, R.W., Vyzas, E., Healey, J.: Toward machine emotional intelligence: Analysis of affective physiological state. *IEEE Transactions on Pattern Analysis and Machine Intelligence* 23(10) (2001) 1175–1191
4. Healey, J.A., Picard, R.W.: Detecting stress during real-world driving tasks using physiological sensors. *IEEE Transactions on Intelligent Transportation Systems* 6(2) (2005) 156–166

Analysis of cardiovascular dynamics: new approach for predicting of pre-eclampsia

H. Malberg¹, R. Bauernschmitt², and N. Wessel³

¹ Karlsruhe Research Center/University of Karlsruhe, Germany

² German Heart Center Munich, Germany,

³ University of Potsdam, Germany

Abstract. Early prediction of Pre-eclampsia (PE), a serious pregnancy complication, is still insufficient in clinical practice. We applied parameters of heart rate and blood pressure variability to detect cardiovascular alterations in order to predict PE.

1 Introduction

PE, a serious pregnancy-specific disorder characterized by proteinuria and hypertension after the 20th week of gestation, is still the main cause of maternal and neonatal morbidity and mortality. It occurs in 3-5% of all pregnancies. As the etiology and pathogenetic factors underlying this complication of pregnancy are still unknown, early risk assessment by Doppler sonography is to improve clinical management and outcome. However, the positive predictive value of Doppler sonography is limited to approximately 30%, as only part of women with disturbed uterine perfusion develop one of the complications of pregnancy, such as PE, pregnancy-induced hypertension (PIH), or intrauterine growth retardation (IUGR) [1]. Analyses of heart rate (HRV) and blood pressure variability (BPV), and baroreflex sensitivity (BRS), have become powerful techniques for assessing autonomic control in cardiovascular diseases [2, 3]. We considered the possibility of a combination of this technique with Doppler sonography being able to improve the prediction of PE.

2 Patients and Methods

The study includes 58 patients with abnormal uterine perfusion (AUP) examined consecutively and 44 normal pregnancies recruited in parallel who underwent Doppler sonography in the second trimester of pregnancy (median 21 weeks, range 18- 22 weeks). All pregnancies were singleton. At the time of examination, the women were healthy, normotensive, without clinical signs of cervical incompetence, and on no medication. After Doppler examination, all women underwent noninvasive continuous blood pressure monitoring via finger cuff (100 Hz, Portapres device Mod. 2, BMI-TNO, NL) for analysis of HRV, BPV, and BRS. The parameters of time domain and frequency domain were calculated to HRV task force standards and adapted to BPV [3, 4]. To

analyze heart rate and blood pressure interactions, we calculated BRS by the Dual Sequence Method [4]. Outcome measures of the study were PE, pregnancy-induced hypertension (PIH) and / or intrauterine growth retardation (IUGR). The Mann-Whitney U test was performed to group differences in variability parameters. Forward stepwise discriminant analysis with a maximum of 3 parameters was used to estimate the group classification rates.

3 Results

Fifty-eight out of 102 pregnancies were characterized by abnormal uterine perfusion around the 20th week of pregnancy.

Parameter	PE	NoPE	p
MeanNN	743.2±125.7	763.6±120.3	n.s.
MeanSBP	129.2±12.8	122.1±17.0	n.s.
MeanDBP	73.2±9.4	67.4±10.9	n.s.
DBP1	8.3±4.5	5.16±1.8	<0.005
BRS1	2.6±0.8	1.8±0.8	<0.001
HRV1	0.44±0.09	0.36±0.13	<0.016

Table 1: Statistical summary of intergroup calculations Preeclampsia Risk (PE) vs. no Preeclampsia Risk (NoPE). MeanNN: Mean value of heart rate, MeanSBP: mean systolic blood pressure, MeanDBP: mean diastolic blood pressure, DBP1: (HF-dBP) high frequency in diastolic blood pressure; BRS1 ($tachy_4 - 6$) the number of tachycardic BRS in a range of 4 – 6 ms/mmHg; HRV1 (VLFn) : normalized very low frequency.

While age, systolic and diastolic blood pressures, as well as heart rate were not altered, this group delivered significantly earlier, and the neonates were characterized by lower birth weight. Sixteen of the 58 AUP pregnancies developed PE, while none of the 44 women with normal uterine perfusion developed any kind of hypertensive disorder. We combined the analysis of uterine perfusion and the variability and baroreflex parameters (see Table 1). In the group of abnormal uterine perfusion, three parameters achieved a sensitivity of 93.7%, a specificity of 85.7%, and improved PPA to 71.4% with a negative predictive accuracy (NPA) of 97.3%. It is important to note that the combination of other parameters did not reach a higher PPA. In Fig. 1 an example of cardiovascular alterations during the course of pregnancy is demonstrated.

4 Discussion

Many attempts have been made to develop a simple clinically feasible test for early prediction of PE. However, previous studies using one-stage or two-stage Doppler sonography alone or combined with humoral or endothelial parameters achieved neither sufficient sensitivity nor positive predictive value or were costly or invasive. Although

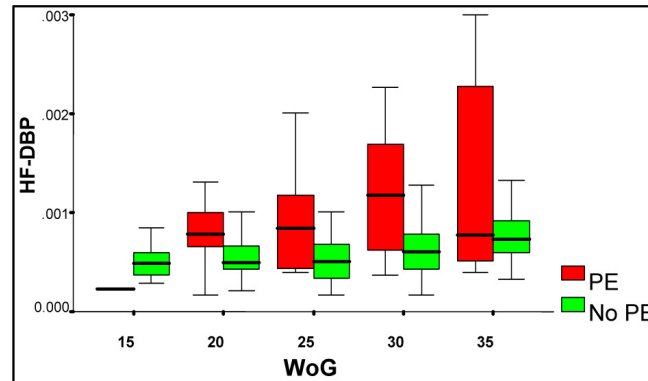


Fig. 1: Alteration in high frequency range of diastolic blood pressure (HF-DBP) during the course of the gestation (week of gestation, WoG) in pregnant women with PE risk (PE) vs. with no PE Risk (NoPE)

HRV and BPV as well as BRS parameters were initially developed for risk stratification in cardiology, the field of clinical applications has broadened in recent years, and these parameters of autonomic cardiovascular control are also influenced in hypertensive pregnancy disorders. Therefore, we tried the hypothesis whether this method would be applicable in predicting PE, as PE-associated endothelial dysfunction was recognized by these parameters early on. In combination with Doppler sonography of uterine arteries, our method achieves the highest predictive level of all non-invasive trials published. Especially the high positive predictive accuracy of 71.4% attests to the clinical relevance of combining Doppler analysis and beat-to-beat dynamics. In clinical practise our main approach is therefore aimed to identify pregnant women who will develop PE. The great negative accuracy allows also excluding women at risk. This is all the more important as our approach of concurrent measurement of uterine perfusion and variability parameters is a feasible, inexpensive, non-invasive one-stop clinical assessment in the second trimester. Follow-up studies must be conducted evaluate prospectively the power of the test. Our data imply early pathophysiological alterations at a time point (20th WoG) where pregnancies with later PE are clinically healthy. Thus, e.g. the increase in diastolic high frequency, which is modulated by respiratory sinus arrhythmia, may reflect early pathological arterial stiffness. This leads to the undamped respiration-induced pulse wave oscillations detected by our method. This is congruent with the hypothesis that patients later developing PE are characterized by early pathological modifications in vessel behaviour. In summary, currently the most precise prediction of PE by concurrent measurement of uterine perfusion and calculation of cardiovascular beat-to-beat parameters in the second trimester may further an early therapeutic strategy to reduce upcoming pathophysiological characteristics of the disease and, consequently, prevent complications which would result in high morbidity and mortality rates [5].

References

1. Chien PF et al. How useful is uterine artery Doppler flow velocimetry in the prediction of preeclampsia, intrauterine growth retardation and perinatal death? An overview *Brit J Obstet Gynaecol* Vol 107, p 196, 2000
2. Wessel N et al. Nonlinear analysis of complex phenomena in cardiological data *Herzschr Elektrophys* Vol 22, 159, 2000
3. Task Force of the European Society of Cardiology and the North American Society of Pacing and Electrophysiology Heart rate variability: standards of measurement, physiological interpretation and clinical use *Circulation* Vol 93, p 1043, 1996
4. Malberg H, et al. Advanced analysis of the spontaneous baroreflex sensitivity, blood pressure and heart rate variability in patients with dilated cardiomyopathy *Clin Sci* Vol 102, p 465, 2002
5. Malberg H, et al. Analysis of cardiovascular oscillations: New approach for early prediction of Preeclampsia *Chaos (Special Issue)* Vol 17, p015113, 2007

Imaging of Biomechanics of Heart Movements by Using Multichannel System for Precardiac Rheography

Y.E. Kirpichenko and D.P. Timohin

Department of Biomedical Techniques, Bauman Moscow State Technical University, Moscow, Russia

Abstract. There are a lot of invasive and noninvasive methods to determine the cardiovascular system's functioning parameters. One of these is a precardiac rheography method (preRCG). Waveform obtained by using the precardiac rheography method depends on electrode system localization. This feature allows to determine heart boundary and to perform real-time analysis of biomechanical heart parameters.

Keywords— **Precardiac rheocardiography, impedance monitoring, real-time measurements**

1 Introduction

For at least ten years developed countries have been expressing an interest in tools for non-invasive monitoring of pumping ability of the heart. One of these tools is a transthoracic rheography method. It is based on the impedance measurement which is caused by changes in blood volume of the body segment. In order to increase the determination cardiovascular system's functioning parameters we can place electrode system in the precardiac area, but for all that we have to develop algorithms and experimental techniques. It is advisable to make use of precardiac rheography (preRCG) technique for solving these problems. Y.T. Pushkar' pioneered the use of this method in 1959.

The essence of this technique is that for measurement purposes 4 electrodes usually have to be applied to the body surface. Two electrodes (usually called current electrodes) are used to pass a constant alternating current with a high frequency (60 - 100 kHz) and very low amplitude (1 mA). The current is imperceptible to the patient and does not cause any physiological reactions. The other two electrodes (usually called measuring electrodes) are placed between the current electrodes and measure the voltage which is caused by the current flowing through the body segment. This voltage corresponds to the impedance of the body segment and changes in blood volume variations. On this basis the blood flow can be measured and analyzed.

2 Precardiac rheography perspectives

In precardiac rheography method's development it is essential to solve a number of general theoretical and practical tasks. The following tasks are chosen among theoretical tasks:

1. Interpretation of the mechanism of precordial rheography signal's generation
2. Requirements for electrodes positioning
3. Layered mediums modelling in order to determine geometrical and electrical characteristics of each of the layers, real-time estimation of these characteristics
4. Phase analysis of precordial signals, data acquisition for heart localization and visualization processes in the heart
5. Determination heart parameters (stroke volume, heart-rate etc.)

3 Heart's boundary localization by using precordial signals analysis

Realized research have shown that basic impedance increases in the area of heart projection on the thorax and decreases outside. This feature allows us to determine heart projection on the thorax and to perform heart imaging. (Fig.1). This property allows using imaging as tomographic technique in the precordial area.

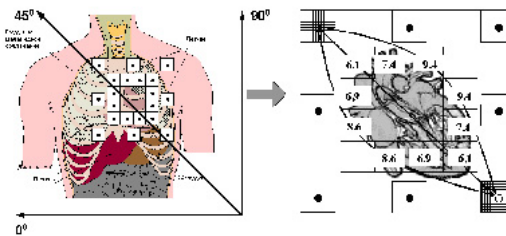


Fig. 1: Basic impedance distribution in the precordial area

Heart's boundary determination by using basic impedance values in different leads is the primary task. It is possible to examine this task as indirect task. In the area of heart projection on the thorax basic impedance value Z_{base} essentially less than in other parts of the thorax. It is possible to choose area $10 \times 10 \text{ cm}^2$ on the thorax surface. Inside this area basic impedance is less than outside it. Provided marking this area by using basic impedance data, it is possible to determine heart projection on the thorax and estimate its dimensions. Heart geometry it is possible to approximate by means of ellipsoid of rotation. It is characterized by 2 parameters: big and small axes. Thus, in order to determine heart's boundary by using precordial signal analysis it is necessary to solve several tasks:

1. Electrode system creation.
2. Algorithms development, which could plot heart projections images, approximation function choice.
3. Impedance imaging
4. Algorithms development, which could determine heart's boundaries by means of impedance distribution.

4 Electrode system

For data

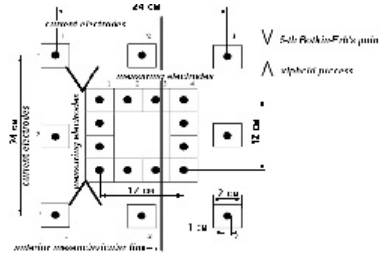


Fig. 2: Electrode system used for the heart boundary determination.

acquisition and subsequent signal analysis prefabricated electrode system is used. Commonly employed electrode system is shown in Fig.2.

Electrode system was designed to cover full surface of thorax. At that perimeter-mounted measuring electrodes were located between 5-th Botkin-Erb's point and cardiac apex. Current electrodes were perimeter-mounted too and located on the outside of measuring electrodes.

Experiments were carried out on the volunteers (men, 22-40 years old). Waveform obtained by using the precordial rheography method depends on electrode system localization. This feature allows us to determine heart boundary and to perform real-time analysis of biomechanical heart parameters. Besides, total measurable impedance consists of basic impedance and pulse constituent. By using basic impedance values it is possible to determine heart boundary. Pulse variations reflect biomechanical processes of one of the heart sections (section of the aortic valve, sections of left or right ventricles depending on heart arrangement) and cardiac apex.

In order to analyze pulse variations we need information about phase composition of precordial rheocardiograms. The electrocardiogram is used as general support signal. Fig.3 shows several types of rheographic signals in the precordial area.

5 Heart movements imaging

Thus, in order to obtain heart's image it is necessary to develop multichannel system and application for acquisition data and solving indirect task. Multichannel system in work is shown in Fig. 4.

For heart's movings imaging Windows-based application has been developed. Its screen shot is show in Fig.5. Here you can see rheographic signals from 32 leads. Also heart's image obtained by using the impedance distribution is presented.

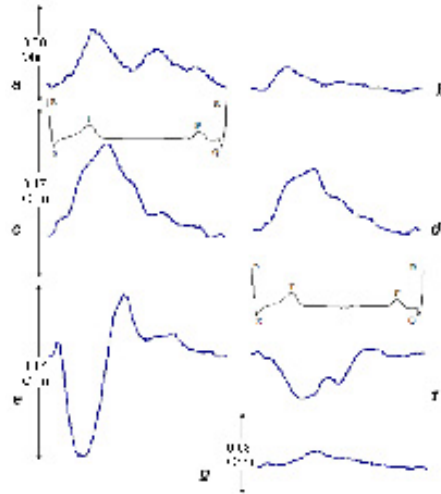


Fig. 3: Precardiac rheogram signals and respective support ECG signals in different leads. Scale of the signals is identical. a) projection of the aorta onto front wall of the thorax, b) out of projection of the heart onto front wall of the thorax, on the left and under the clavicle, c) d) projections of the right and left auricles respectively onto front wall of the thorax, e) f) projections of the right and left ventricles respectively onto front wall of the thorax, g) out of the heart's projection, on the right side.

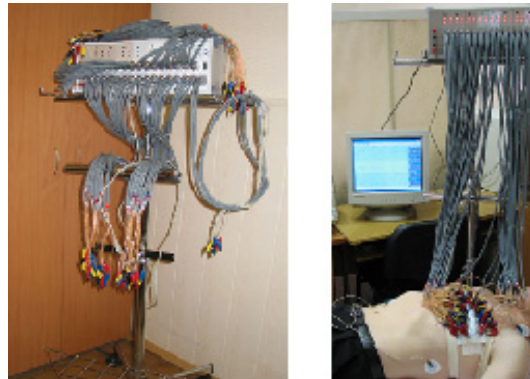


Fig. 4: Multichannel system for rheocardiography applications.

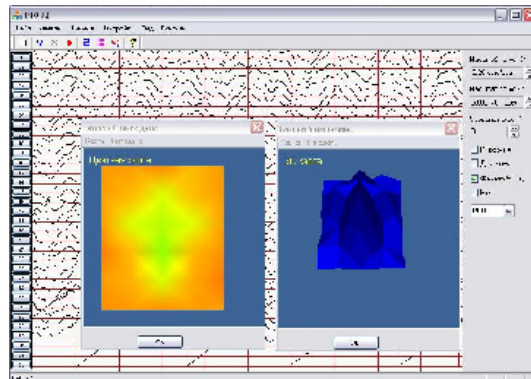


Fig. 5: Heart's image, obtained by multichannel system.

6 Conclusions

In this paper we took up precordial rheography perspectives and main tasks, which we have to solve to implement heart's movements imaging.

References

1. Tikhonov A.N., Samarsky À.À. Equations of Mathematical Physics. - Moscow.: Vyschaya shkola, 1994. - 467 p.
2. Electrical Survey by Using Resistance Technique / by V.K. Khmelevsky and V.À. Shevnin. - Moscow.: MSU, 1994. - 160 p.
3. Yakubovsky Y.V., Renard I.V. Electrical Survey. - Moscow.: Nedra, 1991.

Investigation of Graphic Methods for Rhythmocardiogram Phase Portraits Analysis

Aliaksei I. Maistrou¹

Biomedical Engineering Department, Bauman Moscow State Technical University, Moscow, Russia

Abstract. One of the most informative approaches to human condition diagnostic is the heart rhythm variability (HRV) analysis based on mathematical processing of rhythmocardiograms (RCG). There are a lot of methods for mathematical processing of rhythmocardiograms, but most of them are useful only in case of normal sinus rhythm presence. Phase portraits analysis is one of mathematical approaches to HRV analysis, useful in case of arrhythmia presence. Phase portrait of RCG is its representation in coordinates (RR_i, RR_{i+1}) . Usually phase portrait is approximated with simple geometrical figure, and HVR analysis is carried out using approximating figure area. Approximating figure area describes phase portrait points' deviation and is the most informative index of correlation between current phase portrait and phase portrait, interpreted as norm.

In this study four different methods used to approximate phase portrait of RCG. The first two approaches use ellipse as basic geometrical figure. The third approach uses parallelogram approximation and the fourth method is based on polygon approximation. Various algorithms for polygon approximation have been compared. "Graham scan" and "Jarvis march" have been marked out for the current task. Area value correction algorithm has been presented.

The methods were applied to the RCG records database. It included 50 healthy and 35 diseased (heart diseases) persons. Records were obtained in rest, 200 cardiocircles in length. The most precise approximation was obtained with the polygon approximation. Oversize effects in case of single instances of extrasystole appearance had been analyzed, and correction algorithm was developed. RCG record range was optimized. It was found that after first 60 cardiocircles the rate of area rise slow down in 2 times. After 120 cardiocircles the rate of area rise slow down more then in four times, what corresponding to the period of primary phase portrait infill.

The RCG phase portrait approximation and its area comparison is an informative method of human condition diagnostic, based on heart rhythm analysis. Method of polygon approximation with correction algorithm should be the method of choice for approximating figure area calculation. Parallelogram approximation is effective for allocation of phase portrait linear characteristics. The minimum length of RCG record is equal to 1 minute, and rational period is equal to 2 minutes.

1 Background

Heart Rhythm Variability (HVR) Analysis is a method for evaluation of the state of physiological functions in human organism regulation mechanisms.

One of the most informative approaches to human condition diagnostic is the heart rhythm variability (HRV) analysis based on mathematical processing of rhythmocardiograms (RCG).

Rhythmocardiogram can be obtained by recognition and measurement time intervals between R-picks (R-R intervals or cardiointervals) on electrocardiogram (ECG). Dynamic series of cardiointervals are known as rhythmocardiograms.

There are a lot of methods for mathematical processing of RCG. Its classification is presented on fig.1.

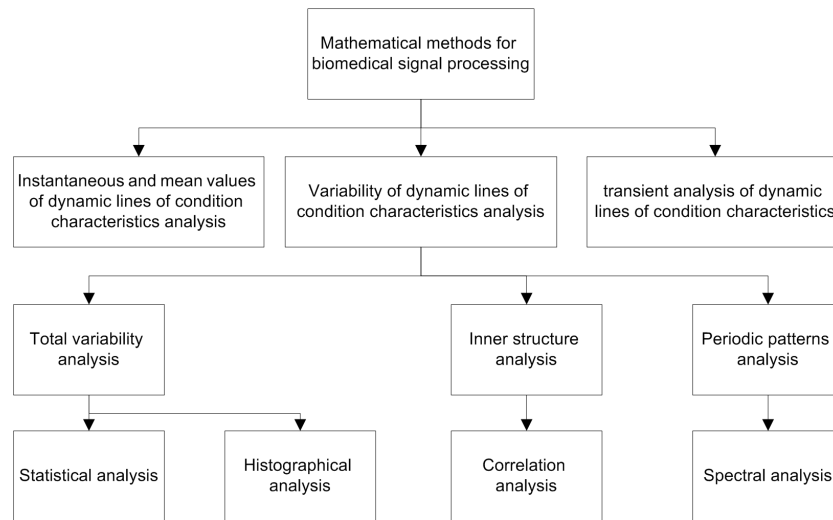


Figure1. Mathematical methods for biomedical signal processing

But these methods are useful only in case of normotopic rhythm presence. Normotopic rhythm holds the following inequality:

$$0,8 < RR_i/RR_{i+1} < 1,2$$

where RR_i – i -th RR -interval latency. Some researchers have an opinion that mathematical methods, presented on fig.1, could be used correctly only in case of 5% non-normotopic RR -intervals presence in ECG record.

Rhythm Phase portraits analysis is one of mathematical approaches to HRV analysis, useful in case of arrhythmia presence.

One of the mathematical approaches to HVR analysis, which could be used for non-normotopic heart rhythm analysis is RCG phase portraits (PP) analysis.

RCG phase portrait is Rhythmocardiogram's presentation in (RR_i, RR_{i+1}) coordinates, and analysis is based on PP's geometric characteristics study. In most of cases analysis is processed after PP approximation by simple geometric figures and analysis is carried out using ratio of approximated and initial PP areas. Approximating figure area

shows the dispersion of RCG PP and is the most informative index of correspondence between current RCG PP and RCG PP, interpreted like normal.

RCG PP of normal sinus rhythm is an ellipse, elongated toward the bisector of the first coordinate angle of PP space. The circle-like form is corresponded to absence of non-respiratory components of arrhythmia; gaunt ellipse is corresponded to prevalence of non-respiratory components (non-normotopic rhythm). It was defined that classic approximation with an ellipse covers the RCG PP nonuniformly in case of non-normotopic rhythm presence. Approximating ellipse area values appears to be too high, and it makes impossible to create automatic HRV analysis algorithms, based on RCG PP analysis method. In this article more effective approximation technique is offered. This technique enables to calculate geometric characteristics of RCG PP approximating figure for patients with non-normotopic rhythm much more precisely.

2 Methods

RCG PP approximation with ellipse is the most frequently used for PP geometric characteristics interpretation. A lot of various algorithms for approximating ellipse searching is known. Two simple and visual algorithms of approximating ellipse determination are presented. For the first algorithm realization the points with maximum (x_1, y_1) and minimum (x_0, y_0) abscissa is searching. Those points define the ends of the first axis of the ellipse. The center of the ellipse is specified as the center of the segment $\{(x_0, y_0), (x_1, y_1)\}$. Then two points with maximum (x_2, y_2) and minimum (x_3, y_3) ordinate is searching. The most distant point from the center is chosen as the third point of the ellipse. This algorithm is effective for linear characteristics of ellipse determination, but not for area calculation. That is why the alternative ellipse construction algorithm is offered.

The second ellipse algorithm is taking into account point's distribution. On the first step the coefficients of the lines $y = a_{e1} \cdot x + b_{e1}$ and $y = a_{e2} \cdot x + b_{e2}$ using least-squares method is founded. The intersection of the lines gives the center of the ellipse. The first axis is considered to be collinear to line $y = a_{e1} \cdot x + b_{e1}$. For full including ellipse definition, the stepping increasing of the axis algorithm is used. This method is more precise in case of extrasystole or other artifacts presence, which form rhythmical gathering. It is more sensitive to non-normotopic cardiointervals presence.

The algorithm of RCG PP covering parallelogram searching is reduced to parallel segments array searching, which divide the RCG PP space to half-spaces: with and without PP points, in different directions. Each four segments, which are parallel and have opposite signs in pairs, form the parallelogram. Then the parallelogram with the least area is choosing.

The algorithm of parallelogram searching is presented on fig.2. Table 1 describes the parameters of variables in the algorithm.

Table 1

Parameters of the variables for the algorithm on fig.2

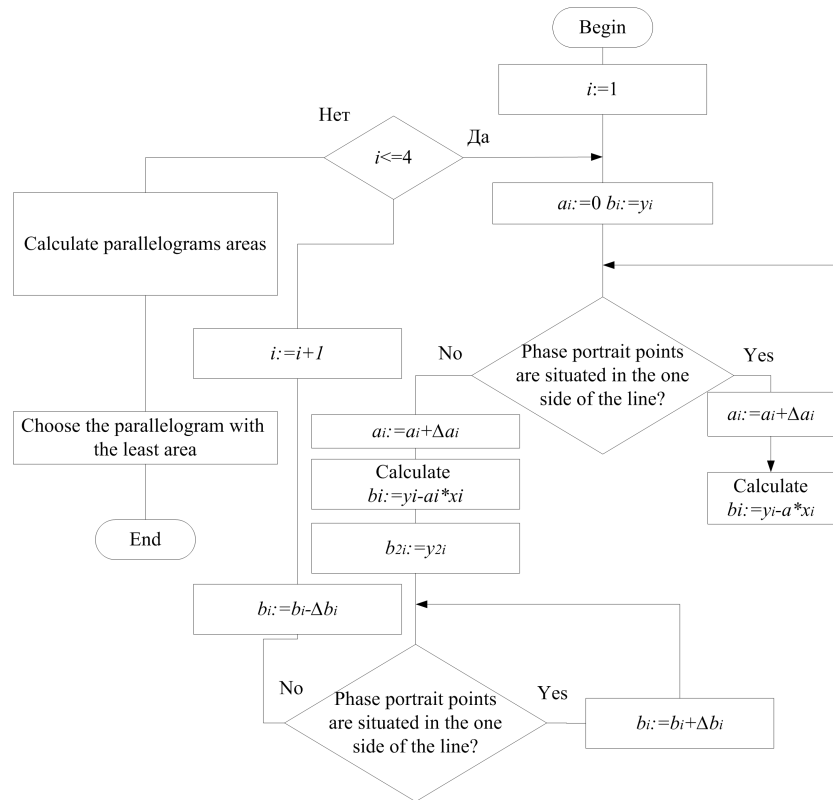


Fig. 1: The algorithm of approximating parallelogram searching

i	y_i	x_i	Δa_i	y_{2i}	Δb_{2i}
1	y_{\max}	$x y = y_{\max}$	< 0	y_{\min}	> 0
2	y_{\max}	$x y = y_{\max}$	> 0	y_{\min}	> 0
3	y_{\min}	$x y = y_{\min}$	< 0	y_{\max}	< 0
4	y_{\min}	$x y = y_{\min}$	> 0	y_{\max}	< 0

During the research, it was determined that in large number of experiments approximation with simplest geometric figure, because of single spikes presence, is not optimal – more then 60% of the approximating area lacks for RCG points. And that is why those areas is not corresponded to integral characteristic of PP useful for HRV analysis.

Error area elimination is needed to provide universal method for HRV analysis. Convex hull approximation helps to get rid of the part of mistakes. “Jarvis march” and “Graham scan” algorithms of polygon approximation were tested. “Graham scan” algorithm appears to be faster than “Jarvis march” for current tasks: time complexity for “Jarvis march” algorithm is equal to $O(n \cdot h)$ and for “Graham scan” is equal to $O(n \cdot \ln n)$ - where n – number of PP points, h – number of vertex of convex hull. The “Graham scan” algorithm is presented on fig.3.

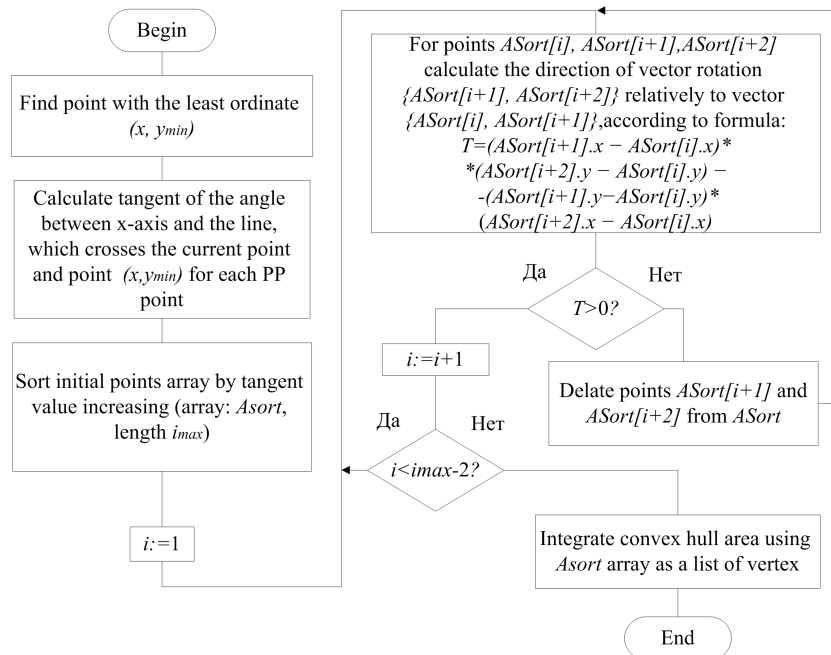


Fig. 2: “Graham scan” algorithm for convex hull determination

It was determined that even convex hull covers empty phase space, and that this errors is mainly connected with single extrasistoles, which is eligible for normotopic rhythms during 2 minutes long record. The correction algorithm for increasing area calculation precision was developed. It is based on two consecutive convex hull approximation, in condition that after first iteration the vertex points are excluded from analysis. This algorithm eliminates single extrasistole and corrects the approximating area. The algorithm works properly only in case of less then 3 artifacts presence. That

is why the length of RCG record must be no longer than 2 minutes. An example of correction is shown on fig.4.

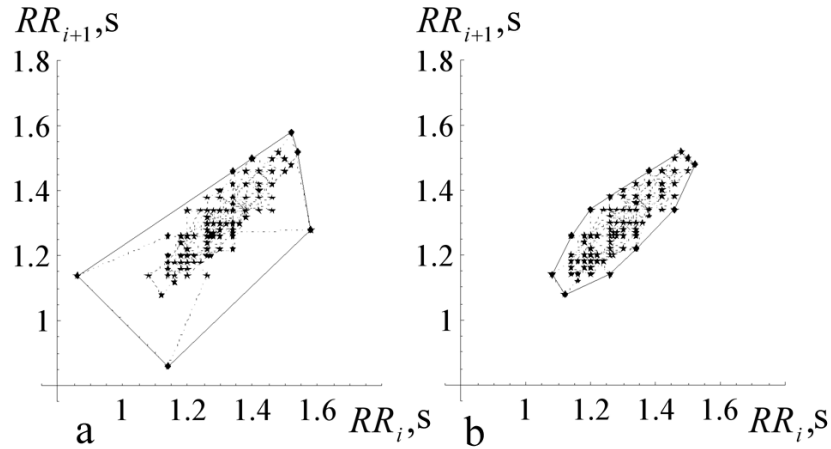


Fig. 3: An example of convex hull area correction

3 Results

Efficiency comparing analysis was proceeded using special software, in which described algorithms was realized. Comparative experiment of approximating figures' areas calculation for normotopic and non-normotopic rhythms was based on RCG records database. It included 50 healthy and 35 diseased (heart diseases) persons. Records were obtained in rest, 200 cardiocircles in length. Results is shown on fig.5, where mean of areas is horizontal lines inside the boxes, limits of 90% area values is the ends of the boxes, the variance ranges are equal to whiskers, 1a – for normotopic patients, ellipse 1 method, 1b – for non-normotopic patients ellipse 1 method, similarly 2a, 2b – for ellipse 2 method, 3a,3b – for parallelogram method, 4a, 4b – for convex hull method.

This results show much more precise area calculation, using convex hull method. Among the simplest geometric figures the most precise results show parallelogram approximation. This approximation could be used for linear characteristics of RCG PP allocation.

The series of experiments for adaptive abilities investigation using approximating area values as integral indexes of cardiovascular system condition were carried out. The changes of HRV, resulting in approximating figures' area changing, in various physiological conditions, show the feedback reactions of the organism. The database includes 35 diseased persons, the experiments were carried out in two conditions: in rest (reclining position) and in orthostasis (upright posture). The results is shown on fig.6, where mean of areas is horizontal lines inside the boxes, limits of 90% area values is the ends of the boxes, the variance ranges are equal to whiskers.

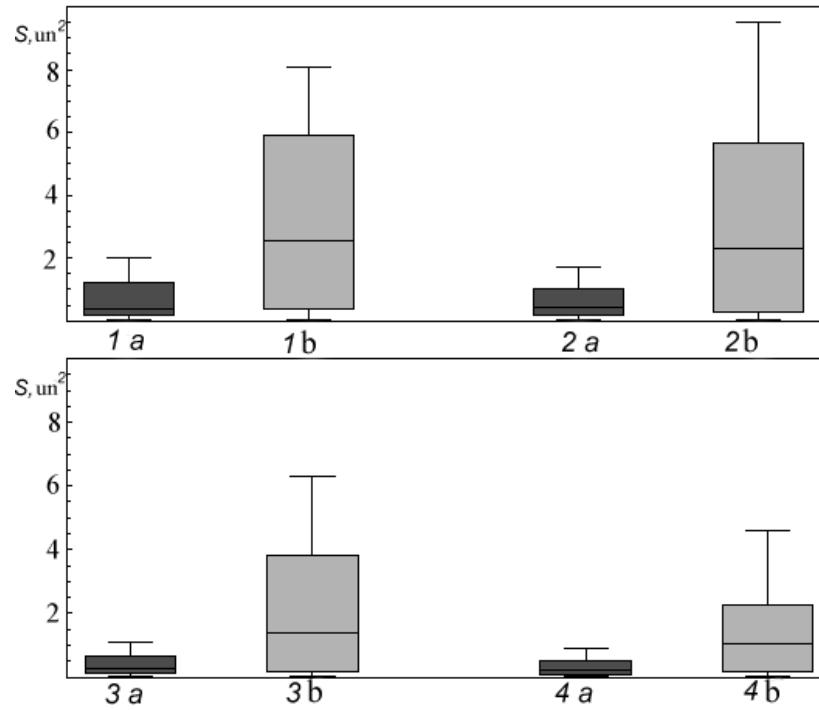


Fig. 4: Precision comparing for the approximating methods

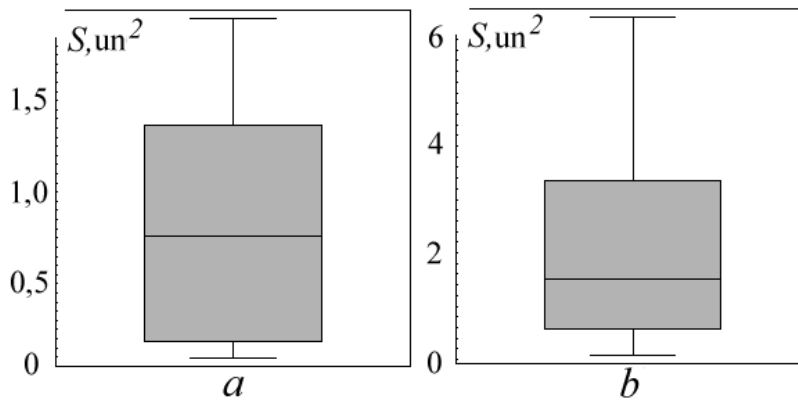


Fig. 5: Approximating polygon areas values for different physiological conditions, *a* – in rest, *b*– in orthostasis

The results show quantitative differences between area values in rest and in orthostasis, but the informative diapasons is still not isolated

4 Conclusion

- The RCG phase portrait approximation and its area comparison is an informative method of human condition diagnostic, based on heart rhythm analysis.
- Method of convex hull approximation with correction algorithm should be the method of choice for approximating figure area calculation.
- Parallelogram approximation is effective for allocation of phase portrait linear characteristics.
- The rational length of RCG record for phase portrait analysis execution is equal to 2 minutes.

Clinical Applications of Advanced Technology

Design of mechatronic drives for implantable systems of left ventricle assist device and artificial heart

V.V. Morozov¹, A.V. Zhdanov¹, and E.A. Novikova¹

Vladimir State University, Russia

1 Introduction

One of the most important problems in running the system of left ventricle assist device (LVAD) or total artificial heart (TAH) is the creation of stable drive providing continuous and permanent blood flow. This article is concerned with the design of mechatronic drive for such systems.

Cardiovascular disease is leading among the reasons of death, exceeding death rate from oncological disease and accidents. Death rate from a cardiovascular pathology is one of principal causes of low life expectancy and demographic crisis in Russia. High deficiency of donor bodies forces to apply artificial replacing devices more widely. Since the 80th years during the treatment of sick heart or search of donor heart the 2-staged schedule of transplantation is applied due usage of implantable systems of LVAD or TAH which perform a role of mechanical "bridge".

Auxiliary blood circulation bases on treatment of cardiovascular disease with the help of the mechanical devices temporarily implanted to cardiovascular system and functioning together with natural heart before rehabilitation of adequate ability of a myocardium. Recently there has been found a clinical application such systems as: HeartMate LVAS, Thoratec VAD (Thoratec, USA), Novacor LVAS (World Heart Inc, USA), AbioCor (Abiomed, USA), Arrow LionHeart (Hershey Medical Center, USA), INCOR (Berlin Heart AG, Germany), etc. However the question of creation of the reliable Russian variant of such system is a very long-felt need.

In that article the description of designs of the planetary screw mechanisms for application for LVAD is given. Researches are ordered by the Science Research Institute of Transplantation and Artificial Organs (SRITAO) and are supported by the Russian Foundation of Basic Research and the Analytic program of Rosobrazovanie "The achievement of high school scientific potential". Some results have been published in proceedings of the ESAO Congresses [1–12].

2 Method

Clinical practice puts a problem of creation of LVAD, capable long time to provide blood circulation with required hemodynamics. The LVAD drive should make reciprocating motion with frequency of 1...2 Hz (meets the pulse of 60...120 min⁻¹), overcoming a rod force 100 N (meets the pressure of 120 mm Hg). In periodical cycles there is traction of left ventricle with expulsion of blood from it (a systole), and relaxation and heart filling (a diastole).

Respectively output elements of the drive are required to fulfill reciprocating cyclic motions. A working cycle goes during a systole and after that it is a reverse during a diastole. Motion of pusher plates of artificial heart ventricles can perform from the one output shaft as well as from two shafts. At first case pusher plates are attached to the ends of the screw. Reciprocating motion of pusher plates causes pressure to ensure blood pumping. At second case both output shafts actuate the plates simultaneously by means of hinge and lever system.

Mechatronic drives meet mostly the requirements to such drives. This fact is explained by high efficiency, small size and mass, high reliability and long life of the device in comparison with hydro- and pneumatic devices. The use of mechatronic drive allows creating autonomous and portable systems of artificial blood circulation instead of stationary centers.

Features of electric drive providing life of the artificial heart tell high requirements to a motor. The usage of rare-earth magnets allows creating dc motors which having the following properties (brushless, torque, portable, low-inertial, high-controllable). They are rather simple on a design, mechanically strong and energetically effective motors and therefore most acceptable for systems of auxiliary blood circulation and artificial heart. The motor specially designed for artificial heart's drive is dc brushless torque motor with three-phase winding on stator and hollow rotor. Inner hole of a rotor is used for putting wires and for assembling of rotor position sensor or input link of a gear.

There are widely used implanted ventricles containing a diaphragm pump and a drive, including dc motor and the converter of rotary movement in linear motion of a pusher. As such converters there are used such mechanisms as screw-and-nut, reciprocating linkage or rack. But those devices have some negatives: big dimensions, poor implantability, big losses on friction (that, in turn, increases power consumption) and big noise.

As actuator for LVAD MU two schemes we offer: rollerscrew mechanism which is built in a hollow rotor of dc motor, and the planetary screw mechanism with rack on the basis of flange motor. Designs are patented [13–17].

3 The rollerscrew mechanism (RSM)

Perspective actuator is rollerscrew mechanism. They differ high loading ability, durability (above 1,000,000 cycles) and efficiency (more than 0.7), provide precise and smooth motion. RSM application allows creating modular units which sizes are approached to natural dimensions of heart as much as possible. Multipointed contact in mating threads in PRM allows obtaining better characteristics, such as: load capacity, rigidity, reduction and efficiency in running at small mass and size and short kinematic chain.

We consider RSM which is designed on the basis of planetary gear, consisting of one central wheel and the satellites fixed in carrier. Instead of the central wheel RSM has a screw with helical threading, and instead of satellites it has rollers with circular grooves. At rotation of an input link which can be screw or nut, the output moves linearly. The number of rollers can be limited only to a neighborhood condition, and the screw can have any number of helical threads. The important advantage of RSM with ring rollers is

presence of the only one gearing at each roller instead of four that dramatically reduces number of passive connections.

On fig. 1 there is a drawing of LVAD drive with RSM [17]. Rollers and a nut have circular grooves, and a screw has right multi-threaded helices. Input link (nut) built in a hollow rotor, and the screw pushes the membrane of artificial ventricle.

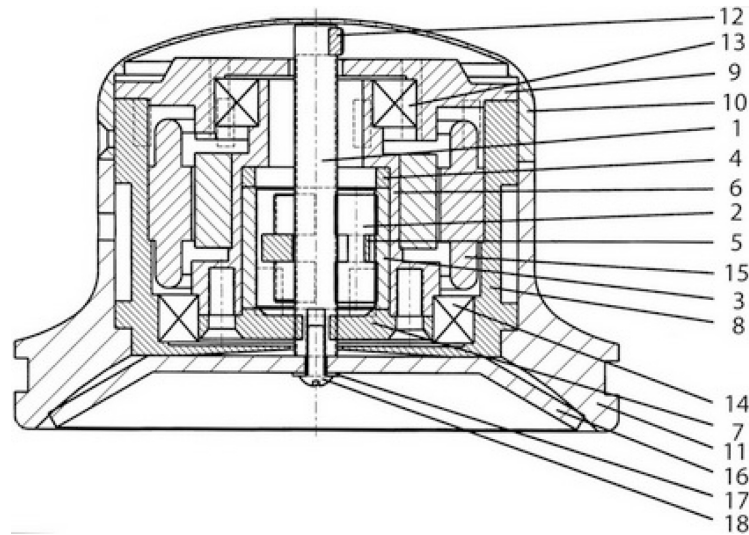


Fig. 1: LVAD with rollerscrew mechanism: 1 – screw; 2 – rollers; 3 – nut; 4 – sleeve; 5 – separator; 6 – cup; 7, 9 – cover; 8 – body; 10, 11 – body parts; 12 – magnet; 13, 14 – bearings; 15 – motor; 16 – membrane; 17 – washer; 18 – screw

4 The planetary screw mechanism with rack

For improvement of implantability and noise reduction the planetary screw mechanism with rack (PSMR) is suggested as an actuator of LVAD drive. In PSMR the electric motor is connected with rack through the planetary gear containing threaded parts. The output carrier gears with the rack, which is rigidly connected to a pusher and makes back and forth motions [16]. The PSMR feature is that threads have large helical angles for increasing of gear ratio.

Rotation of a rotor is transferred to a planetary gear which output link is carrier with helical thread. The carrier engages with the rack forcing to move a membrane of artificial ventricle. On fig. 2 the drawing of LVAD drive with PSMR is shown. That design arrangement allows using advantages both planetary gear with screw parts and rack.

In other design the planetary mechanism contains an input shaft-pinion, satellites, fixed on a carrier, and two ring gears. Feature of the suggested drive is chevronwise for

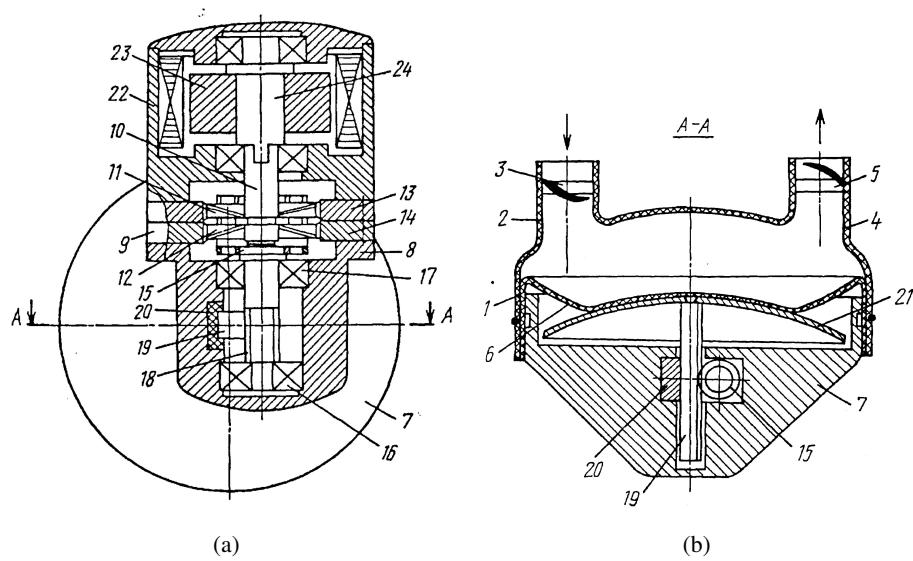


Fig. 2: LVAD with planetary screw mechanism and rack: a – general view; b – section A-A (1 – body; 2 – inlet pipe; 3, 5 – valves; 4 – outlet pipe; 6 – diaphragm; 7 – base; 8 – flange; 9 – planetary gear; 10 – central shaft-pinion; 11, 12 – satellites; 13, 14 – ring gears; 15 – carrier; 16, 17 – bearings; 18 – teeth of carrier; 19 – rack; 20 – slide; 21 – pusher; 22 – body; 23 – motor; 24 – shaft)

compensation of axial load [15]. The input shaft contains two coaxial screw gears from which one has left, and another the right threads with a helix angle more than 80° , and satellites consist two coaxial screw gears, rigidly connected with each other and having opposite directions of threads corresponding to connecting threads of gears of input shaft. Thus satellites have an opportunity to roll on internal surface of the ring gears executed as nuts, rigidly connected with each other and having another directions.

5 Results

On fig. 3 photos of designed mechatronic units of LVAD are shown: on fig. 3a there is a unit with RSM, and on fig. 3b – on base of PSMR. Units are recommended to clinical application in SRITAO.

LVAD drive with RSM has successfully passed a stage of medical and biologic tests in SRITAO. Artificial left ventricle constructed on the basis of our unit was implanted in a calf abdominal cavity. The operation which has been carried out by surgeons of SRITAO under the direction of professor D.V. Shumakov, has shown, that the Russian model artificial left ventricle is implantable and efficient.



Fig. 3: Exterior of LVAD mechatronic unit: a – unit with rollerscrew mechanism; b – unit with planetary screw gear and rack

References

1. Morozov, V.V., Zhdanov, A.V.: Electromechanical unit helps artificial heart. *Artif Organs* (1998) 22: 260-2
2. Morozov, V.V., Kosterin, A.B., Zhdanov, A.V.: Definition of thermal modes in implantable systems of auxiliary blood circulation and artificial heart. *Int J Artif Organs* (1998) 21: 672
3. Morozov, V.V., Kosterin, A.B., Zhdanov, A.: Thermal processes in implantable systems of artificial heart. *Int J Artif Organs* (1999) 22: 398
4. Morozov, V.V., Kosterin, A.B., Zhdanov, A.V.: Design of electric and mechanical drives for implantable systems of auxiliary blood circulation and artificial heart. *Heart and Lung Assistance: Lecture Notes of the ICB Seminars. Warsaw* (2000) 44: 157-63
5. Morozov, V.V., Kosterin, A.B., Zhdanov, A.V., Mamaev, D.V.: Drive of implantable systems of auxiliary blood circulation with lower power consumption. *Int J Artif Organs* (2000) 23: 573
6. Morozov, V.V., Zhdanov, A.V., Novikova, YuA.: Simulation of hemodynamics and design of artificial heart ventricles in CAD/CAM/CAE-systems. *Int J Artif Organs* (2002) 25: 695

7. Morozov, V.V., Kosterin, A.B., Novikova, YuA.: Synthesis of control law for mechatronic drive of left ventricle assist device. *Int J Artif Organs* (2003) 26: 620
8. Tolpekin, V.E., Morozov, V.V., Zhdanov, A.V., Ganin, V.P., Drobyshev, A.A.: CAE simulation of hemodynamics and CAD/CAM design of artificial heart ventricles. *Int J Artif Organs* (2003) 26: 668
9. Tolpekin, V., Kulikov, N., Shumakov, D., Hrupachev, O., Sukhov, D., Morozov, V., Ignatova, N., Melemuka, I., Gasanov, E.: Implanted artificial left ventricle. *Int J Artif Organs* (2004) 27: 600
10. Morozov, V.V., Sergenvina, N.S., Kosterin, A.B.: CAE simulation of hemodynamics in artificial heart ventricle with moving membrane. *Int J Artif Organs* (2004) 27: 627
11. Morozov, V.V., Zhdanov, A.V., Provorova, N.S.: CFX-simulation of influence of valves on hemodynamics in artificial ventricle with membrane. *Int J of Artif Organs* (2007) 30 (to be printed)
12. Morozov, V.V., Ganin, V.P., Zhdanov, A.V.: Research of the biotechnical device for revascularization of ischemized myocardium parts with the aid of CAD/CAM/CAE-technology. *Int J of Artif Organs* (2007) 30 (to be printed)
13. Pat. USSR 1570072, IPC⁷ A 61 M 1/10. Artificial heart ventricle (Kopin VK, Ganin VP, Vasilchikov AN, Morozov VV, Nosatov SP, Kolov PB); prior. 22.08.1988.
14. Pat. USSR 1818100, IPC³ A 61 F 2/24. Artificial heart (Morozov VV, Ganin VP, Nosatov SP, Drobyshev AA); prior. 21.05.1991.
15. Pat. RF 2162177, IPC⁷ F 16 H 1/30. Planetary gear (Morozov VV, Ganin VP); prior. 18.06.1999 .
16. Pat. RF 2180858, IPC⁷ A 61 M 1/12. Implantable artificial heart ventricle (Shumakov VI, Ganin VP, Tolpekin VE, Shumakov DV, Morozov VV, Zhdanov AV); prior. 12.08.1999.
17. Pat. RF 2219956, IPC⁷ A 61 M 1/12. Implantable artificial heart ventricle (Shumakov VI, Ganin VP, Tolpekin VE, Shumakov DV, Morozov VV, Zhdanov AV); prior. 02.04.2002.

Real-time Shaping of the Embedded Waveform for External Defibrillation

B. B. Gorbunov¹, A. N. Gusev¹, and S. V. Selishchev¹

Moscow Institute of Electronic Technology (Technical University),
Moscow, Russian Federation

Abstract. The paper presents a method and apparatus for shaping the electrical waveform delivered by an external defibrillator based on an electrical parameter measured during delivery of the waveform. Software and hardware co-design allow embedding anyone waveform and realizing it independently from transthoracic electrical impedance changes during shock time.

Key words: External Defibrillation, Real-time Control

1 Introduction

Despite years of intensive research, there is no suitable theory for mechanism of defibrillation that explains all the phenomena observed [1]. Moreover, there is no physiological theory that explains the mechanism of action of the bi-directional wave, nor does any theory predict the optimum amplitude and time dimensions for the second inverted wave [2].

Three key factors: (a) excitation propagation velocity, (b) refractory period, and (c) excitation path length - are sustained fibrillation. Propagation velocity is an inherent, temperature-dependent property of cardiac tissue. The refractory period can be prolonged by a strong cathodal shock applied to excited cells. An anodal shock reduces cell excitability. The excitation path length pertains to the size of the fibrillating myocardium, and both anodal and cathodal shocks can alter the path length [2].

On the one hand, an external defibrillator design is based on experimental data for optimum current waveform: strength-duration curve, delivered energy and charge, etc., and the variety of these data is obtained without taking into account transthoracic electrical impedance changes during shock time.

On the other hand, there are methods and apparatuses, which allow measuring patient electrical parameters and continual waveform shape reforming for transthoracic resistance dynamics. For example, it is some recent technical decisions [3,4,5].

The question of what current waveform should be selected as optimum, which independent from transthoracic resistance dynamics needs further elucidation. Two opportunities: forming anyone waveform, and providing this one independently from transthoracic resistance dynamics – are needed for experiments.

The paper presents a method and apparatus for shaping the electrical waveform delivered by an external defibrillator based on an electrical parameter measured during

delivery of the waveform. Software and hardware co-design allow embedding anyone waveform and realizing it independent from transthoracic electrical impedance changes during shock time.

Additional such possibilities may be useful for development a new electrotherapy methods, as electrochemotherapy for cancer treatment.

2 Methods

The both method and apparatus are based on developed high voltage delivery unit (HVD) [6]. Figure 1 is an illustration of it.

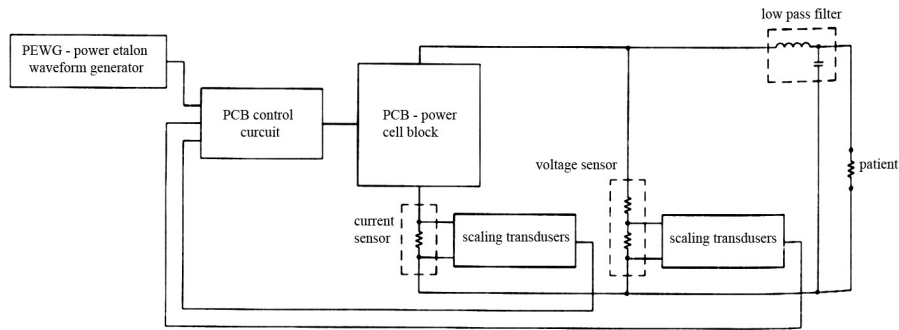


Fig. 1: High voltage delivery unit

The power cell block (PCB) delivers of high voltage to the patient through low pass filter. PCB consists of energy storage capacitors and insulated-gate bipolar transistors (IGBTs) under pulse-width modulation (no more than 50 kHz) with low-stress switching for efficiency.

Voltage sensor is measuring PCB voltage output and current sensor is measuring PCB current output. This data transfer to input of the PCB control circuit through scaling transducers. The value of scaling transducers depends upon the setting defibrillation energy.

The setting power waveform stores into power etalon waveform generator (PEWG). This etalon may be anyone. Its power waveform is setting by software technology. Besides the integral from power waveform etalon on shocktime is setting defibrillation energy.

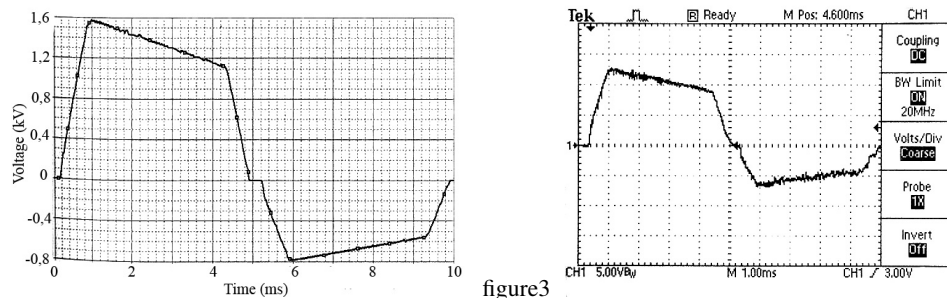
The PCB control circuit is real-time driving the process of high voltage delivery using real-time comparison of PEWG output and scaling transducers output, that is feedback control.

The high voltage delivery unit is simulated by PSpice. Than it was realized by printed-circuit board technology.

3 Results

Figure 2a is illustration of simulation result for high voltage delivery to patient (the voltage-time curve for 200 J delivered energy and 50 Ω load resistance). The simulation model includes the skin breakdown with 100V threshold. It is example of asymmetric biphasic waveform etalon, which now is optimum for external defibrillation [2]. The both duration of the first and second phases are 4 ms at the half-level amplitude maximum of each phase. The amplitude of second (inverted) phase is half of first phase, and pulse tilt is 30 %.

This simulation result corresponds to the worst combination for electrical parameters of the circuit components. The experimental result is presented in Figure 2b.



(a) Voltage-time curve for 200 J delivered Energy and 50 Ω load resistance. figure2
 (b) Experimental voltage-time curve for 100 J delivered energy and 50 Ω load resistance. figure3

Fig. 2: Voltage-time curves for different setups

4 Conclusions

There are both a method and apparatus for shaping the electrical waveform delivered by an external defibrillator based on the PCB output measured and control feedback. Software and hardware co-design allow embedding anyone waveform and realizing it independently from transthoracic electrical impedance changes during shock time.

References

1. W.A. Tacker. External defibrillators. In The Biomedical Engineering handbook, J.D.Bronzino, Eds. Boca Raton, Fla: CRC & IEEE Press, 1995, pp. 1275-1283.
2. L.A. Geddes, and W. Havel. Evolution of the optimum bi-directional (biphasic) wave for defibrillation. Biomedical Instrumentation & Technology, vol. 34, pp. 39-54, January/February 2000.

3. J.E. Brewer, K.F.Olson, B.L. Gilman, and R.E. Bosler. Continal waveform shape reforming method and apparatus for transchest resistance dynamics. US Patent, No.6398967, March 2001.
4. T.Z. Elabbady, F.W. Chapman, J.L. Sullivan, R.C. Nova, and L.A. Borschowa. Defibriliator method and apparatus. US Patent, No.5999852, December 1999.
5. B.E. Gliner, T.D. Lyster, C.S. Cole, D.J. Powers and C.B. Morgan. Electrotherapy method utilizing patient dependent electrical parameters. US Patent, No. 5749904, May 1998.
6. B.B. Gorbunov, A.N. Gusev, S.F. Kurekov, S.V. Selishchev, N.N. Starshinov, and Yu.B. Hlebnikov. Power unit of external defibriliator with embedded waveform. Proc. Int. Conf. "BIOMEDDE-VICE-2000", vol. 2, pp. 212-214, October 2000, Moscow. (In Russian).

Ultrasonic Peeling

V. M. Gorshkova¹

The Bauman Moscow State Technical University, Russia, gorshkova@mail.ru

Abstract. The article suggests a mathematical description of peeling by ultrasound technologies.

1 INTRODUCTION

Ultrasonic peeling can be referred to the surface peeling which is atraumatic because the corneal layer (dead cells) is peeled from the skin surface. A decrease in thickness of the corneal layer permits to remove hyperkeratosis regions, to increase living corneal layers thickness, to improve a skin tint (color) and to clear hyperpigmented regions.

The ultrasonic peeling technology has been developed in the Bauman Moscow State Technical University.

During ultrasonic peeling the ultrasonic vibration effect is produced on the system of a pharmaceutical substance in solution (gel, cream) (antiseptics or α -hydroxy-acids of low concentration) and a biological tissue of the skin (corneal layer and epidermis).

Flow characteristics of solutions can be shown as:

$$\sigma = f(\dot{\gamma})$$

where σ – shear stress; $\dot{\gamma}$ shear rate.

It is known [1] that this relation is similar to one shown in Fig. 1.

μ - viscosity

$\mu \triangleq \frac{d\sigma}{d\dot{\gamma}}$. If $\frac{d\sigma}{d\dot{\gamma}} = const$, the fluid is Newtonian and $tg\alpha = \frac{d\sigma}{d\dot{\gamma}} = const$ in the region of abnormal flow $\frac{d\sigma}{d\dot{\gamma}} = f(\dot{\gamma})$ i.e. shear stress is a function of shear rate.

An investigation of the flow of non-Newtonian fluids is a very intricate theoretical and application problem, which has not been solved till now.

Let $\dot{\gamma}_H$ be maximum shear rate, which can arise in the system.

Obviously $\sigma(\dot{\gamma}) = \int_0^{\dot{\gamma}} \frac{d\sigma}{d\dot{\gamma}} d\dot{\gamma}$

As it follows from Fig. 1, $\frac{d\sigma}{d\dot{\gamma}}$ and $\dot{\gamma}$ relation looks like "flow curves" shown in Fig. 2.

Note that the area under the curve $\frac{d\sigma}{d\dot{\gamma}}(\dot{\gamma})$ can be calculated by the equation

$$\sigma(\dot{\gamma}_H) = \int_0^{\dot{\gamma}_H} \frac{d\sigma}{d\dot{\gamma}} d\dot{\gamma}$$

Let us consider now an equivalent rectangle

$$s_{\dot{\gamma}} = \frac{d\sigma}{d\dot{\gamma}}(\dot{\gamma}^*) \dot{\gamma}_H$$

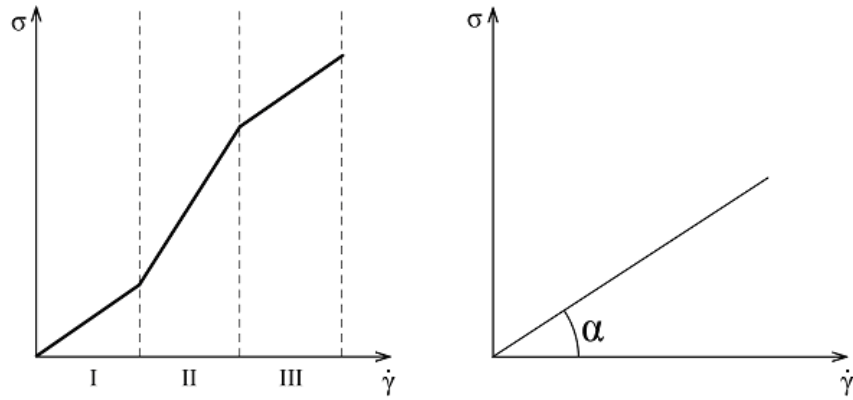


Fig. 1: 'Flow curves' I, III – Newtonian flow; II – abnormal flow

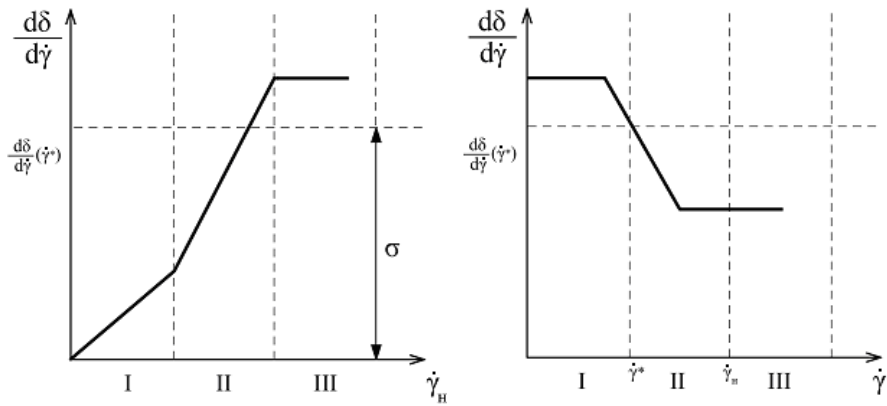


Fig. 2: Viscosity and shear rate relation in Newtonian flow (a) and in general case (b), see designations in Fig.1.

(which area equals $\sigma(\dot{\gamma}_H)$), therefore

$$\frac{d\sigma}{d\dot{\gamma}}(\dot{\gamma}^*) = \frac{1}{\dot{\gamma}_H} \int_0^{\dot{\gamma}_H} \frac{d\sigma}{\dot{\gamma}} d\dot{\gamma}$$

Relation between shear stress and shear rate, being realized to the maximum in the system, is an apparent viscosity:

$$\frac{d\sigma}{d\dot{\gamma}}(\dot{\gamma}^*) = \mu$$

Therefore, within the $0 \dots \dot{\gamma}_H$ range of $\dot{\gamma}$ variation the antiseptic solution can be approximately considered as Newtonian fluid, i.e. $\frac{d\sigma}{d\dot{\gamma}} = const$ (bearing in mind that flow curves are constant).

Viscosity can be calculated as:

$$\frac{\sigma(\dot{\gamma}_H)}{\dot{\gamma}_H} = \frac{d\sigma(\dot{\gamma}^*)}{d\dot{\gamma}}$$

Note, that $\dot{\gamma}_H$ and $\dot{\gamma}^*$ are determined by the flow curve configuration.

Now let us consider the fluid flow, when cavitation process is caused by an ultrasonic vibration transmitter. Resting fluid, lying on the surface (corneal) skin layer is exposed to ultrasonic effect by means of an ultrasonic generator and a tool, which results in formation of microbubbles, i.e. cavitation. Let us analyze properties of a cavitating bubble and its influence on fluid properties.

Let us consider a cavern (bubble), and denote:

P -pressure, created by the surrounding fluid on the cavern; P_H - pressure of saturated vapors in the cavern; P_i - pressure of gases (from air); σ - surface tension coefficient. For simplicity the cavern is assumed to be a sphere. Therefore, equilibrium of the bubble in the fluid is given by the equation:

$$P = p_H + p_\Gamma - \frac{2\sigma}{R}$$

Where R - sphere radius.

From gas dynamics it is known that $p_i = \frac{BT}{R^3}$, where $0 < B = const$; T - temperature °C

Hence, it is obvious that if $P > p_H + p_i - \frac{2\sigma}{R}$, the cavern compresses, if $P < p_H + p_i - \frac{2\sigma}{R}$, the cavern expands.

In view of the Boyle's law $P_\Gamma R^3 = p_{\Gamma_0} R_0^3$, where P_{Γ_0} , R_0 - initial gas pressures and cavern radius, respectively.

Therefore,

$$p_\Gamma = p_{\Gamma_0} \left(\frac{R_0}{R} \right)^3 = \left(p_0 - p_H + \frac{2\sigma}{R_0} \right) \left(\frac{R_0}{R} \right)^3,$$

Where

$$p_0 = p_H + p_\Gamma - \frac{2\sigma}{R_0}$$

Thus,

$$P = p_H + \left(p_0 - p_H + \frac{2\sigma}{R_0} \right) \left(\frac{R_0}{R} \right)^3 - \frac{2\sigma}{R}$$

If the gas state variation law is adiabatic ($p = const$), therefore $\frac{p}{p_{\Gamma_0}} = \left(\frac{R_0}{R} \right)^{3\gamma}$ (γ - specific heat ratio), therefore $p = p_{\Gamma_0} \left(\frac{R_0}{R} \right)^{3\gamma} - \frac{2\sigma}{R}$.

Hence, the cavern varies its radius under the action of an outside force $f = (R, T)$.

In case of the Clapeyron's law

$$f(R, T) = -p + p_H + \frac{BT}{R^3} - \frac{2\sigma}{R}$$

The cavern critical radius is $R_{kp} = \sqrt{\frac{3BT}{2\sigma}}$, and the critical pressure is

$$p_{kp} = p_H - 2 \frac{\left(\frac{2}{3}\sigma \right)^{1/2}}{\sqrt{BT}}.$$

In the isothermal case:

$$R_{kp} = \sqrt{3} R_0 \sqrt{\frac{R_0 p_{\Gamma_0}}{2\sigma^2}};$$

$$f(R, T) = -p + p_H \left(p_0 - p_H + \frac{2\sigma}{R_0} \right) \left(\frac{R_0}{R} \right)^3 - \frac{2\sigma}{R};$$

$$R_{kp} = p_H - \frac{4}{3\sqrt{3}} \frac{\sigma}{R_0} \sqrt{\frac{2\sigma}{R_0 p_{\Gamma_0}}}$$

In the adiabatic case:

$$f(R, T) = -p + p_{\Gamma_0} \left(\frac{R_0}{R} \right)^{3\gamma} - \frac{2\sigma}{R};$$

$$R_{kp} = R_0 \sqrt{\frac{2p_{\Gamma_0}}{\sigma}}; \quad p_{kp} = p_{\Gamma_0} R_0^3 \left(\frac{\sigma}{2p_{\Gamma_0}} \right)^{4/3} - \frac{2\sigma}{R_0} \left(\frac{\sigma}{2p_{\Gamma_0}} \right)^{3/2}$$

Note that the bubble critical radius can be found providing:

$$\frac{\partial f(R, T)}{\partial R} = 0, \quad P_{kp} = P(R)|_{R=R_{kp}}$$

The presence of caverns makes fluid compressible. The latter means that its density depends on pressure. Approximately this dependence can be considered to be a linear one. This fact is theoretically and experimentally validated in [2].

Hence, as a result of interaction of corneal layer cells and microbubbles, the latter collapse, therefore the overpressure (microlocal pressure) is created in the region of their effect, which results in peeling of dead (corneal layer) cells.

There are a lot of imperfections such as cracks (irregularities) on the skin surface (corneal layer). When filled with fluid, air remains in cracks. Besides, penetrating through the surface of the fluid due to diffusion, gases are dissolved therein, cavitation is developed.

For the sake of simplicity the cavern is presumed to be a sphere. Fluid is practically incompressible and at the initial point of time is at rest. Suppose that the fluid motion is irrotational and the fluid is isotropic and homogeneous. Moreover, the bubble moves only along the radius.

Denote $u \triangleq \frac{dR}{d\varphi} = \frac{\partial \varphi}{\partial r}$; $\varphi = \frac{dR}{dt}$, where $R(t)$ - cavern radius at the point of time t .

By virtue of the above assumptions a frictionless liquid and a viscous fluid behaves identically.

Thus, $R \frac{du}{dt} - \frac{3}{r} u^2 = \frac{p_\infty - p(t)}{\rho}$, where p_t - pressure on the cavern wall at the point of time t ; ρ - gas density; p_∞ - fluid pressure in a remote point. Suppose that the bubble is filled with perfect gas, i.e.

$$p_t = p_v - \frac{2\sigma}{R} - \frac{BT}{R^3}$$

where p_v - saturation pressure depending on temperature.

Therefore,

$$\rho \left(R \frac{du}{dt} + \frac{3}{ru^2} \right) = \left(p_\infty - p_v + \frac{2\sigma}{R} - \frac{BT}{R^3} \right) = f_1(R, T),$$

where $f(R, T)$ - outside force (ultrasonic) acting on the cavern radius variation. Obviously, three situations are possible:

- 1) $f_1(R, T) = 0$ at $R = R_{kp}$, i.e. there is an equilibrium;
- 2) $f_1(R, T) > 0$ at $R = R_{kp}$ - cavern growth;
- 3) $f_1(R, T) < 0$ at $R = R_{kp}$ - cavern collapse.

Let us determine the critical value of R_{kp} , when $\frac{\partial f_1}{\partial R} = 0$, hence, $R_{kp} = \left(\frac{3}{2} \frac{BT}{\sigma} \right)^{1/2}$, therefore $R_{kp} = -\frac{4\sigma}{3(p_\infty - p_v)_{kp}}$

Thus, the dynamic conditions of the bubble collapse have been found.

Hence, as a result of interaction of corneal layer cells and microbubbles the latter collapse, therefore, in the region of ultrasonic effect the overpressure is created, which results in peeling of keratinized (dead) cells.

It is known that the corneal layer is an unwettable surface. Note that a criterion for high quality peeling is wettability of surface, which can be described by the following conditions: let σ_1 be surface tension at the skin-air interface, σ_2 - surface tension at the skin-solution interface, σ_3 - surface tension of solution-air, and θ - contact angle.

Condition of the surface wettability is as follows:

$$\sigma_1 = \sigma_2 + \sigma_3 \cdot \cos \theta$$

If $\theta < 90^\circ$ - the surface is wettable, if $\theta > 90^\circ$ - the surface is unwettable.

Therefore, upon carrying out the ultrasonic peeling the skin surface becomes wettable which permits to draw a conclusion about the efficiency of ultrasonic peeling.

2 References

References

1. Vinogradov G.V., Malkin A.Ya. Polymer Rheology.-M.: Chemistry, 1977.- p.438

2. Gorshkova V.M. Development of Technology and Tools for Ultrasonic Impregnation of the Pharmaceutical Substance into the Vascular Wall. Ph.D. thesis – M.1987.- p.184
3. Nikolaev G.A., Loshchilov V.I. Ultrasonic Technology in Surgery - M.: Medicine, 1980
4. Application of Ultrasonic in Medicine. Basic Physics/ Under the Editorship of K. Hill - I.: Mir, 1989
5. Ernandes E.I. Cosmetic Peeling: Theoretical and Practical Aspects. Collected articles. Publishing House "Cosmetics and Medicine"; I. 2003- p.214

Computer Aided Medical Procedures

Registration-free Laparoscope Superimposition for Intra-Operative Planning of Liver Resection

Marco Feuerstein¹, Thomas Mussack² Sandro M. Heining², and Nassir Navab¹

¹ Chair for Computer Aided Medical Procedures (CAMP), Technische Universität München, Munich, Germany,

² Chirurgische Klinik und Poliklinik, Klinikum der LMU - Innenstadt, Munich, Germany

Abstract. In recent years, an increasing number of liver tumor indications were treated by minimally invasive laparoscopic resection. Besides the restricted view, a major issue in laparoscopic liver resection is the enhanced visualization of (hidden) vessels, which supply the tumorous liver segment and thus need to be divided prior to the resection. To navigate the surgeon to these vessels, pre-operative abdominal imaging data can hardly be used due to intra-operative organ deformations mainly caused by appliance of carbon dioxide pneumoperitoneum and respiratory motion. While regular respiratory motion can be gated and synchronized intra-operatively, motion caused by pneumoperitoneum is individual for every patient and difficult to estimate.

Therefore, we propose to use an optically tracked mobile C-arm providing cone-beam CT imaging capability intra-operatively. The C-arm is able to visualize soft tissue by means of its new flat panel detector and is calibrated offline to relate its current position and orientation to the coordinate system of a reconstructed volume. Also the laparoscope is optically tracked and calibrated offline, so both laparoscope and C-arm are registered in the same tracking coordinate system.

Intra-operatively, after patient positioning, port placement, and carbon dioxide insufflation, the liver vessels are contrasted and scanned during patient exhalation. Immediately, a three-dimensional volume is reconstructed. Without any further need for patient registration, the volume can be directly augmented on the live laparoscope video, visualizing the contrasted vessels. This superimposition provides the surgeon with advanced visual aid for the localization of veins, arteries, and bile ducts to be divided or sealed.

1 Introduction

In a typical totally laparoscopic liver resection procedure, a major step towards tumor resection is the successful division of all vessels supplying the respective liver segment. For laparoscopic abdominal surgery, the target region can be deformed due to heartbeat and respiratory motion. While deformations in the abdominal area caused by the heartbeat are negligible [1], the rather large respiratory motion of about 1 cm can be corrected for by gating [2,3] and can be synchronized to e.g. an augmented visualization. Individual deformations of greater extent however occur between pre-operative acquisition of the CT and the beginning of the resection, i.e. during patient and port placement, appliance of carbon dioxide pneumoperitoneum, and the intervention itself. Pneumoperitoneum alone can already cause large liver motions of e.g. 1.8 ± 12 , 4.1 ± 6.4 , and

0.1 ± 0.4 mm in x, y, and z directions, respectively, as shown for two pigs [2]. In this case, using pre-operative rigid imaging data requires an additional intra-operative registration process, which is costly in terms of time and interaction. Therefore, precisely guiding the surgeon to the target area is difficult to perform and hard to validate.

Supplementary to laparoscopic ultrasound, we introduce the use of an optically tracked mobile isocentric C-arm providing cone-beam CT imaging capability to augment contrasted vessels directly on the laparoscopic view intra-operatively. This provides the surgeon with valuable information on the location of veins, arteries, and bile ducts, which supply the liver segment to be resected and therefore need to be divided.

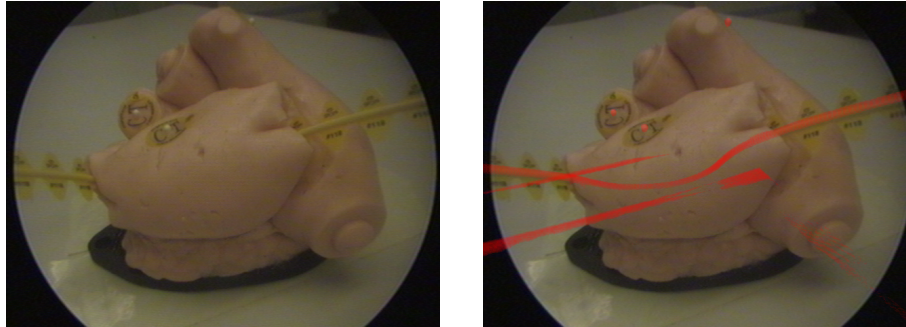
2 Methods

Our prototype mobile C-arm is able to visualize soft tissue intra-operatively, which is not possible with current commercially available mobile C-arms. An optical tracking system determines the position and orientation of both C-arm and laparoscope, which can be brought into the same coordinate system by various offline calibration routines. Intra-operatively, after port placement, appliance of carbon dioxide pneumoperitoneum, and instrument insertion, we contrast the vessel tree of the liver and at the same time acquire a C-arm image series during patient exhalation. Alternatively, C-arm projections can be gated and correlated to respiratory motion in order to acquire a high-quality scan [4]. After reconstruction, we are able to precisely augment the contrasted vessel tree directly on the laparoscopic view just before the beginning of the resection without any time-consuming patient registration process. The augmentation can be synchronized to the patient's respiration and only be displayed during exhalation [1]. 3D texture based volume rendering is used for augmentation, which utilizes pre-defined transfer functions in such a way that only voxel intensities of the contrast agent are rendered. In general, the augmented visualization will only be shown to the surgeon for the intra-operative in-situ planning of the resection to provide a detailed 'roadmap' of the vessels, but not any more when the surgeon starts to cut, since this causes the liver to deform again and invalidates any prior registration.

3 Results

For the determination of the laparoscopic augmentation error, the volume of a rigid plastic model of a heart with three adhered spherical markers of 2.3 mm diameter and a curved line marker representing a vessel was reconstructed. The laparoscope was moved around this plastic model arbitrarily. Augmenting the live laparoscope video, images were taken from a large number of views covering the interventional working space. On all images the markers and their augmented counterparts, visualized in a different color, are visible (cf. figure 1). The absolute distance in mm was measured from the midpoint of a spherical marker and its corresponding virtual projection. The obtained root mean square error was 0.81 mm and the maximum error 1.38 mm.

To clinically evaluate our vessel augmentation, we performed two ex-vivo studies together with our clinical partners, one with a freshly harvested whole porcine liver and a second one with a defrosted whole ovine kidney. Each time we placed the organ in a



((a)) Real, undistorted laparoscope image showing the 3 spherical fiducials and a curved line marker on the plastic heart.

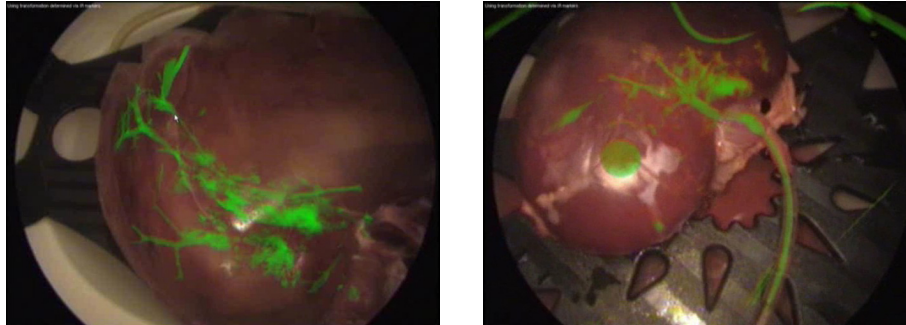
((b)) Augmented laparoscope image. Volume rendered are only the markers; the additional lines are artifacts in the reconstructed volume.

Fig. 1: Plastic heart used for the determination of the augmentation error.

perfusion box. The surgeons catheterized the liver's portal vein and the kidney's renal artery, respectively. Then the iodinated nonionic contrast agent SOLUTRAST[®] 300 was administered into the organ. It was diluted in normal saline and conveyed into the organ by the pump of the perfusion system. We immediately started a C-arm acquisition and reconstructed the organ's 3D volume. In another experiment, we directly injected the pure contrast agent.

The acquisition of 200 C-arm projections takes 64 seconds, which stays within the time limits of holding breath during artificial respiration. After acquisition, the reconstruction of the 3D volume was started, which currently takes about six minutes. However, once the prototype system is commercialized, the reconstruction algorithms will be optimized and parallelized. Additionally, reconstruction will commence as soon as the first projection is acquired. This will lead to reconstruction times of approximately one minute after completion of a scan, as known from modern CT scanners.

The contrasted part was clearly visible in the reconstructed volume for both cases, directly as well as via the perfusion system. The vessels were directly augmented on the laparoscope's view by volume rendering. This direct visualization technique does not require any processing time, since time-consuming segmentation, as it would be needed for surface-based rendering, can be completely avoided. The vessels could be accurately overlaid for most laparoscope positions, as you can see in figure 2 in the case of the kidney, where the real and virtual catheters perfectly overlap. In the case of the porcine liver, only the vessels of one lobe could be contrasted partially, as some liver vessels were accidentally cut at the abattoir. Although in general more vessels could be visualized for the direct administration of contrast agent, artifacts appeared during the 3D volume reconstruction due to the high concentration. We will conduct further studies to find an optimal contrast agent concentration for an artifact-free reconstruction and a clear visualization of all relevant vessels.



((a)) Augmented porcine liver. The speckled areas are reconstruction artifacts caused by a high concentration of contrast agent.

((b)) Augmented ovine kidney. The big spot is the perfusion system's plug, which apparently has a similar Hounsfield unit like the contrast agent.

Fig. 2: Vessel augmentation.

4 Related Work

To guide the division of vessels and the resection, ultrasonography may be used. It is however difficult to understand, how ultrasound (US) images are oriented in relation to the patient. Ellsmere et al. therefore propose an advanced system to intuitively display the laparoscopic US image plane relative to a pre-operative 3D model of the patient [5]. This helps the physician to identify key structures. Intra-operative 3D data provided by our system is not affected by the individual organ movement between pre-operative data acquisition and the beginning of the resection, making it an ideal complement to their navigation system. Instead of using the pre-operative CT, the system proposed by Ellsmere et al. could now use our registered intra-operative CT reconstruction to accomplish the guidance.

Another approach to improve the spatial relation of US images to the patient is taken by Leven et al. [6]. They propose a system to apprehensively overlay the laparoscopic ultrasound image plane or a reconstructed US volume, respectively, directly on the live images of a stereo endoscope. It is however still difficult to interpret low-resolution US images, especially reconstructed volumes. Our new approach of reconstructing a high-resolution 3D volume from cone beam CT intra-operatively and combining it with advanced visualization can be an optimal supplement to their system as well.

Summarizing, our system provides high-resolution 3D data acquired after organ movement mainly caused by carbon dioxide insufflation. It visualizes the data directly onto the laparoscopic images thanks to the new idea of hand-eye calibration and C-arm tracking in a common world coordinate system.

5 Conclusions

This work is an important and encouraging step towards the provision of precise intra-operative visualization aid for laparoscopic liver resection providing automatic intra-operative patient registration. Combining intra-operative imaging, gating, tracking, and visualization, restrictions caused by organ movement between pre- and intra-operative imaging can be easily overcome. Our intra-operative resection planning system is not solely restricted to liver surgery, but can also be applied to various other endoscopic interventions. Our experiments and studies show satisfying qualitative results for intra-operative laparoscope superimposition.

The result provided here could allow different methods proposed in the literature [5,6] to start with co-registered intra-operative cone beam reconstruction in order to improve their advanced visualization solutions.

References

1. Olbrich, B., Traub, J., Wiesner, S., Wiechert, A., Feußner, H., Navab, N.: Respiratory motion analysis: Towards gated augmentation of the liver. In: *Computer Assisted Radiology and Surgery*, Berlin, Germany (June 2005) 248–253
2. Herline, A., Stefansic, J., Debelak, J., Hartmann, S., Pinson, C., Galloway, R., Chapman, W.: Image-guided surgery: preliminary feasibility studies of frameless stereotactic liver surgery. *Archives of Surgery* 134(6) (June 1999) 644–650
3. Clifford, M., Banovac, F., Levy, E., Cleary, K.: Assessment of hepatic motion secondary to respiration for computer assisted interventions. *Computer Aided Surgery* 7(5) (2002) 291–299
4. Kriminski, S., Mitschke, M., Sorensen, S., Wink, N.M., Chow, P.E., Tenn, S., Solberg, T.D.: Respiratory correlated cone-beam computed tomography on an isocentric c-arm. *Physics in Medicine and Biology* 50(22) (November 2005) 5263–5280
5. Ellsmere, J., Stoll, J., Wells, W., Kikinis, R., Vosburgh, K., Kane, R., Brooks, D., Rattner, D.: A new visualization technique for laparoscopic ultrasonography. *Surgery* 136(1) (July 2004) 84–92
6. Leven, J., Burschka, D., Kumar, R., Zhang, G., Blumenkranz, S., Dai, X.D., Awad, M., Hager, G.D., Marohn, M., Choti, M., Hasser, C., Taylor, R.H.: *Davinci canvas: A telerobotic surgical system with integrated, robot-assisted, laparoscopic ultrasound capability*. Volume 3749., Springer-Verlag (September 2005) 811–818

Semi-automatical Validation of SPECT/CT Scanners

Jingfeng Han¹, Christian Bennewitz², Joachim Hornegger¹, and Torsten Kuwert²

¹ Institute of Pattern Recognition, University of Erlangen–Nuremberg, Erlangen, Germany,
jingfeng@informatik.uni-erlangen.de

² Clinic of Nuclear Medicine, University of Erlangen–Nuremberg, Erlangen, Germany

Abstract. Hybrid scanners, which enable the performance of single photon emission tomography (SPECT) and X-ray computerized tomography (CT) in one procedure, have considerable potential as an all-rounder in the nuclear medicine departments. However, challenges remain in validating the accuracy of such hybrid systems. In this paper, a systematic validation method with minimum user interaction is proposed, which has been successfully used on a data-set from a SPECT/Spiral-CT hybrid camera. This method focuses on measuring the distance between the centers of gravity of the SPECT hot spot and its counterpart in the CT image. A novel adaptive threshold method is proposed to automatically segment SPECT hot spots, while the corresponding CT structures are segmented by the semi-automatic random walk method, based on a fast multigrid solver. Accuracy and reproducibility of the validation method have been confirmed by experiments with 21 clinical data-sets.

1 Introduction

Hybrid scanners combining SPECT and CT offer physicians the opportunity to acquire correlated functional and morphological information from a patient in a single session. However, the anatomical accuracy of this hardware-based registration has not yet been sufficiently validated. Phantom studies are not suitable for the validation of the hybrid scanner because it is technically difficult for a phantom to simulate respiratory and cardiac movements, both of which play a key role in mismatching. In a recent study [1], the accuracy of a SPECT/CT system has been quantitatively evaluated by measuring the distance between the centers of gravity of corresponding lesions in two modalities. However, the reproducibility and the accuracy were still questioned, since the selection of centers of gravity was determined by the users. In this paper, we propose a more automatic and more reproducible validation scheme for SPECT/CT hybrid scanners.

2 Methods

We measure the degree of the matching of corresponding structures in SPECT and CT volumes to evaluate the accuracy of the SPECT/CT fusion. The pipeline of validation scheme is demonstrated in Figure 1. In this validation scheme, a hot spot in a SPECT volume and its corresponding structure in a CT volume can be segmented with minimum user interaction. a new fully automatic thresholding method is used to segment SPECT hot spot. The optimal threshold is chosen based on the maximally stable

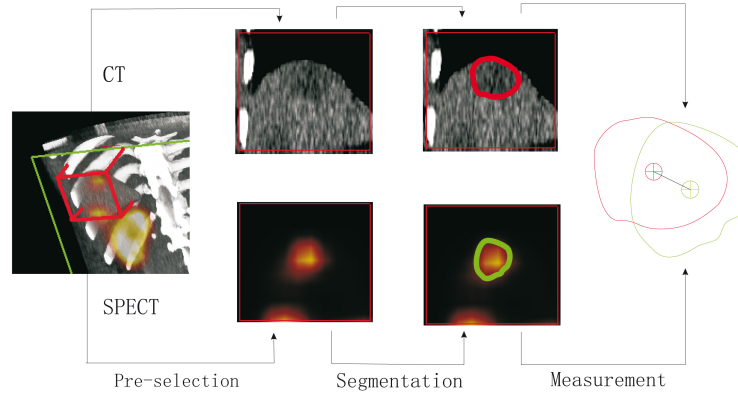


Fig. 1: The work flow of the validation. **Pre-selection:** User manually selects a cubic region that contains both SPECT/CT hot spots from the fused MPR view. Pre-selection of the computation region largely speeds up the following processing operations, but has no influence on the final validation results. **Segmentation:** Segmenting the three-dimensional SPECT hot spot using the adaptive thresholding method (full-automatic). Segmenting the corresponding object in the CT volume via the random walk method (semi-automatic). **Measurement:** Computing the centers of gravity of the segmented SPECT/CT objects. Measuring the distance of two centers to evaluate the quality of the SPECT/CT fusion.

extremal region (MSER) [2,3,4] algorithm. The segmentation actually starts the connected thresholding from the given seed and seek a range of thresholds that leaves the peak of hot spot effectively unchanged. The corresponding CT structure is segmented by a semi-automatic random walk method [5], which allows users to select seeds to intuitively guide the algorithm to separate desired objects from the background. From our experience, drawing the seeds on the middle slice in the axial, sagittal and coronal views is sufficient. The quality of a SPECT/CT fusion is evaluated by the distances between the centers of gravity of the segmented SPECT/CT objects. The validation tool has been successfully integrated into a commercial software of medical image analysis (Syngo, Siemens Medical Solutions).

3 Results

To evaluate the validation tools, we select a set of 21 patients (13 female, 8 male; age range: 10-80 years; mean age: 59.55) examined by a SPECT/spiral CT scanner between November 2006 and March 2007. We choose adenomas of the parathyroid glands on 10 patients and the physiological accumulations of the submandibular gland on the other 11 patients for this study.

The accuracy of the validation tool is evaluated as follows: Two operators perform the validations independently. One operator directly uses the validation tool to measure the distances in X -, Y - and Z -direction (t_x, t_y, t_z) between the hot spot on SPECT and the structure on CT. In the same way, the second operator validates the SPECT/CT volumes,

where the SPECT volume has been artificially shifted in X -, Y - and Z -directions. The shift parameters (s_x, s_y, s_z) are randomly generated between 5 mm and 10 mm or between -5 mm and -10 mm. We denote the distances measured by the second operator as $(\hat{t}_x, \hat{t}_y, \hat{t}_z)$. The extent to which the ground truth shift (s_x, s_y, s_z) and the measured shift $(d_x, d_y, d_z) := (\hat{t}_x - t_x, \hat{t}_y - t_y, \hat{t}_z - t_z)$ match, indicates the accuracy of the validation. The experiment yields a clear linear association between the ground truth and the measurement: The correlation coefficients are 0.9927, 0.9909 and 0.9853 in X -, Y - and Z -directions, respectively. The anatomical inaccuracies, measured by the mean \pm standard deviation of the absolute error, are reported to be 0.7189 ± 0.6298 mm in X -direction, 0.9250 ± 0.4535 mm in Y -direction and 0.9544 ± 0.6981 mm in Z -direction.

To evaluate the intraobserver reproducibility, the distances between the SPECT hot spot and CT structure are measured twenty times in five different patients, yielding a mean standard deviation of 0.2177 mm in the X -direction, 0.3039 mm in the Y -direction and 0.3350 mm in the Z -direction. This indicates a high intraobserver reproducibility of the measurement of the X -, Y - and Z -distances. The mean time needed for a full validation process, including the time for data loading and user operation, is less than 2 minutes on a AMD Athlon 3200+ computer (2.20 GHz, 2.00 GB RAM).

4 Conclusion

The purpose of this paper is to introduce a novel way of validating the anatomical accuracy of the SPECT/CT hybrid scanner through the segmentation of hot spot on SPECT and the corresponding structure on CT. The experimental results show that the measurement of this validation tool is sufficiently accurate and reproducible for the clinical data. In our future work, we plan to apply this validation tool to analyse the variation of the accuracy of hybrid scanners with respect to different positions, tracers or acquisition protocols.

References

1. A. Nömayr, W. Römer, D. Strobel, W. Bautz, T. Kuwert: Anatomical accuracy of hybrid SPECT/spiral CT in the lower spine. *Nuclear medicine communications* 27 (2006) 521–528
2. Donoser, M., Bischof, H.: 3d segmentation by maximally stable volumes (MSVs). In: *proceeding of international conference on pattern recognition (ICPR)*. (2006) 63–66
3. Donoser, M., Bischof, H.: Efficient maximally stable extremal region (MSER) tracking. In: *proceeding of conference on computer vision and pattern recognition (CVPR)*. (2006) 553–560
4. Matas, J., Chum, O., Martin, U., Pajdla, T.: Robust wide baseline stereo from maximally stable extremal regions. In: *Proceedings of the British Machine Vision Conference (BMVC)*. Volume 1. (2002) 384–393
5. L. Grady: Random walks for image segmentation. *IEEE transactions on pattern analysis and machine intelligence* 28 (2006) 1768–1783

Adding navigation to radio-guided surgery: new possibilities, new problems, new solutions

Thomas Wendler¹, Jörg Traub¹, Alexander Hartl¹, Tobias Lasser¹, Maria Burian², Andreas Buck³, Farhad Daghighian⁴, Markus Schwaiger³, Sibylle I. Ziegler³, and Nassir Navab¹

¹ Chair for Computer Aided Medical Procedures (CAMP), TU Munich, Germany,

² Department of Surgery, Klinikum rechts der Isar, TU Munich, Germany

³ Department of Nuclear Medicine, Klinikum rechts der Isar, TU Munich, Germany

⁴ IntraMedical Imaging LLC, Los Angeles, California, USA

Abstract. Hand-held nuclear devices have been used since the late eighties for functional guidance during surgical procedures. Using the tracer principle, these enable to detect and spatially localize radioactively marked processes and thus assist the surgeon by providing him/her with functional information in space, otherwise invisible or difficult to acquire intra-operatively. Here, we review current approaches to improve these procedures by navigation. We focus on the limitations of these systems and discuss ways to solve them thinking of a new generation of intra-operative nuclear imaging approaches that will go beyond prototypes.

1 Introduction

Nuclear medicine has become one of the most dynamic branches in today's diagnostic field. It is based on the use of radio-labeled, highly specific tracers that target functions in the body and can be imaged using 2D szintigraphy, SPECT (single photon emission tomography) or PET (positron emission tomography) [1]. However, issues like bulky equipment, resolution and acquisition time make them unsuitable for intra-operative use, so they are restricted to diagnosis and planning.

In order to overcome these limitations, hand-held radioactivity detectors were introduced [2]. These are common diagnostic devices nowadays, especially during surgery and sentinel lymph node determination [3]. The main advantages of these devices lie in their portability, simplicity, and the possibility of miniaturizing them for intra-operative use. Their main restriction is, however, that they are either non-imaging devices or are restricted to small field of view 2D devices.

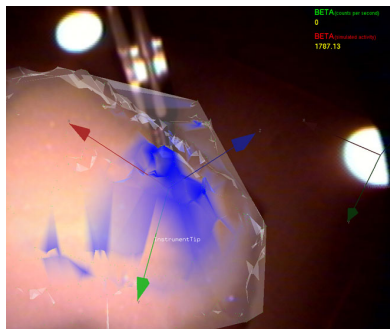
The combination of intra-operative nuclear devices with position and orientation ('pose') tracking is a promising alternative to extend the use of this technology further and recover the 'imaging' component. The idea is to acquire the read-out of the nuclear devices simultaneously with their pose. Depending on the nature of the radiation acquired, two possible imaging modalities arise. On the one hand, the use of beta-particles, which only penetrate thin layers of tissue, enables 3D activity surface reconstruction. On the other hand, the use of higher penetration gamma-rays promises full 3D tomographic imaging.

In this paper we review the current approaches employing tracked nuclear devices, we discuss their limitations and finally present solutions that will bring them a couple of steps further toward standardized intra-operative nuclear imaging.

2 Radioactivity surface reconstruction using tracked beta-probes

A challenging task in tumor resection is the minimal but complete removal of malignant cells. While the security margins are maximized to avoid recurrence, the impact on healthy tissue has to be minimized. As aid for this procedure, beta-probes have been introduced to detect remaining malignant tumor after resection by nuclear labeling [2]. For this means, a positron-emitting cancer marker is injected into the patient before surgery. After the standard tumor extraction the surgeon scans the margins with a beta-probe. The detection of unexpected high activity levels shows the occurrence of residual tumor tissue. However, as the surgeon has to remember the sources of radiation most of the potential accuracy gets lost.

In order to solve this, our group combined beta-probes with pose tracking system to generate 3D activity encoded surfaces [4]. When combined with advanced visualization such surfaces proved to be useful when accurately guiding surgeons to remaining high activity spots and thus remaining tumor deposits (figure 1(a)).



((a)) AR view of radioactivity surface.



((b)) Tracked instruments.

Fig. 1: (a) Augmented reality image of the radioactivity surface reconstruction. The radioactive image is superimposed over the light image of the used phantom. Blue regions indicate higher activity rates and white regions low activity rates; regions where no information is superimposed were not scanned. (b) Laparoscope and beta-probe with optical tracking targets.

There are, however, several limitations still present. First, the statistical nature of the beta-probe read-out results in a very noisy activity distribution, as close measurements in space with similar activity levels may still report completely different readings. Acquiring for longer time at each point is not clinically possible, as it requires the surgeon to hold the probe at a certain pose for almost a second and also prolongates, as a consequence, the duration of the operation.

Secondly, if the scan used to acquire the surface is too coarse, small regions with remaining radioactivity can be missed and the generated image may not be valid. This can also be compensated by slower acquisition times, with the same problems mentioned above.

A third issue is the fact that the readings are not necessarily acquired on top of the surface. Some readings will be above and some below the normal level. This problem does not only make the use of the acquired poses for anatomical surface reconstruction partially invalid, but can affect also the reconstructed radioactivity distribution.

Finally, since the area of application of the introduced system is the abdomen, the effect of motion, both respiratory and also bulk organ motion and deformation caused by the nature of operations makes the reconstructed image only a ‘snapshot’.

Our current research aims at solving these issues. For the first and second problems the evaluation of the scan the rebinning of the readings is being analyzed supported by robust inference approaches. The concept of rebinning can be further used to estimate a degree of confidence and thus guide the surgeon to regions where the readings were too coarse and further information is needed to guarantee a valid image.

For the third and fourth issues, the aimed solution is the integration of anatomical surface acquisition systems. Such systems would not only allow to determine if the acquisition was above the surface or below it, but also to project them to their right position and compensate for the artifacts that arise from deformation. Furthermore monitoring the surface enables the compensation of respiratory and bulk motion and deformation using non-rigid registration.

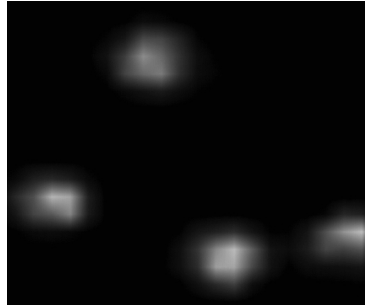
3 Intra-operative 3D imaging using tracked gamma-cameras and probes

One of the few procedures where gamma-probes have become the gold-standard is sentinel lymph node detection in breast cancer and melanoma [3]. It aims at staging a tumor by analysing a biopsy of the first lymph nodes downstream, which requires thus a precise localization of these ‘sentinel’ nodes.

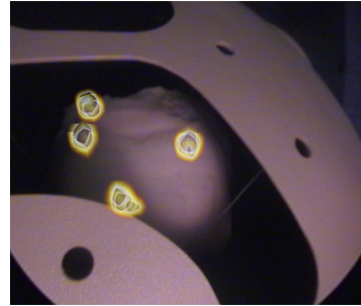
The current developments try to add depth information to 2D mini gamma-cameras [5], which would allow detection of occlusions, aiding the localization of the sentinel lymph nodes around a tumor. 3D imaging would further increase the probability of identify additional marked nodes which are difficult to distinguish using conventional gamma-probes or intra-operative gamma-cameras.

Benlloch et al. proposed tracking of 2D mini gamma-cameras and the use of 2D acquisitions for limited 3D intra-operative functional imaging [6]. In that approach the 3D position of a single point sources is reconstructed from two 2D images taken with an angle close to 90 degrees. In order to guarantee proper detection for the case of more than one source, they also introduced a process where three 2D images with relative angles close to 120 degrees are acquired. The detectable information is, however, limited to point-like sources as a Computer Vision approach based on triangulation of corresponding points is taken for 3D reconstruction. These constraints on the angle, the radioactivity distribution type, as well as the size of the devices greatly reduce the flexibility of this approach.

Our group introduced a different approach employing tracked gamma-probes [7]. When combined with proper algorithms for 3D tomographic reconstruction based on gamma-readings and the synchronized 3D pose of the detector, most of the limitations were removed. Thus, the approach included the advantages of previous systems and surpassed them by allowing easier handling, faster acquisition times and most importantly, 3D intra-operative functional imaging of general distributions (figures 2(a), 2(b)).



((a)) Reconstructed slice.



((b)) AR visualization of 3D volume.

Fig. 2: Reconstructed slice (a) and augmented reality visualization of the 3D volume over phantom. The acquisition took ≈ 6 [min].

Open issues in this case, do not differ too much from the ones discussed in the case of the beta-probe (statistical nature of readings, deformation and motion of anatomy during scan, etc). There are, however, further specific problems. First, the reconstruction of a tomographic image can only be guaranteed to be free of artifacts if a complete set of projections is acquired. This would mean in practice a big amount of measurements over 180° at approximately the same distance for each slice. For fully 3D reconstruction, such a set of measurement should be repeated for each single slice. This implies a huge amount of readings which yields very long acquisition times and thus cannot be thought of clinically. Furthermore this problem would restrict the gained flexibility by imposing constraints on the poses of acquisition.

Second, in order to obtain clinically usable images, one has to aim to a resolution that is even better than the one of pre-operative imaging devices. This would mean, however, an ill-posed reconstruction problem and an increasing memory and computation burden. To compensate for the first more readings from different positions can help, which increases the requirements on the processing and storage capacities and thus makes the second problem even worse.

In order to solve the mentioned issues our group is working further in on-line evaluation of the quality of the acquisition and automatic calculation of the best next projection for acquisition guidance and thus a reduction of reconstruction artifacts. Intra-operative anatomical information has been considered to restrict the volume of interest and incorporate information for attenuation correction. Approaches like rebinning can be also used here to improve the statistics and reduce the computational burden. Hardware based accelerations and adaption of the algorithms are also current research.

4 Conclusions

In the last years the combination of navigation with intra-operative nuclear information has opened the possibilities of nuclear imaging in the operation room. The initial results reviewed in this work show encouraging results and play a role as proof-of-concept.

There are several points that have not been dealt with yet. However, the major drawbacks do not seem to be impossible to compensate, and most important: in comparison to the standard methods, the introduced methods can offer images to applications that in the past did not dream to have.

References

1. Wernick, M.N., Aarsvold, J.N.: Emission Tomography: The Fundamentals of PET and SPECT. Academic Press (2004)
2. Hoffman, E.J., et al.: Intraoperative probes and imaging probes. *Eur J Nucl Med Mol Imaging* 26(8) (August 1999) 913–935
3. Harish, K.: Sentinel node biopsy: concepts and current status. *Front Biosci* 10 (2005) 2618–2644
4. Wendler, T., Traub, J., Ziegler, S., Navab, N.: Navigated three dimensional beta probe for optimal cancer resection. In: Proceedings of MICCAI 2006. Number 1 in LNCS 4190, Copenhagen, Denmark, Springer (Oct. 2006) 561–569
5. Pitre, S., et al.: A hand-held imaging probe for radio-guided surgery: physical performance and preliminary clinical experience. *Eur J Nucl Med Mol Imaging* 30(3) (Mar 2003) 339–343
6. Benlloch, J.M., et al.: The gamma functional navigator. *IEEE Trans Nucl Sci* 51(3) (June 2004) 682689
7. Wendler, T., Traub, J., Ziegler, S., Navab, N.: Navigated three dimensional beta probe for optimal cancer resection. In Larsen, R., Nielsen, M., Sparring, J., eds.: Proceedings of MICCAI 2006. Number 1 in LNCS 4190, Copenhagen, Denmark, MICCAI Society, Springer (Oct. 2006) 561–569

Imaging in Diagnosis and Therapy

The Model of Proportional Scattering Medium for Optical Tomographical Imaging of Biological Tissues

Sergey Tereshchenko

Moscow Institute of Electronic Technology (MIET), Department of BioMedical Systems,
MIET, Moscow, 124498, Russia

The tomographical reconstruction of the internal structure in high scattering media (HSM) is an important problem of modern physical optics [1,2]. The radiation transport equation (RTE) is most general way for description of interaction between radiation and medium [3,4]. The most important characteristics of scattering medium included in radiation transport equation are radiation absorption coefficient $\mu_a(\mathbf{r})$ and angle differential radiation scattering coefficient (nonhomogenous scattering indicatrix) $\mu_s(\mathbf{r}, \Omega' \Omega)$, where \mathbf{r} is a point of the medium, Ω' and Ω are directions of the photon before and after scattering respectively. Thus in most general problem formulation it is needed to reconstruct two independent functions of three variables ($\mu_a(\mathbf{r})$) and four variables ($\mu_s(\mathbf{r}, \Omega' \Omega)$). Nevertheless in this formulation the problem becomes too difficult for solution and interpretation, therefore there are considered more simple models and consequently more simple objects for the reconstruction.

In our view there is perspective the approach based on the model "The scattering straight back" [5], reducing the process of the single scattering to a backscattering by redefinition of absorption, scattering and extinction coefficients. It is possible to write the stationary RTE in the single-velocity approximation as follows:

$$\begin{aligned} \Omega \text{grad} \Phi(\mathbf{r}, \Omega) + \mu(\mathbf{r}) \Phi(\mathbf{r}, \Omega) - \\ - \iint_{4\pi} \Phi(\mathbf{r}, \Omega') \mu_s(\mathbf{r}, \Omega' \Omega) d\Omega' = S(\mathbf{r}, \Omega) \end{aligned} \quad (1)$$

where $\Phi(\mathbf{r}, \Omega)$ is a photons flux density in a point \mathbf{r} for photons which move in a direction Ω , $S(\mathbf{r}, \Omega)$ is a radiation source distribution function and $\mu(\mathbf{r}) = \mu_a(\mathbf{r}) + \iint_{4\pi} \mu_s(\mathbf{r}, \Omega' \Omega) d\Omega'$ is an extinction coefficient.

We shall consider only those photons, which move along an axis of the initial ray. As the returning of photons, scattered away from the axis, to the motion along the axis is low-probability event, it is possible to consider, that the process of photon scattering is reduced to a backscattering along the axis. We shall name such approximation as "scattering straight back" (SSB). It is natural, that on the axis there are only two fluxes of photons, which move in direct and in back directions. Thus we are principally not interested in photons, which are not being near-axis and therefore we must to provide the discrimination of off-axis photons at the detecting.

For a mathematical writing of the formulated approximation it is necessary to use the delta-function of angular variables $\delta_2(\Omega \Omega')$ – 2-D delta-function on the surface of the unit sphere. It has the name "The surface delta-function" [4]. Thus, the main assumption of the SSB-model for the scattering indicatrix can be written as

$$\mu_s(\mathbf{r}, \Omega' \rightarrow \Omega) = m_s(\mathbf{r}) \delta_2(-\Omega' \Omega) \quad (2)$$

where $m_s(\mathbf{r})$ is a scattering coefficient of SSB-model. In this model for energy balance saving it is possible to consider the photons scattered away from the axis as absorbed. Therefore the absorption coefficient $\mu_a(\mathbf{r})$ must be increased, and it is necessary exchanged with some coefficient $m_a(\mathbf{r})$, which is an absorption coefficient of SSB-model. It is convenient also to introduce an extinction coefficient of this model $m(\mathbf{r}) = m_a(\mathbf{r}) + m_s(\mathbf{r})$. Thus, all introduced quantities have the clear physical sense, and the integral-differential RTE (1) reduces to the differential partial equation

$$\begin{aligned} \Omega \text{grad} \Phi(\mathbf{r}, \Omega) + m(\mathbf{r}) \Phi(\mathbf{r}, \Omega) - \\ - m_s(\mathbf{r}, -\Omega) = S(\mathbf{r}, \Omega) \end{aligned} \quad (3)$$

As in the usual tomographical measurement scheme there is not to simultaneously reconstruct two unknown functions $\mu(\mathbf{r})$ and $\mu_s(\mathbf{r})$, the additional assumption is necessary for reducing unknown quantities. For example, it is possible to consider one of these functions is known including the case that it is equal to a known constant. The similar way was used for deducing exponential Radon transform [5]. Other way is a postulation of the functional connection between $\mu(\mathbf{r})$ and $\mu_s(\mathbf{r})$. Let's assume, that spatially non-uniform scattering and extinction coefficients are connected by a ratio

$$m_s(\mathbf{r}) = \beta m(\mathbf{r}) \quad , \quad (4)$$

where β is a coefficient not dependent on coordinates. Such scattering medium we shall name as proportional scattering medium (PSM). The substantiation of the assumption (4) can be a representation about absorbing-scattering centers that are non-uniformly distributed in space. Each of these centers can absorb and scatter the photon with some probability. Then both the absorption coefficient and scattering coefficient should be proportional to the same density of such centers. Combining (2) and (4), we shall receive a ratio determining PSM:

$$\mu_s(\mathbf{r}, \Omega' \Omega) = \beta m(\mathbf{r}) \delta(-\Omega' \Omega) \quad . \quad (5)$$

Then RTE reduces to

$$\begin{aligned} \Omega \text{grad} \Phi(\mathbf{r}, \Omega) + m(\mathbf{r}) \Phi(\mathbf{r}, \Omega) - \\ - \beta m(\mathbf{r}) \Phi(\mathbf{r}, -\Omega)' = S(\mathbf{r}, \Omega) \end{aligned} \quad (6)$$

Let's remark that the equations (3) and (6) is not approximated but exact RTE for HSM with the property (2) and (4) in contrary to other models, for example, to the diffusion approximation.

The equation (6) has the exact solution, and on the base of PSM-model there was developed the exact tomographical algorithm for a reconstruction of an unknown function $m(\mathbf{r})$ [5].

The efficiency of the offered reconstruction algorithm was investigated on model scattering objects. Experimental scattering medium filled in a cylindrical deepening (\emptyset 28 mm) in polymethylmethacrylate parallelepiped. As a distortion exists at the border of two media it is necessary to use materials allowing to minimize the value of a relative

refraction index. The refraction index of the polymethylmethacrylate is $n_1 = 1.491$. As the second medium the flax oil ($n_2 = 1.485$, $n_{21} = 0.996$) can be enough effectively used. It is necessary to note, that the similar value of a refraction index ($n = 1.4$) is in a biotissue of a breast. The scattering medium has consisted of 0.5 % emulsion of intralipid in flax oil filled in the cylindrical deepening. For a creation of heterogeneity either the polymethylmethacrylate cylindrical rod (\emptyset 10 mm) or polymethylmethacrylate cylindrical pipe (\emptyset 15 mm and wall thickness 4 mm) were placed at the center of the cylindrical deepening. Such model object represents the HSM homogeneous on a refraction, but absorbing and scattering heterogeneous.

The result of the reconstruction of the spatial distribution for an extinction coefficient of the radially symmetric high scattering object is represented in the figure for the heterogeneity as the rod (a), and as the pipe (b).

Thus, the experimental verification of proposed algorithm was executed, and the images of the internal structure of model scattering objects are reconstructed. The efficiency of the offered algorithm of the reconstruction for spatial distributions of an extinction coefficient for high scattering objects in an approximation of a proportional scattering medium is experimentally proved.

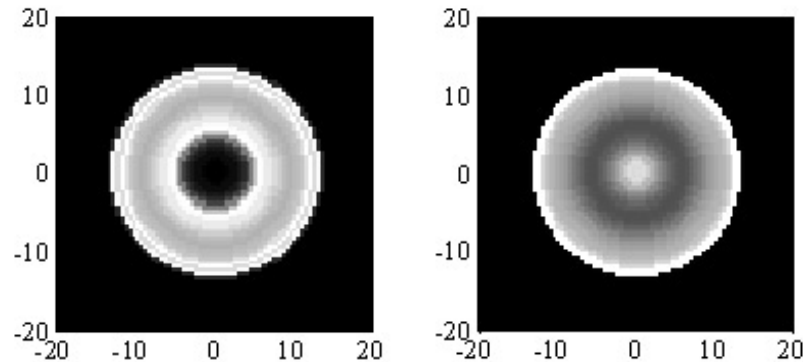


Figure. The result of the reconstruction of the spatial distribution for an extinction coefficient of the radially symmetric high scattering object for the heterogeneity as the rod (left), and as the pipe (right)

There is established, that it is possible to visualize the internal structure of scattering objects by the size down to 2 mm.

1 References

References

1. Medical optical tomography: functional imaging and monitoring. G.I.Müller et al., eds. Proc. SPIE, vol. IS11 (1993).

2. Theoretical study, mathematical, experimental model for photon transport in scattering media and tissue. Proc. SPIE, vol. 2326 (1994).
3. A. Ishimaru. Wave propagation and scattering in random media.– N.Y., Academic (1978).
4. K.M.Case and P.F.Zweifel. Linear transport theory.– Reading, Mass., Addison-Wesley (1967).
5. S.A.Tereshchenko. Methods of Computed Tomography.– Moscow: Fizmatlit, 2004. 320 p. (In Russian).

Image Based Time Series Synchronization for Periodically Moving Targets

Christian Schaller¹, Ali Khamene², and Joachim Hornegger¹

¹ Lehrstuhl fuer Mustererkennung, University of Erlangen-Nuremberg, Marten Str. 3, 91058 Erlangen Germany

`Christian.Schaller@informatik.uni-erlangen.de`

² Imaging and Visualization Dept., Siemens Corporate Research, 755 College Road East, Princeton NJ 08540, USA

`Ali.Khamene@siemens.com`

Abstract. Since it is possible to process a huge amount of data using today's computer hardware, the demand for algorithms dealing with this type of data is increasing. A major environment where these algorithms can be applied is obviously found within medical diagnosis and therapy. Nowadays, physicians are able to observe 3D volumes over time. By using such four dimensional datasets, they are able to observe and study movement of certain targets within the patient's body. Usually there are two main sources causing this movement: the patient's respiration and the beating heart. Both sources are producing a periodic movement and there is often a demand to know how such a periodic movement affects internal tissue. In this paper, a method is presented to address such periodical moving targets within the body. The paper introduces a method to synchronize a 4D volume data time series with a 2D image time series. In general an assumption is made, that both of the time series are representatives of two corresponding processes with a sufficient amount of overlapping data. Synchronization is defined as the allocation of both time series by using an optimal mapping that relates any frame of one series to a corresponding frame of the other series. In order to consider variations within the time series, the algorithm is based on a probabilistic underlying markov process and is able to detect whether there is any correspondence or not. As the mapping procedure is designed as an optimization process it can be solved by using an optimization technique like simulated annealing or dynamic programming. The effectiveness of the proposed method is shown on an example out of the field of medical therapy. In general the solution can also be used within diagnosis of cardiac motion abnormalities, respiratory motion compensation in image guided interventions, respiratory motion management in radiation therapy and segmentation and registration of 2D+time or 3D+time series.

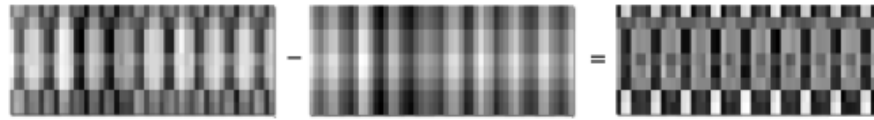


Fig. 1: From left to right: original similarity matrix with gain, computed bias field, similarity matrix without bias field

1 Introduction and Background

The synchronization of two time series in general is well known and has been studied in literature, considerably [1][2]. The main application, that has been looked at in literature deals with indexing very large time series databases [1]. To find a mapping between two time series in general, euclidian distance metrics can be used. Furthermore, dynamic time warping has also to be considered as a technique to accommodate time differences between an input series and a reference series. A classical one dimensional example application for dynamic time warping is the synchronization of two utterances of the same word, known as Levenshtein distance [4]. Furthermore, dynamic time warping can also be used to synchronize two dimensional image time series. As dynamic time warping is based upon dynamic programming [7], it is taken into consideration for solving the stated problem. As dynamic time warping is not suitable to deal with periodicity within the time series, we are using a markov process to incorporate the time dependency and periodicity in the solution [10].

Various image similarity measurement techniques can be used to compare image pairs and have been studied in literature [3]. We focused on mutual information as primary image similarity measurement [5]. Additionally, we are also using singular value decomposition to enforce rank criteria [9].

2 Image Based Synchronization

We consider a 4D image time series, consistent of i 3D volumes as reference sequence. This sequence contains one complete cycle of the periodic moving target. Therefore, the movement is divided into i different phases and each 3D volume represents one particular phase. In order to be able to compare these phases to the second 2D image time series, including j images, the dimension of the volumes has to be reduced by factor one. This is done efficiently by calculating projections of the volume using the same geometry as was used during the acquisition of the 2D image time series [8].

We use a similarity metric to compute the level resemblance among all possible pairs of the two time series [3]. In general it is possible to use any proper metric; by performing tests we identified mutual information as the most suitable metric to use. By using this metric we build up a matrix and apply a normalization technique. Therefore, we are using singular value decomposition to reduce the amount of bias by taking various image pairs into account. Concluding, the result of a rank one forced similarity matrix is subtracted from the original similarity matrix (see figure 1).

Furthermore, we introduce a stochastic process, which represents both of the time series. Since, we are looking for the indices of the second time series with respect to

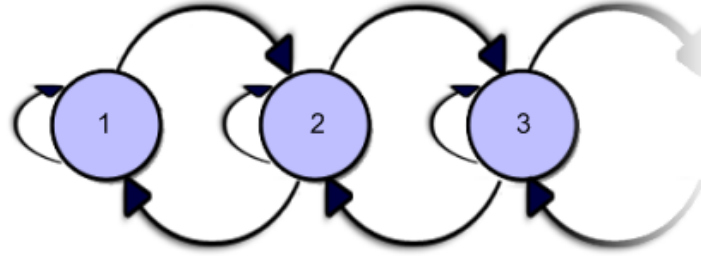


Fig. 2: An example for a markov chain, the blue circles indicate the states including the transition probability directions

the reference sequence without loosing generality we assume that the elements of the reference time series are in fact the states of the stochastic process. A common way to represent a stochastic process can be performed by using a markov model, which includes the initial probability of each state and a transition matrix that expresses the probability of the next states with respect to the previous state (see figure 2). The state transition probabilities can be estimated by using the Baum-Welch algorithm [6]. In order to account for possible deviations from the reference states, we add an additional unknown state to the reference set. This unknown state accounts for any possible new conditions that can happen on the second series and has not been present in the reference sequence. The image similarity level for this additional state quantifies a non-matching (poorly matching) case. For this purpose, since the number of none matching pairs supersedes the number of matching pairs, we use the median of the maximums of various columns. By subtracting the range of the similarity values of the corresponding column from this value we have determined the similarity level for the additional state.

In order to compute the mapping function, we set up a cost function, in which the parameters are the labels for any image in the second time series relating them back to the reference states including the unknown state. The cost function consists of two terms, where the first one represents the image similarity matrix (data) and the second one the markov process (model). According to this, we set up a function where we can maximize the a posteriori probability by using Bayes' theorem. In respect of the Bayes theorem the first term represents the likelihood and the second term the a priori knowledge as shown in equation 1.

$$\tilde{\mathcal{L}} = \arg \max_{\mathcal{L}} \left(\underbrace{\prod_{j=0}^{j < K} M(\mathcal{L}(j), j)}_{likelihood} \right) \times \left(\underbrace{P_0(\mathcal{L}(0)) \prod_{j=1}^{j < K-1} \mathbf{S}(\mathcal{L}(j), \mathcal{L}(j+1))}_{prior} \right) \quad (1)$$

We are optimizing this cost function by using a dynamic programming approach which incorporates the a priori knowledge.

$$\mathbf{Q}(i, j) = \begin{cases} \infty & j < 0 \\ \mathbf{M}(i, j) \times P_0(i) & j = 0 \\ \mathbf{M}(i, j) + \max_i (\mathbf{Q}(i, j - 1) \times \mathbf{S}(i, j)) & \text{otherwise} \end{cases} \quad (2)$$

Once we have computed the matrix \mathbf{Q} in equation 2 recursively, we can solve the above stated optimization problem as follows:

$$\tilde{\mathcal{L}}(j) = \tilde{i} = \arg \max_i \mathbf{Q}(i, j) \quad \text{for } j \in [0, K]. \quad (3)$$

3 Experimental Results

In order to evaluate the performance and usability of the proposed method, it was applied and tested on a medical therapy problem. Gated radiation therapy is one application where a periodical motion is occurring and needs to be determined. We took several 4D-CT scans from patients with a corresponding fluoroscopic sequence and used the algorithm to synchronize both sequences. The goal was to determine the position of a tumor related to the actual breathing phase based on the reference sequence. We tested the algorithm using both, synthetic generated fluoroscopic sequences and real acquisitions. As the 4D dataset was acquired prior to the fluoroscopic sequence, all these sequences had slightly different patterns than the reference sequence. To judge the quality of the algorithm we define two error measures, where the first error metric indicates wrong labeled 'no-match' situations and the second wrong labeled frames. Correct correspondences for each frame out of the reference sequence were determined by using split-screen and a blending display method. All tests were performed on an Intel Centrino Duo CPU with 2.0 GHz and 2 GB of RAM using a NVIDIA Quadro FX 2500 display adapter. The average error of wrong labeled 'no-match' situations was 11 percent and 9 percent for wrong labeled frames. Therefore in average 91 percent of all frames are correctly labeled.

4 Summary and Conclusion

We proposed a model based image synchronization technique based on Dynamic Programming. The procedure is able to find a mapping between a 4D data set used as a reference and a 2D image sequence. By building up an image similarity table first, we establish and solve a cost function afterwards. This function incorporates both the image similarity values and the temporal aspect by using a stochastically model based on a markov model as the underlying process. The method was tested on synthetic and patient data and shows in average a correct labeling of the frames in 91 percent.

References

1. Keogh, E., Chakrabarti, K., Pazzani, M., Mehrotra, S., Locally adaptive dimensionality reduction for indexing large time series databases. In: Proceedings of ACM SIGMOD conference on management of data, May, 2001, pp 151-162

2. Berndt, D., Clifford, J., Using dynamic time warping to find patterns in time series. AAAI-94 workshop on knowledge discovery in databases, 1994, pp 229-248
3. Penny, G. P., Weese, J., Little, J. A., Desmedt, P., Hill, D. L. G., Hawkes, D. J. A comparison of similarity measures for use in 2D-3D medical image registration, IEEE Trans Med Imaging 17, Aug, 1998 pp. 586-595
4. Levenshtein, V. I., Binary codes capable of correcting deletions, insertions and reversals, Soviet Physics Doklady, 10(8), February, 1966, pp. 707-710
5. Wells, W., Viola, P., Atsumi, H., Nakajima, S., Kikinis, R., Multi-modal volume registration by maximization of mutual information, Medical Image Analysis, 1996, 1(1), pp. 35-51.
6. Baum, L. E., Petrie T., Soules G., and Weiss N., A maximization technique occurring in the statistical analysis of probabilistic functions of Markov chains, Ann. Math. Statist., 1970, 41(1) : pp. 164-171.
7. Bellman, R., Dynamic Programming, Princeton Univ. Press, Princeton, NJ, 1957.
8. Khamene, A., Bloch, P., Wein, W., Svatos M., Sauer, F., Automatic registration of portal images and volumetric CT for patient positioning in radiation therapy. Medical Image Analysis, 2006, 10: pp 96-112.
9. Trefethen, L. N., Bau, D., Numerical Linear Algebra, SIAM: Society for Industrial and Applied Mathematics, 1997.
10. Markov, A., Extension of the Limit Theorems of Probability Theory to a Sum of Variables Connected in a Chain, in R. Howard (Hrsg.): Dynamic Probabilistic Systems (Volume I: Markov Models), Kap. Appendix B, John Wiley & Sons, Inc., New York City, 1971, pp. 552-577.

Quantitative Measurement of Kidney and Cyst Sizes in Patients with Autosomal Dominant Polycystic Kidney Disease (ADPKD)

V. Daum¹, H. Helbig¹, R. Janka³, K.-U. Eckardt², and R. Zeltner²

¹ Friedrich–Alexander–University of Erlangen–Nuremberg (FAU), Institute of Pattern Recognition, Martensstr. 3, 91058 Erlangen, Germany

² FAU, Medical Clinic 4 (Nephrology und Hypertensiology), Krankenhausstraße 12, 91054 Erlangen, Germany

³ FAU, Chair of Diagnostic Radiology, Maximiliansplatz 1, 91054 Erlangen

Abstract. The Autosomal Dominant Polycystic Kidney Disease (ADPKD), which is characterized by the growth of cysts in the kidneys, is one of the most common genetic disorders. In order to better understand the disease and how it impairs the renal function, as well as to develop new methods of treatment, it is necessary to be able to perform quantitative longitudinal studies.

This work deals with the extraction of the desired measurement information from Magnetic Resonance Imaging (MRI) scans with as much accuracy and as little effort as possible. The proposed workflow uses a 3D random walk segmentation technique for the semi-automatic segmentation of the kidneys and employs the watershed transform for the segmentation of the cyst volume as well as individual cysts.

1 Introduction

The Autosomal Dominant Polycystic Kidney Disease (ADPKD) is one of the most common genetic disorders, affecting an estimated 12.5 million people worldwide. Over the course of the disease numerous cysts develop in the kidneys, thus increasing the size of the kidneys and destroying the kidney parenchyma. Oftentimes ADPKD is also accompanied by a cyst growth in the liver. In the end-stage of the disease, renal replacement therapy (i.e. dialysis or renal transplantation) becomes usually necessary.

In order to better understand the course of disease of ADPKD and how it leads to renal failure, longitudinal studies measuring the size of the kidneys, the cysts and the remaining parenchyma have to be performed. Magnetic Resonance Imaging (MRI) has already been used in several studies concerning ADPKD (see f. e. [1], [2]), but to our knowledge, segmenting and evaluating the data has been done primarily “by hand” or with simple thresholding techniques and not with segmentation approaches that offer a higher degree of automation.

2 Material

For the experiments in this work we used coronal MRI scans of the abdomen, that were acquired with a so called TRUFI (True Fast Imaging With Steady Precession) FS (Fat

Saturated) 3D sequence on a Siemens Avanto 1.5 T whole body scanner. The volumes have an in-plane resolution of 320×320 and 60 to 90 slices depending on patient and kidney sizes. The corresponding voxel size is $1.4 \times 1.4 \times 2.5 \text{ mm}^3$ (see Fig. 1a).

3 State of the Art

Currently the most often employed method to perform volumetric measurements of the kidney is a manual segmentation using stereology [3]: A regular grid showing crosses as the grid points is superimposed on a slice view of the volume. An observer manually determines slice by slice whether a grid point is positioned over the kidney, a cyst or any other tissue. This method is obviously rather laborious and also, depending on the spacing of the superimposed grid, rather imprecise. Even more work is the manual slice by slice segmentation of the kidneys' outline. For higher resolution volumes and larger studies these methods become quickly infeasible.

The cysts, which appear bright white in the T2 weighted MRI images, are commonly either segmented by stereology or by thresholding techniques. In general thresholding is not ideal for this application, since MRI images often suffer from bias effects that make a good global threshold impossible. Additionally it sometimes happens that cysts are filled with blood as well as water. In this case the blood filled cyst appears dark instead of bright white, which makes a solely intensity based segmentation unfeasible.

4 Segmentation of Kidneys

In order to segment the kidneys the heterogeneous tissue consisting of kidney parenchyma and small as well as larger cysts has to be differentiated from the surrounding tissue and from the usually also cystic liver. As the cysts completely deform the kidneys, it is also not possible to employ prior knowledge about the shape of the kidney. Due to these problems a semi-automatic method, the Random Walk segmentation is employed.

For the segmentation of the kidneys the Random Walk (RW) (see f. e. [4]) technique is used. RW segmentation is essentially a graph based algorithm. In the case of images or volumes each pixel is viewed as a node of the graph. Neighboring voxels are connected by edges, which have a weight attached to them that depends on the gray value difference of the voxels. A Gaussian weighting is used to emphasize edges.

$$w_{ij} = w_{ji} = \begin{cases} e^{-\beta \|g_i - g_j\|} & \text{if } i \text{ and } j \text{ are neighboring voxels} \\ 0 & \text{else} \end{cases} \quad (1)$$

where g_i and g_j are the gray value intensities at node i and j respectively, β is a scaling factor for the edge strength (in our experiments $\beta = 700$) and w_{ij} is the resulting weight. Additionally a set of nodes has to be labeled by the user, for example by simply drawing lines into the volume (see Fig 1c). Each non-labeled node is then associated with the label region that a random walker started in that node would reach with the highest probability. The probabilities that determine into which neighboring node the random walker steps are determined using the weights w_{ij} .

$$p_{ij} = \frac{w_{ij}}{\sum_j w_{ij}} \quad (2)$$

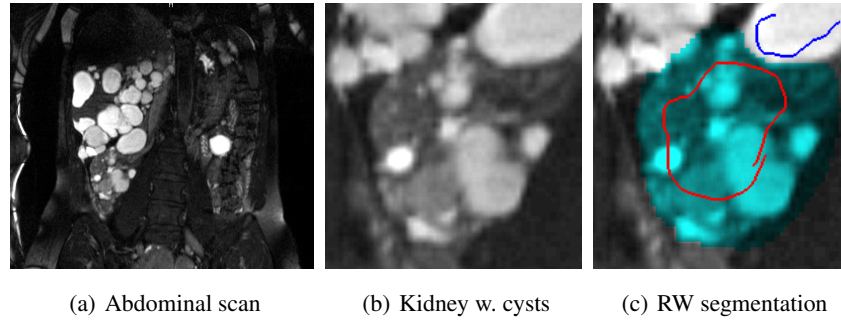


Fig. 1: (a) T2 weighted, abdominal TRUFI 3D scan of an ADPKD patient; (b) closeup of the right kidney with cysts; (c) segmentation of the kidney with cysts; red and blue lines are the user initialization.

with p_{ij} denoting the transition probability from node i to node j . All in all it is now simple to determine the conditional probabilities that the random walker reaches a set \mathcal{A} of user labeled nodes, before reaching a second set \mathcal{B} .

$$P(\mathcal{A}|v_i) = \begin{cases} 1 & \text{for } v_i \in \mathcal{A} \\ 0 & \text{for } v_i \notin \mathcal{B} \\ \sum_j p_{ij} P(\mathcal{A}|v_j) & \text{else} \end{cases} \quad (3)$$

Assembling the conditional probabilities $P(\mathcal{A}|v_i)$ into a vector x we can write (3) as the linear system

$$\underbrace{\begin{pmatrix} 1 & -p_{12} & 0 & & \cdots & 0 \\ -p_{21} & 1 & -p_{23} & & & \\ 0 & -p_{32} & 1 & \ddots & & \\ & & & \ddots & & \\ \vdots & & & & 0 & 1 & 0 & 0 \\ & & & & \ddots & \ddots & & -p_{n-1,n} \\ 0 & \cdots & 0 & -p_{n,n-1} & & 1 & & \end{pmatrix}}_A \underbrace{\begin{pmatrix} P(\mathcal{A}|v_1) \\ P(\mathcal{A}|v_2) \\ P(\mathcal{A}|v_3) \\ \vdots \\ P(\mathcal{A}|v_i) \\ \vdots \\ P(\mathcal{A}|v_n) \end{pmatrix}}_x = \underbrace{\begin{pmatrix} 0 \\ 0 \\ 0 \\ \vdots \\ 1 \\ \vdots \\ 0 \end{pmatrix}}_b \quad (4)$$

where $v_i \in \mathcal{A}$ is a user labeled node. The system matrix A is large, sparse and, due to its diagonal dominance, positive definite. It is therefore possible to employ iterative, sparse matrix solvers to (4). [4] employs a GPU based conjugate gradient (CG) method as their linear solver. In our implementation we use a CPU based multigrid method in 3D, similar to the 2D method presented in [5]. On a Pentium 4 3.0 GHz with 2GB of main memory the calculation of the RW segmentation takes about 50 seconds for a 5.7 million ($256 \times 256 \times 88$) voxel volume. A future GPU based implementation should greatly reduce this runtime.

5 Segmentation of the Cysts

After the kidney is segmented, the cysts inside the kidney can be identified by using the watershed transform on a smoothed gradient image. We used the implementation provided by the Insight Toolkit [6]. The watershed basins corresponding to cysts are selected manually, in order to avoid segmenting parts of the renal pelvis as cysts. Naturally this also makes the segmentation of the darker blood filled cysts possible. The manual selection of watershed basins also allows the identification of individual cysts. If a cyst is oversegmented, all of its basins can be combined as well. This makes the generation of statistics about the cyst sizes possible.

6 Results

The described methods have been incorporated into a commercially available software for clinical evaluation. The segmentation of the kidney by the Random Walk method was compared to a manual slice by slice segmentation (see table 1). The results show a difference between the measurements of about 4% to 5%. This is almost on par with the inter-observer variance of about 3.8% that we measured in previous experiments with the manual segmentation. The time needed for the segmentation of one kidney was reduced from about half an hour when using the manual segmentation to less than 5 minutes, while still obtaining a comparable accuracy.

7 Conclusions

It has been shown that image processing methods can reduce the effort in performing volumetric measurements in MRI images while still attaining a high accuracy. Semi-automatic methods allow this while retaining the control in the hands of the physician performing the evaluation.

References

1. P. C. Harris, K. T. Bae, S. Rossetti, V. E. Torres, J. J. Grantham, A. B. Chapman, L. M. Guay-Woodford, B. F. King, L. H. Wetzel, D. A. Baumgarten, P. J. Kenney, M. Consugar, S. Klahr, W. M. Bennett, C. M. Meyers, Q. J. Zhang, P. A. Thompson, F. Zhu, J. P. Miller, and the CRISP Consortium, Cyst number but not the rate of cystic growth is associated with the mutated gene in autosomal dominant polycystic kidney disease, *Journal of the American Society of Nephrology*, vol. 17, pp. 3013–3019, November 2006.
2. C. Sise, M. Kusaka, L. H. Wetzel, F. Winklhofer, B. D. Cowley, L. T. Cook, M. Gordon, and J. J. Grantham, Volumetric determination of progression in autosomal dominant polycystic kidney disease by computed tomography, *Kidney International*, vol. 58, pp. 2492–2501, December 2000.
3. K. T. Bae, P. K. Commean, and J. Lee, Volumetric measurement of renal cysts and parenchyma using MRI: Phantoms and patients with polycystic kidney disease, *Journal of Computer Assisted Tomography*, vol. 24, no. 4, pp. 614–619, 2000.
4. L. Grady, Random walks for image segmentation, *IEEE Transactions on Pattern Analysis and Machine Intelligence*, vol. 28, no. 11, pp. 1768–1783, 2006.

Data	Manual	RW	Rel. Err.	Abs. Err.	Cysts
1	483.18	469.1	2.91%	14.08	143.62
2	574.04	502.4	12.48%	71.64	254.51
3	600.18	588.6	1.93%	11.58	183.57
4	608.43	563.7	7.35%	44.73	159.15
5	614.7	588.4	4.28%	26.3	229.71
6	621.79	600.1	3.49%	21.69	324.67
7	648.22	607.3	6.31%	40.92	379.48
8	699.53	671.6	3.99%	27.93	395.47
9	765.19	728.2	4.83%	36.99	444.50
10	796.46	705.8	11.38%	90.66	345.68
11	796.65	780.4	2.04%	16.25	392.09
12	813.26	760.4	6.50%	52.86	462.64
13	819.03	797.1	2.68%	21.93	430.48
14	856.63	803	6.26%	53.63	454.45
15	861.36	819.1	4.91%	42.26	373.14
16	1060.13	1145.1	8.02%	84.97	593.03
17	1165.42	1125.8	3.40%	39.62	893.73
18	1195.33	1170.9	2.04%	24.43	693.49
Average:			5.27%	40.14	
Average (w/o 2 and 10):			4.43%	35.01	

Table 1: Evaluation of the Random Walk (RW) segmentation, using a manual segmentation as ground truth. In the datasets 2 and 10 it is very hard to tell the liver from the kidney (due to the cysts) even in a manual segmentation which makes some segmentation errors very likely. Results have therefore been provided with and without these datasets included.

5. L. Grady and T. Tasdizen, A geometric multigrid approach to solving the 2D inhomogeneous Laplace equation with internal boundary conditions, in Proceedings of ICIP 2005, vol. 2, pp. 642–645, IEEE, October 2005.
6. L. Ibáñez, W. Schroeder, L. Ng, and J. Cates, The ITK Software Guide. Kitware Inc., second ed., 2005.

A Boosting Approach for Multiple Sclerosis Lesion Segmentation in Multi-Spectral 3D MRI

Michael Wels¹, Martin Huber², and Joachim Hornegger¹

¹ Institute of Pattern Recognition, University Erlangen-Nuremberg, Germany

² Siemens AG, CT SE SCR 2, Erlangen, Germany

Abstract. In this paper we present a fully automated approach to multiple sclerosis lesion segmentation in multi-spectral brain MRI data. The proposed segmentation framework is based on the recently introduced probabilistic boosting trees, which is a strategy for supervised learning. Foreground and background voxels are distinguished by considering a 2D context surrounding the voxel of interest and its transformation to a large set of Haar-like features. This allows for building a discriminative model that captures class specific characteristics despite of the well-known drawbacks of MR imaging. Training the model itself involves two major steps: successively selecting and combining features that best separate the training data by means of boosting and inductively grouping the resulting boosted classifiers in a tree structure. By applying the equivalence of boosting and additive logistic regression the approach is capable to derive a discriminative model for voxel classification in terms of posterior probabilities. The final segmentation is obtained after post-processing the preliminary result by stochastic relaxation and a standard zero level set segmentation approach. The applicability of the proposed method is demonstrated by quantitative evaluation within a leave-one-patient-out cross-validation.

1 Introduction

Quantitatively assessing disease progression is a major concern in the case of multiple sclerosis (MS)—a common neuropathological disease of young adults that primarily affects cerebral white matter within the human brain. One of the indices characteristic for the progression of the disease is lesion volume. However, manual quantitative measurements on volumetric magnetic resonance (MR) images suffer from substantial intra- and inter-rater variability [1], such that providing accurate and reliable automatic segmentation tools to facilitate valid MS lesion quantification is of enormous interest. Therefore, we propose a knowledge-driven approach for MS lesion segmentation in multi-spectral 3D brain MRI data based on the recently introduced [2] probabilistic boosting trees (PBT).

2 Methods

In order to distinguish foreground, i.e. lesion, and background, i.e. non-lesion, voxels within multi-spectral (FLAIR, T1, T2) MR volumetric data ($408 \times 512 \times 19$ and $408 \times 512 \times 21$) without contrast enhancement we build a PBT in a similar manner

to [3] to derive a discriminative model in terms of posterior probabilities for individual voxels from manually segmented training data. Subsequently in the segmentation process, the results obtained by PBT are refined by stochastic relaxation [4] and a standard zero level set approach from the Insight Segmentation and Registration Toolkit (ITK, www.itk.org). The latter uses anisotropic diffusion filtering [5] on one of the input images to obtain a feature image guiding evolution of the zero level set. As the axial resolution of the input data is low we restrict our approach to operate on down-sampled 2D axial slices (256×256) without taking into account inter-slice voxel neighborhood relations. The overall processing pipeline is depicted in Fig. 1.

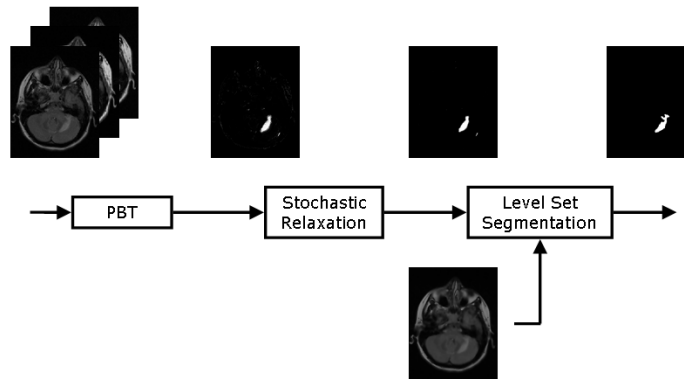


Fig. 1: The proposed segmentation framework.

The framework's first step PBT recursively groups boosted ensembles of weak classifiers to a tree structure during learning from annotated data. When Discrete AdaBoost [6] is chosen as the boosting strategy this resembles building a binary regression tree as the final boosted classifier

$$H(\mathbf{x}) = \sum_{t=1}^T \alpha_t h_t(\mathbf{x}) \quad (1)$$

generated within each inner node for a feature vector \mathbf{x} through a weighted combination of $T \in \mathbb{N}$ weak classifiers $h_t(\mathbf{x})$ with individual weights $\alpha_t, t \in \{1, \dots, T\}$, asymptotically approaches the additive logistic regression model [7]:

$$H(\mathbf{x}) \approx \frac{1}{2} \ln \frac{p(y = 1|\mathbf{x})}{p(y = -1|\mathbf{x})} \quad (2)$$

where $y \in \{-1, 1\}$ denotes the classification outcome. Therefore, at each inner node v of the resulting PBT with strong classifier H_v and outgoing arrows r_v^{-1} and r_v^1 associated with the possible classifications an approximation of the overall posterior proba-

bility $\tilde{p}_v(y|\mathbf{x})$ can be computed via the recursive formula

$$\begin{aligned} \tilde{p}_v(y|\mathbf{x}) = & \tilde{p}_{\beta(r_v^{-1})}(y|\mathbf{x}) \cdot \frac{e^{-2H_v(\mathbf{x})}}{1 + e^{-2H_v(\mathbf{x})}} \\ & + \tilde{p}_{\beta(r_v^1)}(y|\mathbf{x}) \cdot \frac{e^{2H_v(\mathbf{x})}}{1 + e^{2H_v(\mathbf{x})}} \end{aligned} \quad (3)$$

where $\beta(r)$ denotes the node where arrow r ends. At leaf nodes a hard classification $\tilde{p}_v(y = -1|\mathbf{x}) = 1$ and $\tilde{p}_v(y = 1|\mathbf{x}) = 0$ or $\tilde{p}_v(y = -1|\mathbf{x}) = 0$ and $\tilde{p}_v(y = 1|\mathbf{x}) = 1$ is returned.

For the purpose of classification it is tried to capture the structural variability of foreground and background voxels by not only considering multi-spectral intensity and gradient values but also, additionally, 17,472 Haar-like features [8] computed on a 15×15 square centered at the voxel of interest. Those features derived from a subset of the extended set of Haar-like feature prototypes [9] are represented implicitly in memory by so-called ‘‘Integral Images’’. This allows for fast re-computation of the features with respect to a given voxel when actually assessed.

For a given voxel i the posterior probabilities $p(y_i = 1|\mathbf{x}_i)$ and $p(y_i = -1|\mathbf{x}_i)$ obtained by PBT that determine the segmentation are smoothed by stochastic relaxation independently from the initial features used by PBT itself. For this purpose the segmentation \mathbf{y} is assumed to form a Markov random field (MRF) with individual spatial priors

$$p(y_i) = p(y_i|y_{\mathcal{N}_i}) = e^{-\frac{\beta}{2} \sum_{j \in \mathcal{N}_i} V_{ij}(y_i, \bar{y}_j)} \quad (4)$$

where $V_{ij}(y_i, \bar{y}_j)$ denotes the two-elemented clique potential of the classification y_i at voxel i and the mean classification \bar{y}_j of a neighboring voxel j . In this notation $d(i, j)$ denotes the Euclidian distance. In our implementation we use 10 iterations of an algorithm similar to iterated conditional modes (ICM) [10] doing mean field-like approximation to the true posteriors $p(y_i)$. The neighborhood \mathcal{N}_i considered for each individual voxel i is an intra-slice 8-neighborhood.

3 Material and Experimental Setting

For evaluation of the proposed method there were 6 manually segmented multi-spectral MRI scans (FLAIR, T1, T2) of sizes $408 \times 512 \times 21$ and $408 \times 512 \times 19$ available. It takes less than five minutes to process one of the MRI volumes in a non-optimized C++ implementation of our segmentation framework on a Fujitsu Siemens Computers notebook equipped with an Intel Pentium M 2.0 GHz processor and 2 GB of memory. In fact, processing may be significantly accelerated as soon as traversal of the learned PBT is properly restricted by soft thresholding as originally proposed in [3]. Though, we currently rely on complete traversal. The leave-one-patient-out approach was used to train six different classifiers from approximately 70,000 randomly selected training samples, i.e. voxels inside the head of the patients, uniformly distributed over all the input slices. The maximum number of features selected by AdaBoost in each tree node were increased level-wise beginning with 1 at the root node. The maximum depth of the

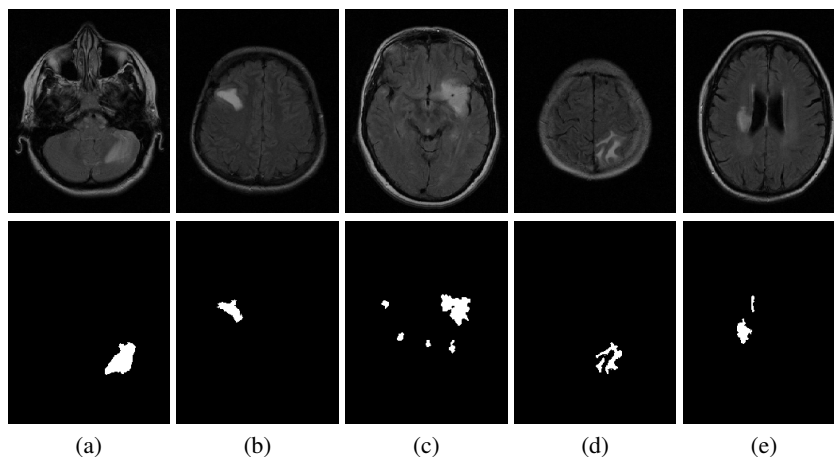


Fig. 2: Segmentation results obtained by leave-one-out validation. The first row shows selected slices of the FLAIR sequences of five different data sets. The second row shows the associated segmentation result

Table 1: Performance indices obtained by leave-one-out validation for all of the examined data sets.

	Dice	Pearson	Sens.	Spec.	PPV	NPV
1	0.7338	0.7356	0.8014	0.9989	0.6767	0.9994
2	0.7509	0.7575	0.6578	0.9995	0.8746	0.9984
3	0.5602	0.5601	0.5220	0.9987	0.6044	0.9981
4	0.8570	0.8581	0.9371	0.9967	0.7895	0.9992
5	0.0000	-0.0001	0.0000	0.9995	0.0000	0.9998
6	0.4912	0.5067	0.3929	0.9997	0.6550	0.9990

trees learned was restricted to 10. For stochastic relaxation $\beta = 1.2$ was chosen for empirical reasons. The settings for anisotropic diffusion filtering and Laplacian zero level set segmentation were adopted from ITK's introductory example. With the hardware and implementation mentioned above the duration of building one classification tree is about 12 hours.

4 Results

As can be seen from the quantitative results in Tab. 1 three of the six classifiers reach a Dice coefficient of more than 70% on their test data set, two reach about 50% and one fails with 0% due to the lack of significant MS lesions in the associated data volume. However, for a fully automated approach volumetric overlap of more than 50% can be considered a remarkable achievement. Figure 2 gives a visual impression of the segmentation results obtained.

5 Conclusion

The method for segmentation of MS lesions in multi-spectral 3D brain MRI data discussed in this paper makes use of structural information by additionally taking into account the context of a voxel for the purpose of classification. The presented results show that by doing so supervised techniques like PBT can be employed for MRI tissue classification even though they are usually—when relying on individual voxel intensities only—considered inappropriate due to the typically large inter-scan variations. This encourages further investigation of medical image segmentation approaches based on boosting weak classifiers in the sense of features from large sets of feature candidates. Future work involves further assessment and refinement of the proposed method and investigation of alternative structural features that can be used in the context of boosting.

References

1. van Leemput, K., Maes, F., Vandermeulen, D., Colchester, A., Suetens, P.: Automated segmentation of multiple sclerosis lesions by model outlier detection. *IEEE Trans. Med. Imag.* 20(8) (2001) 677–688
2. Tu, Z.: Probabilistic boosting-tree: Learning discriminative models for classification, recognition, and clustering. In: *IEEE Intl. Conf. Comput. Vis.*, Beijing, China. (2005) 1589–1596
3. Tu, Z., Zhou, X., Comaniciu, D., Bogoni, L.: A learning based approach for 3D segmentation and colon detagging. In: *Europ. Conf. Comput. Vis.*, Graz, Austria. (2006) 436–448
4. Sonka, M., Fitzpatrick, J.M.: *Handbook of Medical Imaging, Vol. 2: Medical Image Processing*. SPIE/The International Society of Optical Engineering, Bellingham, Washington, USA (2004)
5. Weickert, J.: *Anisotropic Diffusion in Image Processing*. ECMI Series. Teubner-Verlag Stuttgart, Germany (1998)
6. Freund, Y., Schapire, R.E.: A decision-theoretic generalization of on-line learning and an application to boosting. In: *Europ. Conf. Comput. Learning Theory*. (1995) 23–37
7. Friedman, J., Hastie, T., Tibshirani, R.: *Additive logistic regression: a statistical view of boosting*. Stanford University, Department of Statistics, Technical Report (1998)
8. Viola, P., Jones, M.: Robust real-time object detection. In: *2nd International Workshop on Statistical Learning and Computational Theories of Vision*, Vancouver, Canada. (2001) 1–25
9. Lienhart, R., Kuranov, A., Pisarevsky, V.: Empirical analysis of detection cascades of boosted classifiers for rapid object detection. In Michaelis, B., Krell, G., eds.: *DAGM-Symposium*. Volume 2781 of *Lect. Notes in Comp. Sci.*, Springer (2003) 297–304
10. Besag, J.: On the statistical analysis of dirty pictures. *J. R. Stat. Soc. Ser. B Stat. Methodol.* 48(3) (1986) 259–302

Image Compression Algorithm Based on Encoding of Tree-Arranged Wavelet Coefficients

Sergei V. Umnyashkin, Dmitri M. Koplovich, Andrei S. Pokrovskiy, and Andrei A. Alexandrov

Moscow Institute of Electronic Technology (Technical University)
Moscow, K-498, Russia, Email: vrinf@miee.ru

Abstract. A computationally effective image compression algorithm is proposed, which applies multi-model arithmetic encoding for RD-optimized zerotree structured wavelet coefficient.

1 Preliminaries and General Statement of the Problem

During the last decade, functional bases of wavelets have attracted extraordinary attention of researchers, both mathematicians and engineers. That useful tool has been applied for digital image compression in JPEG-2000 standard. Development of image compression algorithms is a very important point for numerous applications including medical imaging and telemedicine.

Let $\mathbf{X} = \{x_{k,m}\}$ be a matrix of grayscale image samples, let transformed matrix of the same size $\mathbf{W} = \{w_{k,m}\}$ be obtained from \mathbf{X} by means of $(n+1)$ -level wavelet decomposition, as a result of n steps of two-dimensional processing with dyadic filter bank, $\mathbf{W} = W(\mathbf{X})$. We shall refer the term *wavelet spectrum* to \mathbf{W} . In many cases wavelet coefficients $\{w_{k,l}\}$ are convenient to be treated as a set of $2^n \times 2^n$ -element tree structures with root nodes lying in the lowest frequency subband. The root node has three offspring nodes (direct descendants) and corresponds to the decomposition coefficient at scaling function. Other tree nodes correspond to wavelet coefficients, each node having four direct descendants, except for the leaf nodes of highest frequency subband, see Fig. 1. Moving from root to leaves we increase both spatial resolution of base functions and their frequency.

The approach of zerotree quantization traces back to the work of Lewis and Knowles [1]: when scanning tree nodes from parents to descendants, it is possible to predict contribution of wavelet coefficients into image decomposition from already processed (encoded/decoded) subbands, taking into account spatial properties of wavelets in image domain. Lewis and Knowles introduced certain rules to make choice for every non-leaf node, whether to prune its branch (zerotree quantize) or not. If pruned, all the coefficients of branch are excluded from output data stream by coder and set to zeros by decoder before image reconstruction. Apart from pruning, uniform scalar quantization is applied to those wavelet coefficients which are kept in non-pruned branches: $\tilde{w}_i = \text{Round}(w_i/q)$, where q is quantization step. For reconstruction, decoder uses dequantized values $\hat{w}_i = q\tilde{w}_i$.

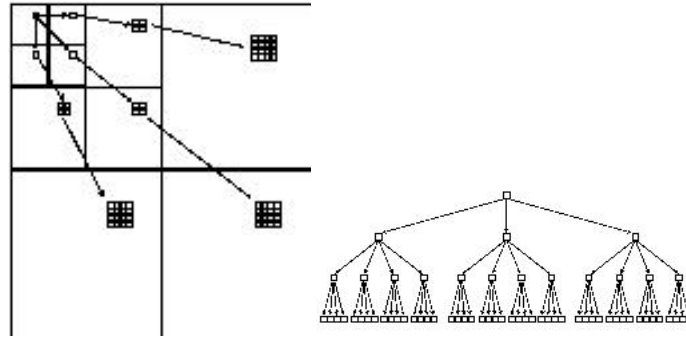


Fig. 1: Tree structures and parent-offspring relations of wavelet coefficients. Example for 3-step transform.

According to [2] we use the following notations. For n -step wavelet transform, we refer T to original full tree of all its $2^n \times 2^n$ nodes, which are denoted by indexes i , $i=0, \dots, 2^{2n}-1$. A *pruned subtree* $S \subseteq T$ is any subtree of T , which shares its root node. We call *leaves* those nodes $\{i\}$ of S or T which have no child nodes. Only root node $i=0$ has three children, all other non-leaf nodes have four children, see Fig. 1. By definition, let *residue tree* U_i be a set of all descendants of node i , that is, $U_i = T_i \setminus \{i\}$. Let C_i denote a set of direct descendants (children) of i , then we can represent residual tree as $U_i = \bigcup_{j \in C_i} T_j$. We call *tree level* or *resolution level* L_k ($k=0, \dots, n$) a horizontal layer of nodes in tree structure organized as shown in Fig. 1, greater index k is equal to higher spatial resolution. Among the $n+1$ levels of n -step transform, $L_0 = \{0\}$ contains only root node, and the set of the original leaves of T is $L_n = \{2^{2(n-1)}, \dots, 2^{2n}-1\}$. Each level corresponds to three spectrum subbands.

Developing compression algorithm, we shall restrict our consideration to the only parameter for coding non-pruned nodes, which is step q for uniform quantization of wavelet coefficients, similar to [2]. Therefore, we have to find a scheme to encode both topology structure of S and quantized values $\tilde{w}_i = \text{Round}(w_i/q)$ of nodes $i \in S$. Within the scheme, finding the best choice of (S^*, q^*) can be expressed in conventional terms of rate-distortion theory in the following way: for the given $\lambda \geq 0$, among all topology variants $S \subseteq T$ and quantization steps $q \geq 0$ find the pair (S^*, q^*) that minimizes Lagrange RD-function,

$$J(S^*, q^*) = \min_{S \subseteq T, q \geq 0} [D(S, q) + \lambda R(S, q)], \quad (1)$$

where D is the distortion (data losses) caused by scalar and zerotree quantization and R is the bit rate needed to encode the tree S . The externally given parameter λ balances rate and distortion: to increase compression at the expense of greater error, λ should be set higher. Following [2], the implementation of (1) is assumed to be two-level procedure, which varies q and for each q finds the optimal topology $S^*(q)$. That is

$$J(S^*, q^*) = \min_{q \geq 0} \min_{S \subseteq T} [D(S, q) + \lambda R(S, q)]. \quad (2)$$

Thereby, the key task of optimization lies in performing the internal minimization of

(2) to find the optimal topology for given λ and q :

$$J(S^*) = \min_{S \subseteq T} [D(S) + \lambda R(S)], \quad (3)$$

$$q = \text{const}, \quad \lambda = \text{const}.$$

2 Specific Features of the Proposed Algorithm

2.1 Arithmetic encoding

For entropy encoding, we apply multi-model arithmetic coder, which may be considered as multiple objects of basic coder [4], each model corresponds to particular input dataflow, with special extension added to simplify estimation of rates: entropy rate needed to encode symbol c from input flow f is calculated by fast functions $H(f, c)$ using tabulated values of $\log_2(x)$ and the same internal statistical modeling which is applied for entropy encoding (outputting bits) itself.

2.2 Encoding the topology structure of tree

To encode topology of S , it was proposed [2] to create binary map $\{n_i\}$ which indicates whether all the descendants of node i is zeroquantized or not: if $U_i = \emptyset$ then $n_i=0$ and $n_i=1$ otherwise (i.e. at least $C_i \neq \emptyset$); see Fig. 2A. As the elements of any set C_i may belong or not belong to zero-tree all together only, it is essentially to tie the indications $\{n_j\}_{j \in C_i}$ into united data symbol $N_i=(n_{i1}, n_{i2}, n_{i3}, n_{i4})$, a 16-symbol alphabet is to be used to describe zero-tree map then [3]. Obviously, the concatenated symbols N_i can be expressed numerically as $N_i=8n_{i4}+4n_{i3}+2n_{i2} + n_{i1}$. In order to exploit the correlation of original indications $\{n_j\}_{j \in C_i}$, the symbols $\{N_i\}$ are arithmetically encoded. Because of the introduced changes, concatenated indication N_i becomes related with the node i of the higher level, see Fig. 2B.

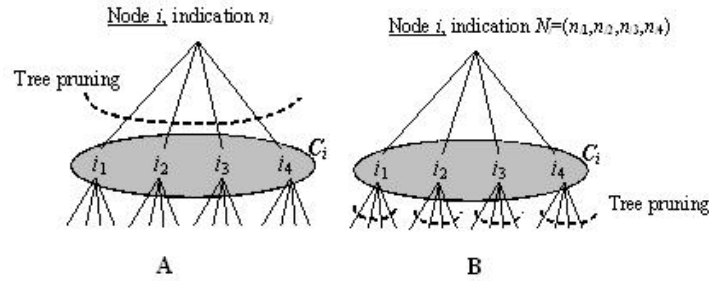


Fig. 2: Difference in analysis for tree pruning: A – [2], B – proposed algorithm

2.3 Using statistical dependencies between wavelet coefficients

The common idea used in [2] almost the same way as in [1] lies in the observation that lower absolute value $|w_i|$ or energy w_i^2 of parent node entails higher probability of zerotree root to emerge at the node i . It is possible to predict presence or absence of zerotree more precisely building up predictor P_i as a sum of both energy w_i^2 and energy of wavelet coefficients neighboring the node i in subband [1][2][3]. In order to let decoder form the same predictions, quantized wavelet coefficients must be applied to calculate predictors P_i , either $\tilde{w}_i = \text{Round}(w_i/q)$ or $\hat{w}_i = q\tilde{w}_i$. In our design, we use the following weighted sum for predictor calculation:

$$P_i = \frac{1}{16} \left(4|\tilde{w}_i| + 2 \sum_{m \in I_1(i)} |\tilde{w}_m| + \sum_{m \in I_2(i)} |\tilde{w}_m| \right), \quad (4)$$

the summation indices are defined for subband neighbors of node i according to Fig. 3.



Fig. 3: Weight coefficients used to build up predictor (4)

To encode concatenated indications $N_i=(n_{i1}, n_{i2}, n_{i3}, n_{i4})$ several statistical models are used. The rule of selecting appropriate model is defined by the function $\text{MapIndex}(\bar{P}_i)$, where $\bar{P}_i = \frac{1}{4} (P_{i1} + P_{i2} + P_{i3} + P_{i4})$:

$$\text{MapIndex}(x) = \begin{cases} 1, & \text{if } x < 0.3 \\ 2, & \text{if } 0.3 \leq x < 1.1 \\ 3, & \text{if } 1.1 \leq x < 4 \\ 4, & \text{if } 4 \leq x \end{cases} \quad (5)$$

To select particular models meant to encode those wavelet coefficients $\{\tilde{w}_i\}$ which are not included into zerotrees, the function $\text{SpectrumIndex}(i)$ is constructed. Both inter-subband (between parent and children) and intra-subband (between neighbors) dependencies are taken into account. To build up the intra-subband prediction component for a current node j , its three already processed (encoded/decoded) neighbours are applied:

$$s_j = 0.36P_i + 1.06 (|\tilde{w}_{j_y}| + |\tilde{w}_{j_x}| + 0.4|\tilde{w}_{j_d}|), \quad (6)$$

where j_y, j_x, j_d are the three already processed vertical, horizontal and diagonal neighbors, respectively; and P_i is defined for parent node i (note that $j \in C_i$) by (4). To

select particular model for \tilde{w}_j encoding/decoding, the following definition is used:

$$SpectrumIndex(j) = \begin{cases} 5, & \text{if } j > 3 \text{ and } s_j < 1.72 \\ 4, & \text{if } j > 3 \text{ and } 1.72 \leq s_j < 4.10 \\ 3, & \text{if } j > 3 \text{ and } 4.10 \leq s_j < 9.80 \\ 2, & \text{if } j > 3 \text{ and } 9.80 \leq s_j < 26 \\ 1, & \text{if } 0 < j \leq 3 \text{ or } 26 \leq s_j \\ 0, & \text{if } j = 0 \end{cases} \quad (7)$$

The model selecting thresholds for the rules (5) and (7) have been empirically obtained in experiments carried out for test images.

3 Experimental Results and Conclusion

To assess performance of the proposed compression algorithm conventional characteristics were used, when rate is expressed in bits per image pixel (bpp) and mean square distortion is measured as peak signal to noise ratio (PSNR). Results reached for *Lena* test image are shown in Fig 4. Five-step wavelet transforms were applied in all cases. Commonly used 9/7 wavelet filters applied in JPEG-2000 were employed in experiments represented in Fig. 4.

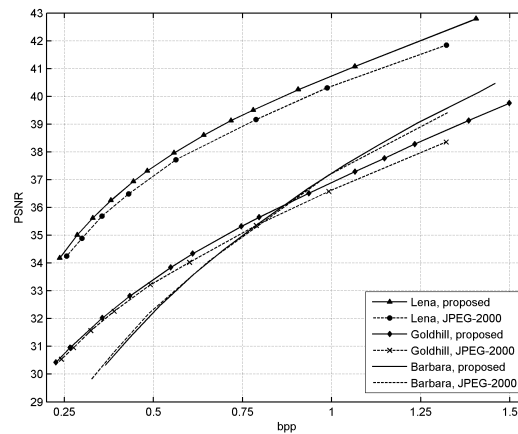


Fig. 4: Comparative performance of the proposed algorithm and JPEG-2000. ACDSSee Pro Version 8.1 (Build 99) used to measure JPEG-2000 characteristics

The algorithm described in this paper showed high results outperforming many other state-of-the-art image compression algorithms. Free demo program implementing the proposed algorithm is available at <http://www.miet.ru/struct/6/ckb.html>

References

1. Lewis A.S., Knowles G. Image Compression Using the 2-D Wavelet Transform // IEEE Trans. Image Proc. – Vol. 1. -No. 2, 1992. – P. 244-250.

2. Z.Xiong, K.Ramchandran and M.T.Orchard.Space-frequency Quantization for Wavelet Image Coding // IEEE Trans. Image Proc. Vol.6, May 1997, P. 677-693.
3. Umnyashkin S.V. Image compression based on mixed predictive modeling of wavelet trees // Reports from Växjö University (Sweden) – Mathematics, natural sciences and technology. – Nr.11 (September), 2001. – 18 pages.
4. Witten I., Neal R.M., Cleary J.G. Arithmetic coding for data compression // Comm. ACM. - 1987. - Vol.30. - No. 6. – P. 520-540.

Appearance-based Approach to Extract an Age-related Biomarker from Retinal Images

Rüdiger Bock¹, Jörg Meier¹, László G. Nyúl¹, Simone Wärtges²,
Georg Michelson², and Joachim Hornegger¹

¹ Institute of Pattern Recognition, University of Erlangen-Nuremberg,
Martensstraße 3, 91058 Erlangen

`ruediger.bock@informatik.uni-erlangen.de`

² Department of Ophthalmology, University of Erlangen-Nuremberg,
Schwabachanlage 6, 91054 Erlangen

Abstract. We present an appearance-based method that extracts a new age-related biomarker from retina images. The Principal Component Analysis is applied on intensity values of the illumination corrected green channel of fundus images. The algorithm does not use segmentation, is robust and shows a high range of reliability. It identified an age-related feature with a strong influence of the temporal parapapillary area and the optic nerve head. The feature correlates with chronological age of the participants and is significantly influenced by the appearance of cardiovascular risk factors such as smoking and hypertension, and thus it can be designated a biomarker. We extract and validate a medical parameter from retina images applying a purely data-driven approach without using any prior knowledge.

1 Introduction

1.1 Concept of Biological Age

The concept of biological age is established as a general measure to quantify the “true global state of [an] aging organism” [1]. Because of the complexity of the human body and the aging process the biological age (BA) is commonly understood as a combination of several biomarkers. A valid biomarker must correlate with age and the influence of the risk factors has to be validated.

1.2 State of the Art

One common approach to determine the BA is to combine several age-dependent biomarkers into a BA index using statistical methods [2,3]. Age-related biomarkers obtained by multiple regression analysis, factor analysis [4], or principal component analysis (PCA) [5] were combined into a new BA index.

The aging process can also be well observed on retinal images, especially changes of the retinal tissue [6] and the cardiovascular system. As described in [7], the blood flow in the optic nerve head is significantly correlated with age. These biomarkers are mainly based on measurement of specific regions of the retina. The regions are obtained manually or by automatic segmentation.

1.3 Purpose

The purpose of the presented study is to extract and validate an age-related biomarker from retina images using a purely data-driven approach. In contrast to extensive and error-prone segmentation, this appearance-based technique [8] applies the unsupervised Principal Component Analysis (PCA) on pixel intensities [9] of digital fundus images.

2 Methods

2.1 Image Processing and Feature Extraction

As the green channel of the RGB retina image provides the highest contrast among the relevant structures, only that is used for further investigations. The images can be illuminated unequally within the sample set and mostly show inhomogeneous background. In order to eliminate illumination variations, illumination correction by mean filtering [10] is applied. The region of interest is restricted to a circular area around the papilla center with a radius of 300 pixels. For PCA calculation, the selected circular ROI is transformed to vector representation. Application of PCA on a set of input images yields multidimensional, but compact representations of these images. Each vector component of the output is considered as a feature, independently from the others.

2.2 Statistical Analysis

The SPSS software (release 13.0; SPSS Inc. Chicago, IL, USA) was used for statistical analysis. Measurement values from the transformation were standardized by subtracting the mean value from raw data and divided by the standard deviation. Correlation between a feature and age was expressed using the Spearman-Rho coefficient. The intraclass correlation coefficient of reliability was calculated by determination of Cronbach alpha at the 95 % confidence interval. The F-statistics tested whether the mean values between different subjects and between images of the same subject differed significantly. The significance between controls and subjects at cardiovascular risk was calculated using the Mann-Whitney test. All values are expressed as mean \pm SD. A p-value $<$ 0.05 was considered significant.

3 Data

The used database of the population-based screening project “TalkingEyes” [11] includes more than 45,000 pairs of retina images acquired since 2002 during a clinical non-experimental cross-sectional survey. Color images of the retina (optic nerve head centered, resolution 1216×1600 , field of view 45°) were acquired in a standardized process. They were taken with a fundus camera (KOWA, nonmyd-alpha 45, Japan) without pharmacological dilation of the pupil. Only images from the right eye of sufficient quality were evaluated. The PCA transformation for identification of age-related image features was developed based on a randomly selected training set of 65 men (44.2 ± 11.4

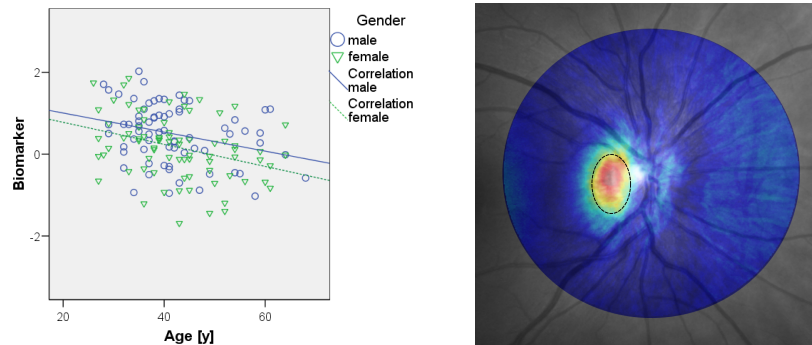


Fig. 1: Left: Age-dependency of the retinal feature in participants without cardiovascular risk factors and retinal diseases. Right: The absolute eigenimage is depicted as an overlay onto a gray-scale representation of the retina fundus image. The outlined region has a strong influence to the proposed biomarker and is located at the temporal parapapillary area and the optic nerve head.

years) and 60 women (48.8 ± 12.6 years) without cardiovascular risk factors and without pathological eye diagnosis. The resulting algorithm was tested on another subset of controls (70 men; 41.8 ± 9.2 years and 78 women; 42.6 ± 9.6 years) without hypertension, diabetes, hyperlipidemia, manifest ocular diseases, microaneurysms, cotton-wool spots, hard exudates, bleedings, neovascularizations, abnormalities of macular pigment epithelium and with a refractive range of -5 to $+5$ diopters.

3.1 Reliability

Fundus images from further six participants (four men and two women) provided a basis for assessing the reliability of the algorithm. Five fundus images were taken from the right eyes of the six healthy subjects in one minute interval by one observer.

3.2 Cardiovascular Risk Factors

For estimating the influence of cardiovascular risk factors on the biomarker, the control group was matched for age and gender to hypertensive subjects and smokers, respectively, without any other cardiovascular risk factors. Forty-four men (45.5 ± 9.3 years) and 26 women (51.2 ± 7.3 years) from the control group were opposed to the same number of hypertensive subjects (age 45.5 ± 9.4 years; hypertensive for 5.9 ± 6.7 years and age 51.2 ± 7.3 years; hypertensive for 7.9 ± 7.1 years, respectively). Fifty-seven male controls (41.7 ± 8.4 years) and 60 female controls (43.2 ± 9.4 years) were opposed to the same number of male smokers (age 41.8 ± 8.5 years; smoking for 20.6 ± 9.8 years; 15.3 ± 8.6 cigarettes per day) and female smokers (age 43.2 ± 9.5 years; smoking for 20.1 ± 10.7 years; 13.5 ± 8.1 cigarettes per day).

Table 1: Biomarker values for smoking and hypertensive participants

Gender	Hypertension			Smoking		
	Risk factor	Control	Sig.	Risk factor	Control	Sig.
Male	0.10 ± 0.84	0.57 ± 0.95	0.01	-0.16 ± 1.29	0.72 ± 0.92	< 0.001
Female	-0.46 ± 1.23	0.06 ± 0.99	0.09	-0.12 ± 1.10	0.24 ± 0.98	0.048

4 Results

4.1 Correlation of the Retinal Biomarker with Age

The PCA generates a multidimensional and compressed representation of an image. The PCA transformation was determined using the training set. The images of the training set were compressed using this transformation and each vector component was evaluated for age correlation. One feature showed a significant correlation with age. To check the feature, the correlation was also tested on the control group. In male control subjects Spearman coefficient was -0.284, $p = 0.017$ and in female control subjects -0.374, $p = 0.001$. Figure 1 shows decreasing feature values with increasing age.

4.2 High Influence Regions of Retina to Biomarker

The PCA calculates several linear combinations that are applied to the input data. As each linear coefficient is associated to a pixel position, it can be illustrated as a so-called eigenimage.

The absolute eigenimage of the biomarker is presented in Figure 1 and allows an anatomical interpretation of image regions. The regions with the highest impact to the biomarker are located at the temporal parapapillary area and at the optic nerve head. This region is medically relevant and changes with age.

4.3 Retinal Biomarker in Subjects with Cardiovascular Risk

The biomarker in age-matched hypertensive patients and smokers differs significantly from control. As shown in Table 1, the existence of a cardiovascular risk factor like smoking or hypertension causes a significantly lower biomarker value.

4.4 Reliability

A Cronbach alpha = 0.953 indicates high reliability of the algorithm. Mean values between subjects ($df = 5$) and between the images of one subject each ($df = 4$) did not differ significantly ($F = 0.87$, $p = 0.985$).

5 Discussion

In the present study, we have established an age-related biomarker derived from retina images. The algorithm is based on fairly simple PCA and does not use segmentation. It is robust and shows a very good range of reliability. The temporal parapapillary area was identified as retinal region with the highest impact to the proposed biomarker. The validity of the biomarker was proven by the significant influence of cardiovascular risk factors such as hypertension and smoking. In conclusion, it was possible to extract and validate a medically relevant parameter by applying a purely data-driven approach without using any a priori knowledge.

Acknowledgment

Supported by German Research Foundation (DFG), project SFB 539. The authors are grateful to Ralf Horstmann for providing image data from the “TalkingEyes” project.

References

1. Klemera, P., Doubal, S.: A new approach to concept and computation of biological age. *Mechanism of Ageing and Development* 127(3) (2006) 240–248
2. Duggirala, R., Uttley, M., Williams, K., Arya, R., Blangero, J., Crawford, M.: Genetic determination of biological age in the mennonites of the midwestern United States. *Genetic Epidemiology* 23(2) (2002) 97–109
3. Guéguen, R.: Proposition of an aging indicator from general health examination in France. *Clinical Chemistry and Laboratory Medicine* 40(3) (2002) 235–239
4. MacDonald, S., Dixon, R., Cohen, A., Hazlitt, J.: Biological age and 12-year cognitive change in older adults: Findings from the Victoria Longitudinal Study. *Gerontology* 50(2) (2004) 64–81
5. Nakamura, E., Tanaka, S.: Biological ages of adult men and women with downs syndrome and its changes with aging. *Mechanisms of Aging and Development* 105(1-2) (1998) 89–103
6. Panda-Jonas, S., Jonas, J.B., Jakobczyk-Zmija, M.: Retinal pigment epithelial cell count, distribution, and correlations in normal human eyes. *American Journal of Ophthalmology* 121(2) (1996) 181–189
7. Boehm, A.G., Koeller, A.U., Pillunat, L.E.: The effect of age on optic nerve head blood flow. *Investigative Ophthalmology and Visual Science* 46(4) (2005) 1291–1295
8. Hornegger, J., Niemann, H., Risack, R.: Appearance-based object recognition using optimal feature transforms. *Journal of Pattern Recognition* 33(2) (2000) 209–224
9. Turk, M., Pentland, A.: Eigenfaces for recognition. *Journal of Cognitive Neuroscience* 3(1) (1991) 71–86
10. Hoover, A., Goldbaum, M.: Locating the optic nerve in a retinal image using the fuzzy convergence of the blood vessels. *IEEE Transactions on Medical Imaging* 22(8) (2003) 951–958
11. Michelson, G.: Talkingeyes-and-more. *Biomed Tech (Berl)* 50(7-8) (2005) 218–226

Stent Structure-Graph Based Mapping

Benjamin Keck¹, M. Prümmer¹, and Arun Ganguly² Rebecca Fahrig²

¹ Friedrich-Alexander-Universität Erlangen-Nürnberg,
Department of Computer Science, Institute of Pattern Recognition (LME),
Martensstr. 3, D-91058 Erlangen, Germany.

² Radiological Sciences Laboratory (RSL),
Stanford University,
1201 Welch Road,
Palo Alto, CA, 94304, USA.

Abstract. Stents implanted in the superficial femoral artery have a high fracture rate, and the exact reasons for this are not known. No studies have quantified the exact stent deformation *in-vivo*, but it is hypothesized that such stents undergo significant bending and torsion during normal activity, causing such fractures.

Providing information about the nature of the deformation has the potential to help to elucidate stent fracture mechanisms in the superficial femoral artery as well as describe mechanical loading boundary conditions to guide the design of future stents. In order to get an impression about the deformation we compared the stent structures. Therefore we developed a framework for extraction of stent structure representing graphs and a new mapping method. Our framework allows the computation of basic information, such as stent length and magnitude of bending, of C-arm CT imaged stents. This computation is based on a center-line extraction, which forms the basis for the stent structure-graph representation, enhanced with feature-points on the stent grid.

Our new structure based mapping (SBM) of this stent structure representation provides an impression of the stent deformation by overlapping the straightened stent structure-graphs. In the results we verified the algorithm by mapping simulated, *in-vitro* phantom and *in-vivo* data sets and comparing these with a straight-forward rigid registration of the 3D stent structure-graphs.

We show the advantages of the developed algorithm and compare it to a rigid registration. Further more we point out the ability to map stent structures with several deformations. Our method can illustrate structural stent deformation based on stent grid points currently limited for non-rotational and non-torsional deformations.

1 Introduction

The superficial femoral artery (SFA) is prone to the development of atherosclerotic lesions, and is often treated with the combination of percutaneous transluminal angioplasty and stent deployment [1]. Unfortunately, the restenosis / reocclusion rate of SFAs after angioplasty and stenting has been reported to be high, with 1-year failure rates from 19% to 71% (see [2] and [3]). Recent studies estimate that stents in the SFA fracture at a rate as high as 35%, and it has been hypothesized that these fractures may be correlated to restenosis and the return of clinical symptoms (see [4] and [5]). Due

to limitations in current pre-clinical testing, device failures are often not detected until clinical use. It has therefore become a high priority among the stent manufacturers and the FDA³ to elucidate the *in-vivo* mechanical environment of the SFA and fracture mechanisms of implanted stents. Vascular stent fractures have been reported in different arteries, however, it is suspected that the SFA may experience these fractures at a higher rate. The SFA is hypothesized to undergo dramatic non-pulsatile deformations in the adductor canal including axial compression and extension, radial compression, bending, and torsion [4]. Due to research on the axial and twisting deformations of the SFA [6] it is clear that these deformations are unpredictable a priori, but have strong symmetries between left and right SFAs in terms of arc length, length change, and direction of twist.

2 Mapping

Due to the fact that MR can visualize soft tissues and is not able to visualize thin metal structures like them of SFA-stents, we developed a framework to visualize the influence of deformation forces on the stent structure. Therefore we extract the structure information out of C-arm CT imaged stents using grid crossing feature-points. We previously developed a centerline computation to extract basic information out of C-arm CT acquired stent images. By combining this centerline with the extracted feature-points, henceforth called leaf-points, we created a tree-like graph which represents the stent structure. This convenient representation builds the basis of our approach. The computed centerline is sampled and represented by a 3-dimensional linear B-spline with n control-points. For each leaf-point, mesh grid crossing, we compute the orthogonal projection onto the centerline, defining the appropriate fork-point. A leaf-point and the corresponding fork-point define then a feature-vector.

To map a template stent structure-graph onto a reference we first use the centerline and their representation. Applying a linear mapping of the template centerline control-points onto the reference centerline implies that the starting and end point of the centerlines are the same. Since the deformation influences also the length of the centerline, it is scaled linearly. In the second step the feature-vectors are translated by mapping the fork-points in the same way as the control-points onto the mapped centerline. Due to the fact that the feature-vectors lose the property to be perpendicular to the centerline it is necessary to transform them. We compute the perpendicular part for each projection of the feature-vector onto the mapped centerline to keep the orientational direction. By normalizing this part and afterwards scaling it with the original length, we achieve again the perpendicular feature-vectors. The basic idea of the SBM technique is sketched in Figure 1 while an acquired stent phantom shows the relation between the stent structure and the stent structure-graph in Figure 2. Figure 3 shows an visualized example (reference, template and mapped stent structure-graph) of our mapping technique.

A pseudo algorithm can be defined in the following steps:

³ U.S. Food and Drug Administration

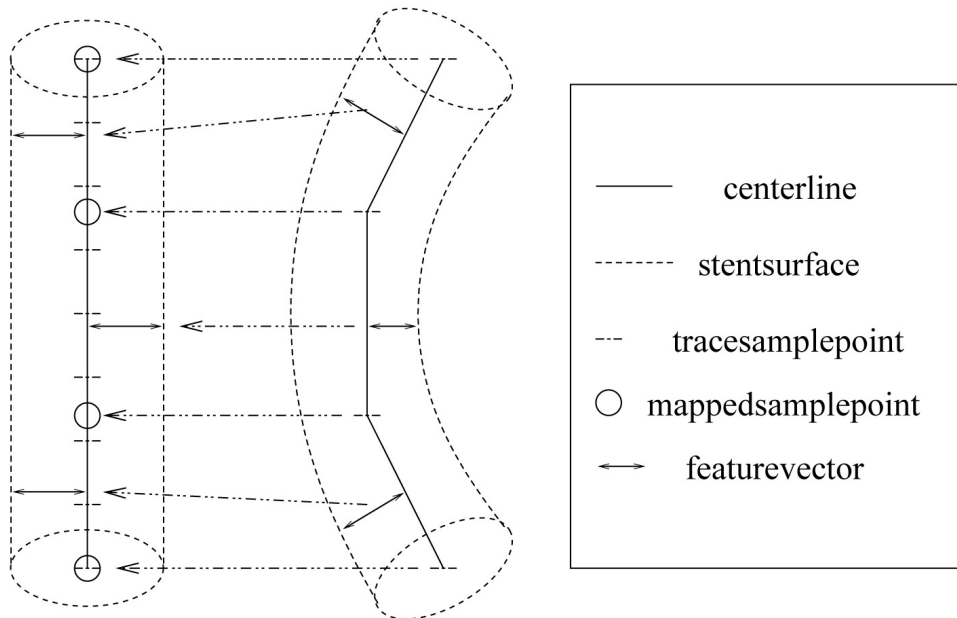


Fig. 1: Principle of centerline and feature-vectors. The control points of the template centerline on the right are mapped to points on the reference centerline on the left and define the mapped centerline, while three example feature-vectors are also translated and aligned.

1. Map the centerline by scaling the length and compute the corresponding control-points on the reference centerline.
2. Translate the feature-vectors by mapping the fork-points onto the mapped centerline.
3. Transform the feature-vectors such that they are again perpendicular to the centerline. §

3 Results

To compare our approach with a straightforward 3D-rigid registration of the extracted stent structure representing graphs, we used simulated data, where the point correspondences between reference and template stent structure-graphs for the leaf-points are known. By mapping a translated and transformed (due to stretching or bending) stent structure-graph, generated with certain uniform distributed added noise, onto a straight one, we could measure the number of correct mapped nearest neighbor paired leaf-points and compute the detection rate. The detection rate is defined by the ratio of correct mapped leaf-points and overall possible correct paired leaf-points. We examined the influence of noise on both algorithms. Further measured the mean detection rate for stretching and bending deformations and finally the influence of missing leaf-points, which simulates missing feature-points. Overall we simulated over 50 experiments with

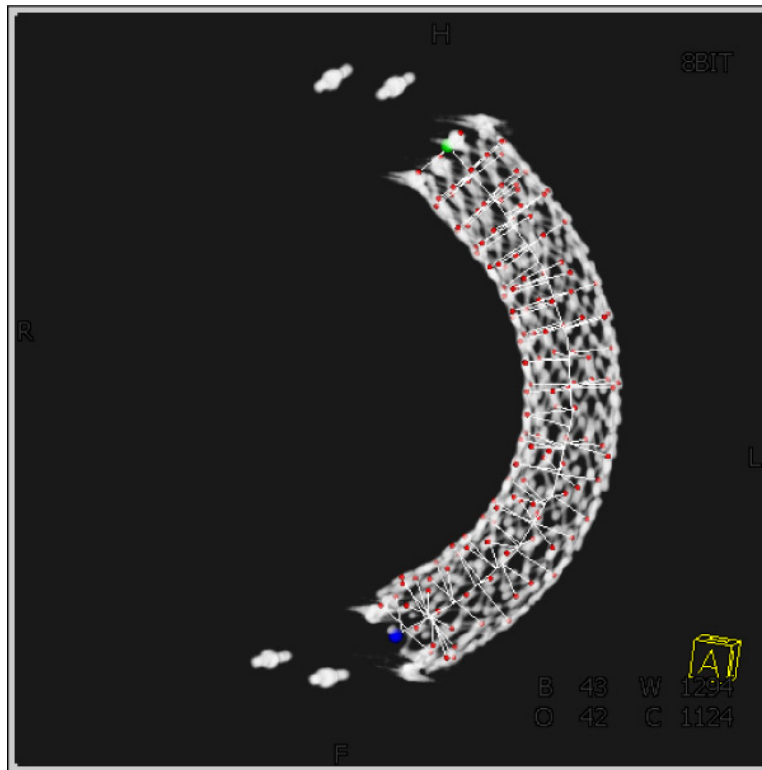


Fig. 2: The correspondence between extracted features from a *in-vitro* phantom data presented as a stent structure-graph and the *in-vitro* stent structure of the phantom is shown. Start- and end-point of the centerline is indicated by the green and blue sphere. The leaf-points are visualized as red spheres.

different setup to achieve realistic results. Table 1 shows the results represented by the mean detection rates for our simulations. The table indicates, that our method is more sensitive to noise, but outperforms the 3D-rigid registrations in all other simulations. However for the test with the stretch and bend deformation, this result could be assumed, but the 3D-rigid registration is more sensitive to the number of missing feature-points. The computed parameters and visualized mapping results indicate clearly different kind of deformations.

4 Summary & Conclusions

We showed a developed stent structure-graph mapping based on the centerline computation of stents and features on the stent surface. The achieved results show the coherence on the stent structures and indicate different kind of deformations.

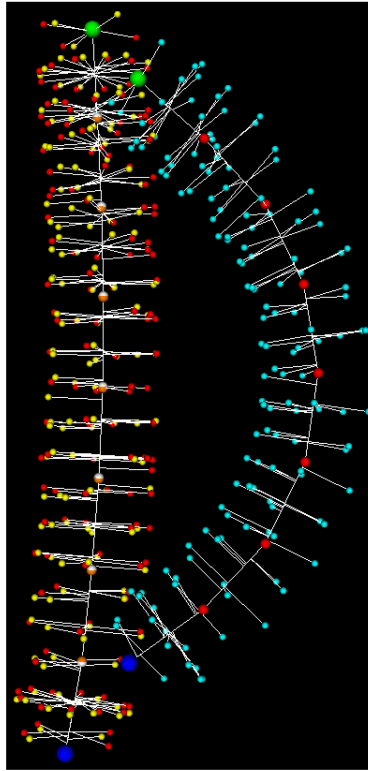


Fig. 3: The centerline sample points and feature-vectors of the template stent structure-graph (light blue leaf-points) are mapped on the reference stent structure-graph (red leaf-points). The mapping result (yellow leaf-points) shows the advantage of our method.

In contrast to a straightforward 3D-rigid registration, our proposed algorithm enables the visualization of structural deformations. With respect to the simulations our algorithm performed better results for stretch and bend deformations and is less sensitive to missing feature-points.

We conclude that the mapping technique is very well suited to compute and evaluate different kind of deformation on stent structures. Our visualization allows guiding the development of future stents.

Acknowledgments

The basis of our framework was developed by Alex Schneider.

Mean detection rates for experiments with simulated data		
Test/Method	SBM	3D-rigid
Noise Test	20.10%	22.20%
Stretch Test	85.70%	29.30%
Bend Test	87.20%	55.10%
Missing Points Test	89.48%	57.27%
Overall	70.12%	40.96%

Table 1: Result overview for simulated experiments with our structure based mapping (SBM) and a 3D-rigid registration.

References

1. Henry, M., Amor, M., Ethevenot, G.: Palmaz stent placement in iliac and femoropopliteal arteries: primary and secondary patency in 310 patients with 2- 4-year follow-up. *Radiology* 197 (1995) 167–174
2. Duda, S., Pusich, B., Richter, G.: Sirolimus-eluting stents for the treatment of obstructive superficial femoral artery disease: six month results. *Circulation* 106 (2002) 1505–1509
3. Gray, B., Sullivan, T., Childs, M., Young, J., Olin, J.: High incidence of restenosis/ reocclusion of stents in the percutaneous treatment of long-segment superficial femoral artery disease after suboptimal angioplasty. *Journal of Vascular Surgery* 25 (1997) 74–83
4. Allie, D., Hebert, C., C.M., W.: Nitinol stent fractures in the SFA. *Endovascular Today* 1 (2004) 22–34
5. Smouse, H., Nikanorov, A., LaFlash, D.: Changes in major peripheral arteries during joint movement before and after stent placement in the cadaver model, *Annual Radiology and Endovascular Therapy Seminar* (2004) <http://www.miit.com/2004/slides.htm>.
6. Cheng, C., Wilson, N., Hallet, R., Herfkens, R., Taylor, C.: In Vivo MR angiographic quantification of axial and twisting deformations of the superficial femoral artery resulting from maximum hip and knee flexion. *Journal of Vascular and Interventional Radiology* 17(1) (2006) 979–987

Life Science Electronics

Smartphone-based Mobile Solutions for Health Control in Humans

Alexander V. Kobelev¹, Igor K. Sergeev¹, and Sergey I. Schookin¹

Department of Biomedical Techniques, Bauman Moscow State Technical University, Moscow, Russia

Abstract. Techniques of physiologic data control (e.g. heart rate) as they are non-invasive are especially effective and give an opportunity of automation. Mobile solutions for health control problems are based on ECG-registration with small-sized mobile gauge and subsequent analysis of heart rhythm variability. By using as hardware one wireless small-sized gauge and modifying the program on a mobile phone or PDA, it is possible to use various techniques of functional health condition estimation depending on the system applications.

Index Terms – smartphone, Bluetooth, vital parameters, ECG

1 INTRODUCTION

Now methods and means of health control are important for sports medicine, fitness and home care, which is due to the fact that we can see that more emphasis is now placed on the prevention of diseases rather than treatment. In all industrially developed countries, a healthy lifestyle is intensely advocated and popularized. Regular sports activities and exercise are viewed as one of the most essential components of a healthy lifestyle, however, an analysis of the impact of exercise on individual human health shows that it often has no invigorating effect and sometimes even causes a worsening of an individual's health. Nevertheless, any sports activities and exercise are a powerful factor influencing a person's health. As a rule, the absence of medical monitoring or quality self-control essentially reduces the invigorating effect of exercise [1].

One of the best ways to measure the influence of exercise on a human body is to analyze its physiological parameters (pulse, blood pressure, body temperature, etc.). Currently fitness management devices are represented on the market only by pulse monitors produced by Polar, Reebok, CardioSport, FreeStyle and Sensor Dynamics [2]. However, monitoring health condition by pulse measurement is acceptable for no more than 50% of the population. This is related to the fact that this method of control does not provide a complete account of individual and age-determined features of the human body. In addition, the method does not allow efficient planning of exercise. Therefore, the use of pulse monitors does not preclude the necessity of supplementary observation of the athlete's condition by medical doctors and coaches.

Fitness management based on diagnosing the functional states of the body does not have these disadvantages. Diagnostics and registration of functional states of a human body are considered to be an optimal method of selecting any kind of exposure,

including exposure to exercise. Monitoring the condition of an organism enables consideration of individual features of people, planning their workload, discovering signs of overstrain and, consequently, exercising on a higher quality level.

The evaluation of the functional body state in clinical and sports medicine is carried out with the help of techniques based on studying the functional state of separate body systems: the organs of blood circulation, respiratory apparatus, organs of the nervous system and the muscular system. Such methodologies include the PWC-170 test, the Harvard step test and the evaluation of the maximum quantity of oxygen consumed. Despite their reliability their use in sports practice is fairly limited. The main reason is that these methodologies are laborious, hard on the athlete undergoing testing and require medical control.

During the last 10-15 years the evaluation of the functional body state based on the analysis of the heart rate variability (HRV) has become wide-spread. This method is successfully used in professional and clinical medicine as it is non-invasive, especially effective and gives an opportunity of automation.

2 OVERALL REVIEW

One-channel ECG-registration system working under continuous monitoring conditions has been developed by us to evaluate functional body state by means of HRV. Hardware based on a small-sized mobile gauge consists of electrode system, biopotential amplifier, information accumulation system and self-contained power supply.

In case of natural person's body mobility ensuring convenient and qualitative ECG-registration is a big trouble. To avoid this we have implemented the gauge's electrode system as an elastic belt with extensive electrodes made from conductive rubber and located on the internal side of the belt. The extensive electrodes provide good condition for natural sweating, which reduces physiological artifacts. The mobile gauge has a very useful location at the metasternum level, does not prevent person's movements and provides bipolar electrocardiogram lead registration, which is close to the 1st Einthoven's electrocardiogram lead.

Having generalized modern microcontroller's achievements in the given work we have decided to use 8051-compatible microcontroller Cygnal from the F06 family manufactured by SiLabs [7]. The microcontroller has a built-in 16-bit ADC with sample rate of about 1 billion samples per second. The controller is not only good at energy saving, but also has efficient production of up to 25 MIPS. To date it is one of the most powerful controllers as compared to a combination of analog and digital peripherals. The usage of such controller has proved to be able to provide a signal oversampling and averaging in order to increase signal-to-noise ratio from 98 to 116 dB.

The storage battery with the rated voltage of about 3.7 V and the capacity of 800 mAh has been utilized for the purposes of electrical safety, decreasing the overall power consumption, increasing off-line supply source downtime and reducing overall dimensions of the mobile gauge.

3 WIRELESS TECHNIQUE

Note that electronic devices are connected to one another in a variety of ways: a cable connects a computer's processing unit to a display, a data cable and a docking cradle connect a personal digital assistant (PDA) or a cellular phone to a computer, radio waves connect a cordless phone to its base unit, an infrared beam connects a remote control pad to a television. An elaborate array of connectors among electronic devices calls for a better solution, especially in mobile gauge.

There are two approaches to the organization of a biotelemetry channel in radio-frequency technology: self-development of radio transmitters or usage of standard radio transmitters to solve a reliable data transfer problem over short distances. Among modern wireless standards, as you might know, are Wi-Fi, ZigBee and Bluetooth.

The most energy-saving radio-technology is ZigBee, whose radio-transmitters can work up to 5 years using one AA-battery. Nevertheless, ZigBee technology couldn't be used for continual monitoring, which is due to very long sleep-time in comparison with active one.

Too high data rate (up to 54 Mbps) and high range (100 m) in Wi-Fi have resulted from increased overall power in a mobile gauge and in all very small-sized mobile devices as well.

Consequently, we have selected Bluetooth technology from a set of popular wireless techniques mainly because of its low-cost, short-range and energy-saving technology that has become popular among those who want to create personal area networks (PANs).

4 POST-PROCESSING

While Bluetooth hardware has advanced, there had been no standardized way to develop Bluetooth applications - until special application programming interface (API) JSR-82 came into play [3, 4]. It is the first open, non-proprietary standard for developing Bluetooth applications using the Java programming language (with J2ME in mind). It hides the complexity of the Bluetooth protocol stack behind a set of Java APIs that allow you to focus on application development rather than the low-level details of Bluetooth. Bluetooth and J2ME can work together to achieve this unified vision. Bluetooth allows devices to communicate wirelessly and J2ME allows you to write custom applications and deploy them on mobile devices [5, 6].

Thus, there is a possibility of using a mobile gauge to register ECG signal and smart phone application or PDA (such as Palm or Pocket PC) with built-in Bluetooth support for subsequent ECG post-processing. In such a way we have developed a J2ME program, which can be connected to a mobile gauge. On establishing a connection the digitized ECG is displayed on the smartphone's screen. The adaptive algorithm of electrocardiogram QRS detection using combined adaptive threshold works at pseudo-realtime implementation on the Smartphone and provides heart rate visual representation.

5 CONCLUSION

The system is aimed at using in fitness and Life Science. The hardware extension with a GPS-receiver (with Bluetooth interface) allows supervising person's movements, which is useful in sports medicine. Automatic SMS messaging allows signaling emergencies which expands the system's capabilities in home care. GPRS-network presence allows monitoring of physiologic parameters at home or in remoted places.

Thus, using as hardware one wireless small-sized gauge and modifying the program on a mobile phone or PDA, it is possible to use various techniques of functional health condition estimation depending on the system applications.

6 REFERENCES

1. Finkelstein SM, Speedie SM, Potthoff S , (2006) **Home telehealth improves clinical outcomes at lower cost for home healthcare**. *Telemedicine and e-Health*, 12:128-136.
2. **Polar** at <http://www.polar.fi/polar/channels/eng/>
3. Qusay H. Mahmoud: **Wireless Application Programming with J2ME and Bluetooth**. February 2003
<http://developers.sun.com/techttopics/mobility/midp/articles/bluetooth1>
4. Qusay H. Mahmoud: **The Java API for Bluetooth Wireless Technology**. April 2003
<http://developers.sun.com/techttopics/mobility/midp/articles/bluetooth2>
5. Enrique C. Ortiz: **Using the Java APIs for Bluetooth Wireless Technology, Part 1 - API Overview**, December 2004
<http://developers.sun.com/techttopics/mobility/apis/articles/bluetoothintro/>
6. Enrique C. Ortiz: **Using the Java APIs for Bluetooth, Part 2 - Putting the Core APIs to Work**. February, 2005
<http://developers.sun.com/techttopics/mobility/apis/articles/bluetoothcore/>
7. Silicon Laboratories: **Improving ADC Resolution by Oversampling and Averaging**. Application Notes #118, Rev. 1.2 12/03, 2003.

Integrated Measurement Circuits with Low Power Consumption for ECG-Application

Hans Hauer¹, Edward Ryabov², and Slawa Efimov²

¹ Fraunhofer Institute for Integrated Circuits, Erlangen, Germany,
johann.hauer@iis.fraunhofer.de,

² Vladimir Polytechnical University, Vladimir, Russia

Abstract. In medical instrumentation the demand for small battery wearable measurement and control equipment is still growing. In the field of Electrocardiography 24 hour ECG recorders for medical applications and wireless pulse per minute measurement belts with watch displays for consumer applications are on the market. The discussed solution addresses high precision time measurement between ECG pulses. An integrated circuit was developed which measures the pulse duration with 12 bit resolution. The device includes preamplification, fully integrated bandpass filter, peak detector, time measurement unit and FSK modulator for wireless transmitter. The chip consumes 200 uA at 3.3 V supply and occupies an area of 2.1 mm² on a 0.35 um CMOS DPTM Process with 0.5 mm² core area only.

1 Introduction

Electrocardiography signals show a typical signature with a peak for each heart beat. For some heart diseases, like arrhythmics, measurement of the duration between two peaks is very important. Using clinical ECG equipment these measurements can be done by calculations on the stored data.

Our aim however was to develop a low power pulse duration measurement device which is equipped with short distance wireless transmission. So the user may wear it quite unseen on his body with a receiver in his pocket, his watch or mobile phone for outdoor activities or a computer for indoor patient monitoring.

First we had to decide on the measurement resolution. An analog decision error can be calculated by equation 1.

$$terr = \frac{Vreferr}{S} . \quad (1)$$

Assuming a typical peak slope S of 15mV/ms for a normalized 0.5 V peak amplified by a factor of 100 and a noise floor on the reference voltage Vreferr of 5mV the analog decision error is about terr = 0.33ms. Based on the expected analog accuracy we decided on a relaxed resolution of 1 ms for the digital time counter. This is good enough for consumer applications and for most clinical measurements, too. With a 12 bit time counter an ECG pulse time from 15 beats per minute up to more than 200 beats per minute can be evaluated.

Next the measurement bandwidth must be decided. The IEC IEC60601-2-47: "Medical

electrical equipment” norm defines a measurement band width of 0.67 Hz to 40 Hz for portable applications. For high precision clinical applications an extended bandwidth of 0.6 to 250 Hz or even 1 kHz is recommended. For our peak detection application a reduced bandwidth of 0.8 Hz up to 20 Hz is quite enough. In this case an additional 50/60 Hz power line notch filter is not necessary [1].

The module will be supplied by a lithium cell with 3.3 Volt and 24 mAh. Supply current for the total measurement module should be less than 1mA to guarantee a 24 hour operation. Fig. 1 shows a block diagram of the module consisting of a master clock generator, the measurement chip and an FSK-Modulator for a 128 kHz low frequency short distance transmission.

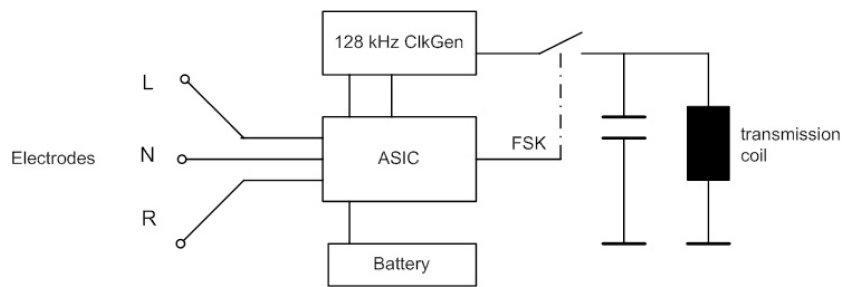


Fig. 1: Module Block Diagram

2 Chip Architecture

One of the main requirements was to integrate as many elements as possible in the device. A block diagram of the device is shown in Fig. 2.

A differential preamplifier with a gain of 10 is used for acquisition of the signal from the body. The following band pass is implemented with a switched capacitor high pass and a low pass function driven by a non overlapping clock of 500 Hz. The 3 dB-frequency of the high pass is specified with 0.8 Hz and 20 Hz for the low pass [4].

The filtered signal is amplified by the following stage by a factor of 10. The peak detector consists of a comparator function, a digital debounce circuit and a pulse former. Consequent pulses from the peak detector are used to start/stop the 12 bit gate counter. The pulse can be observed at pin R. A 16 bit serial data output frame is formed in the modulator block adding two leading and two trailing bits to the data. The 16 bit data word is transmitted three times for transmission security. FSK-modulated data is available on pin FSK for wireless transmission.

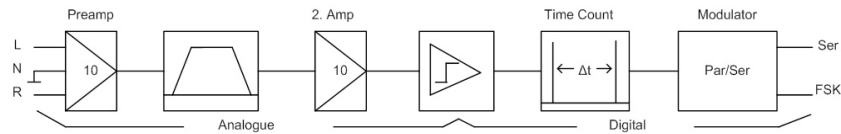


Fig. 2: Block Diagram of the Pulse Measurement IC

3 Operational Amplifier

A new type of operational amplifier RE_OB09 was designed for the application (Fig. 3) [2], [3]. Simulations show an open loop gain of 55 dB, GBW is 5.2 MHz and phase margin is 57 degree for a load of 1 pF. The OPAMP is optimized for low noise and low power. A comparison between the new designed cell and library standard cells given in Table 1 shows a figure of merit of 6816 compared to 29000 for the next best low noise operational amplifier.

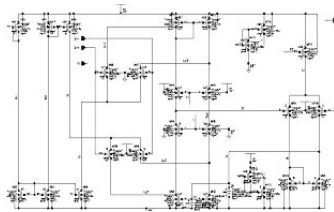


Fig. 3: OPAMP RE_OB09

OPAMP	Noise at 10 Hz	IDD
	[nV\sqrt{Hz}]	[uA]
Standard OP	550	100
LowNoise OP	100	290
Wideband OP	150	1500
RE_OP09	426	16

Table 1: Noise over supply current

4 Simulation and Measurement Results

Fig 4 shows the simulated bandwidth of the differential preamplifier. Gain is 20.9 dB. The 3 dB frequency is 60 kHz and the power consumption is 50 uA. For the following SC- band pass filter a 3 dB frequency of 0.8 Hz was measured for the lower band and 11 Hz for the upper band. Figure 5 shows measured results for a square wave test signal of 1Hz at the differential input. The lower curve (3) is measured at the output of the second amplifier, the middle curve (1) is the pulse output R of the peak detector and the upper curve (2) shows the burst of the 16 bit data word at pin SER transmitted 3 times. Figure 6 shows the data start peak R (1) for the measurement, the serial data (2) from the last measurement cycle and the FSK modulated output (3). From the measured serial data stream for different pulse signals with fixed frequency a total error of less than +/5 ms can be expected.

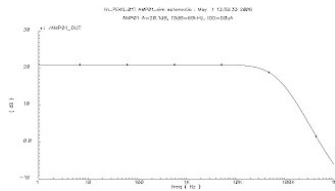


Fig. 4: Frequency response of preamplifier

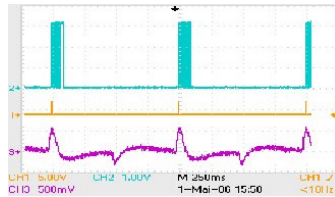


Fig. 5: Measured output for 1 Hz input signal

Heartbeat bpm	Pulse [s]	Serial Data [digits]	Data Error [digit]
54.5	1.1	1096	-4
60.0	1.0	1000	0
66.6	0.9	902	+2
75.5	0.8	798	-2
85.7	0.7	702	+2

Table 2: Measured serial data output

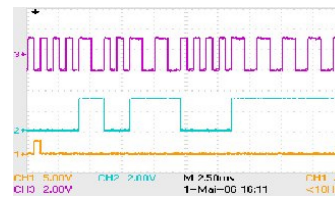


Fig. 6: Diagrams for serial and FSK modulated data

5 Chip Design

The device is implemented on a 0.35 μm DPTM CMOS process. Analogue and mixed signal simulations are done with SPECTRE. The layout is shown in figure 7. Chip size is 1.4 mm x 1.5 mm.

6 Conclusion

A pulse measurement unit for electrocardiographic applications was developed, integrated and evaluated. A new operational amplifier was developed with a good noise performance and low power consumption. A fully integrated switched capacitor high pass filter with a 3 dB frequency of 0.8 Hz @ 500 Hz clock frequency was used to remove the low frequency signals. The macro function can be implemented easily in ECG acquisition systems.

References

1. IEC 601-2-25 Medical electrical equipment- Particular requirements for safety of electrocardiographs, IEC, Genf, Swiss 1993
2. Gray, P. R.: Analysis and design of analog integrated circuits. ISBN 0-471-32168-0 Copyright 2001 John Wiley & Sons, Inc.
3. Allen, P. E., Holberg, D. R.: CMOS Analog Circuit Design. ISBN 0-03-006587 Copyright 1987 by Saunders College Publishing, a division of Holt, Rinehart and Winston.

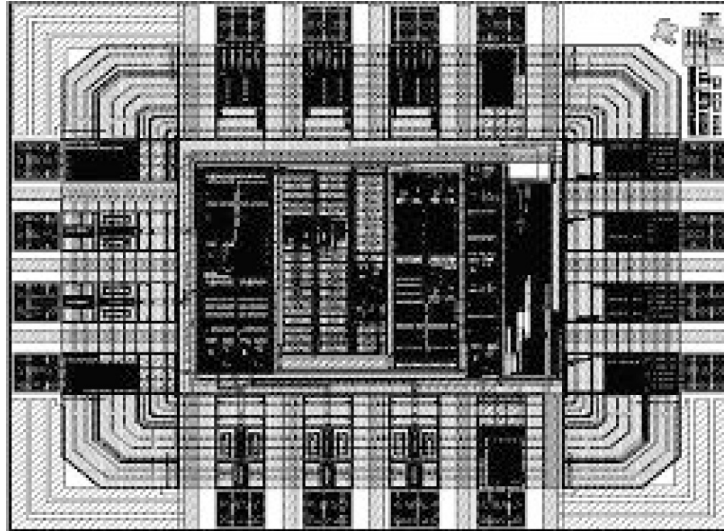


Fig. 7: The layout of IC

4. Winder, S.: Filter Design ISBN 0 75062814 6 Printed in Great Britain by Antony Rowe Ltd., Eastbourne 2001

Mathematical Methods for Medical Engineering

Solving direct and indirect tasks of tissue modelling in the precardiac area

Y.E. Kirpichenko¹ and D.P. Timohin²

¹ Department of Biomedical Techniques, Bauman Moscow

² State Technical University, Moscow, Russia

Abstract. Medicine is going to use noninvasive instrumental methods where they are possible. Precardiac rheocardiogram technique could be considered as an additional tool for ultrasound or even as a self-dependent procedure for the determination of heart's functionality. In precardiac rheography method's development it is essential to solve several tasks: direct task and indirect task. Solving direct and indirect tasks in the precardiac rheocardiography (preRCG) and calculating parameters of the heart's model, we can estimate location of the heart and also determine its biomechanical parameters.

1 Introduction

It is difficult to overestimate the importance of state-of-the-art and precise heart diagnostics, such as the determination of disorders in the hemodynamic function of a cardiovascular system. It is associated with a large number of lethal outcomes as a result of heart diseases. It is significant that heart diseases rank among the world's most dangerous diseases. Stress and bad ecology aggravate the situation. Hence, it is necessary to develop some medico-engineering solutions which could allow us to control hemodynamic parameters for a long time.

There are a lot of invasive and noninvasive methods to determine the cardiovascular system's functioning parameters. Nowadays medicine is going to use noninvasive instrumental methods where they are possible. Thus, the precardiac rheocardiogram technique could be considered as an additional tool for ultrasound or even as a self-dependent procedure for the determination of heart's functionality. In precardiac rheography method's development it is essential to solve several tasks, one of these being the distribution of electric potentials modeling in the precardiac area (direct task) and the other one being the determination of model parameters by means of these distributions (indirect task).

Thereby, solving direct and indirect tasks in the precardiac rheocardiography (preRCG) and calculating parameters of the heart's model, we can estimate the location of the heart and also determine its biomechanical parameters, such as stroke volume, heart-rate etc.

2 Precardiac rheocardiography technique

Examinations carried out are connected with tool elaboration to determine cardiovascular system's functioning parameters by using impedance methods. At the same time

measurements are realized in the precardiac area, since such allocation of current and measuring electrodes allows increasing method's precision.

The essence of this technique is that for measurement purposes 4 electrodes usually have to be applied to the body surface. Two electrodes (usually called current electrodes) are used to pass a constant alternating current with a high frequency (60 - 100 kHz) and very low amplitude (1 mA). The current is imperceptible to the patient and does not cause any physiological reactions. The other two electrodes (usually called measuring electrodes) are placed between the current electrodes and measure the voltage which is caused by the current flowing through the body segment. This voltage corresponds to the impedance of the body segment and changes in blood volume variations. On this basis the blood flow can be measured and analyzed.

Two biological tissue models are used for solving direct and indirect task in precardiac rheography method:

- Precardiac area is considered as horizontally layered medium with two layers: upper layer (thickness h_1 and specific resistance ρ_1) and lower layer (semi-infinite layer with specific resistance ρ_2) – two-layered model
- Precardiac area is considered as horizontally layered medium with three layers: upper layer (thickness h_1 and specific resistance ρ_1), middle layer (thickness h_2 and specific resistance ρ_2) and lower layer (semi-infinite layer with specific resistance ρ_3) – three-layered model

Besides, we take into the following considerations for polylayer model's construction:

- Electrical properties of each layer are invariant under direction
- Employed electrodes are dotty and they are placed on the surface of the upper layer
- Field function caused by the current electrodes meets the Laplace's equation everywhere, excepting placement of the current electrodes.

3 Direct task

Provided poly-layer model using we consider tissue compound, which contains muscle tissue ($\rho_{muscle} = 5 \text{ Ohm}\cdot\text{m}$), pulmonary tissue ($\rho_{pulm} = 8 \text{ Ohm}\cdot\text{m}$), myocardium ($\rho_{myo} = 5 \text{ Ohm}\cdot\text{m}$, $h_{myo} = 0.02 \text{ m}$) and bone tissue ($\rho_{bone} = 10 \text{ Ohm}\cdot\text{m}$). In case of two-layered model this compound is replaced by effective specific resistance ρ_1 , upper layer's thickness is determined by occurrence depth of the heart, $h_1 = 0.1 \text{ m}$, and specific resistance of lower layer corresponds with specific resistance of blood ($\rho_{blood} = 1.0\text{-}1.5 \text{ Ohm}\cdot\text{m}$). In case of three-layered model we consider myocardium layer as separate layer.

The major mathematical modeling of preRCG involves calculation of the forward and inverse problems. In the forward problem the governing equations in the preRCG field are derivable from Laplace's Equation (electrostatic approximation for low frequency).

A three-layered model will be considered in this section, because such mould imitates precardiac area properties very well. A three-layered heart's model is shown in

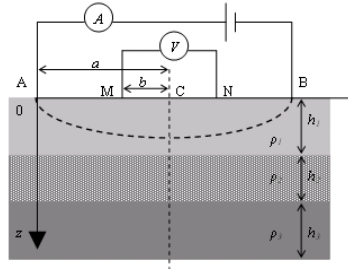


Fig. 1: Three-layered heart's model

Fig.1. In points A and B current electrodes are placed, measuring electrodes are placed in points M and N, respectively.

In case of cylindrical symmetry of the model, Laplace's Equation is written as:

$$\frac{\partial^2 \varphi}{\partial r^2} + \frac{1}{r} \cdot \frac{\partial \varphi}{\partial r} + \frac{\partial^2 \varphi}{\partial z^2} = 0 \quad (1)$$

To solve equation (1) we can make use of the boundary conditions, i.e. the potential's continuity and current density's normal component's continuity at the bedding interface. Besides, we take into consideration that air is not a good electrical conductor and potential at infinity must be equal to 0:

$$\begin{aligned} \varphi_i \Big|_{z=h_i} &= \varphi_{i+1} \Big|_{z=h_i} \\ \frac{1}{\rho_i} \cdot \frac{\partial \varphi_i}{\partial z} \Big|_{z=h_i} &= \frac{1}{\rho_{i+1}} \cdot \frac{\partial \varphi_{i+1}}{\partial z} \Big|_{z=h_i} \\ \frac{\partial \varphi_1}{\partial z} \Big|_{z=0} &= 0, \quad \text{as } \rho_{\text{air}} = \infty \\ \varphi_{\text{semi-infinite}} \Big|_{z \rightarrow \infty} &\rightarrow 0 \end{aligned} \quad (2)$$

By using these boundary conditions the expression for impedance on the body's surface is:

$$R(a, b) = \frac{\rho_1}{\pi} \cdot \left[\frac{1}{a^2 - b^2} + \int A_1(m) \cdot J_0[m \cdot (a - b)] dm - \int A_1(m) \cdot J_0[m \cdot (a + b)] dm \right]$$

$$A_1(m) = \frac{N}{D_1 + D_2}$$

$$N = (\rho_2 - \rho_1) \cdot (\rho_3 + \rho_2) \cdot e^{-4 \cdot m \cdot h_1} + (\rho_2 + \rho_1) \cdot (\rho_3 - \rho_2) \cdot e^{-4 \cdot m \cdot h_1 - 2 \cdot m \cdot h_2}$$

$$D_1 = (\rho_1 + \rho_2) \cdot (\rho_3 + \rho_2) \cdot e^{-2 \cdot m \cdot h_1} + (\rho_2 - \rho_1) \cdot (\rho_3 - \rho_2) \cdot e^{-2 \cdot m \cdot h_1 - 2 \cdot m \cdot h_2}$$

$$D_2 = (\rho_1 - \rho_2) \cdot (\rho_3 + \rho_2) \cdot e^{-4 \cdot m \cdot h_1} + (\rho_1 + \rho_2) \cdot (\rho_2 - \rho_3) \cdot e^{-4 \cdot m \cdot h_1 - 2 \cdot m \cdot h_2}$$

Final impedance vs. range between current electrodes relationship is shown in Fig.2 (range between measuring electrodes is 0.05 m).

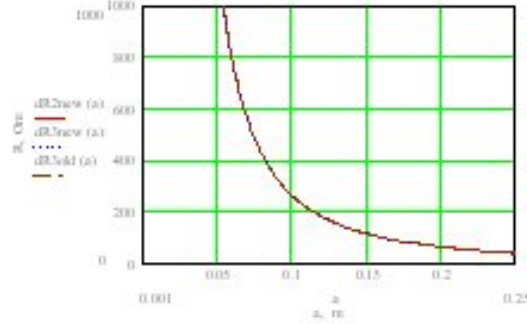


Fig. 2: Impedance vs. range between current electrodes (distance between measuring electrodes equals 5 cm)

4 Indirect task. Apparent resistivity conception.

For homogeneous half-space with specific resistance $\rho(r)$ relationship looks:

$$\rho(r) = \frac{2 \cdot \pi \cdot r^2}{I} \cdot \frac{\partial \varphi_1(r, 0)}{\partial r} \quad (3)$$

In case of tetra polar gradient electrode system (Fig.1), provided $MN \ll AC$:

$$\rho \approx \frac{\pi \cdot AM \cdot AN}{MN} = \frac{\pi \cdot (a-b) \cdot (a+b)}{2} b \cdot R_{MN} \quad (4)$$

If medium is not homogeneous ρ is called apparent resistivity. It is denoted ρ_k . For two-layered model:

$$\rho_k = \rho_1 \cdot \left[1 + 2 \sum \frac{K^n \cdot r^3}{[r^2 + 2 \cdot n \cdot h_1^2]^{3/2}} \right] \quad (5)$$

If $r \ll h_1$ $\rho_k \approx \rho_1$, and so if $r \rightarrow \infty$ $\rho_k \rightarrow \rho_2$. Apparent resistivity vs. half-range between current electrodes dependence is shown in Fig.3 (ρ_2 variable) and Fig.4 (h_1 variable).

Thus, the indirect task is the determination of model parameters by means of impedance distributions. In order to determine the model's parameters by using impedance distribution we make use of the apparent resistivity conception. We need to determine 3 parameters (ρ_1, ρ_2, h_1) of two-layered model and 5 parameters ($\rho_1, \rho_2, \rho_3, h_1, h_2$) of three-layered model. Having measured the apparent resistance we can determine electrical specific resistance of one of the layers. Also, by using the demonstrated application it is possible to define the layer's thicknesses.

In order to automatize determination of parameters we have developed application. It allows us to calculate impedance distributions by using model parameters and otherwise: it calculates model parameters by using set of impedance values. The precision of calculation you can see in Table 1.

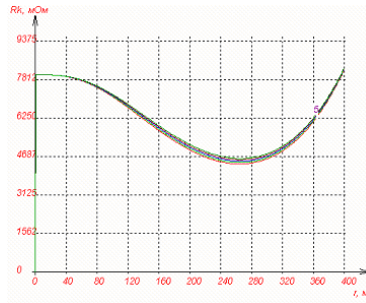


Fig. 3: Set of dependencies apparent resistivity vs. half-range between current electrodes (three-layered model, $\rho_1 = 8 \text{ Ohm}\cdot\text{m}$, $\rho_2 = 400\text{-}600 \text{ Ohm}\cdot\text{m}$, $\rho_3 = 1.35 \text{ Ohm}\cdot\text{m}$, $h_1 = 0.09 \text{ m}$, $h_2 = 0.02 \text{ m}$).

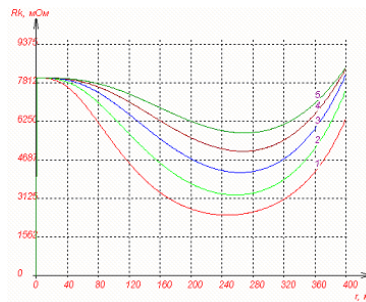


Fig. 4: Set of dependencies apparent resistivity vs. half-range between current electrodes (three-layered model, $\rho_1 = 8 \text{ Ohm}\cdot\text{m}$, $\rho_2 = 500 \text{ Ohm}\cdot\text{m}$, $\rho_3 = 1.35 \text{ Ohm}\cdot\text{m}$, $h_1 = 0.03\text{-}0.12 \text{ m}$, $h_2 = 0.02 \text{ m}$).

In this table with index “gen” genuine parameters is shown and with index “calc” calculated parameters is shown. Besides, we display miscalculation of model’s parameters determination for every parameter.

5 Conclusions

In this paper we took up main features of the precordial rheography technique and examined general poly-layer models to simulate the precordial area tissues. Solutions for direct tasks (by solving Laplace’s equation by using the boundary conditions) and determination of model’s parameters by solving indirect task (using apparent resistivity method) are presented. As is shown the miscalculation of the model’s parameters determination is less than 1% for parameter ρ_1 , about 2-3% for parameter h_1 and about 20% for parameter ρ_2 . The lessening of the miscalculation is considered as the future step of presented work to implement this method in order to determine human’s biomechanical heart parameters.

Table 1: Precision of model parameter's determination in case of solution of indirect task by using apparent resistivity conception.

N	ρ_{1gen} Ohm·cm	h_{1gen} cm	ρ_{2gen} Ohm·cm	ρ_{1calc} Ohm·cm	h_{1calc} cm	ρ_{2calc} Ohm·cm	$\delta\rho_1$ %	δh_1 %	$\delta\rho_2$ %
1	750	5	120	749	4.9	131	< 0.5	2.0	9
2	820	7	110	819	6.8	134	< 0.5	3.0	22
3	760	11	130	760	10.7	160	< 0.5	2.7	23
4	750	9	140	750	8.9	150	< 0.5	1.1	7
5	770	10	150	770	9.9	159	< 0.5	1.0	6

References

1. Tikhonov A.N., Samarsky À.À.: Equations of Mathematical Physics. Moscow.: Vyschaya shkola (1994) 467
2. V.K. Khmelevsky and V.À. Shevnin: Electrical Survey by Using Resistance Technique. Moscow.: MSU (1994) 160
3. Yakubovsky Y.V., Renard I.V.: Electrical Survey. Moscow.: Nedra (1991)

Nonlinear Diffusion Noise Reduction in CT Using Correlation Analysis

M. Mayer¹, A. Borsdorf¹, H. Köstler², J. Hornegger¹, and U. Rüdè²

¹ Lehrstuhl für Mustererkennung, (Informatik 5),

² Lehrstuhl für Systemsimulation, (Informatik 10),
Friedrich-Alexander Universität Erlangen-Nürnberg

Abstract. Noise reduction in CT images gains more and more attention. It provides a possibility to increase signal-to-noise ratio, hence giving more space for a further reduction of radiation dose. Nevertheless, a reduction of noise also bears the risk of suppressing medical relevant information. We propose a new noise reduction method that tries to minimize this risk by estimating the real image structure out of the correlations of two input data sets affected with uncorrelated noise. Such data sets can be achieved by reconstructing a CT scan with only the odd and the even numbered projections respectively. Furthermore, the method adapts itself to the spatially changing behavior of noise on CT images by estimating the local noise variance out of the difference of the input images. It can be applied to 2D and 3D data, with the latter giving better results due to the fact that more pixels are available for correlation computation and variance estimation. Examples show that the new method easily surpasses standard approaches and leads to noise suppression rates of about 66%.

1 Introduction

Common noise reduction methods often fail to produce convincing results when dealing with CT images. The reason for this lies in the unknown distribution of the noise in the reconstructed data. The intensity of the noise is spatially varying and directed noise structures appear. We present a new denoising method based on nonlinear isotropic diffusion that adapts itself to changing noise variance in different image regions and reduces oriented noise without noticeable loss of resolution by taking correlations of input images with uncorrelated noise into account. The approach is suitable for both 2D and 3D data.

2 Previous Work

In [1] Borsdorf proposed a Wavelet based denoising method for CT images. By separately reconstructing the odd and even numbered projections of a CT scan two sets of slices are obtained which include the same information but noise between the data is uncorrelated. By using correlation analysis in the wavelet domain combined with an orientation and position dependent noise estimation [2] only those wavelet coefficients containing image structure are kept for reconstruction of a noise suppressed image. In this work, the idea of this approach, e.g. using two data sets with uncorrelated noise, is picked up and transferred to the spatial domain and nonlinear diffusion methods.

3 Method

Noise is removed by minimizing an energy functional, which results in the following Euler-Lagrange equation:

$$u - u_0 = \tau \operatorname{div}(g(\|\nabla u\|)\nabla u) \quad (1)$$

This is equivalent to solving a Perona and Malik nonlinear isotropic diffusion equation [3] for a fixed artificial timestep τ . The initial image u_0 is set to the average of the two input images u_1 and u_2 . The sought-after solution is u . At the image boundary a homogeneous Neumann condition is applied. $g(\|\nabla u\|)$ is called an edge-stopping function regulating the diffusion process. Numerous edge-stopping functions have been proposed by the researching community, we have chosen to use the Tukey edge-stopping function introduced in [4] because of its good edge preserving properties.

For denoising CT images we have to modify $g(\|\nabla u\|)$ to achieve adequate results. Two ways of exploiting the availability of two input images with uncorrelated noise are to compute the correlation between both and to estimate noise variance. Because of the spatially varying noise properties in CT images these analysis is done locally in a neighborhood $\Omega_{\mathbf{x}}$ around a pixel \mathbf{x} . Additionally the influence of the neighboring pixels \mathbf{i} is weighted with gaussian weights $w(\mathbf{i}, \mathbf{x})$ depending on the distance between pixel \mathbf{i} and \mathbf{x} .

A local estimate for the correlation of two image regions is given by:

$$c_w(\mathbf{x}) = \frac{\sum_{\Omega_{\mathbf{x}}} (u_1(\mathbf{i}) - \bar{u}_1)(u_2(\mathbf{i}) - \bar{u}_2)w(\mathbf{i}, \mathbf{x})}{\sqrt{\sum_{\Omega_{\mathbf{x}}} (u_1(\mathbf{i}) - \bar{u}_1)^2 w(\mathbf{i}, \mathbf{x}) \cdot \sum_{\Omega_{\mathbf{x}}} (u_2(\mathbf{i}) - \bar{u}_2)^2 w(\mathbf{i}, \mathbf{x})}}, \quad (2)$$

$$C_w(\mathbf{x}) = \begin{cases} 1 & c_w(\mathbf{x}) > 0, \\ 0 & c_w(\mathbf{x}) \leq 0; \end{cases} \quad (3)$$

Because in our case only the amount of similarity between image regions is interesting, the values below 0 of the weighted correlation coefficient c_w , denoting anticorrelation, are set to 0, yielding in a local similarity measure C_w .

Two input images give us the possibility to estimate the local noise variance of the average of the input images by:

$$V(\mathbf{x}) = \frac{\sum_{\Omega_{\mathbf{x}}} w(\mathbf{i}, \mathbf{x})(u_1(\mathbf{i}) - u_2(\mathbf{i}))^2}{4 \sum_{\Omega_{\mathbf{x}}} w(\mathbf{i}, \mathbf{x})}; \quad (4)$$

Based on the Tukey edge-stopping function we now derive a new function taking into account V and C_w . The fixed parameter for the noise standard derivation of the Tukey edge-stopping function is replaced by $V(\mathbf{x})$, with a parameter β serving as an additional weighting factor:

$$g_V(x) = \begin{cases} \left(1 - \left(\frac{x^2}{V(\mathbf{x})}\right)\right)^2, & |x| \leq \beta\sqrt{V(\mathbf{x})}, \\ 0, & |x| > \beta\sqrt{V(\mathbf{x})}. \end{cases} \quad (5)$$

The square root of the product of the gradients on the input images is taken as the input for the edge-stopping function. It is further linearly scaled by the local similarity measure with a parameter λ . The idea behind this is to weaken high gradients in image regions with small similarity, e.g. in homogeneous regions, and to enlarge the gradient where similarity is high, i.e. when image structure is present.

$$g(\|\nabla u_{1,2}\|) = \begin{cases} g_V(x)(\|\nabla u_{1,2}\| \cdot W(\mathbf{x})) & \text{if } W(\mathbf{x}) > 0, \\ g_V(x)(0) & \text{else;} \end{cases} \quad (6)$$

where $\|\nabla u_{1,2}\| = \sqrt{\|\nabla u_1\| \cdot \|\nabla u_2\|}$ and

$$W(\mathbf{x}) = 1 + \lambda(2C_w(\mathbf{x}) - 1). \quad (7)$$

This edge-stopping function is used in the Perona and Malik diffusion equation as presented in equation (1) to denoise CT images.

The diffused images of the two input images u_1 and u_2 and the average u_A are calculated for a fixed timestep τ . All diffusion processes are regulated by the same edge-stopping function $g(\|\nabla u_{1,2}\|)$. The gradients are discretized by finite differences and the equation system by finite volumes. The method is implemented both in 2D and 3D. The partial differential equation system is solved by a nonlinear multigrid solver [5,6]. The solver of the diffusion equation updates u_A , u_1 and u_2 simultaneously, calculating $g(\|\nabla u_{1,2}\|)$ from the current images u_1 and u_2 to preserve nonlinearity. The output of the denoising method is the diffused image u_A .

4 Results

Fig. 1 shows results from the proposed method and one standard nonlinear diffusion method applied to a thin reconstructed slice (0.8 mm) of a liver CT scan compared to the average of the input images, which reflects the result of a reconstruction of all projections. It is referred to as the original image. In Fig. 2 the difference images to the original image are shown, providing an impression of the denoising behavior of the different approaches. Fig. 2b clearly shows that a standard nonlinear diffusion method fails to denoise a CT image with spatially varying noise power in an adequate manner. While noise in the center of the image is nearly unchanged, the outer regions are already blurred. Using the proposed method in 2D, Fig. 2c shows that this method is capable of adapting itself to the local noise variance, thus removing noise more uniformly. A noise reduction of 45% is achieved throughout the image. To get a proper estimate of the correlation of the input images a gaussian window with a standard deviation of 2 was used in a 9×9 neighbourhood. Because image structures like edges have influence on the correlation value of distant pixels in their neighbourhood, unfortunately noise remains around high contrast edges. Hence, if a natural look of the image should not be sacrificed the noise suppression must be kept weak. Using 3D data reduces this problem, because pixels for estimating the noise variance and correlation can be taken from the neighbourhood in all three dimension. Fig. 2d shows the result using a gaussian window of standard deviation 1.5 in a $5 \times 5 \times 5$ neighbourhood. It can be seen clearly that a

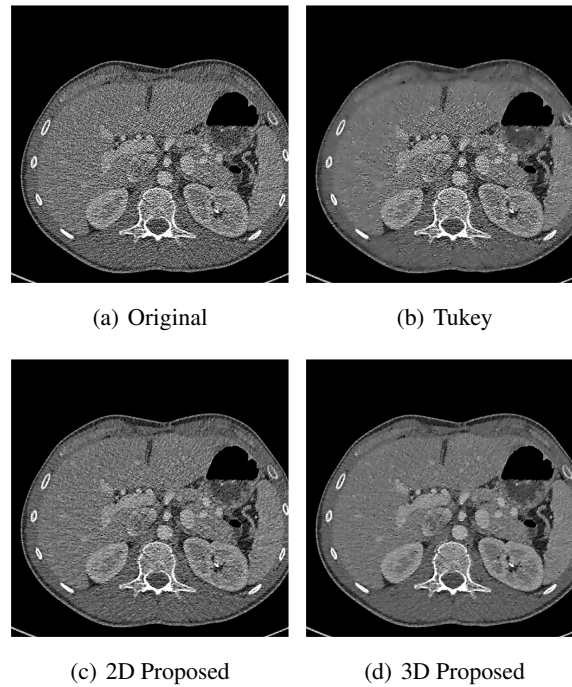


Fig. 1: Denoising results for a CTA of a liver, displayed with $c = 200$ and $w = 700$.

strong noise suppression of about 66% is achieved while image structure nearly remains unharmed.

5 Conclusions

A modified Perona-Malik diffusion process was presented that is able to deal with the special noise characteristics of CT data. The method surpasses standard diffusion methods due to its adaption on local noise variations and its regularizing of the diffusion depending on an estimation of the real image structure by calculating correlations between two input images with uncorrelated noise. A noise suppression rate of about 66% can be achieved.

References

1. A. Borsdorf, et al., Wavelet based Noise Reduction by Identification of Correlation, in Pattern Recognition (DAGM 2006), Lecture Notes in Computer Science, K. Franke, et al., Eds., vol. 4174. Berlin: Springer, 2006, pp. 21–30.
2. A. Borsdorf, et al., Separate CT-Reconstruction for Orientation and Position Adaptive Wavelet Denoising, in Bildverarbeitung für die Medizin 2007, A. Horsch, et al., Eds. Berlin: Springer, 2007, pp. 232–236.

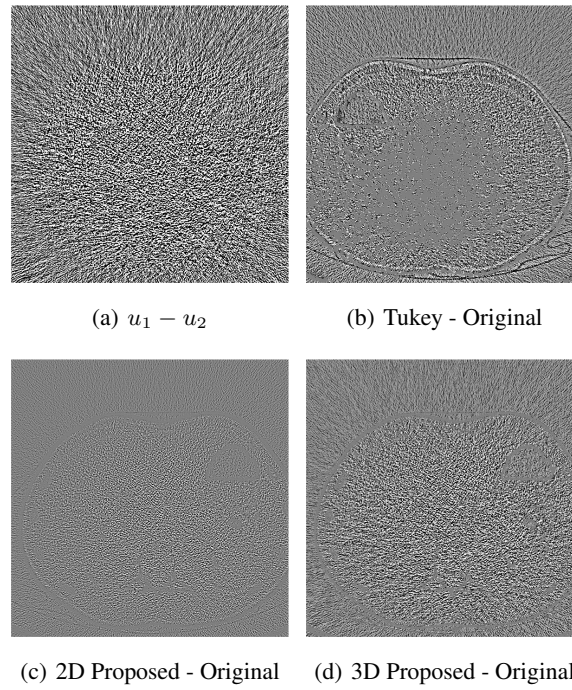


Fig. 2: Difference images, displayed with $c = 0$ and $w = 200$.

3. P. Perona and J. Malik, Scale-space and edge detection using anisotropic diffusion, *IEEE Trans. Pattern Anal. Mach. Intell.*, vol. 12, no. 7, pp. 629–639, 1990.
4. M. J. Black, et al., Robust anisotropic diffusion, *IEEE Trans. on Image Processing*, vol. 7, no. 3, pp. 421–432, 1998.
5. U. Trottenberg, et al., *Multigrid*. Academic Press, San Diego, CA, USA, 2001.
6. H. Köstler, et al., A fast full multigrid solver for applications in image processing, *Proceedings of the 12th Copper Mountain Conference on Multigrid Methods*, 2007.

The Computer Modeling of Normal and Pathological Tissue Growth using Cellular Automata Conception

E. M. Arkushina¹ and V. V. Kotin¹

Biomedical Techniques Department, Bauman Moscow State Technical University, Russia,
arkushina@rambler.ru

Abstract. Cellular automata are considered to be a perspective bio-adequate concept for modeling biological processes of normal and pathological tissue growth. In this paper results of the computer modeling of normal and pathological tissue growth using cellular automata conception are reviewed. The results of the modeling are qualitatively in a good agreement with verbal biomedical descriptions of tumor growth.

1 Biological background

Cancer - the malignant tumor is formed from epithelial cells of a leather, mucous membranes and parenchyma bodies. In most cases in the tissue adjoining with an environment and covered multilayered flat epithelia flat cells cancer arises. It can also appear in bronchial tubes. Cancer is one of the most widespread reasons of death.

The main problem of this work is to describe and make prognosis for such tumors to make the treatment more effective.

2 Model formulation

As the modeling tool the cellular automata conception is chosen. The basic advantages of this approach is that

- The model describes geometrical distribution of a tumor;
- The model includes algorithmic description of tumor cells reaction and allows considering process of influence on tumor growth of various external factors and process of chemotherapy;
- At last the model allows visualizing tumor growth process.

Cellular automata feature is that they possess characteristics of imitating and dynamic model. It allows approaching behavior of automata to behavior of real biological objects, but thus complicates analysis of the final results.

According the conception of cellular automata tissue consist of 3 types of cells

- Normal cells {NC};
- Pathological cells {CC};
- Empty cells {EC};

Each cell is characterized by number of parameters

- Type of cell;
- Time of live $\{T_l\}$;
- Mitosis period (in the simplification of the model the mitosis period is constant and independent on growth time) $\{T_m\}$;
- Needing resource (the minimum amount of the resource which is required cells for survival) $\{r_i\}$;
- Getting resource (the amount of the resource which cell get in current cycle) $\{R_i\}$;
- Factors of dependence on the resource (the parameters which characterize the influence of getting resource on cell life time, in the model we consider the logistic type of dependence life time on the resource) $\{R_i/r_i\}$;

There are several rules of transitions for each type of cells:

1. NC and CC transformed to EC when life time of NC or CC $> T_{life}$;
2. EC transformed to NC or CC when mitosis time of NC or CC in Moore area is equal to T_m
3. if the is no EC in the Moore area of the CC NC with minimum life time from CC Moore area transformed to CC when CC mitosis time is equal to T_m (such process is named recruiting);
4. The amount of the resource is limited;
5. CC in which Moore area there are at list one NC and NC in which Moore area there are no CC get the needing resource amount. All another cells get the living resource part proportional to a required resource.
6. Modeling chemotherapy course influences for the CC life time according the equation:

$$T_l(t+1) = T_l(t) - ch_t(t)/ch_0(t) * T_l(t) * ch_{lim}, \text{ where}$$

T_l – current life time;

ch_t – chemotherapy agent concentration in the current moment;

ch_0 – chemotherapy agent total concentration;

ch_{lim} – effectiveness of chemotherapy.

7. Chemotherapy agent concentration is decrease in time according the equation:

$$ch_t(t) = \exp(-k_{ch} * ch_t(t)) * ch_t(t), \text{ where}$$

ch_t – chemotherapy agent concentration in the current moment;

ch_{lim} – effectiveness of chemotherapy;

k_{ch} – decreasing coefficient of concentration chemotherapy agent.

8. Modeling Immune reaction influences for the CC life time according the equation:

$$T_l(t+1) = T_l(t) - I_n/I_0 * T_l(t) * I_{lim}, \text{ where}$$

T_l – current life time;

I_n – number of NC in the Moore area of CC;

I_0 – total number of signal from NC;

I_{lim} – effectiveness of the immune system.

9. The total effect of the immune reaction is equal the sum of NC signals, each signal is the number of CC in the Moore area of NC.

According to the medical description the larger tumor provides the less immune reaction. In our model according to the algorithm of immune reaction such dependence has a place.

At the Fig.1 the station and transition graph of the model is shown. In the graph the condition of cell and the condition of transition is represented.

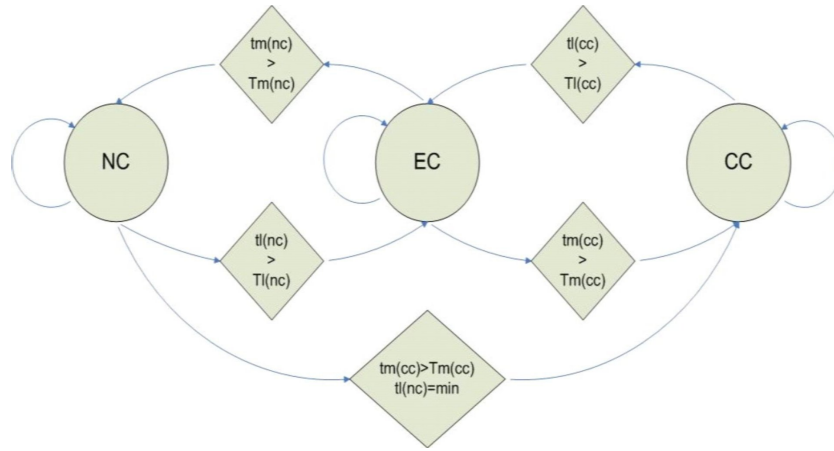


Fig. 1: The station and transition graph of the model

3 The numerical parameters of the model.

In the model we use such parameters:

1. The time of life - approximately 5-7 days;
2. The mitosis period - approximately 16-24 hours;
3. The main resource - glucose;
4. Pathological cells consume the resource in 10 times more than normal cells;
5. The total amount of the resource is chosen according to the equation

$$R_{max} = N * k * C_{norm}, \text{ where}$$

N – total number of cells in the model area;
 R_{max} – total concentration of the resource;
 C_{norm} – the needing resource for normal cells;
 k – stock factor.

4 The main results

4.1 Tumor morphology depends on the resource

The Fig.2 represents the tumor condition after 150 hours grows. At the cells automata area (40 by 40 cells) red, green and blow color means CC,NC and EC accordingly. The Fig.3 represents dependence CC number on time.

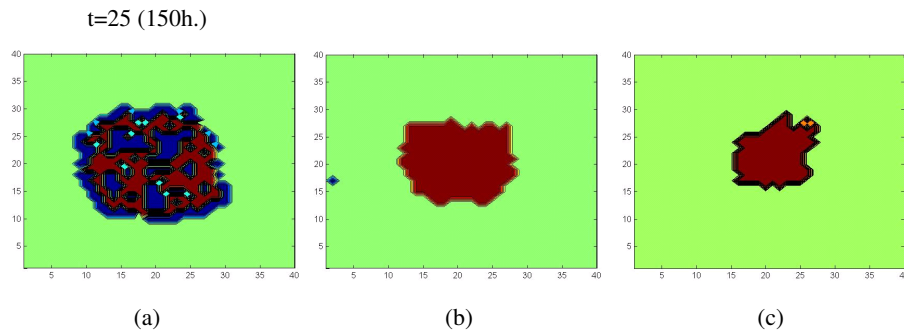


Fig. 2: The tumor condition after 150 hours grows (less amount of the resource (a), enough amount of the resource with recruiting (b), enough amount of the resource without recruiting (c))

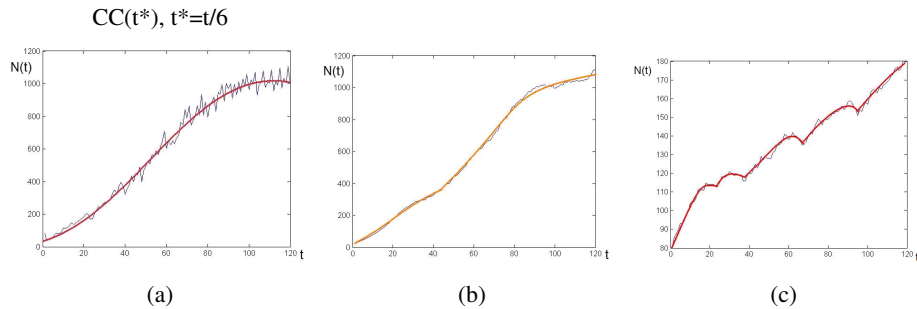


Fig. 3: Dependence CC number $N(t)$ on time (less amount of the resource (a), enough amount of the resource with recruiting (b), enough amount of the resource without recruiting (c))

When resource is not enough the increase of tumor cells number is very fast and the tumor is heterogeneous, contain necrotic parts, rounded by necrotic tissue. Such solid tumor according with Emmanuel researches have logistical increase of number of tumor cells. In the result figure we can also see Logistical function.

If recruiting mechanism is not taken into account, the larger amount of the resource we take the slower growth of tumor we get, but the tumor in the case of enough amount of the resource is homogeneous. Such tumor grows step by step with stationary periods. It is also according with scientific resource.

If recruiting mechanism is taken into account, the tumor grows faster then in the case of not enough resource but it is homogeneous and rounded by normal cells.

4.2 Tumor grouse dependence on the resource, endogenous and exogenous factors

The result of modeling is represented on the Fig.4. According the result the bound resource concentration is equal to stock factor 1.6.

On Fig.5 results of immune reaction and chemotherapy treatment are represented. The immune reaction is slowing tumor grows in the stage of local tumor, but such mechanism of immune reaction is not effective in the case of solid tumor. Chemotherapy influence leads to tumor apoptosis. Using chemotherapy with immune reaction lead to slow tumor grows after chemotherapy apoptosis.

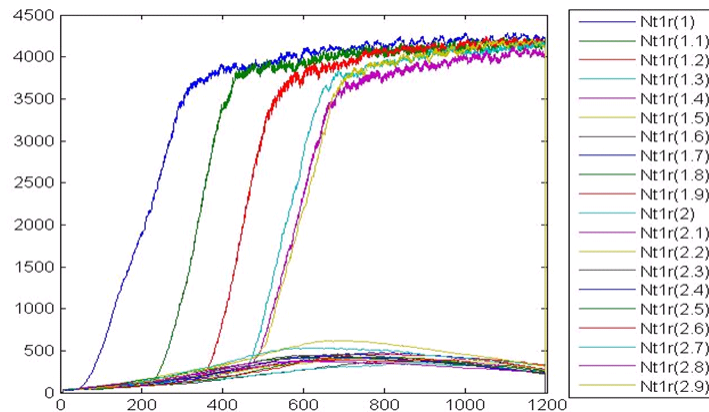


Fig. 4: Tumor grouse dependence on the resource (without recruiting).

5 Possible model improvement

- Taking into account several resources types;
- Considering more complex forms of cells and cells area;
- Taking into account another mechanism of immune reaction;
- Taking into account time dependent cell parameters;
- Taking into account causes of CC appearances and mutation;
- Model parameters identification;
- Changing biological underground of cells automata cell.

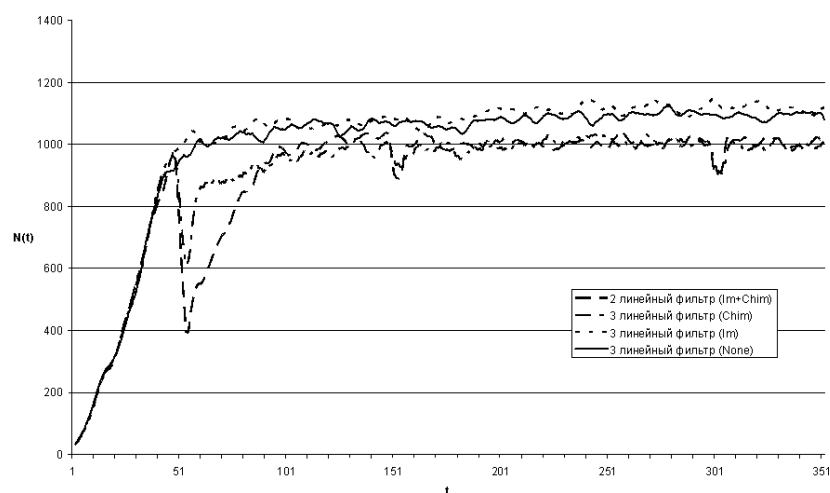


Fig. 5: Fig.5 Tumor grows dependence on immune reaction and chemotherapy ("None" – regular tumor growth, "Im"- immune reaction, "Chim"- chemotherapy).

6 Conclusions

Computer modeling using cellular automata conception is in general qualitatively agreement with medical verbal description and allows one to develop and test hypotheses which can lead to a better understanding of this destructive biological process.

Modeling cancer growth and tumor reaction on different influence can help one to make more effective complicated individual treatment plan for the patient that accounts for the disease and the patients' health.

References

1. L.V. BELOUSSOV* and V. I. GRABOVSKY: "A common biomechanical model for the formation of stationary cell domains and propagating waves in the developing organisms".- Computer Methods in Biomechanics and Biomedical Engineering, Vol. 8, 6, December 2005;
2. T. J. Newman "Modeling multi-cellular systems using sub-cellular elements".- arXiv:q-bio.QM/0504028 v1 20 Apr 2005;
3. J.D. Murray "Mathematical biology. I. An introduction", 3rd ed/ p. cm.— (Interdisciplinary applied mathematics) Rev. ed. of: Mathematical biology. 2nd ed. c1993 Includes bibliographical references;
4. J. J. Westman, B. R. Fabijonas, D. L. Kern, F. B. Hanson "Cancer Treatment Using Multiple Chemotherapeutic Agents Subject to Drug Resistance" Math. Biosci. (submitted 2001);
5. N.M. Emanuel, "Kinetics of experimental tumor processes", Moscow: Nauka (1977) (in Russian).
6. Yu.A. Ershov, V.V. Kotin. "Mathematical models of tumor processes and strategies of chemotherapy", Chemical and Biochemical kinetics. New horizons, Volume 1, Chemical kinetics (Ed. by E.B. Burlakova, A.E. Shilov, S.D. Varfolomeev, G.E. Zaikov), Brill Academic Publishers, Leiden-Boston, p.p. 302-321.

7. Yu.A. Ershov, V.V. Kotin. "Mathematical models of tumor processes and strategies of chemotherapy", Chemical and Biochemical physics: new frontiers, (Ed. By G. E. Zaikov) Nova Science Publishers, New York, 2006, p.p. 87-111;
8. Yu.A. Ershov, V.V. Kotin, S.K. Kirilova, R.K.Kabisov. "Cancer diseases revealing on the basis of tumor growth kinetic analysis and increase of efficiency", Biomedical Radioelectronics, 10, 2005(in Russian);
9. S. Y. Berkovich "cellular automation as a model of reality: search for new representations of physical and informational processes".- Moscow: MSU 1993 (in Russian);
10. T. Toffoli, N. Margolus "A cellular automata mashine"- Moscow: MIR, 1991 (in Russian);
11. V.V.Smolianinov "Mathematical models of biological tissues".- Moscow, Nauka, 1980 (in Russian).

Numerical Method to Solve Inverse Problem for Horizontally Layered Model of Precardiac Tissues

Alexander V. Kobelev¹, Sergey I. Schookin¹, and Igor K. Sergeev¹

Department of Biomedical Techniques, Bauman Moscow State Technical University, Moscow, Russia

Abstract. The goal of our project is the development of the mobile system for monitoring of a number of cardiac parameters by means of pre-cardiac tetrapolar rheocardiography measurements. We have developed algorithm to solve inverse problem for horizontally layered model of precardiac tissues and now we might be able to find conductivities and heights for each model's layer.

Index Terms – rheocardiography, inverse problem, precardiac tissues

1 Introduction

Non-invasive rheocardiography methods and techniques for monitoring of cardiac parameters are crucially important for patients with chronic diseases, especially having high risk of severe consequences like myocardial infarction or stroke. The goal of our project is the development of the mobile system for monitoring of a number of cardiac parameters by means of pre-cardiac tetrapolar rheocardiography measurements. Therefore we should solve the inverse problem for model of precardiac tissues in order to determine the corresponding layer's conductivities and heights.

2 Method

The inverse problem consists of using the actual result of pre-cardiac tetrapolar rheocardiography measurements to infer the values of the parameters that characterize the system. We represented precardiac tissues as horizontally layered structure having two or three layers. Among them are: skin and upper soft tissues (the first layer), myocardium (the second layer) and blood in ventricle of heart (the third layer). Each layer except the third has corresponding conductivity and height needs to find out. For the last layer we should determine only conductivity which gives information about hematocrit volume. In several cases two lower layers were combined into one which results in significant simplification of the model.

The inverse problem has multiple solutions (in fact, an infinite number) [1]. Because of this, in the inverse problem, one needs to make explicit a priori information on the model parameters. One also needs to be careful in the representation of the data uncertainties [2]. For the a priori information we used the following parameters: upper soft tissues (the first layer) has height 40 – 100 mm and conductivity about 8 Om-m; myocardium (the second layer) has height 10 – 20 mm and conductivity about 5 Om-m; blood in ventricle of heart (the third layer) has conductivity about 1.0 Om-m.

It is impossible to solve inverse problem without forward one. Therefore we solved the forward problem provided by means of theoretical solution Laplace's equation [4] and numerical calculations using Finite Element Analysis [3]. Also, we determined contribution of different layers parameters into output signal. For example, lower layer don't make one's contribution to result signal if distance between current's electrodes is less than height to lower layer.

To solve the inverse problem we used the simplest way: iteration by model's parameters in a priori interval. Forward problem was solved for each set of parameters and then result was compared with input signal by means of least-squares method. Minimum of this functional gives solution for model's parameters needs to find out.

3 Conclusion

We developed algorithm to solve inverse problem and now we might be able to find conductivities and heights for each model's layer. In future this approach allows determining cardiac parameters (e.g. stroke volume) in real-time mode.

References

1. Tikhonov A.N., Samarskiy A.A. **Equations of mathematical physics**. - High School, 1994. - 467.
2. Tarantola, Albert. **Inverse problem theory and methods for model parameter estimation**. QA371.T357 2005 515.357—dc22
3. Release 10.0 Documentation for ANSYS. Operations Guide.
4. Feynman D.: Feynman Lectures On Physics, Vol. 5 – Editorial, 2004. – 304.

Implementation of Adaptive Filters for Biomedical Applications

Jennifer Baraniak¹, Johann Hauer², Norbert Schuhmann², and
Günter Leugering¹

¹ Institut für Angewandte Mathematik 2, Friedrich Alexander Universität Erlangen-Nürnberg,
Germany,

² Fraunhofer Institut für Integrierte Schaltungen, Erlangen, Germany

Abstract. In biomedical signal acquisition like electrocardiography ECG or electroencephalography EEC one of the main problems is to separate the small input signals from noise and disturbances caused by the 50 Hz power supplies, high frequency interference and random body voltages. Different types of analogue and digital filters are used to remove the unwanted spectral parts. In most applications the filter bandwidth of those filters are fixed and will not adapt to changing interference patterns.

Adaptive filter techniques are required to overcome this problem. Different adaptive filter types have been analyzed. Finite Impulse Response (FIR) filters are preferred because of their better stability. An adaptive filter was implemented which suppresses known noise sources in an ECG application. Simulations were done with MATLAB and VHDL. The filter was coded in VHDL and tested on a FPGA.

A 50 Hz interference on the ECG input signal was attenuated by 50 dB. The convergence time for the adaptive algorithm was less than 3 sec. The filter implementation needed 9500 equivalent gates and worked with $7.1 \mu W$ for a filter clock speed of 1.8 kHz.

1 Introduction

In many applications for biomedical signal-processing the information-bearing signals are superposed by further components. Thus signals get distorted and the extraction of information is complicated. In electrocardiography interferences may have a technical source, for example a power supply unit, or a biological source, for example respiration. Commonly frequency-selective filters with fixed coefficients are used to suppress a specific frequency range of a signal. If the frequency spectrum of signal and interference overlap or the characteristic of the interference is time dependent or not exactly known, filters with fixed coefficients can hardly meet the demands. Often the filter's transfer behavior can't be specified sufficiently exact or those spectrals of the ECG which fall in the filter's cut-off region get lost [1], [2].

These difficulties can be handled using an adaptive filter, a system with variable instead of fixed coefficients. This is a time-variant systems which is able to adapt its coefficients to the environment during operation. In contrast to frequency-selective filters adaptive systems enable direct gripping of the eliminated signal. If it is not exclusively an unwanted signal, the included information can be processed where required.

The 50 Hz power line hum resulting from power supply units is commonly eliminated from the ECG by using notchfilters. In this paper an alternative in the form of an adaptive filter is presented.

2 Methods

The concept of interference cancellation with adaptive filters is shown in Fig. 1. Starting point is a mixture of signals $d[n]$ consisting of the information-bearing ECG signal $ekg[n]$ and an interfering component $noise[n]$. Having a reference signal which is correlated with $noise[n]$ and uncorrelated with $ekg[n]$, it is possible to eliminate the interference using an adaptive filter. In order to suppress the 50 Hz power line hum, the reference signal $x[n]$ is gripped at the power supply. It has the same frequency, but different amplitude and phase compared to $noise[n]$. Unlike using frequency-selective filters the adaptive filter is applied to $x[n]$ instead of the primary input $d[n]$. The filter output $y[n]$ is an estimate of $noise[n]$. Subtracting this from the underlying signal $d[n]$ we get the deamed signal $e[n]$, an estimate of $ekg[n]$.

Adaptive filters are preferably designed as FIR filters known for their good stability properties and simple cost function.

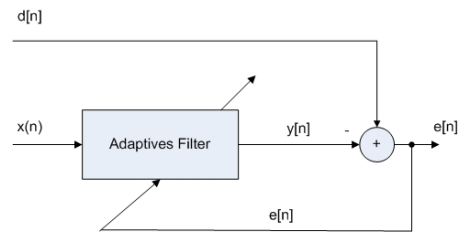


Fig. 1: Concept of interference cancellation

In order to minimize the power of $e[n]$ different cost functions as functions of the filter coefficients are possible. One is the MSE³-criterion that leads to the following optimization problem:

$$J = E\{e^2[n]\} = (d[n] - y[n])^2 \rightarrow \min .$$

For a filter with filter order N this results in a quadratic cost-function with a global minimum. R is the autocorrelation matrix according to $x[n]$ and p is the crosscorrelation-

³ Minimum square error

vector between $x[n]$ and $d[n]$.

$$J = E\{e^2[n]\} = E\{d^2[n]\} - 2w^T p + w^T R w .$$

with

$$w = (w_0, w_1, \dots, w_{N-1})^T: \text{filtercoefficients}$$

There are several algorithms to solve the minimization problem. Due to the simple implementation the LMS⁴-algorithm was considered. It is derived from the gradient-method by using stochastic instead of exact gradients.

For each iteration step the filtercoefficients for the next step $w(n+1)$ are computed the following:

$$w(n+1) = w(n) + \mu e[n]x(n) .$$

In order to guarantee convergence for the LMS-algorithm, μ has to be adapted to the maximal amplitude of the reference signal ($ma(x)$). An upper bound can be defined:

$$\mu_{max} = \frac{2}{3N \cdot ma(x)^2} .$$

The LMS-algorithm does not converge to the exact solution but to a sufficient good approximation. As a measure for the deviation between approximation and exact solution the so called misadjustment M is introduced. It depends on the average power of the reference signal ($power(x)$) and the stepsize μ . In order to achieve a small misadjustment a small stepsize is required.

$$M = \frac{\mu}{2} \cdot N \cdot power(x) .$$

But a small stepsize leads to a large convergence time. The convergence time τ can be expressed like the following where α is the applied stepsize normalized to the maximum possible μ_{max} . λ_{max} is the largest, λ_{min} the smallest eigenvalue of R .

$$\tau \approx \frac{1}{4\alpha} \kappa(R) .$$

with

$$\kappa(R) = \frac{\lambda_{max}}{\lambda_{min}} \quad \text{conditon number}$$

So the speed of convergence also depends on the condition number of R and therefore on the character of the reference input $x[n]$. The LMS-algorithm shows slow convergence for signals with non-smooth and fast convergence for signals with uniformly distributed spectrum.

⁴ Least Mean Square

Among suiting the parameters N and μ to the problem, several optimization strategies can be applied in order to improve the behaviour of the LMS-algorithm. Different strategies lead to different filter types. Normalization of the stepsize μ according to signal power in each step or reducing $\kappa(R)$ via orthogonal transforms are just a selection of possibilities. Above all the hardware complexity has to be considered.

The 50 Hz power line interference noise(t) only has a frequency component at 50 Hz and is assumed to be a sine. It can be expressed as follows:

$$\begin{aligned} \text{noise}(t) &= a_n \sin(\omega t + \varphi) \\ &= a_n (\sin(\omega t) \cos(\varphi) + \cos(\omega t) \sin(\varphi)) \\ &= a_n \cos(\varphi) \cdot \sin(\omega t) + a_n \sin(\varphi) \cdot \sin(\omega t + \Delta) \\ &= w_0 \sin(\omega t) + w_1 \sin(\omega t + \Delta) \end{aligned}$$

According to this the filter order has been set to $N = 2$. Because of the small filter order the LMS-filter was designed without one of the mentioned optimization strategies. Both for $d[n]$ and the outputs $y[n]$ and $e[n]$ a 16-bit-representation is used, whereas for $x[n]$ a 8-bit-representation is required.

First simulations of the filter behaviour were done with MATLAB. At this stage the influence of μ on the signal quality of $e[n]$ and $y[n]$ was established. After choosing μ the filter was coded in VHDL and simulated with Modelsim on different levels of abstraction. To monitor quantisation effects the MATLAB-filter was used as a reference-model for the VHDL-models in each level. Using a simulation environment developed for this application, both models were simulated parallel and results were compared. Finally the filter was tested on a FPGA with ECG signals.

3 Results

The ECG of an healthy adult has a fundamental frequency from about 60 bpm⁵ up to 80 bpm. For certain disease patterns fundamental frequencies down to 20 bpm occur. At physical stress frequencies up to 200 bpm are observed [4]. The adaptive filter was tested for ECG signals with different fundamental frequencies. For frequencies up to 160 bpm good results were achieved, whereas the signal quality is downgrading for higher frequencies. Furthermore the filter was applied to ECGs with a power line interference of different frequencies. For interfering frequencies from 30 Hz to 100 Hz the filter turned out to be well suitable. The influence of the amplitude of the superposed signal was also studied. Interfering components with amplitudes from 0,05% to 100% relating to the maximum ECG amplitude can be extracted. Depending on the amplitude of the superposed signal, the interference was damped by 4 dB up to 50 dB. Convergence time of the adaptive algorithm is less than 3 sec.

For a VIRTEX E FPGA [3] from Xilinx the filter realisation needs 9500 equivalent gates and the calculated power loss is 7.1 μW . Using a sampling frequency of 256 Hz for the ECG the filter clock speed is 1.8 kHz.

⁵ beats per minute

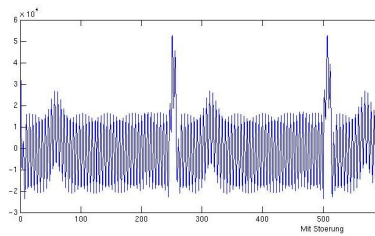


Fig. 2: ECG before filtering

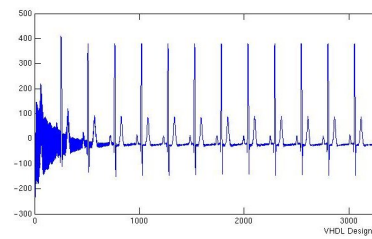


Fig. 3: ECG after filtering

4 Conclusions

Commonly notchfilters with fixed coefficients are used to suppress the 50Hz power-line interference in ECG signals. The alternative introduced in this paper has the advantage of better flexibility compared to frequency-selective filters. The disturbance is also eliminated if its frequency is shifted. One disadvantage of the developed adaptive filter are worse results with increasing ECG's fundamental frequency. The degradation of signal quality is noticeable from a fundamental frequency of 160 bpm. Before applying the designed adaptive filter to higher frequencies occurring in stress ECG the design would have to be adjusted. Furthermore unlike frequency-selective filters adaptive systems need a proper reference signal for the interference. But this also opens an interesting method to search for a known signal in distorted or superposed signals.

References

1. Baraniak, J.: Entwurf und Optimierung adaptiver Filter zur Trennung überlagerter Sensorsignale, Diplomarbeit. Friedrich-Alexander-Universität Erlangen-Nürnberg (2007)
2. Farhang-Boroujeny, B.: Adaptive Filters, Theory and Application. Wiley England: Wiley-Verlag (1998)
3. Meyer Bäse, U.: Digital Signal Processing with Field Programmable Gate Arrays. Berlin: Springer Verlag (2004)
4. So Dr. Cook-Sup: Praktische Elektrokardiographie. New York: Georg Thieme Verlag Stuttgart (1993)

Medical Communication and Sensor Systems

Application of the Radar Technology in Medicine for Remote Monitoring of Human's Breath and Pulse

A. Bugaev¹, V. Chapursky¹, S. Ivashov¹, V. Razevig¹, A. Sheyko¹, I. Vasilyev¹, and T. Bechtel²

¹ Remote Sensing Laboratory, Research Institute of Applied Mathematics and Mechanics, Bauman Moscow State Technical University

² University of Pennsylvania, PA, USA

Abstract. The main objective of the project is creation of effective radar technologies for remote detection and registration of breathing and heart beat parameters of a human on a background of reflections by local objects and optically nontransparent obstacles. The advantage of bio-radiolocation is the possibility to detect remotely any presence of humans behind lightproof obstacles and obtain information about human functional condition. Search for live people blocked under ruins, after disasters such like earthquakes, avalanches, industrial accidents, etc., is very important.

Keywords: Bio-radiolocation, Heart beat, Breathing, Radar.

Nowadays there is a keen interest in using radiolocation devices in monitoring and diagnostics of living subjects, especially humans, in different conditions. Partly, such an interest results from the availability of cheaper and smaller radar constituents, computational resources opening the way to more complex signal processing also become available.

The detection and diagnostics of humans, even behind lightproof obstacles, by means of radar could be named as bio-radiolocation. This technique rests on the modulation of a reflected radio signal caused by the human skin and internal organs movements when breathing and heartbeat are present, or when different movements of organs and parts of the body happen. Thus, the modulation is caused by:

- cardiac beat (frequency band between 0.8 and 2.5 Hz, the chest movement amplitude is 2-3 mm);
- movements of the thorax when breathing (frequency band between 0.2 and 0.5 Hz, the chest movement amplitude, depending on the type of breathing, ranges between 0.5 and 1.5 cm);
- articulation, or vocal apparatus movements (the leaps, tongue, larynx);
- movements of other parts of the body.

Potential areas of bio-radiolocation application in medicine may include:

- somnology, or patient monitoring at sleep with the purpose to detect sleep disfunctions such as sleep apnea/hypopnea syndrome;
- cardioreanimation when application of contact sensors is difficult or impossible;

- functional diagnostics, the implementation as a diagnostic feedback with the purpose to evaluate therapy effectiveness (by medicine or physiotherapy) by the analysis of heart rate slow variations; study of heartbeat and breath rhythms interaction;
- patient's heart rate and breathing monitoring when application of contact sensors is difficult or impossible, e.g. monitoring of a patient with burns.
- fetus monitoring instead of application of existing contact ultrasound sensors requiring a direct contact with a patient;
- evaluation of blood vessels elasticity by measuring blood pressure impulse speed during heartbeat, which can be used to determine susceptibility to heart diseases;
- non-contact evaluation of the psycho-emotional human condition, e.g. the emotional condition of machinery complex operators.

In some of the application areas mentioned above, especially when detecting movements of human behind building constructions, there already exist experimental radiolocation devices or prototypes. However, medical applications lack for research and improvement, which can be associated with the absence or imperfection of application technique with the aid of bio-radiolocation equipment.

The existing prototypes and models of radars implement both continuous-wave [1] and video pulse (time-domain impulse) [3, 4] signals differing significantly in design complexity. The simplest of them have an LED diode as an indicator and no range selection, while others may have a color LCD display and high range resolution. The radars with continuous-wave single-frequency signals have the simplest signal processing such as detection of reflected signal low frequency components by means of the Fourier transform and have no range resolution. The radars with video pulse signals may have range resolution but have a short detection range. It is worth mentioning that no one device have found any significant area of use. This can be explained by small equipment sensitivity when sensing through obstacles, e.g. detection of people buried alive under ruins after disaster, low noise immunity, and the absence of angular selection.

The possibility of remote detection and diagnostics of the human with his breath and heartbeat frequencies and amplitudes observations was confirmed during these experiments. A sketch of the experiment presents in Fig. 1.

The width of the wall that the probationer was behind was about 10 cm. The probationer himself was at a distance of 1.5 m from the wall. The radar antenna was placed immediately on the wall. Technical specifications of the radar were as follows:

- Operating frequency 1.6 GHz (wavelength of 19 cm)
- Antenna gain 40 dB
- Detected signal bandwidth 0.03 – 3 Hz
- Detected signal dynamic range 60 dB
- Sampling frequency 20 Hz
- Antenna dimensions:
 - Diameter 120 mm
 - Height 200 mm

The choice of the radar operating frequency was caused by the requirement to probe through a wall. In spite the fact that the implementation of higher frequencies could be

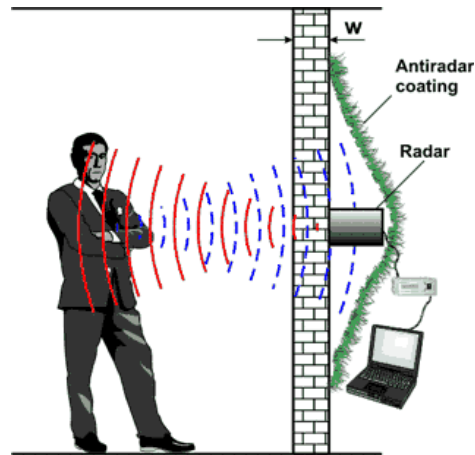


Fig. 1: Experiment sketch.

more advantageous in detection and diagnosis of heartbeat, this bandwidth has intensive attenuation in building materials, especially when they are wet, and can not be implemented practically. When working on frequencies less than 1 GHz, the wavelength becomes greater than the size of a sounding object, which causes the magnitude of useful signal to drop.

Some results of the experiments registering breathing, heartbeat, and articulation are presented in Fig. 2 – 4. In normal condition, the probationer's heartbeat rate was 65 beats per second. As movement amplitude and the volume of lungs are much bigger than that of heart, heart muscle contractions look like high frequency modulation on the background of greater thorax movement as seen in Fig. 2. Fig. 3 presents the heartbeat record when the probationer stopped breathing. Fig. 4 presents the probationer's articulation when he spoke words - one, two, three ... (in Russian).

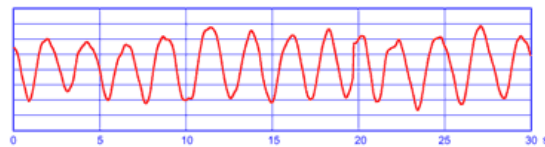


Fig. 2: Oscillogram of radio signals reflected by normally breathing human.

Following Fig. 5 and Fig. 6 depict spectra of the signals obtained from heart muscle contractions when breathing had been held for 30 and 60 seconds correspondingly. It can be noticed that holding breath for a longer period causes both heartbeat frequency and heart muscle contraction amplitude to increase due to oxygen starvation. Thus, holding breath for 30 seconds resulted in 77 beats per minute, while a pause of 1 minute

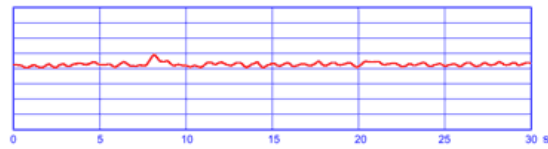


Fig. 3: Oscillogram of radio signals representing the probationer's heartbeat when he stopped breathing.

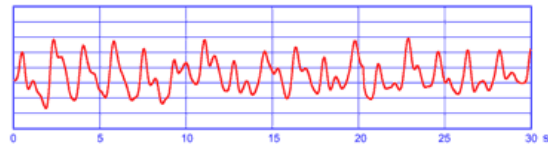


Fig. 4: Oscillogram of radio signals taken when the probationer was speaking.

caused the heartbeat to increase to 92 beats per minute. This fact is well known in medicine and it is used to determine subject's tolerance to hypoxia (Stange's test and Hench's test). This example shows that radar measurements at least in some cases can be used for remote diagnosis of functional condition of individual's organism.

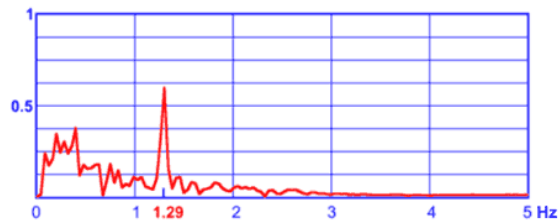


Fig. 5: Spectrum of a heart beat signal when breathing was held for 30 seconds.

The main stress in the research is laid on the development of a distributed antenna system and more sophisticated signal processing, which, as researchers believe, will make it possible to obtain the disposition of people in a sounding area, extract information from biological objects themselves, e.g. obtain information depicting their disposition and working condition of their organs. Proposed in the project deployment of multi-frequency sounding signals in spatially distributed radar antenna will merge the advantages of time-domain and continuous signals to produce a system with better performance [2]. Such a system must have a larger detection range, spatial selection capability, possibility to overview the sounding space to the stage of extracting breathing and heartbeat waveforms as well as articulation features.

Fulfilment of the researches will allow to pass to practical use of the given technology in various medical applications. In particular, now in frame of the National

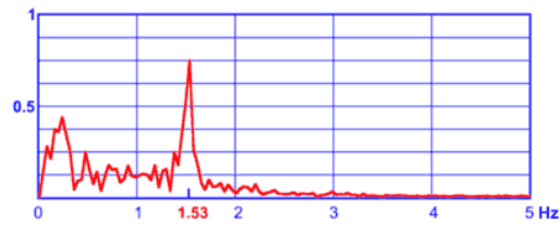


Fig. 6: Spectrum of a heart beat signal when breathing was held for 60 seconds.

Project "Education" in cooperation with the Faculty "Biomedical Engineering" of Bauman University the educational stand on remote measurement of parameters of human pulse and breath is created, Fig. 7.

Conclusion

At development of bases of remote detection and diagnostics of the person in the previous research works, the opportunity of definition of frequency and amplitude of breath and palpitation in radar system with a continuous monochromatic signal has been experimentally confirmed. Also mathematical modeling of these processes for multi-frequency mode has been performed. In particular, it has been shown, that at a detected radar-tracking signal can be present not only main tone of breath and palpitation, but also their combinational frequencies.

Acknowledgment

The research is carried out under support of Russian National Project "Education" and Scientific Program "Development of Scientific Potential of the Higher School".

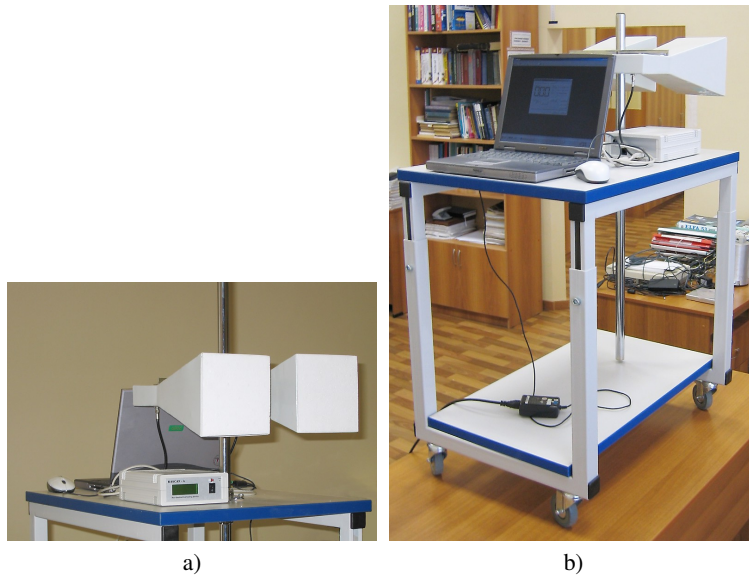


Fig.7: Views of radar that is designed in frame of National Project “Education”

References

1. Ivashov S.I., Razevig V.V., Sheyko A.P., Vasiliev I.A. Detection of Human Breathing and Heartbeat by Remote Radar. Proceedings of the Progress in Electromagnetics Research Symposium, PIERS 2004, Pisa, Italy, 28-31 March 2004, pp. 663-666.
2. Bugaev A.S., Chapursky V.V., Ivashov S.I. Mathematical Simulation of Remote Detection of Human Breathing and Heartbeat by Multifrequency Radar on the Background of Local Objects Reflections. 2005 IEEE International Radar Conference Record. 7-12 of May 2005. Alexandria, Virginia, USA.
3. Staderini E.M. UWB Radars in Medicine. IEEE Aerospace and Electronic Systems Magazine, January 2002, pp. 13-18.
4. Immoreev I., Samkov S., Teh-Ho Tao. Short – Distance Ultrawideband Radars. Theory and Designing. IEEE Aerospace and Electronic Systems Magazine. v.20, No. 6, 2005, pp 9-14.

Generic Medical Data Persistence with the VITAL Framework

Matthias Struck¹, Svetoslav Pramatarov², and Christian Weigand¹

¹ Fraunhofer Institute for Integrated Circuits (IIS)
Am Wolfsmantel 33, 91058 Erlangen, Germany
matthias.struck@iis.fraunhofer.de

² Lehrstuhl für Medizinische Informatik
Krankenhausstraße 12, 91054 Erlangen, Germany

Abstract. The progress of information technology has become irreplaceable in the field of medical applications in the past few years. In both the intensive clinical and home care region wireless communication between medical devices acquiring physiological parameters allows convenient monitoring of vital signs. In order to guarantee readability of patient related medical data information by several institutions in the future, standardized and efficient storing methods are indispensable. That is why a new user interface within our Vital framework was created. This interface permits real-time persistence of all the data acquired in the medical work flow. Based on our design and implementation we evaluated different file formats such as the *European Data Format* (EDF), the *File Exchange Format* (FEF) and the *Standardized Communication of Information in Physician Offices and Hospitals using XML* format. We will present and discuss the main results.

1 Introduction

The trend of medical devices acquiring, processing and visualizing vital signs in real-time is from the isolated stand-alone ones toward a network of connected medical devices. The integration of such a network into a hospital information system provides the medical data information to be accessed by several physicians at different places and at different times. Essential requirements to integrate medical devices of different manufacturers in those networks are standardized data representation and well-defined communication protocols. Standardized communication is afforded, for example, by the CEN ENV13734/35 standard for Vital Signs Information Representation (VITAL)[3]. Nevertheless, at the current state-of-the-art, there is no interface for data persistence of medical parameters represented by VITAL objects. But standardized data persistence is required in order to guarantee readability and exchange of medical data by hospitals respectively between medical institutions in the future.

2 The Vital Framework

The purpose of the CEN ENV13734/35 standard for Vital Signs Information Representation (VITAL) is to define an object oriented model of medical devices and vital

parameters that are identified by a unique nomenclature [2]. Furthermore, it specifies a communication model consisting of protocols and services based on the ISO/OSI standard. The implementation of this standard results in a VITAL library. This library is embedded into a generic framework. It defines interfaces for the integration of different medical devices, communication protocols, graphical user interfaces, annotation and signal processing units (see figure 1). Those modules are implemented and integrated into the framework as plug-ins.

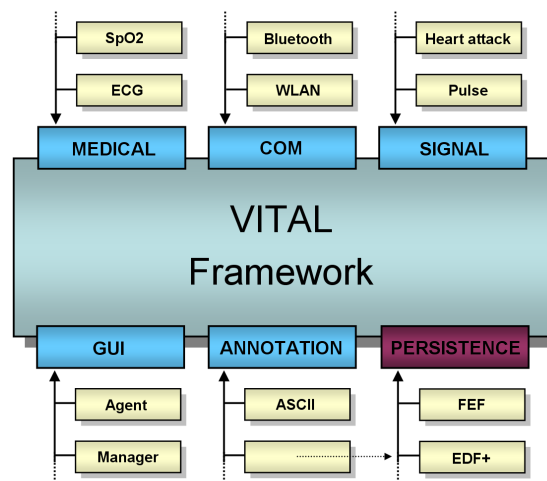


Fig. 1: Interfaces of the Vital Framework

Some examples for medical devices are an electrocardiogram (ECG), plethysmographies and temperature sensors. Bluetooth, WLAN, IrDA etc. are possible communication protocols. Signal processing plug-ins analyzing physiologic parameters of patients support physicians in their diagnosis. The automatic detection of cardiac infarctions is a typical example. Individual graphical user interfaces can be realized to visualize vital signs. A vital agent is the system directly connected to the medical device and a vital monitor is typically running on a standard PC or PDA (see figure 2). Annotation plug-ins give physicians the opportunity to save certain events, for example, the injection of a medicament while operating a patient.

3 Persistence Interface

3.1 Requirements

There are many essential aspects dealing with an interface for data persistence. It has to define general methods that only describe their achievement. The functionality has



Fig. 2: Communication between a vital agent and two vital monitors

to be implemented as plug-ins. In addition, file formats have to be independent of specific hardware technologies. Therefore, the interface incorporates with the byte order problem. Furthermore, the file formats have to allow fast access to all important data and they should contain as less redundancy as possible. Another aspect is the degree of information loss after a system crash. That is why the vital signs must be written on the storage medium continuously.

3.2 Realization

In order to satisfy all those claims, we divided the persistence interface into three methods that have to be implemented for each plug-in describing a specific file format: The first method stores the patient demographic data that are entered by an user dialog. The second method determines the vital object hierarchy. This is important for the organization of the file structure. At last the third method is called whenever the intern buffers containing the acquired medical data are full. Consequently, visualizing and storing are done in parallel.

4 Basics of the ASN.1

The Abstract Syntax Notation One allows the description of data structure rules that are independent of particular programming languages. After specifying data structures, an ASN.1 compiler generates source code, for example in C/C++, containing the data types of the data structures. In addition, the source code provides methods that can serialize respectively deserialize data structures. With the help of those methods data structures can be easily written to hard disc or transferred over a network. Lots of data encodings have been developed for ASN.1. After showing an example how an easy data structure in ASN.1 specification is transformed to C++ code, we will concentrate on BER (Basic Encoding Rules) and XER (XML Encoding Rules):

```
Data_Structure ::= SEQUENCE          typedef struct Data_Structure
```

```

{
    int_value_1 INTEGER,
    int_value_2 INTEGER OPTIONAL
}
{
    int int_value_1;
    int* int_value_2;
} Data_Structure_t;

```

5 Evaluation of file formats

Concentrating on the choice of specific file formats, there are additionally requirements such as their degree of deployment in the clinical routine and the quality of tools visualizing medical data information. To give a conclusion about the suitability of different formats, the following data file formats have been evaluated: EDF, EDF+, FEF and SCIPHOX. The European Data Format (EDF) is a simple format for storing multi channel bio-signals. The main advantages of EDF are its high distribution in hospitals and the existence of many non-commercial viewing tools. An extension of EDF is EDF+. In contrast to the first version, EDF+ can deal with interrupted signals. Beyond this, one of the EDF+ channels can be encoded to store medical alerts, for example, the battery status or annotations made by the physician. The File Exchange Format (FEF) is more universal than EDF/EDF+. It is based on the VITAL CEN ENV13734/35 and has become an own standard with the CEN/TS 14271. It uses the same nomenclature and Domain Information Model (DIM) [3] as the VITAL standard. Consequently, persistence with FEF is free of information loss in the sense of VITAL. Furthermore, the FEF standard defines a multimedia section that contains multimedia data such as patient images and audio/video data. In contrast to the file formats discussed so far, SCIPHOX is no binary file, but is based on the XML syntax. Because of the high redundancy resulting from the encoding of numerical data, it concentrates on demographic and administrative data. Nevertheless, an advantage of SCIPHOX is the possibility interpreting the content by arbitrary XML parsers. It was basically specified for the communication and data exchange between practising physicians and hospitals.

6 Summary and Discussion

We presented a generic interface for medical data persistence that was integrated into the VITAL framework. Different file formats storing medical information can be realized as plug-ins. The design of the interface assures a minimum of information loss having a hardware or software crash. Different file standards have been evaluated. They can be implemented respectively generated using an ASN.1 compiler. FEF has the advantage storing the full information represented by the vital objects. It can be realized in both, binary and in XML syntax. In contrast to FEF the EDF has the benefit being almost a standard in medical institutions. Due to the fact that FEF is the most universal format, which is completely consistent to the VITAL standard, the persistence of medical data with the File Exchange Format is an adequate solution. Unfortunately, the FEF standard was first published after lots of "isolated applications" have already been introduced into the clinical routine. Consequently, it is of limited practical use up to now. In order to guarantee both the full information acquisition of the VITAL standard and also its immediate practical usage it is meaningful to store the data in FEF format and also provide a tool that can convert FEF to EDF/EDF+ file format. Therewith full information persistence as well as the consistence with existing clinical applications can be achieved.

References

1. Walkin, L.: Open Source ASN.1 compiler. Webdocument <http://lionet.info/asn1c>

2. Weigand, C.: VITAL - Use and Implementation of a Medical Communication Standard in Practice. *IEEE Computers in Cardiology* 2005; pp. 319-322
3. Zywiets, C.: Standardized Representation of Vital Signs for Continuous Care in Cardiology. *IEEE Computers in Cardiology* 1998; pp. 205-208

A Fall Detection System Based On A Wireless Zigbee Sensor Network

C. Hofmann¹ and S. Feilner¹

Fraunhofer Institute for Integrated Circuits, Germany,
christian.hofmann@iis.fraunhofer.de, feilnesn@iis.fraunhofer.de

Abstract. A sensor system for fall detection was subject of a research project at Fraunhofer Institute for Integrated Circuits. Starting with position analysis based on measured sensor data (3 axis acceleration sensor), various movement patterns had been tracked and analyzed (walking, climbing stairs, fall) with to develop simple and efficient algorithms in time domain. These algorithms had to be designed for microcontroller capabilities to create a tiny, low power and intelligent sensor unit. Data acquisition, signal processing and wireless communication is all done by a single microcontroller inside ZigBee communication module.

1 Introduction

The situation for elder people has changed in many varieties in our times. While earlier several generations lived together in one house – grandparents, parents and children – and took care of each other, this former kind of common living today has nearly completely disappeared. Not only in big cities, even in rural regions most grandparents and parents live separately. Along with these sociological changes the demographic progression in our society aggravates the situation when special care is needed. With most parents being both employed, there is a huge problem of child-care, so who has the time to look for the grandparents?

More and more seniors are moving into elderly housings to spend their retirement. The atmosphere is familiar and a special daily schedule fits the seniors' needs. But even here the mentoring is limited. Nurses have many tasks to do all over the day, so part of the day the elderly are unattended.

If seniors in these unattended situations fall, they may be hurt and a person that directly could help is not present. Statistic analysis on falls in the Elderly show frightening results when looking to the high percentage of people not being able to stand up again without help. Also the quantity and the heaviness of injuries, mostly fractures of hip and tight, stress the need for immediate help when a senior fell down.

For these specific situations a helpful sensor system has been developed at Fraunhofer IIS (Institute for Integrated Circuits) that monitors persons' movements and detects possible falls. An alarm indication is automatically generated and sent to a nurse using wireless communication technology.

2 Methods

The movement signals are measured using a tiny MEMS acceleration sensor (Micro Electro Mechanical System). This sensor derives from a sleep analysis system. In that use case it is used to determine the current position of a patient (e.g. patient lying on belly or back, lying on left or

right side, number of turns per night).

In a first system concept all the raw data was sent to a PC using ZigBee radio technology. With a sampling frequency of 50 Hertz and a data resolution of 8 bit a data stream of 400 bit/s was generated for each channel, i.e. 1200bit/s for all three axes, which is equal to 150 bytes/s.

With the PC's powerful CPU and system resources the measurement data was processed and analyzed in several steps. Two main objectives had been pushed: an investigation on movement signals in general, but with a special focus on falls, and a stable algorithm for fall detects. Several measurement series have been accomplished and different algorithms have been tested.

Finally, the signal processing was implemented into for a microcontroller on the movement sensor. With this intelligent / smart sensor device only a single, coded byte is sent containing information about the patient's position and possible fall events. Using a predefined lookup table the receiving unit can decode this byte and either indicate visual information on a monitor in a nurse's station or even line up respective emergency procedures.

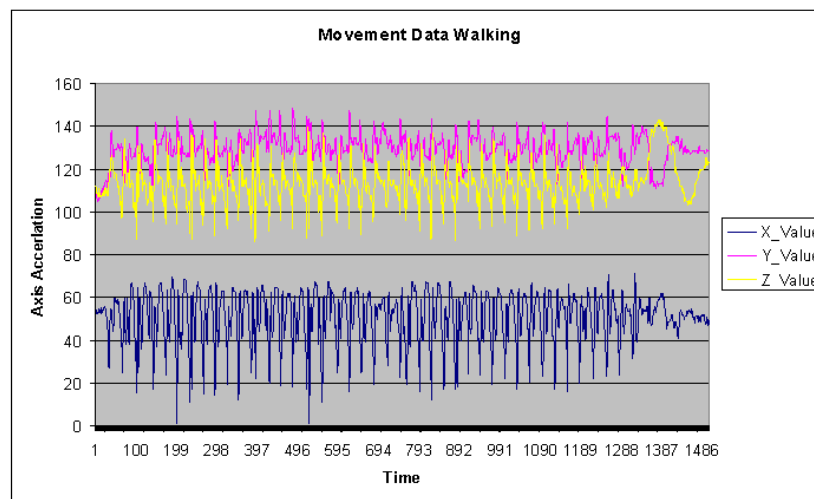


Fig. 1: Movement Data: Person walking

3 Technological Advantage

The usage of the radio technology ZigBee – a low power technology based on IEEE standard 802.15.4 and with specifications from the promoting industry consortium ZigBee-Alliance – enables a very low power system for three reasons:

- The technological concepts for channel access (CSMA-CA: Carrier Sense Multiple Access with Collision Avoidance) and spread spectrum (DSSS: Direct Sequence Spread Spectrum) cause a very low power consumption over the time. Unlike some other wireless technologies, the ZigBee RF circuitry – which has a current draw of approximately 27 mA when active – must only be activated for sensing the channel and sending the data. When no data is pending, the RF circuitry can remain in a power saving state. This is a big advantage compared

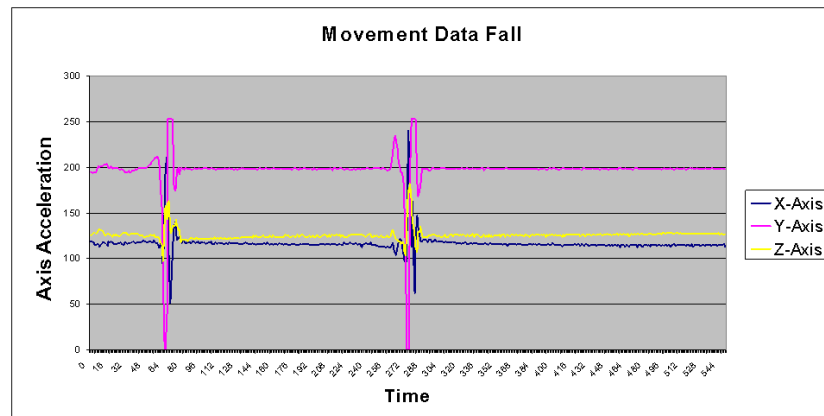


Fig. 2: Movement Data: Fall

to systems using Frequency Hopping Spread Spectrum (FHSS), which have to continuously participate in frequency hops and synchronization procedures and thus continuously consuming a higher level of energy.

- Due to the special design of the ZigBee protocol stack, a microcontroller inside a ZigBee module can perform two main objectives: realizing the communication with according to ZigBee protocol routines and driving one or even several user applications. In this way only one processing unit has to be placed on a sensor board lowering energy consumption, form factor and costs for components at the same time!

For this special project the user's movement data is processed directly on the sensor. The result coded into a single byte is sent to a receiver. Compared to the first system concept (with data rate of 150 bytes per second, see above) the data volume could be reduced to just a single byte. The less data is sent over the air, the more energy could be saved for longer operating time.

4 Further Improvements

Besides a ultra low power implementation of the sensor module another technological feature brings out the usability of the whole sensor system:

While most ZigBee applications currently are realized with microcontroller based modules (e.g. sending data from a stand alone sensor module to receiving module connected to a PC), a mobile system unit has been integrated at Fraunhofer IIS. Using a ZigBee SDIO card a portable PDA (Personal Digital Assistant) now is able to receive ZigBee data packages. With a special implementation of the protocol stack for operating systems in mobile devices (e.g. Pocket PC 2003, Windows Mobile 5.0) the user application on the PDA is able to extract data from received packages and process it according to the user's needs. This system enhancement now allows nurses, currently working in a patient's room, to be informed about a nurse call or emergency situation from other patients in other sections of the building.

5 Discussion and Conclusions

With the ZigBee technology basically aiming for large sensor networks in industrial environment the implementation of the Fall Detection System at Fraunhofer IIS proves this communication concept to be suitable also in medical applications. In this special case the Fall Detection System makes a great contribution to everyday's life of the Elderly in both, home area and residential homes. The low power features provide a long operating time with large area coverage and stable signal transmission, all at the same time.

Current and future research projects focus on larger sensor networks with a higher number of network nodes, deeper analysis of movement data (going, walking, steps) and the combination of several vital signs (such as heart rate and temperature) to suggest activity and effort.

References

1. M. Runge: Ein Sturz hat viele Väter. Mobiles LEBEN 1 (2002)

Multi-channel electrical impedance system: hardware, architecture, topology

I.K. Sergeev¹ and A.V. Kobelev¹

Department of Biomedical Techniques, Bauman Moscow State Technical University, Moscow, Russia

Abstract. In work the development of a multi-channel electrical impedance system is represented. The 32-channel rheographic system developed allows registration of the electrocardiogram and the transthoracic rheogram simultaneously with up to thirty precordial rheocardiograms. The system has a combined modular structure including 16 higher precision current sources and 32 impedances registration channels. Each from sixteen modules has the current generator and synchronous detector. Selection of useful signal to be made on each from 32 low-pass filters. For reduction of a stray capacity of cable systems length of cables precordial of channels makes no more than one meter. The most significant problem, however, is the relatively large capacitance of multiplexer devices. Typically the input capacitance is in range 30 – 50 pF. The important aspect of designing was the creation of the high-quality, precision input source differential amplifier working on frequency 100 kHz and common-mode rejection ratio (CMRR) not less than 80 dB.

Keywords: — Rheocardiography, impedance monitoring, multi-channel system.

1 Introduction

The modern period of medical instrument development is characterized by high interest to non-invasive technologies of diagnostics, thickening of signal analysis algorithms. The tendencies of medical instrument making development require of the medical equipment developers to create systems of flexibly configured and a modular type. Dignity of such systems is the unification of inter modular interaction, possibility of the extension and interchangeability.

2 Methods

2.1 Descriptive hardware

The realization of impedance techniques in modern means requires development of reliable automated systems in view of advanced reaching in the field of signal transformation and processing [1].

The effective solution of the delivered problem is possible only because of biotechnical systems (BTS) theories.

Basis of BTS theory is the principle of adequacies demanding harmonic operation of biological and technical elements in BTS uniform.

In a considered system the rheocardiography method is used. The impedance rheocardiography method is based on a passage high-frequency (40 – 100 kHz) current of small amplitude (1 - 5 mA) through the chest and registration of the dynamic changes in a tissue impedance caused by the blood circulation and breathing.

Such effect does not infringe conditions of normal operation of an organism, ensures adequate interaction of BTS main parts.

Distinctive feature represented BTS is the modular concept of construction of the hardware. 15 modules (30 channels) registration of impedance signals, 1 module registration of transthoracic impedance signals and ECG from a uniform electrode system enter into a structure of a system. Such structure allows to realize area precordial mapping of heart, observation behind transition of heart in dynamics, integrally to evaluate cardiovascular parameters of a cordial ejection on the base analyses of transthoracic impedance signal and analyses, to analyze a phase structure of cordial activity on binding to phases the ECG.

The analysis of existing modern micro systems has shown that the best performance for a solution of a problem has the microcontroller Texas Instruments MSP430F149. This microcontroller in the best way approaches for realization of impedance signals registration module. As it has small consumption of energy. The controller has an extended hardware rim with 8 channel 12^{th} digit, high-speed ADC (up to 200 ksps) and possibility of programming on the sequential interface. After digitization the signals previously packed by the microcontroller into appropriate packages arrive on the data bus. The protocol corresponds to the interface RS-485. The management on the data bus is made by the central microcontroller C8051F320. For maintenance of interface with computer the built-in receiver transmitter UART-USB is used. The interface has a high transfer rate of information, sufficient for organization of the multi-channel recording system.

The use of the standard universal asynchronous receiver transmitter UART, included in structure of microcontrollers architecture MSP430F149 and C8051F320 allows by an optimum method to connect them in a uniform network of a reception - transfer on the standard interface RS-485. The choice of the interface RS-485 allows flexibly to configure a system and to supplement it by necessary number of modules of registration. It is important for want of for debugging and monitoring of serviceability. The system has a possibility to disconnect and to connect modules without a modification of the modules microcontrollers program.

Especially it is necessary to pay attention to a principle of current generator construction with temporary separation of channels. In the block diagram of hardware maintenance the common current generator for each module of registration is realized for maintenance of stable work of all channels of registration of an impedance and decrease of mutual influence of channels. The decrease of outflow currents level of in source circuits of measuring channels is ensured due to galvanic isolation. The current generator is isolated by the transformer. The source cascades of impedance measuring channels are not switched and constantly are connected to the patient Fig. 1. [2]

2.2 Descriptive topology

Frequency digitization of each channel makes 500 Hz. Hence time of scanning of 32 channels makes 2 ms. Thus time of scanning of one channel makes $62.5 \mu s$, that at frequency of a probing current 100 kHz makes $6 \frac{1}{4}$ periods of a harmonious current. Severe constraints of registration of impedance signals and the requirement to accuracy of measurement of an impedance demand realization of precision schemes of detecting.

Time diagrams of work of channels are presented in Fig. 2. The 1-st and 2-nd channels are a part of the 1-st module of the device and are scanned by the same current generator. Synthesis of probing currents is made by formation of two meanders shifted on $1/6$ periods Fig. 3.

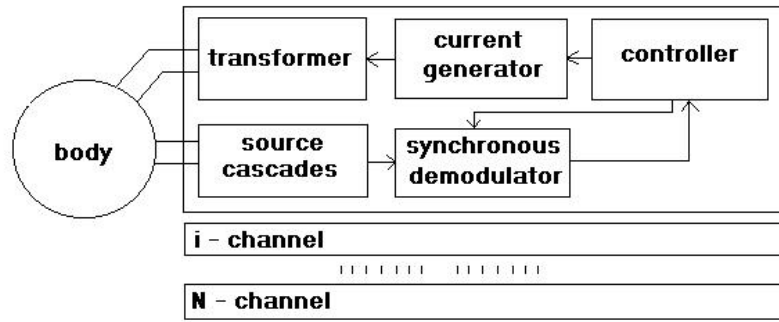


Fig. 1: The hybrid scheme of construction of the multi-channel recording impedance system

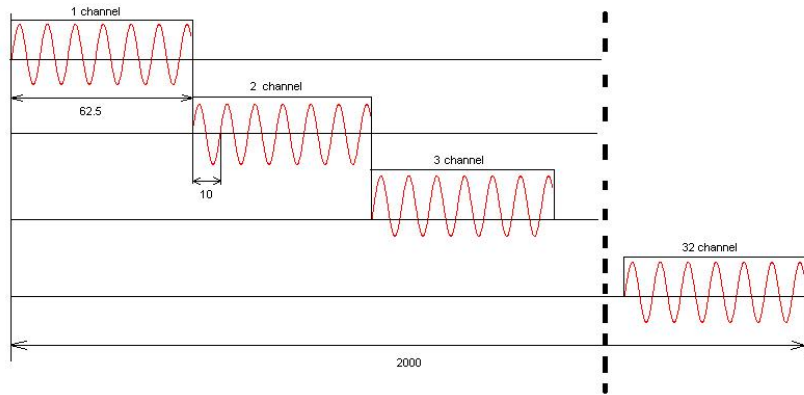


Fig. 2: Time diagrams of work of channels

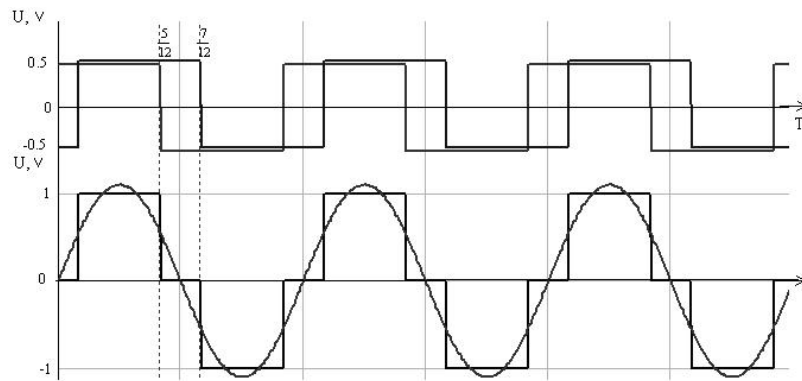


Fig. 3: Synthesis of probing currents

The given way of probing current formation allows synthesizing a harmonious signal with low Total Harmonic Distortion that is important for registration of an impedance signal. FFT three-level signal $U(t)$ allows to see, that the spectrum of this fluctuation does not contain even, and also 3 and to multiple it harmonics, besides, after the first harmonic the fifth follows, and its amplitude is already lowered five times.

$$U(t) = \frac{2 \cdot A \cdot \sqrt{3}}{\pi} \cdot \left[\cos\left(\frac{2 \cdot \pi}{T} t\right) - \frac{1}{5} \cos\left(\frac{5 \cdot 2 \cdot \pi}{T} t\right) + \frac{1}{7} \cos\left(\frac{7 \cdot 2 \cdot \pi}{T} t\right) - \frac{1}{11} \cos\left(\frac{11 \cdot 2 \cdot \pi}{T} t\right) + \frac{1}{13} \dots \right]$$

For reduction of influence of any origin additive noise it is useful to reduce area of entrance signal averaging, accumulating a signal on an exit of the synchronous detector in time when the probing current reaches an extreme.

Averaging of target signals of the synchronous detector on the period of the fifth harmonic completely weakens influence of this (and all multiple a heel) harmonics on a target signal, and a phase component of the fifth harmonic with basic fluctuation thus are insignificant Fig. 4.

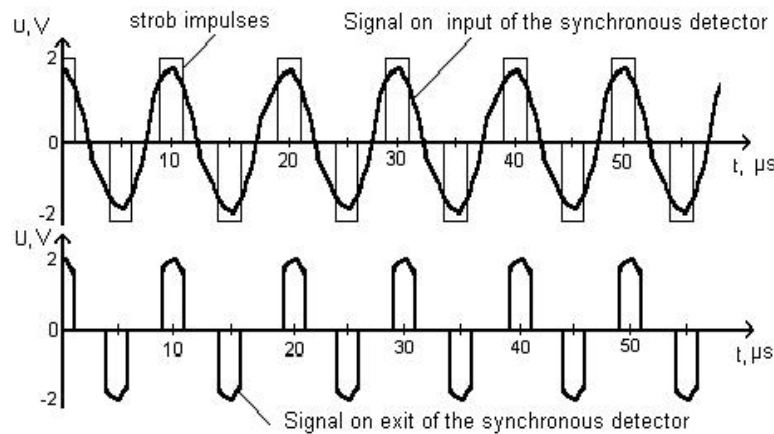


Fig. 4: Principle of synchronous detecting

Specific features of designing of the multi-channel recording system:

- Realization of temporary separation of channels,
- Sequential scanning of channels,
- Management and switching of the current generator each from channels,
- Realization of long and stable monitoring impedance signals and ECG.

There is a high probability of distortion registered rheogramm in precordial of area due to large amplitude of movement and breathing artifacts and limited dynamic range ADC.

It is necessary to develop a compact multi-channel system with large number of modules. It is possible for want of correspondence to rigid requests on consumption of energy and sizes of used components.

The restriction on power consumption from the power supply requires application of special measures and low power of solutions for want of hardware designing.

The high characteristics of impedance measuring converters are determined:

- quality of construction of currents generators,
- selective properties of detectors impedance signals,
- account of capacity cable systems properties.

It especially is actual for want of designing of the multi-channel impedance measuring system.

Till now in impedance converters for calibration applied sinusoidal or rectangular electrical signals. The signals passed through a part of the measuring channel. Such testing non-impedance signal attracts emerging measuring of problems. It is connected to set-up of device gauging and with recalculation of an electrical signal in impedance.

Developed a principle and procedure of calibration allow to calibrate all measuring tract, including a cable of the patient. The impedance source of calibration permitting directly to compare outcomes of calibration with precision (of 0.1 %) by significances of gauge impedances is selected.

Each channel of the system was calibrated in absolute units of the measured bioimpedance. Spatial-time reproducibility of the registered signals has been observed for each channel

In order to minimize a systematic error and to receive stable and reproducible estimations of the cardio activity parameters, a continuous *phase correction* of the registered rheographic signals was conducted [3].

Chebyshev non-recursive symmetrical digital filter of low frequencies was applied for *the breathing pattern extraction and elimination* from the TTRG and PreRCG signals [4].

3 Conclusions

During the conducted work the following goals have been reached and results obtained:

1. A scheme and a model of the multi-channel computer based impedance monitoring system were designed.
2. Time division of channels, both for each module, and between channels is realised.
3. Consecutive scanning of channels is realised.
4. Management and switching of the current generator for each of channels,

The system providing long and steady monitoring of impedance signals and ECG is realized.

4 Acknowledgement

This work was supported by the RF Ministry of Education and Science grant No. RNP.2.1.2.3962.

References

1. Safonova L P, Schookin S I (2005) Impedance precordial mapping of cardioactivity: information capacity study. Biomedical technologies and radioelectronics 9:4-11 (In Russian) at <http://www.radiotec.ru/catalog.php?cat=jr6&itm=2005-9>

Parameter	Value
Input PreRCG channels	Up to 30
Input TTRG channels	1
Input ECG channels	1
Sample rate	Up to 500 Hz
Rheogramm: measurement method	tetrapolar 3 mA, 100 kHz
measuring current (effective value)	1 – 250 Om
base impedance range, Z	± 2 Om
range of impedance changes, ΔZ	0.5 mOm
sensitivity	0.17... 68 Hz
pass range	$3, 10^{-6}$ V
ECG: from the rheographic electrodes	0.17... 68 Hz
arbitrary noise, not more than pass band	
ADC	12 bit
Input PreRCG channels	Up to 30
Input TTRG channels	1
Input ECG channels	1
Sample rate	Up to 500 Hz
Rheogramm: measurement method	tetrapolar 3 mA, 100 kHz
measuring current (effective value)	1 – 250 Om
base impedance range, Z	± 2 Om
range of impedance changes, ΔZ	0.5 mOm
sensitivity	0.17... 68 Hz
pass range	$3, 10^{-6}$ V
ECG: from the rheographic electrodes	0.17... 68 Hz
arbitrary noise, not more than pass band	
ADC	12 bit
Input PreRCG channels	Up to 30
Input TTRG channels	1
Input ECG channels	1
Sample rate	Up to 500 Hz

Table 1: Main technical characteristics of the 32-channel rheographic system for the IPM

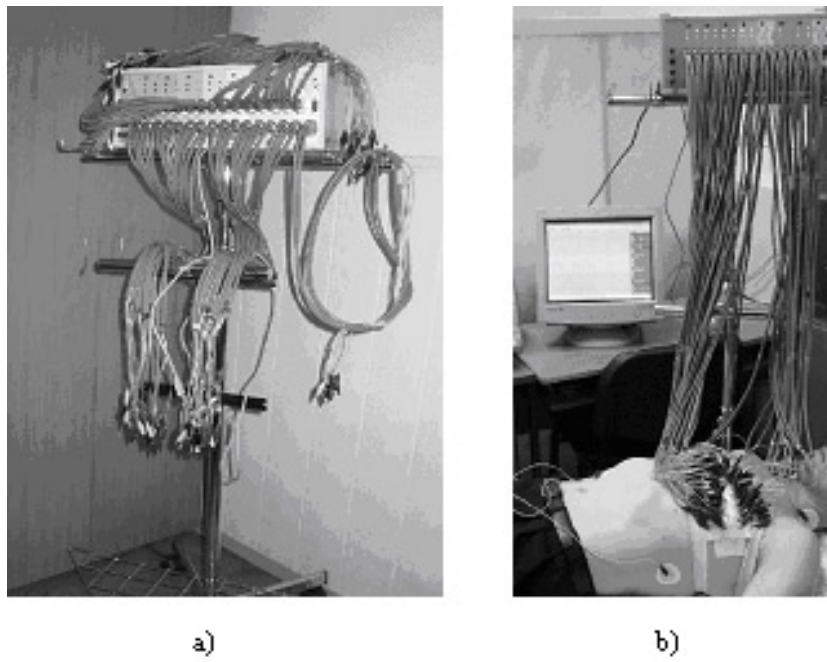


Fig. 5: A model (a) of the 32-channel rheocardiographic system and the experimental setup (b)

2. older D S et al. (2005) Electrical impedance tomography. Methods, History and Applications. IOP Publ London
3. elyaev K R, Morozov A A (1993) Correction of phase distortions and biomedical signal analysis. BMSTU Bulletin 4:40-53 (In Russian)
4. ubenko V G, Morozov A A, Petrov V I et al. (2003) Study of an individual variability of the heart pump-function parameters with an account of cardiodynamic instability. Biomedical technologies and radioelectronics 9:26-35 (In Russian) at <http://www.radiotec.ru/catalog.php?cat=jr6&itm=2003-9>

Features of Brain Hemodynamics Research at the Multichannel Rheoencephalography and Electroencephalography

E. M. Astapenko, P. V. Luzhnov, and L. A. Shamkina

MSTU n.a. N.E. Bauman, Moscow

Various diagnostic methods are used for the analysis of brain structures. It is important to note an electroencephalography, a rheoencephalography and infrared spectrometry among them. The rheoencephalography (REG) is a non-invasive method which can repeatedly be used for long registration of general and regional brain hemodynamics in rest and at various functional and pharmacological tests.

The rheography technique is based on tissues impedance registration when the high-frequency current is injected through them. Electric resistance of human body parts depends on volume blood changes in them. It underlies rheograms registration. The rheogram is a graphical registration of tissues electric resistance changes when weak high-frequency current is injected through them. The changes of tissues impedance is caused by pulse increase of an investigated part of a body or an organ volume.

There are bipolar and tetrapolar techniques of rheogram registration. The tetrapolar techniques are used during our investigations. There is an opportunity to put electrodes for the transversal and the longitudinal REG- registration. The longitudinal rheoencephalography from symmetric areas of various head regions is more perspective and valuable as it gives representation about hemodynamics in symmetric brain areas.

To determine blood circulation parameters of brain H. H. Yarullin used the following electrodes positions: frontally-mastoidal (F-M) used for cerebral hemispheres blood circulation registration; frontal (F-F1), frontally-central (F-C) and frontotemporal (F-T) determine blood circulation in anterior cerebral artery; parietotemporal (P-T), roland-temporal (R-T), parietocentral (P-C) and temporotemporal (T1-T2) show blood circulation in medial cerebral artery; occipitomastoidal (O-M) and occipitoparietal (O-M) show hemodynamics parameters of vertebral artery (Fig. 1). H. H. Yarullin has suggested the system of leads most full describing brain blood circulation. The disadvantage of this system is the fact of presence a quantity of electrodes that leads to essential inconvenience at tetrapolar REG-signal registration. To determine optimum electrodes quantity we shall visualize anatomic brain structure. If we visualize the main brain arteries and their branches, it is possible to choose common carotid, internal and external carotids, vertebral artery and their branches. The purpose of our experiments was data acquisition about cerebral blood flow in various brain areas. To determine blood circulation parameters in each of areas electrodes were put on large arteries of brain. In our work three main methods of electrodes fixation have been observed: on the basis of elastic belts, a rigid design and rubber belts helmet.

If there is no asymmetry in blood circulation of brain, the right and left carotid arteries should bring in the equal contribution to brain blood supply. It is obtained that the contribution of both carotid arteries to brain blood supply makes about 80% during experiment. And therefore the remained 20% of blood come in from vertebral artery.

Now we are starting investigation of joint registration of electroencephalographic (EEG) and REG-signals. The joint registration of EEG- and REG-signals supplementing each other can promote not only deep studying of some theoretical questions but also functionalities of diagnostics of vascular and other brain diseases.

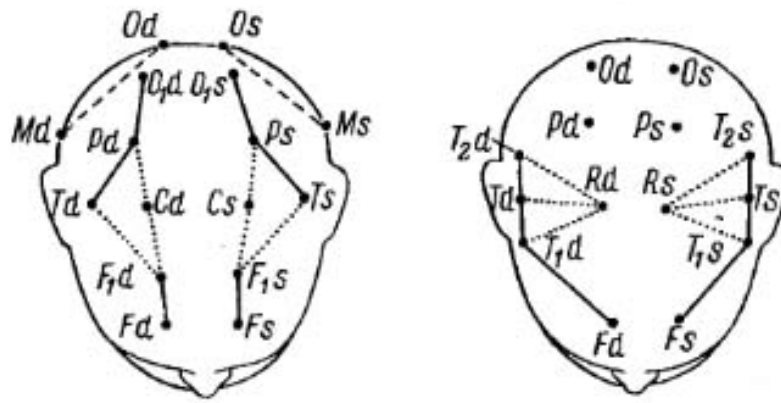


Fig. 1: REG-electrodes position by H.H.Yarullin

The EEG- and REG-signals joint registration assumes use of large number of electrodes. And therefore it is necessary to restrict their quantity so that to save an appreciable part of information that they have. In this case we shall be guided by the anatomic brain structure, namely a brain hemodynamics and its division into 4 lobes. According to EEG-standards, the used electrodes schemes of EEG-leads should correspond to some basic requirements. First, all basic parts should be presented in the scheme, i.e. frontal, central, parietal, occipital and front and back temporal. Secondary, electrodes should put symmetrically concerning a median sagittal line of a head because of essential symmetric of normal EEG.

Observing the projection of the electrodes locations scheme onto brain anatomic structure we have assumed that it is convenient to use 16 monopolar leads at electroencephalography and 10 ones at rheoencephalography (Fig. 2). Such electrodes location will provide registration of both signals in each of 4 brain lobes that enables to characterize them separately.

The rubber belts helmet has been developed for joint registration of EEG- and REG-signals. It took place because of joint usage inconvenience of the rigid design for REG-electrodes fixation and electroencephalographic helmet. Therefore we have modernized the helmet for EEG-researches to create the helmet for these both methods.

We have carried out the experiment and recorded signals in 16 EEG-leads and 2 REG-leads (F-M in left and right hemispheres). The developed helmet for joint registration EEG- and REG-signals has appeared convenient during experiment. We have analyzed the results of this experiment and found out correlation of amplitude asymmetry of EEG- and REG-signals in the following leads F3A1, F4A2 and Fs-Ms, Fd-Md accordingly. Thus, it is possible to conclude that the blood circulation changes in internal carotids can lead to changes of electric activity first of all in F3A1 and F4A2 leads.

At joint registration of EEG- and REG-signals we offer to apply 16 monopolar EEG-leads and 10 REG-leads. Further we plan to determine correlation between described above 10 REG- and 16 EEG-leads, research changes electric activity of brain depending on breath phases.

The simultaneously registration of REG and EEG signals allows us to estimate correlation between destruction of electrical activity and blood circulation of brain. First of all it is very important for treating obliterating diseases of vessels and acute stroke. It is known destruction blood circulation preceded of stroke is not momentary process. The problem of cerebral circulation functioning accumulates from little failures to haemorrhage. We can diagnose any variation

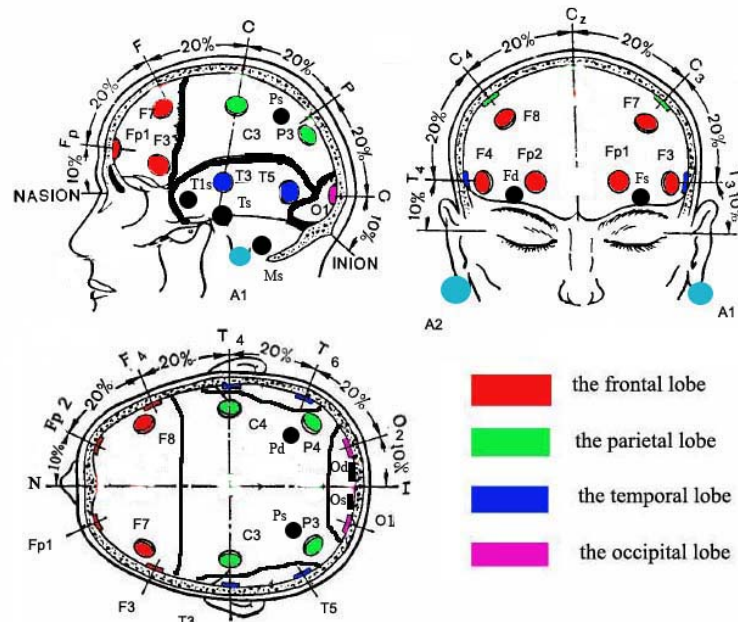


Fig. 2: Electrodes location at joint EEG- and REG-signals registration

of cerebral blood circulation in the beginning of stroke treatment but changes in electrical activity of brain are not determined on this period. The second we can determine changes during the therapeutic session, for example the session of bioadequate electromagnetic stimulation (BEMS) with active diagnostic.

Diagnostic efficiency therapy is proved by blood flow changing in the part of a body under consideration. One of the most appropriate techniques to define blood filling parameters using therapy is the analysis of a rheographic signal. It also enables us to implement synchronized stimulation, which is carried out by rheographic (or pulse wave) signal or by a breathing signal.

Active diagnostics allows a doctor to react immediately to any change in a patient's condition and to carry out individual selection of therapeutic parameters for each patient. For example form and time parameters of stimulation. At present the most urgent question is the estimation of therapeutic efficiency so that the doctor could choose the most appropriate parameters and the duration of exposure. We suggest using the number of vessel tone changes per unit time as such a parameter.

It is known that the pulse wave signal has several typical forms. They can be classified into hypertonic, normotonic, hypotonic and dystonic. These types are determined by using factors DCI and DSI. These factors are amplitudes ratio of the first pulse wave (systolic wave), insicere and the second pulse wave (diastolic wave).

Normally only one type of a vessel tone prevails in a human being. If there is pathology, the vessels tone constantly varies. We have proved that therapeutic stabilises a vessels tone. For example this figure (Fig.3) shows the vessels tone indicated by numbers 1(hipotonic), 2(normotonic) and 3(hypertonic) before electromagnetic exposure, during the session and after the expo-

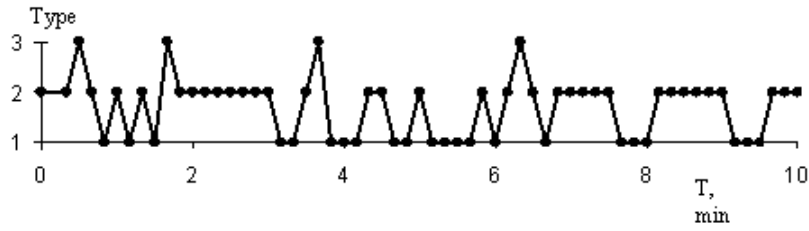
sure. It can be seen that before the session of electromagnetic exposure the vessels tone changes chaotically but after the session it is normalized and tends to one normotonic value.

Thus, the number of changes in the vessels tone per unit time allows us to estimate the patient's condition objectively and to choose individually optimized parameters of stimulation.

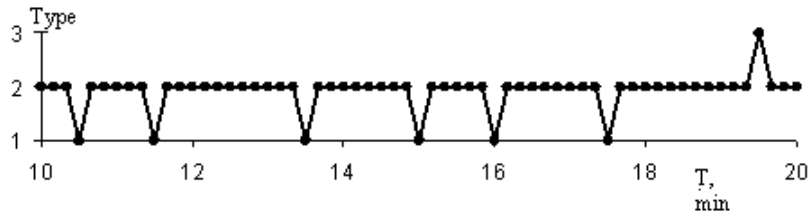
After the number of changes decreases below a certain threshold value, it is necessary to stop a therapeutic session since a refractory period comes (that is tissues become unsusceptible to external stimulation).

The number of sessions composing one BEMS course is chosen in the same way. To implement the methods suggested we have developed special software.

before the EMS



during the EMS



after the EMS

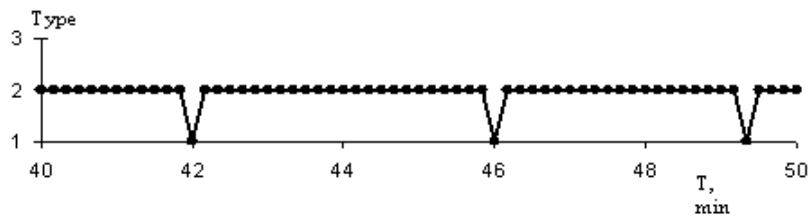


Fig. 3: Patient with the venous electromagnetic stimulation (EMS)

Methods and principals suggested in this article allows us to investigate of simultaneously registered signals of electric activity of brain and cerebral blood circulation.

References

1. Ivanov L.B., Makarov V.A., Lektsii po klinicheskoj reografii. - M.: Antidor, 2000. - 320s.
2. Luzhnov P.V., Morozov A.A., Shchukin S.I., Programmno-algoritmicheskie sredstva sistem pli biosinkhronizirovannogo E1MV // Biomeditsinskie tekhnologii i radioelektronika. - 2002. - N09. - S.42 - 48.

Effect of Respiratory Gases Composition on Duration of Forced Expiratory Tracheal Noises

Alexander I. D'yachenko^{1,2,4}, Vladimir I. Korenbaum³, Elena V. Kir'yanova³, Irina A. Pohekutova³, Yury A. Shulagin¹, and Antonina A. Osipova¹

¹ State Scientific Center of the Russian Federation – Institute of Biomedical Problems of the Russian Academy of Sciences 76-a Khoroshevskoye shosse, Moscow, 123007, Russia.

Ph.: 7-(495) 195-22-53; Fax: 7-(495) 195-15-73

² General Physics Institute named by A.M. Prokhorov of the Russian Academy of Sciences 38 Vavilova Str., Moscow, 117942, Russia.

alexander-dyachenko@yandex.ru

³ V.I. Il'ichev Pacific Oceanologic Institute, Far Eastern Branch, Russian Academy of Sciences 43 Báltiyskaya Str., Vládívístok, 690041, Russia.

Tel.: 7-(4232) 311-631; Fax: 7-(4232) 311-631

v-kor@poi.dvo.ru

⁴ Department of Biomedical Techniques, Bauman Moscow State Technical University, Moscow, Russia

Abstract. We studied duration of forced expiratory tracheal noises T_a in normal pressure and different respiratory gas mixtures: air, oxygen-helium mixture (O_2 -He) and oxygen-krypton mixture (O_2 -Kr). With the flow meter we measured standard flow and volume parameters of the forced expiration including T_s – volumetric duration of forced expiration. Also we got flow-volume and flow-time charts. Mean group acoustical and volumetric durations of forced expiration increased with gas mixture density. Individual reactions on increase of gas density were different. Probably expiratory airway conductance depends much upon individual details of pleural pressure dynamics during forced expiration. We believe that measurement of duration of forced expiratory tracheal noises could be useful in monitoring respiration in divers.

Keywords: Respiratory noises, biomechanics of forced expiration, gas mixture density.

1 Introduction

Duration of forced expiratory tracheal noises T_a increases in patients with chronic obstructive respiratory disease (COPD) and bronchial asthma (BA) [1]. The duration is a sensitive parameter to detect a reduced airway conductance. This parameter is more sensitive than forced expiratory flows in detection of abnormal airway conductance in a group of patients with light bronchial asthma [1]. We suppose that duration of forced expiratory tracheal noises will be a useful parameter for estimation airway conductance in divers.

Purpose of this paper is to study duration of forced expiratory tracheal noises in different respiratory gas mixtures and normal pressure.

2 Methods

We studied 20 normal volunteers (13 men, 7 women) aged 20-57 years. All the volunteers performed forced expirations breathing air with 21% O₂ and oxygen-helium mixture (O₂-He) with 21% O₂. Seven volunteers performed forced expirations breathing oxygen-krypton mixture (O₂-Kr) with 21% O₂.

Each volunteer trained to perform forced expiration. Then a volunteer breathed from pneumatic system contained a bag, valves and gas switches. We filled the bag with air, O₂-He, or O₂-Kr and calibrated the flow meter ETON-01-22 (Russia) for each gas mixture. The volunteer breathed 3-4 minutes to fill lungs with a gas mixture, then inspired to vital capacity, switched from the bag to a flow meter and performed forced expiration. Simultaneously with gas flow we registered forced expiratory tracheal noises by virtue of electret microphone with stethoscope nozzle. The volunteer fixed microphone by his hand on the anterior lateral larynx wall. The volunteer made forced expiration a few times.

We analyzed digitized flow and sound signals in the following way. The sound signal was filtered (Band Pass; center - 1100 Hz; width - 1800 Hz; steep – slowest). The resulting signal is within 200-2000 Hz band and contains the main part of forced expiratory tracheal noises. We considered signal visually and measured duration of forced expiratory tracheal noises T_a as time interval between start and disappearing of tracheal sounds above the pre- and past-expiration levels. We choose 3 maneuvers with maximal T_a in each gas mixture.

By means of flow meter ETON-01-22 respiratory parameters were determined: VC - vital capacity; FVC - forced vital capacity; PEF - peak expiratory flow; MEF₂₅, MEF₅₀, MEF₇₅ - the maximal expiratory flows at exhalation levels of 25%, 50%, 75% FVC, FEF₂₅₋₇₅ - averaged expiratory flow between 25% - 75% levels of FVC, T_s - volumetric duration of forced expiration. In addition the flow-volume curve was transformed in flow-time dependence. For this purpose the flow-volume curve was digitized in separate axes "Volume" and "Flow". Increment of volume dV between two nearest points was evaluated in axis "Volume". Increment in flow rate dV/dt was evaluated in axis "Flow" for these two points of digitizing. An interval of time was determined dt = dV / (dV/dt) for which there was an increment of volume. This procedure was repeated for all points of digitizing of flow-volume from the beginning of forced expiration. Intervals of time dt were accumulated from the beginning of forced expiration and thus value of current time t to which the digitized flow rate of an exhalation was received.

We analyzed the data with non-parametric Wilcoxon t-test.

3 Results

The averaged T_s was more in air (3.89 s) then in O₂-He (3.76 s) and less then in O₂-Kr (5.00 s) (Table 1). Thus T_s was increased with an increase of the density of gas mixture. VC and FVC did not change with gas mixture. In the group PEF, MEF₂₅, MEF₅₀, MEF₇₅ were reduced with increasing the gas mixture density (p<0.02). The data are in accordance with concepts of the forced expiration mechanics. Our data are the first with experimental proof that flows are reduced when nitrogen in air is substituted for krypton. While individual variations of this relationship are large. In some subjects there is no significant difference between flow-time relationships for a pair of different gas mixtures. There is no any difference between flow-time relationships for all gas mixtures in the flow range < 2.5 l/s.

The mean T_a was 2.84 s, 2.43 s, 3.90 s in air, O₂-He and O₂-Kr respectively. Wilcoxon t-test of group differences of T_a for different gas mixtures demonstrated that T_a is more in O₂-Kr than in O₂-He (p < 0.02, Table 1). Differences between all other pairs of T_a are not significant.

Table 1: Volumetric duration of forced expiration T_s (average \pm SD) and duration of forced expiratory tracheal noises T_a (average \pm SD). P - significance of differences of duration of forced expiratory tracheal noises T_a between Gas mixture 1 and Gas mixture 2.

Gas mixture 1	T_s , s	T_a , s	Gas mixture 2	P
Air	3.89 ± 2.41	2.84 ± 1.17	O ₂ -He	0.073
O ₂ -He	3.76 ± 2.13	2.43 ± 0.67	O ₂ -Kr	0.017
O ₂ -Kr	5.00 ± 2.46	3.90 ± 1.87	Air	0.090

Analysis of individual T_a revealed that increase of gas mixture density did not result in increase of T_a in some patients.

We studied correlation between individual acoustical duration of forced expiratory tracheal noises and flow-volume parameters of forced expiration. In all the gas mixtures a maximal correlation (Spearman coefficient) was obtained between T_a and ratio FVC_1/FVC ($r = -0.64$ in O₂-He; $r = -0.89$ in air; $r = -0.89$ in O₂-Kr; $p < 0.003$).

A significant correlation between T_a and T_s was obtained only in O₂-He ($r = 0.61$; $p < 0.005$) and in air ($r = 0.87$; $p < 0.00001$). There is no significant correlation between changes in T_a and changes in flow-volume parameters of forced expiration when gas mixture was changed.

4 Discussion

Analysis of individual values of T_a shows, that a transition to denser gas mixture was not accompanied by augmentation of forced expiratory noises duration in some subjects. For example, under transition from O₂-He to air ($n = 20$) T_a increased essentially in 9 subjects, and was decreased in 4 subjects. Essential increase is an augmentation more than 17 % [2]. At the same time under transition from air to O₂-Kr and from O₂-He to O₂-Kr ($n = 7$) the response of essential augmentation of T_a was dominated. Individual differences of effect of gas mixtures on T_a and T_s demonstrate that expiratory airway conductance depends upon both gas mixture density and individual lung and airway parameters and peculiar details of pleural pressure dynamics during forced expiration. One may suppose that some details of such dependence could be revealed by a simulation.

Acknowledgment

This work was supported by the State Program of Support for Leading Scientific Schools project NSh - 5616.2006.1, grants of RFBR 06-08-08069-OFI, FEB RAS 06-1-P12-043 (program of RAS Presidium "Fundamental Sciences – to Medicine").

References

1. Korenbaum V.I., Pochekutova I.A. Acoustical-biomechanical interdependences in human forced expiratory noises production, Vladivostok: Dalnauka, 2006. 148 p. ISBN 5-8044-0564-0.
2. Pochekutova I.A., Korenbaum V.I., Agapov Ya.V. Acoustical and spirometric indexes of respiratory function in oxygen divers, Military-medical J. 2006. V. CCCXXVII. P.58-61.

Micro- and Nanotechnology in Bio-Medical Engineering

Prevention of implant associated nosocomial infections by impregnation of biomaterials with activated nanocrystalline silver

J. Peter Guggenbichler

Department of Pediatric Infectious Disease and Preventive Medicine, Univ. of
Erlangen-Nuremberg

1 Introduction

Health care associated infections are the fourth leading cause of disease in industrialised countries and the most common complication affecting hospitalized patients. Based on a conservative estimate, 10% of the European population is hospitalised each year. Thereof, it is assumed that 5% (3.8% on a general ward, 15.3% in intensive care units) acquire at least one nosocomial infection. Based on these figures, it can be estimated that some 1.75 million hospitalised patients are affected annually by a nosocomial infection in Europe. Assuming a conservative 10% attributable mortality rate, this equals a minimum of 175,000 deaths every year. Recent reports from the US by the NNIS indicate that nosocomial infections account for 2 million infections and 90,000 preventable deaths per year. An increasing number of highly vulnerable patients together with emerging of antibiotic-resistant microbes, especially *Staphylococcus aureus*, *Enterococcus* species and Gram-negative microorganisms producing extended spectrum beta-lactamases (ESBL) are encountered. The situation is aggravated by the fact that in the future there will be few new antibiotics under development to compensate for the increasing resistance. An excess length of stay (mean, 10 d; median, 5 d; $p = 0.007$) and increased direct costs (mean difference, \$34,508; $p = 0.008$) have been described. In 2000, the US Centers for Disease Control and Prevention estimated the total costs of nosocomial infections to be in excess of 5 billion US \$. In Germany, it is estimated that approximately 2.4 billion EUR are spent annually for treatment of these infections. These figures don't include the disabilities caused by nosocomial infections, the decrease of healthy life expectancy, the impact on the loss of productivity due to early death or chronic illness. The most significant hospital-acquired infections, based on frequency and potential severity, are those related to implantable medical devices, including urinary tract infection, pneumonia in patients on artificial ventilation and bacteraemia related to intravascular devices. There is ample evidence that at least two thirds of all cases of nosocomial infections are associated with implantable medical devices. A review of the recent literature indicated the following incidence of devices related infections

- Peripheral venous catheters 0.2 per 1000 device days
- CV catheters 1.5 - 12/1000 catheter days. av. 6.7/1000
- Sheldon catheters 35% of patients
- Hickman Catheter 0.7- 1.2/1000 in the literature. KISS data 1.97/1000 i.e. 25% - 48% of patients
- Port - catheter: 8 - 12% infection, preliminary explantation 25%
- Tenckhoff catheters 15% of patients
- Transurethral catheters: cumulative daily increment of 5 - 8%
- External ventricular drainage systems 12.8% of patients

- Thoracic drainage systems 25%
- Ventilator associated pneumonia, i.e. endotracheal tube related infection 25%
- Joint implants 0.2 - 2.5%

Microorganisms gain access to the body by multiple pathogenetic pathways. They are significant both for their potential severity (illness and/or death), but also because of the potential preventability of these infections. Beside decreased patients' host defence and colonisation of mucous membranes by pathogenic microorganisms, the disruption of the integrity of the surface of the body caused by implantable medical devices and direct and indirect access of microorganisms into the respiratory tract, the urogenital tract, bloodstream and cerebrospinal space are major routes. Multi-resistant nosocomial pathogens are the most common organisms difficult to eradicate because bacteria that cause these infections live in well-developed biofilms.



Fig. 1: Biofilm on a polyurethane surface after contamination with *S. epidermidis* 10^7 CFU/ml for 6 hours.)

The clinical diagnosis of a device related infection is difficult. For evaluation of the clinical efficacy of an antimicrobial polymer a more precise diagnostic tool was designed. On the basis of the CDC/HICPAC criteria and in accordance with the NIDEP study for nosocomial infections a scoring system was established which was found to be substantially more sensitive without loss of specificity as existing diagnostic criteria. Conservative therapy of a device related infection is difficult. It has been accepted that antibiotics penetrate poorly into the biofilm and are therefore less successful in eradicating the offending microorganisms. In vitro and in vivo investigations with artificially contaminated catheters were less satisfactory. In case microorganisms are eradicated debris consisting of lysed cell wall components still cover the catheter surface of the device favouring recolonization with microorganisms.

2 Strategies to minimise the risk of infection associated with implantable device related infections assume highest priority.

It has to be emphasised that for maximum benefit an integral approach is necessary: This implies for any procedure performed on patients the blockage of microbial invasion from all possible sources. Strict adherence to hygienic rules, vigorous barrier precautions during insertion or implantation of the device as well a continuing care are aspects of particular importance. The development of new materials which could withstand microbial adherence and colonization has

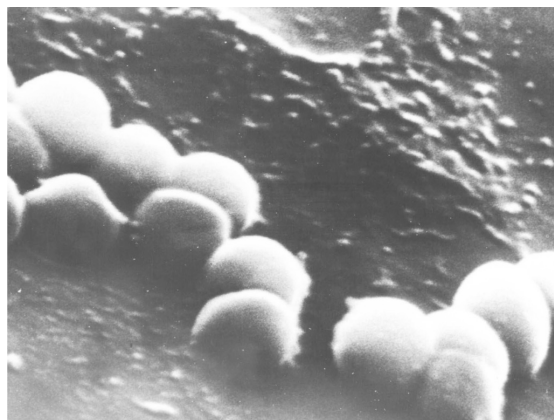


Fig. 2: Surface of a catheter contaminated with *S. aureus* after continuous perfusion with 100 fold MIC of Cefamandole over 24 hours.

become a major topic in recent years. Several surface modification techniques have been proposed to improve the performance of devices. These include the immobilization of biomolecules, the incorporation of hydrophilic grafts to reduce protein adsorption, and the creation of hydrophobic surfaces, of microdomains to regulate cellular and protein adhesion, new polymers and antimicrobial coatings. A reduction of the frequency of infection was investigated by catheter materials coated or impregnated with antimicrobial substances e.g. antibiotics or antiseptics. Technologies with various antimicrobial technologies have been recommended for central venous catheters, external ventricular drainage systems and urologic catheters. Very high concentrations of ampicillin, vancomycin and linezolid are required to inhibit enterococcal biofilms in vitro. All currently available antibiotics and also disinfectants are effective only against a limited range of organisms. Moreover, in recent years nosocomial pathogens have become increasingly resistant to antibiotics and disinfectants. When bacteria adhere to biomaterial surfaces they undergo dramatic metabolic changes. Intensive investigations revealed that sessile microorganisms require 100 to 250 fold higher concentrations for eradication compared to planktonic microorganisms. Water soluble antibiotics and disinfectants are eluted rapidly from the polymer and limit the activity largely to 7 days.

3 Oligodynamic activity of metal ions.

The antimicrobial activity of silver as well a copper and other metal ions, has been well known for centuries as oligodynamic activity. Silver is the element with the highest antimicrobial activity and the lowest toxicity for animal cells. The antimicrobial activity of silver ions includes the majority of bacterial microorganisms: gram-positive and gram-negative cocci as well as gram-positive and gram-negative rods, fungi and many viruses. The activity of silver is limited by the availability of free silver ions. An excellent bactericidal silver ion concentrations can be achieved with substantially enlargement of the surface. A technology developed in our institution used a vast increase of the surface of silver in polyurethane which resulted in an increased release of free silver ions over a period of several months. It was technically feasible to fill the spaces between the thermoplastic polyurethane elastomers with billions of nanoparticles of metallic silver (3 - 5 nm in diameter) evenly distributed throughout the polymer matrix providing a surface of

$> 2000\text{cm}^2$ of silver per g polyurethane. Silver nanoparticles are fixed on a carrier e.g. barium sulphate preventing the existence of free nanoparticles in the environment which exhibit a 10 000 fold greater bioreagibility than micro-size particles.

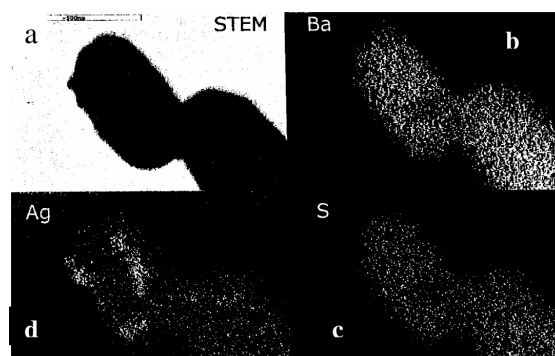


Fig. 3: Transmissions Electron Micrography: Nanoparticles of silver on a carrier (Barium Sulfate) Figure 7 b = Barium, c = Sulfate, d = silver: Element mapping of a polyurethane catheter with nanoparticles of silver on a BaSO₄ carrier. The silver nanoparticleds are fixed on the carrier providing a surface of $> 2500\text{cm}^2/\text{g}$ polyurethane.

A further improvement of this technology has been achieved by combination of nanoparticles of Ag₀ with poorly water soluble silver salts e.g. silver sulphate, silver fluoride or silver orthophosphate which is generated during the manufacturing process. This combination called activation of nanoparticles provide a galvanic element with a substantially increased release of silver.

Prospective randomised clinical studies in approximately 1000 patients revealed a reduction of catheter related infections between 75 and 95%. Also long term Hickman catheters showed an excellent antimicrobial activity as well as a external ventricular drainage system.

4 Summary

The endowment of polymers with nanoparticles of activated silver providews a large surface within the catheter matrix. This results in an excellent antimicrobial activity with good biocompatibility. CE certified devices are on the market and result in a substantial reduction of device related nosocomial infections.

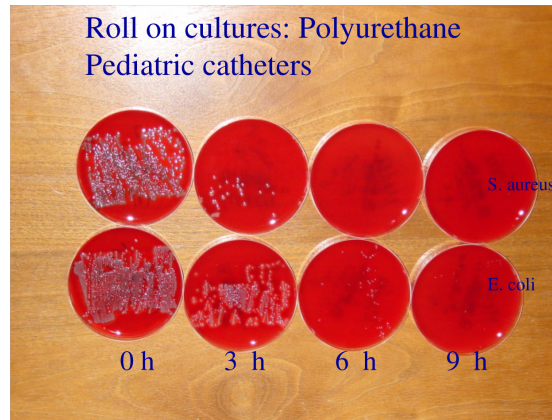


Fig. 4: Antimicrobial activity of a polyurethane catheter with% activated nanosilver determined by the roll on cultures after contamination with 10^9 CFU of *S. aureus* for 4 hours. The material is non-cytotoxic, non-thrombogenic and shows excellent biocompatibility.

Paradontitis: Therapy and prevention with a nano-silver containing toothpaste - Experimental and clinical data

W. Wanninger and JP Guggenbichler

Department of Pediatric Infectious Diseases and Preventive Medicine
Univ. Erlangen/Nürnberg

1 Introduction

Periodontitis/paradontitis is a frequent problem affecting at least 10 % of the world population. Data indicate that patients with periodontitis suffer twice as frequently from myocardial infection and stroke.

The etiology is multifactorial, bacterial microorganisms play a major role in the pathogenesis either as primary etiologic agent or secondary due to impaired host defense mechanisms e.g. decreased innate immunity.

Antimicrobial active compounds have been used e.g. Triclosan with varying success. Silver with its broad antimicrobial activity could serve as an excellent compound for therapy and prevention of paradontitis. This has been investigated in experimental and clinical studies.

2 Manufacturing activated nanosilver in toothpaste

Activated nanosilver, tightly fixed on an anorganic carrier, is manufactured according to a patented production process. Silver particles (5 – 20 nm in diameter) are attached to a carrier (inorganic substances e.g. Barium sulphate, Titanium oxide, hydroxyl apatite etc.) during the manufacturing process. Water insoluble silver salts are formed on the nanoparticles creating an electrolytic

element with release of bactericidal concentrations of silver ions. This technology results in a substantial increase of antimicrobial activity compared to nanosilver alone.

The permanent fixation of nanosilver particles on a carrier with a diameter of 2 – 5 μm resolves the problem of potential toxicity of free nanoparticles. It has been documented that the carrier with attached nanoparticles does not penetrate the epithelial cell barrier.

3 Experimental investigations

3.1 Investigation of antimicrobial activity:

Measurement of release of free silver ions from a 1 g sample of a toothpaste containing 0.1 % of nanosilver over 24 hours was performed with mass spectrometry. There is a release of 0.3 μg release of silver into the eluate over 24 hours. Within a clinically relevant time frame of 1 – 2 hours concentrations of 25 ng are detectable. Colloidal silver is converted by hydrochloric acid in the stomach into the water insoluble nonabsorbable silver-chloride. The silver toothpaste containing 0.25 % of the additive, containing 5 % nanosilver on the carrier is considered safe. Concentrations of silver in drinking water a concentration of 50 $\mu\text{g/l}$ (US) 100 $\mu\text{g/l}$ in EU is considered safe.

3.2 Determination of antimicrobial activity:

1 g of toothpaste with activated nanosilver (0.25 %) was mixed with 10^9 , 10^8 – 10^7 CFU of *S. aureus*, *E. coli* and *P. aeruginosa*. Three hourly determination of colony forming units has been performed by plating 10 μl of each sample on an agar plate. Plates are incubated for 24 hours at 37 ° Celsius. Thereafter photodocumentation of the plates is performed.

3.3 Investigations of cytotoxicity

Cytotoxicity was investigated with the NBT Test. MRC5 (mouse fibroblasts) cells were incubated with an 24 hours eluent of 1 g toothpaste with 1 % activated nanosilver. Then the colorless farmazan was added to the test cells. Viable cells generate oxygen which converts farmazan into nitro-blue tetrazolium. After 6 hours the color change of the test cells was determined by optical density measurements.

A loss of viability of the test cells of less than 10 % was found. This means that the toothpaste lacks cytotoxicity and is safe for longterm use.

Histologic investigations of epithelial cells after 24 hours contact of the carrier material with attached nanoparticles were performed. There was no penetration of carrier material nor of nanoparticles into epithelial cells.

4 Clinical investigation:

4.1 Prospective randomised evaluation

40 patients with parodontitis were enrolled in the study. Initially a baseline evaluation was performed with determination of the depth of the sulcus, measured by two independent investigators. Patients were randomly allocated to one of 4 samples containing 1%, 0.25 %, 0.1% and 0.01 % of nanosilver in the toothpaste for two weeks. Cleaning with the antimicrobial toothpaste was performed twice daily. After two weeks patients were reevaluated.



Fig. 1: Antimicrobial activity of 1 g toothpaste containing 0.1 % of the additive with 5 % activated nanosilver after a 24 hour elution

Ag-Active Study Evaluation of patients 0,25% Nanosilver									
Pat	Sulcus			1st interv.		2nd interv.		Overall	
	start	14 days	28 days	% points	%	% points	%	% points	%
1	10,49	8,64	10,49	-1,85	-18%	1,85	18%	0,00	0%
6	21,52	8,33	29,86	-13,19	-61%	21,53	100%	8,34	39%
9	20,13	8,33	25,69	-11,80	-59%	17,36	86%	5,56	28%
10	19,33	7,33	15,33	-12,00	-62%	8,00	41%	-4,00	-21%
15	25,30	16,04	24,07	-9,26	-37%	8,03	32%	-1,23	-5%
19	22,22	5,55	18,05	-16,67	-75%	12,50	56%	-4,17	-19%
21	8,88	1,66	10,00	-7,22	-81%	8,34	94%	1,12	13%
28	14,03	6,14	19,29	-7,89	-56%	13,15	94%	5,26	37%
31	9,61	12,82	8,97	3,21	33%	-3,85	-40%	-0,64	-7%
33	14,10	5,12	15,38	-8,98	-64%	10,26	73%	1,28	9%
Mean	16,561	7,996	17,713	-8,565	-48%	9,717	55%	1,152	7%

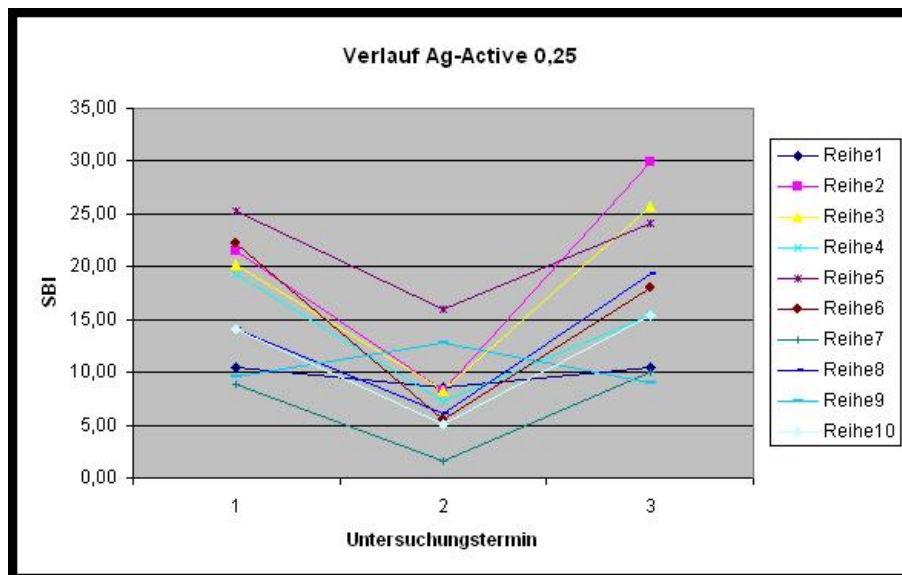


Fig. 2: This graph shows the results of this study.

Ag-Active Study Evaluation of patients 0.1 %									
Pat	Sulcus			1st interv.		2nd interv.		Overall	
	start	14 days	28 days	% points	%	% points	%	% points	%
4	13,54	7,29	13,02	-6,25	-46%	5,73	42%	-0,52	-4%
12	7,40	3,08	9,87	-4,32	-58%	6,79	92%	2,47	33%
17	23,45	16,66	16,04	-6,79	-29%	-0,62	-3%	-7,41	-32%
18	8,97	3,84	8,97	-5,13	-57%	5,13	57%	0,00	0%
24	18,58	11,53	18,58	-7,05	-38%	7,05	38%	0,00	0%
25	15,47	5,35	8,92	-10,12	-65%	3,57	23%	-6,55	-42%
26	13,69	13,69	22,02	0,00	0%	8,33	61%	8,33	61%
36	12,00	10,00	17,33	-2,00	-17%	7,33	61%	5,33	44%
39	18,39	19,54	17,24	1,15	6%	-2,30	-13%	-1,15	-6%
40	10,00	8,88	10,55	-1,12	-11%	1,67	17%	0,55	6%
Mean	14,149	9,986	14,254	-4,163	-32%	4,268	38%	0,105	6%

The data are part of the Inaugural dissertation of W. Wanninger, Zahnarzt in Straubing, Bahnhofplatz 2

Laser irradiation application for creating volumetric nanocomposits for medical purposes

Podgaetsky V.M.¹, Sàvransky V.A.², Selishchev S.V.¹, Simunin M.M.¹, Titkova D.A.¹

¹ Moscow Institute of Electronic Engineering (MIEE), Department of BioMedical Systems, Moscow, 124498, Russia

² Institute of General Physics (RAS), Russia

Development of the nanotechnology industry determines the whole technological state of present century. It is difficult to find some area of practice, development of which doesn't depend on the progress made in this industry. A great significance is attached to application of nanomaterials allowing performing therapeutic action at the cellular and more underlying levels.

Among well-known nanomaterials a thread-like modification of carbon – carbon nanotubes (CNT) – is especially valuable. Size and properties of the carbon nanotubes are perfectly suitable for drug transportation inside biological tissues, manufacturing of subminiature diagnostic sensors and robots for fine monitoring of the physiological processes, production of nanosurgical armaments and etc. There is hope that CNT can be of great use at solving the problem of volumetric nanocompositions manufacturing, as nanocompositions are very suitable materials for applied medicine, but so far only the two-dimensional structures of nanoparticle conglomerates (junctions) at the orienting substrates have been produced.

One of the acute problems of the modern bioengineering is to create artificial human organs. For this purpose the manufacturing technique of the implants of high mechanical strength and long-time reliability has to be designed. The implants should meet medical practice requirements. Such kind of properties may be inherent in the volumetric nanocompositions serving the role of the scaffold materials which allow the self-organization (self-assembly) of the biological tissues

Biomedical applications of nanotechnology arouse significant interest as conventional methods of surgical prosthesis are facing certain difficulties. For example, metal and plastic implants of hip joints are not always firm and require surgical replacement after short period of exploitation, inducing feeling of discomfort and creating possible complications while operating. On the other hand, autographs (from the tissues of the patient itself) and allographs (from the tissues of another man) are scarce and difficult to buy, moreover implementation of surgical operations becomes complicated because of biological distinctive features of patient's organism.

At present the biocompatibility of carbon nanotubes (CNT's) has been demonstrated for neural and bone cells that proved the principal possibility of cultivation, reproduction and proliferation of such cells on CNT substrates. After cell phenotype modification CNT's are probably capable of causing the regeneration of human organism tissues so they can be considered as the alternative filling material of artificial implants [1, 2].

So it is timely to set and solve the problem of manufacturing nanocompositions which will sustain tissue self-assembling. While transplantating the nanoimplants *in vivo* to the place of their application the laser welding method excluding the pathologic flora penetration into patient's organism can be used as it delivers some advantages over the other methods of human organ stitching. The next step in given direction can be done with the use of laser radiation, which thermal and (probably) orienting effects will sustain the creation of volumetric biocompatible material.

Multiwalled CNT's (MCNT) dissolved in process solution were used for nanocomposition making. The CNT's were produced from the ethanol by catalytic pyrolysis method. The choice of the method was stipulated for purity of the reagent and the possibility of getting material with

less percentage of admixture due to oxidation of thermodynamically unstable intermediate carbon structures. Internal section of the chamber for CNT manufacturing was made of ceramics with low thermal conductivity, and external wall – of heat-resistant steel. Carbonaceous gas-vapor mixture puffing was performed owing to disparity between pressure in retort with mixture and pressure in chamber. MCNT were produced using sol-gel catalyst.

The product produced was examined using atomic-force microscopy (AFM) methods. The CNT diameters ranged between 3 and 30 nm. The material was composed of CNT's with Ni insertions which are responsible for its magnetic activity. The AFM method findings demonstrated the CNT structure perfection.

After that CNT's were introduced into the water colloidal solution of the bovine or human serum albumin. This protein performing transport function in animal and human organisms was chosen due to its successful using as a part of tissue laser solders (with the dye ICG addition) while performing laser welding of biological tissues. The nanotube concentration varied from 10 to 50 g/l. The process solution was sonicated during several hours. Absorption spectrum of the solution is represented in the figure 1.

The irradiation of process solution was carried out using diode IR laser ($\lambda = 0,97 \mu\text{m}$, $N \leq 10 \text{ W}$) with the fiber-optic outlet, equipped with light target designator. The solution was placed in glass vessel of volume from 5 to 10 ml. The solution irradiation continued till the complete liquid evaporation and black product formation at the bottom of glass vessel. Measures were taken to prevent the untimely albumin denaturation. The quality and hardness of the material produced depended on the intensity and duration of the laser irradiation. The consistence of product samples varied from paste-like (suitable for medical purposes) to vitreous one.

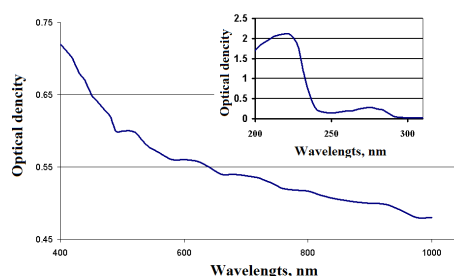


Fig. 1: Visible region of absorption spectrum of 20% water albumin-CNT solution (layer thickness 1 cm). In the insert – ultraviolet region of absorption spectrum of bovine serum albumin water solution (layer thickness 1 cm, $c=6.5 \mu\text{M/l}$)

To take pictures of surface structure of the nanocomposites at the nanoscale dimension atomic-force microscopes (AFM) Solver P4 + Solver P47 were used. In the figure 2 AFM picture of the nanocomposit film, which was taken after local vaporization of the drop of the solution at the silicon substrate, is shown. Scanning was performed in the picture area $3 \times 3 \mu\text{m}$. Light areas represent heights, dark areas – deepening, and blue color corresponds with grade level.

As can be seen from the figure 2, nanomaterial is a volumetric quasi-periodic structure of round globules with diameter of those varying from $200 \mu\text{m}$ to $500 \mu\text{m}$, visible altitude – $30\text{-}40 \mu\text{m}$. In the other areas of the tape globules of the similar size but of ring-shaped form can be seen. In the figure 3 (picture area $3 \times 3 \mu\text{m}$) overview of the object and cross-section of one of the globules are shown.

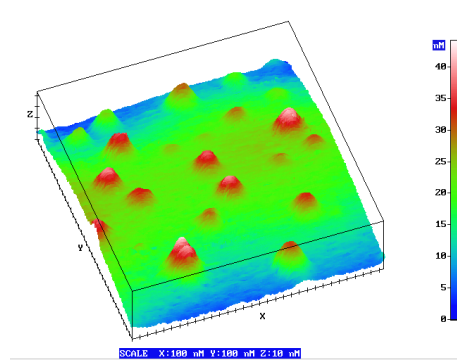


Fig. 2: AFM picture of the nanomaterial film - Picture area $3 \times 3 \mu\text{m}$. Division value of the axes: X and Y = 100 nm, Z = 5 nm.

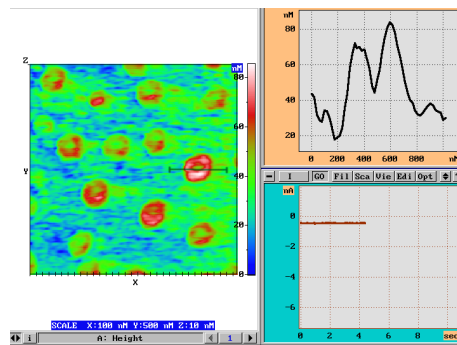


Fig. 3: AFM picture of the nanomaterial film and section of the ring-shaped globule. Picture area $3 \times 3 \mu\text{m}$. Division value of the axes: X and Y = 100 nm, Z = 10 nm.

With the purpose of eliminating the possible presence of the bacterial material in the paste sample ultraviolet irradiation (with lamp PRK-4 for 4 minutes at the distance ~ 20 cm) and iodination (during 3 minutes) of product films were performed. As AFM pictures of irradiated and iodinated films were similar to those obtained for source material, bacterial infection of paste sample is unlikely.

Microscopic study of the material at a magnification of 100x showed the presence of piece of micron-sized particles.

A study of photodiode current diagrams was performed. Photodiode received signals from AFM microscope cantilever (holder) oscillated at the scanned surface. The study showed that light areas in the figures 2 and 3 corresponds to attraction of the cantilever to the surface, and dark areas – to repulsion. It means that globules consist of electrically charged material that might represent CNT convoluted into a ball with past-like denaturated albumin as an intermediate material.

It worth noticing that possible alternative ways of CNT volumetric composition formation (namely thermal and ultrasonic methods) from protein solution didn't produce a result because of albumin decay into flakes without binding together with CNT's).

In this paper a previously unknown method of laser manufacturing of quasi-periodic nanocompositions from the CNT-protein solution under the laser irradiation has been offered. Medical application of the material produced is stipulated for the possibility of achieving the effect of biological tissues self-assembly on the nanotube scaffold. The further investigations must be devoted to searching of optimal conditions of nanomaterial and CNT compounds manufacturing with the aim of producing biocompatible implants of novel type which can be used in plastic reconstructive surgeon.

References

1. Mattson M.P., Haddon R.C., Rao A.M. *J. Mol. Neurosci.*, **14**, 175 (2000)
2. L.P.Zanello, B.Zhao, H.Hu, R.C. Haddon. *Nano Letters*, **6**, 562 (2006)

**MUSTOF-Endoscopy for Natural Orifice Transluminal
Endoscopic Surgery**

An Innovative, Safe and Sterile Sigmoid Access for NOTES (ISSA)

D. Wilhelm^{1,2}, J. Penne⁴, S. v. Delius³, A. Meining³, J. Hornegger⁴, and H. Feussner^{1,2}

¹ Department of Surgery, Klinikum r.d. Isar, Technical University, Munich
(Prof. Dr. Dr. J.R.Siewert)

² Workgroup for minimal invasive Surgery MITI, Klinikum r.d. Isar, Technical University, Munich

³ 2nd Medical Department, Klinikum r.d. Isar, Technical University, Munich
(Prof. Dr. R.M.Schmid)

⁴ Computer Science Department, Pattern Recognition, University of Erlangen
(Prof. J. Hornegger)

1 Background

The use of natural orifices of the human body (NOTES) allows surgical treatment without any incision of the abdominal wall and therefore is supposed to further reduce known drawbacks of open surgery like postoperative pain, wound infection rates and incisional hernias. Up to now most groups performing NOTES procedures are using a transgastric approach to enter the peritoneal cavity for diagnostic purposes and to treat intraabdominal organs as the gallbladder^{1,2}, the stomach^{3,4}, the uterus⁵ or the fallopian tubes⁶. Unfortunately the transgastric approach offers only a limited view to the upper abdomen as an inverted view is necessary. Additionally the missing availability of a practicable sealing method for the entry site^{7,8} is still a problem.

For these reasons other access routes than the transgastric approach are of high interest. Fong et al were the first to describe a transcolonic advancement, but much more than the transgastric approach this technique was combined with an increased bacterial contamination rate of the abdominal cavity⁸.

We developed an innovative sigmoid approach in order to reduce the risk of laceration of intraabdominal organs and to allow for a sterile introduction of the flexible endoscope. This approach additionally allows the leak-proof closure of the entry site and therefore offers an interesting alternative to known techniques.

2 Material and Methods

Evaluation of the innovative transsigmoid access was based upon 10 acute and 5 survival porcine models. In the non-survival part, all pigs were sacrificed after completion of the intervention immediately followed by necropsy, whereas observation over 10 days with subsequent euthanasia and necropsy was undertaken in the survival model. The study protocol of the latter model was approved by the commissioner of animal welfare of the Government of Upper Bavaria.

All animals received regular feeding until 24 hours before the procedure. Subsequently, they had a liquid diet until 12 h before the intervention.

After preanesthesia sedation, general anesthesia was initiated. After endotracheal intubation and throughout surgery, maintenance of anesthesia was achieved by continuous inhalation of isofluran with bolus application of fentanyl. Before performing the transsigmoid approach an

antibiosis was applied to all pigs. Intervention was performed in a supine position of the pig. The ano-rectum was cleaned by administration of tap-water enemas and repeated irrigation with sterilized isotone fluids.

The main procedure consists of 4 consecutive steps:

1: Instillation of the protective fluid

In the beginning, a hydroperitoneum is established using a sterile Verres needle which was inserted below the navel. Via this needle 1 part of taurolidin and 2 parts of Ringer solution at a total amount of 1/10 of the body weight of the pig are installed into the abdominal cavity. Taurolidin solution is a decontaminating fluid widely used in general surgery for the prevention and therapy of peritonitis. The pigs then are positioned in an anti-Trendelenburg position (head raised up 30°), what separated the pelvic content (small intestine) from the pelvic floor and the rectosigmoid.

2: Identification and preparation of the entry point

Then the rectosigmoid is entered at a point which is demarked by a rectocele, an excavation of the rectosmoid caused by the installed fluid. Surrounding the future entry point a purse string suture was placed for sealing of the bowel wall afterwards.

3: Introduction of the guide tube

Then a specially designed, sterilized endoscopic guide is introduced. With its sharp tip, the entry point is perforated giving entry into the abdominal cavity. Then the endoscopic guide is advanced and as soon as the peritoneal cavity is intruded, the inlay is slowly removed. The outer end of the guide tube is connected to an airtight valve unit and a gas-sterilized flexible endoscope is inserted via the guide tube into the abdomen to perform the further intervention.

4: Removal of the guide tube, closure of the entry site

After the inspection of the peritoneal cavity being finished and the intraabdominal fluid and air being removed by suction, the flexible endoscope is withdrawn with the guide tube. Under visual control, the purse string suture is closed. Finally, the small nipple resulting from the purse string is additionally secured by the application of a linear stapler

To assess the value of the transsigmoid approach it was aimed to inspect at least both upper abdominal quadrants including liver, spleen and the gall bladder. Standard endoscopic manipulations, such as rotation, torque, retroflexion and tip deflection were mandatory. In 5 pigs of the acute porcine model a cholecystectomy was performed. In the survival model which served for evaluating of the approach, surface swabbings were taken from the tip of the guide tube when extracted, to evaluate bacterial contamination.

For the survival porcine model all pigs received an antibiotic therapy during the first two postoperative days with peroral enrofloxacin application. In the following, all pigs were investigated daily for signs of infection and temperature was acquired twice a day. All animals were allowed for free oral feeding the day after the intervention. On the 10th day, the pigs were weighted and finally sacrificed as mentioned. In postmortem analysis the abdominal cavity was inspected for signs of infection, bleeding, perforation or peritonitis. As soon as the peritoneum was opened, surface swabbings were taken for microbiologic testing. Inspection of the peritoneal cavity was performed focused upon the entry point and adjacent structures to identify any leakage, fistula, adhesions or laceration. The rectosigmoid was excised in accordance to usual surgical techniques and further examined. In addition, tissue specimes from the entry site were obtained for histopathologic examination.

3 Results:

The transsigmoid approach was technical feasible in all animals. An adequate entry point could be identified by the help of direct inspection and endoluminal ultrasound in each case. The incision

of the rectosigmoid could be performed without relevant immediate complications in all animals. The guide tube could always be easily advanced into the peritoneal cavity and allowed for direct introduction of the endoscope. Endoscopic manipulation was not impaired for the tube guided endoscope as compared for traditional approaches.

The average time to accomplish the procedure was 9,3 min (+/- 1,3) for the incision process and 7,8 min (+/- 2,3) for the withdrawal of the scope and closure of the entry site. The most time consuming part was the induction of the fluidoperitoneum through the Verres needle which took 20-30 minutes. Visualization of the upper abdomen was excellent. Identification of the liver, spleen and stomach could be achieved within moments, a direct access to the gallbladder was possible within 2 minutes without the need of retroflexion.

NOTES-cholecystectomy could successfully be performed in 3 of 5 pigs. In one pig bleeding complication occurred due to injury of hepatic vessels, exposition of the gall bladder was impossible in another pigs because of an oversized liver lobe.

For the survival model almost all animals showed an excellent condition during the observation period. All animals had a regular bowel function with a defecation starting at the 2nd postoperative day in median. The pigs were ambulated freely and showed a normal behaviour without any signs of distress.

In postmortem examination there were no signs of infection or peritonitis in all cases, which was confirmed in microbiologic testing with no bacterial growth after 48 hours. The entry sites in most cases could hardly be identified on the peritoneal aspect of the colon and appeared as well-healed, pale scar. There was no major bleeding observed during the insertion part of the procedure, no organs damage was identified. The closure of the entry site was successful in all animals and resulted in a leak proof sealing without any narrowing of the lumen .

4 Discussion:

Natural orifice transluminal endoscopic surgery (NOTES) is supposed to further reduce the invasiveness of transabdominal surgery by eliminating abdominal incisions and multiple trocar puncture sites⁹. Most NOTES procedures recently are performed transgastrically with the need for awkward retroflexion to visualize structures and to perform therapeutic manipulations in the upper abdomen^{2,5,10}. Especially, the ability to identify, manipulate, and resect the gallbladder has proven to be technically challenging^{2,11}. To overcome these obstacles encountered through a transgastric incision, a transcolonic approach that provides an en face orientation to organs in the upper abdomen for better visualization and scope stability was first employed by the Boston group^{1,8}. Unfortunately the approach was combined with increased bacterial contamination of the abdominal cavity and the closure of the entry site turned out to be critical. In our series we had no such complications, what may be due to several modifications and additional precautions we made. Prior to the colonic incision we instilled taurolidin solution, a decontaminating fluid widely used in general surgery for the prevention and therapy of peritonitis, into the abdominal cavity. The usage of a sterilized guide tube might have also contributed to the safety of the procedure with regard to infection. We believe, that procedures requiring multiple intubations, such as cholecystectomy, would profit even more as repeated passages along colonic mucosa could be avoided. Lastly, the full-thickness apposition and surgical closure of the entry point led to reliable leak proof sealing of the colonic wall without compromising the lumen. We consider the surgical approach advantageous compared to clip closure as the latter may become insufficient due to mechanical extension of the relatively thin-walled colonic incision as mentioned previously^{8,12}, the circumscribing purse string at the incision site provided additional support by sealing the incision around the guide tube during the procedure.

The exposition of the gall bladder using a transsigmoid approach was easily performed in 4 of 5 pigs. It allowed for surgical manipulations and cholecystectomy in 3 of 5 pigs. This reflects the convenience of an en-face proceeding, realized by the transsigmoid approach.

In conclusion, we demonstrated that the transcolonic approach to the peritoneal cavity with systematic abdominal exploration is feasible and safe. The use of preprocedural intraabdominal instillation of a decontaminating fluid, the application of a sterilized guide tube and the surgical closure of the entry point resulted in a procedure with nearly no complications in our series. Furthermore, enhanced manoeuvrability and stabilization was provided by the intraabdominal part of the guide tube. Future studies in the animal model are mandatory for evaluation of our innovative, safe and sterile sigmoid access (ISSA) for NOTES procedures in the upper abdomen before translation to human applications.

References

1. Pai RD, Fong DG, Bundga ME, Odze RD, Rattner DW, Thompson CC. Transcolonic endoscopic cholecystectomy: a NOTES survival study in a porcine model (with video). *Gastrointest Endosc* 2006; **64**(3):428-34.
2. Park PO, Bergstrom M, Ikeda K, Fritscher-Ravens A, Swain P. Experimental studies of transgastric gallbladder surgery: cholecystectomy and cholecystogastric anastomosis (videos). *Gastrointest Endosc* 2005; **61**(4):601-6.
3. Bergstrom M, Ikeda K, Swain P, Park PO. Transgastric anastomosis by using flexible endoscopy in a porcine model (with video). *Gastrointest Endosc* 2006; **63**(2):307-12.
4. Kantsevov SV, Jagannath SB, Niiyama H, et al. Endoscopic gastrojejunostomy with survival in a porcine model. *Gastrointest Endosc* 2005; **62**(2):287-92.
5. Wagh MS, Merrifield BF, Thompson CC. Survival studies after endoscopic transgastric oophorectomy and tubectomy in a porcine model. *Gastrointest Endosc* 2006; **63**(3):473-8.
6. Jagannath SB, Kantsevov SV, Vaughn CA, et al. Peroral transgastric endoscopic ligation of fallopian tubes with long-term survival in a porcine model. *Gastrointest Endosc* 2005; **61**(3):449-53.
7. Ryou M, Pai R, Sauer J, Rattner D, Thompson C. Evaluating an optimal gastric closure method for transgastric surgery. *Surg Endosc* 2006.
8. Fong DG, Pai RD, Thompson CC. Transcolonic endoscopic abdominal exploration: a NOTES survival study in a porcine model. *Gastrointest Endosc* 2007; **65**(2):312-8.
9. Bhoyrul S, Vierra MA, Nezhat CR, Krummel TM, Way LW. Trocar injuries in laparoscopic surgery. *J Am Coll Surg* 2001; **192**(6):677-83.
10. Wagh MS, Merrifield BF, Thompson CC. Endoscopic transgastric abdominal exploration and organ resection: initial experience in a porcine model. *Clin Gastroenterol Hepatol* 2005; **3**(9):892-6.
11. Swanstrom LL, Kozarek R, Pasricha PJ, et al. Development of a new access device for transgastric surgery. *J Gastrointest Surg* 2005; **9**(8):1129-36; discussion 1136-7.
12. Merrifield BF, Wagh MS, Thompson CC. Peroral transgastric organ resection: a feasibility study in pigs. *Gastrointest Endosc* 2006; **63**(4):693-7.

Auto-Gain Approach for Use with Time-Of-Flight Examination in Minimally Invasive Surgery

P. Ritt¹, K. Höller¹, J. Penne¹, A. Schneider², J. Hornegger¹, and H. Feussner²

¹ Institute of Pattern Recognition (LME), University Erlangen-Nuremberg, Germany,

² Workgroup for minimal invasive Surgery MITI, Klinikum r.d.Isar, Technical University, Munich, Germany

Abstract. The use of time-of-flight cameras (TOF) in minimally invasive surgery is expected to grow over the next years. Some of the camera parameters like modulation frequency, integration time or focal point of the camera lens are still controlled by hand. In order to make the handling of a MUSTOF (Multi sensor TOF) endoscopic system more convenient the automation of these parameters with the help of pattern-recognition-methods is a desirable aim [1]. We present a new approach for the automation of the control of one of those parameters, the integration time. We achieve an improvement in time consumption over existing approaches while retaining accuracy of the distance measuring process.

1 Introduction

Distance measuring time-of-flight (TOF) cameras are already widely used in many sectors. It is easily understood that 3D views are a big gain for minimally invasive surgery (MIS) and natural orifice transluminal endoscopic surgery (NOTES), improving both, precision and convenience of such treatments. For that reason the development of the use of TOF-cameras in minimally invasive surgery has been intensified. Before commercial products can be realized there are still hurdles to overcome.

One of those hurdles is reaching a sufficient accuracy of the distance measuring process. So far, under best conditions TOF-cameras reach a distance accuracy of 1-2 mm for distances up to 50 cm. Outside the best conditions the distance measurements rapidly loose accuracy, thus it is essential to operate the TOF-cameras in best conditions. One important parameter that influences the precision is the amount of received light. The amount of received light is directly controlled by integration time, which is the time-span where the CCD-sensor receives light.

But let's first have a look at the basic principle of the TOF-camera [2][3]:

- Modulated light is sent out by the camera (active illumination), scattered by the object and received again by the camera.
- The camera measures the phase difference ϕ_d between the sent and received light.
- The phase difference is measured by sampling the received signal at 4 measurement points (fig. 1). The phase difference is calculated by

$$\phi_d = \arctan\left(\frac{a_0 - a_2}{a_1 - a_3}\right).$$

- The distance d now is calculated by

$$d = \frac{c}{2f_0} \frac{\phi_d}{2\pi}. \text{ (with the speed of light } c \text{ and the modulation frequency } f_0)$$

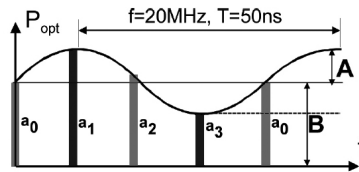


Fig. 1: Sampling points of the received signal

2 Problem description

Our measurements show that it is necessary to be within a certain range in integration time, in order to obtain accurate distance information. It can be seen on fig. 2 that a too low integration

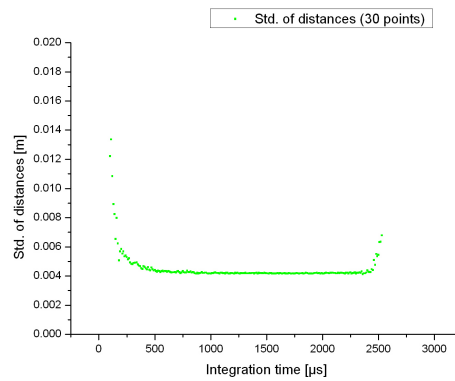


Fig. 2: Standard-deviation vs. Integration time

time results in a high uncertainty (high standard-deviation). This is caused by statistical effects of the electron-generation/photon-absorption process. A too high integration time also leads to high uncertainty. This is caused by saturation effects. The region of 'correct' integration time varies with distance and reflectivity of the observed object. For less reflectivity or further away objects, this region is shifted to higher values (longer integration time) and for higher reflectivity and closer objects to lower values (shorter integration time)(fig. 3). It is therefore necessary to find the right integration time for any observed object, which is one of the aims of our work. The adjustment in integration time also needs to be as fast as possible or at least within 1-2 seconds as it is not reasonable for a surgeon to wait any longer until she/he has access to accurate distance data. Manually adjusting the integration time has major drawbacks. Our measurements show that it takes between 5-10 seconds to adjust manually. The adjusting process also needs a

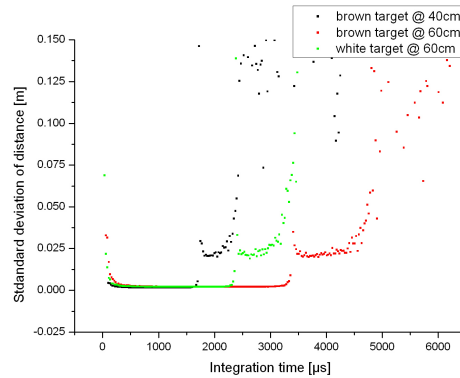


Fig. 3: Standard-deviation vs. Integration time for different distances/reflectivities

lot of attention of the surgeon or alternatively of a second person that controls integration time. So we try to discuss and provide solutions for the following questions:

- Is there a reliable way of judging which integration time is good and which is not?
- Is an automation of the integration-time-adaption possible? Can it be realized in such ways that the adaption process is fast enough in order to avoid irritations and inconveniences for the surgeon/medical staff?

3 Methods

During our experiments we found out that the amplitude image that the cameras supply is a good indication of the reliability of the distance values (fig. 4). We see that the curves for different reflectivities/distances cover very well, which means that a certain amplitude can be interpreted as an indicator for accuracy. The amplitude value is usually based on the evaluation algorithms implemented in the camera. Basically the amplitude A depends (fig. 1) on the measured values according to $A \sim \frac{1}{2} \cdot \sqrt{(a_3 - a_1)^2 + (a_0 - a_2)^2}$. Yet the amplitude range that offers a good reliability has to be measured for every camera model.

For the adjustment of the integration time, our first realizations were simply increasing integration time by a fixed step if amplitude is too low and decreasing it if amplitude is too high. This approach had two major drawbacks. It is quite slow, as the curves for low reflectivity or high distance are very shallow compared to high reflectivity or short distances (fig. 5). It would take a lot of steps for low reflectivities/high distances to reach the desired region of amplitudes. We can also see (fig. 5) a region with negative slope. If our camera somehow is in this region, the algorithm would find a too low amplitude and would therefore increase the integration time, resulting in an even lower amplitude.

Consequently the next approach involved slopes to a) estimate how big the consecutive steps need to be in order to reach a good amplitude as fast as possible and to b) determine on which side (positive slope/negative slope) of the curve it is right now. Unfortunately this didn't work very well, we needed a lot of measurement points to calculate a reliable slope, which is quite easy to

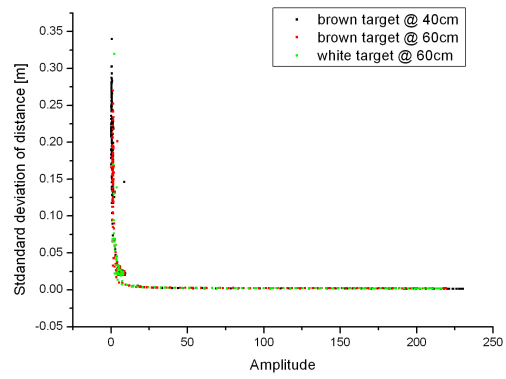


Fig. 4: Standard-deviation vs. Amplitude for different distances/reflectivities

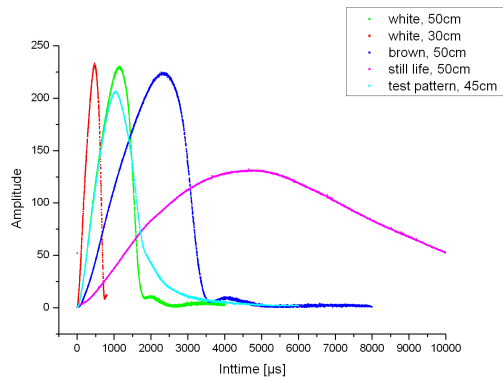


Fig. 5: Amplitude vs. Integration time for different distances/reflectivities

understand if we look at a detailed view of the integration time - amplitude curve. The points are heavily scattered, therefore it is not possible to calculate a reliable slope out of a maximum of 10 points (again every point means one frame). Even if we got a reliable slope, this could only give coarse clue for the position on the curve, as we already know that the curves have different shapes for different reflectivity/distances (fig. 5).

When dealing with this problems we noticed that the curves for different reflectivities/distances

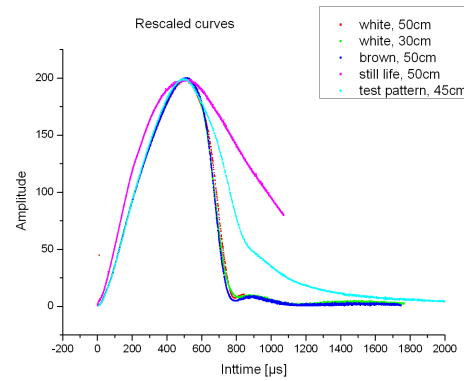


Fig. 6: Rescaled curves: Amplitude vs. Integration time for different targets/distances

look somehow similar. We found out that the curves are linear scaled on the integration time axis up to a certain degree. So if we rescale the curves to a reference curve they are nearly congruent (fig. 6). This can be used for adjusting the integration time, our algorithm does the following steps to calculate the correct integration time.

1. Before we can even use our algorithm, we need a reference curve. So we direct the camera to a static scene (typically similar to the later use of the camera) and record the amplitude values for consecutive integration time values (for example, $100 \mu\text{s}$, $200 \mu\text{s}$, $300 \mu\text{s}$...). For a reliable curve, we measure a few frames for every integration time and calculate the mean value of the amplitude data. In the end we get a curve with (typically a few hundred) n pairs $(I_x; A_x)$, $0 < x \leq n$, consisting of an integration time I_x and the belonging to its amplitude A_x . This is our reference curve.
2. In the auto gain process we need a reliable data pair on our (now unknown) curve which consists of an integration time I_m and the measured amplitude A_m . This is done by a multiple measurement of the amplitude at the constant integration time I_m with following calculation of the mean value. Before this the integration time is risen until a certain minimum amplitude is reached. This is necessary because the measurement points are heavily scattered for low amplitudes and therefore have got a high inaccuracy.
3. In the next step the amplitude A_m of our data pair is compared to the amplitudes of the reference curve. The amplitude A_b that matches our measured amplitude best (that means, which is closest to the measured amplitude) is identified and the belonging to its integration time I_b is read out.

4. The scaling factor s is calculated. It is the ratio of the integration time used for the measurement and the read out integration time. $s = \frac{I_m}{I_b}$
5. Now the target amplitude is compared with the amplitudes in the reference curve, again the amplitude closest to the target amplitude is identified and the belonging to its integration time I_b read out.
6. The target integration time I_t can now be calculated according to $I_t = s \cdot I_b$.

4 Results

The knowledge of the scaling factor s allows to jump directly to the appropriate integration time I_t , without having to do any intermediate steps. The reference curve usually needs only to be obtained once for every camera-endoscope setup.

With the help of the described procedure it is possible to speed up the auto gain process. Our experiments have shown that manually adjusting the integration time normally takes 5-10 seconds, depending on how much the integration time needs to be changed. First automatic approaches took about 10-20 seconds. Our method normally needs 9-12 frames to adjust to the right integration time, 3 frames under good conditions (only small adjustment needed), which results in 1-3 seconds and for good conditions below 1 second.

5 Outlook

The method is still limited to a region of about 1 meter around the distance in which the reference curve was obtained, as the curves are only scaled in first approximation by a constant factor. With bigger differences in distance the non-linearities grow and limit the accuracy of the method. At this point development is still necessary, we are confident that we are able to adapt the usability to a wider distance range.

References

1. Penne, Jochen ; Höller, Kurt ; Krüger, Sophie ; Feußner, H.: NOTES 3D: Endoscopes learn to see 3-D; Basic Algorithms for a Novel Endoscope. Second international Conference on Computer Vision Theory and Applications (VISAPP 2007), Barcelona, Spain, Insticc Press (2007) 134–139, ISBN 978-972-8865-75-7
2. Lange, R.: 3D Time-of-Flight Distance Measurement with Custom Solid-State Image Sensors in CMOS/CCD-Technology. Ph.D. Dissertation, University of Siegen, Germany (2000) 26–29
3. Heinol, H.: Untersuchung und Entwicklung von modulationslaufzeitbasierten 3D-Sichtsystemen. Ph.D. Dissertation, University of Siegen, Germany (2001) 51–54

Photorealistic 3-D Surface Reconstructions Using TOF Cameras

Jochen Penne¹, Kurt Höller¹, Dirk Wilhelm², Hubertus Feußner², and Joachim Hornegger¹

¹ Chair for Pattern Recognition, Friedrich-Alexander-University Erlangen-Nuremberg

² MITI Group, Klinikum rechts der Isar, Munich

Abstract. TOF (Time-of-Flight) technology enables the real-time 3-D surface reconstruction of the current field of view of a TOF camera with a constant lateral resolution. We propose algorithms for the calibration of a TOF camera which in combination with rigidly mounted standard cameras enables the photorealistic 3-D surface reconstruction of the current field of view by registering the optical centres of the involved cameras and projecting the 3-D surface reconstruction into the standard camera image plane. For various applications not only the surface in the current field of view has to be reconstructed: We propose an algorithm to register consecutively acquired 3-D surface reconstructions of static scenes.

1 Introduction

In many applications, such as medical imaging, robotics, biometrics, automobile security and navigation and surveillance a three-dimensional representation of the environment is required. The acquisition of 3-D data has become one of the most important challenges in the design of modern electronic image sensors as the acquisition of 3-D data is favoured over alternative methods based on ultra-sonic or radar. Furthermore, by the direct acquisition of 3-D information time-consuming processing steps to compute the 3-D information from 2-D information are obsolete. The main advantage of *optical* systems is the capability of a very fast 3-D data acquisition, an eye-safe system setup and a high lateral resolution.

Standard acquisition techniques incorporate scanning systems or stereo systems with complex filtering and correlation processing units. But the real-time requirement which is done for most applications implies that neither the complex calculation of a distance map nor a scanning component should lead to an additional processing time-delay. Optical cost-efficient real-time 3-D cameras thus are hardly realizable with these techniques. Consequently, for 3-D imaging of the whole field of view pixel matrices are required with each pixel capable of delivering the distance information of one point in the field of view. Thus, these pixels are termed *smart pixels*.

The time-of-flight (TOF) technique is one possible method for the fast optical acquisition of distance information. The time that light needs to travel from the measurement system to the object and back again corresponds directly to the distance R , and is called time-of-flight (TOF):

$$TOF = \frac{2R}{c}, \quad (1)$$

where c is the light velocity ($c \approx 3 \cdot 10^8 \frac{m}{s}$). The method is very suitable for ranges starting from some centimetres to several hundreds of meters with relative accuracies of 0,1%. Nevertheless, the relative accuracies depend strongly on the illumination conditions and the effective suppression of multiple reflections. Based on smart demodulation lock-in pixels the parallel measurement of the distance can be realized for some thousand points in a scene [1]. Two methods for measuring the TOF are distinguished:

- A light pulse is sent out and its turn-around time is measured directly.
- A continuously-modulated, e.g. sinusoidally modulated, light wave is emitted and the phase delay between the original and received light signal is estimated to compute the time or distance information.

The latter method is used in available range imaging sensors.

2 Model description

TOF technology enables the direct acquisition of the distance information about a world point which is projected on a sensor element [2]. Currently, framerates of 12...50 fps are achieved by TOF cameras.

TOF cameras illuminate the scene actively with an optical reference signal. By Smart Pixels, which are integrated into the TOF camera chip (TOF chip), the reflected optical wave is analysed and for each pixel the phase shift compared to the reference signal is estimated. Assuming a constant speed for the spread of the signal the phase shift is directly proportional to the distance of a point in the recorded scene. Currently, lateral resolutions of up to 144×176 pixel and z-resolutions of 1 mm are available. Simultaneously to the phase delay, the amplitude of the reflected optical wave is estimated. This information provides a gray-scale image of the scene, with the reflectivity of the material being encoded in the gray-values. We will reference the amplitude and distance data as one *frame* acquired by a TOF camera.

The registration of this data with simultaneously acquired color data of a standard 2-D camera will be described in the following section. Furthermore, the registration of consecutively acquired 3-D surface reconstructions is described. The amplitude value acquired with a TOF camera at pixel (i, j) is denoted with $a_{i,j}$. The corresponding distance value measured in *mm* is denoted with $d_{i,j}$. The color value in the 2-D camera at position (i, j) is denoted with $p_{i,j}$. TOF camera and 2-D camera are modeled as pinhole cameras. The intrinsic parameters (f : focal length, (c_x, c_y) : principal point) and the extrinsic parameters ($R \in \mathbb{R}^{3 \times 3}$: rotation matrix, $t \in \mathbb{R}^3$: translation vector) are denoted as given for the 2-D camera and denoted with a $'$ for the TOF camera.

Using homogenous coordinates (indicated by $\underline{\quad}$) a 3-D point q is projected to the 2-D camera pixel p , according to

$$p = K[R|t]\underline{q} \quad (2)$$

and to the TOF camera pixel p'

$$p' = K'[R'|t']\underline{q}, \quad (3)$$

where K is the calibration matrix containing the intrinsic camera parameters [3].

Let (p_x, p_y) and (p'_x, p'_y) denote the physical dimensions of a sensor element of the 2-D or TOF camera in *mm*. Given a distance value $d_{i,j}$, let $d_x = (i - c'_x)p'_x$ and $d_y = (j - c'_y)p'_y$ be the distance of the pixel from the principal point measured in *mm* and $d_z = \sqrt{d_x^2 + d_y^2 + f'^2}$ be the distance of the optical centre to the pixel measured in *mm*, the corresponding 3-D point $q = (q_x, q_y, q_z)^T$ is computed by

$$q_x = \frac{d_x d_{i,j}}{d_z}, \quad q_y = \frac{d_y d_{i,j}}{d_z}, \quad q_z = \frac{f' d_{i,j}}{d_z}. \quad (4)$$

As the 3-D coordinates are associated with pixels which are arranged in a regular 2-D grid in the image plane an 3-D triangulation of the 3-D point cloud can easily be achieved. The 2-D pixel grid is triangulated and then the triangulation is transferred to the 3-D points leading to a regular triangulation. Thus, for each frame acquired with a TOF camera a consistent triangulation of the reconstructed surface can be provided. Assuming the 2-D and TOF camera being rigidly mounted

implies that the spatial relation between the optical centres of both cameras can be described by a relative rotation $R_r \in \mathbb{R}^{3 \times 3}$ and translation $t_r \in \mathbb{R}^3$, with

$$R_r = RR'^{-1}, t_r = t - R_r t', \quad (5)$$

where R, R', t and t' describe the pose of the corresponding camera in a common world coordinate system.

3 Calibration

Two cameras are to be calibrated: the 2-D and the TOF camera. Tsai's widely used algorithm [3] is in principle applicable to both cameras:

1. Capture image of a calibration pattern with N calibration points.
2. Determine 2-D calibration points c_i , $1 \leq i \leq N$.
3. Assigning 3-D world points w_i , $1 \leq i \leq N$ to 2-D calibration points.
4. Estimation of intrinsic (K) and extrinsic (R, t) camera parameters involving Levenberg-Marquardt non-linear optimization [4].

For the 2-D camera the algorithm needs no modification. Considering TOF cameras the low lateral resolution and the relative big size of the sensor elements (approx. 0.04 mm) lead to unstable calibration results. By involving all the capabilities of a TOF camera the results can be stabilized by not only minimizing the squared backprojection error

$$\sum_{i=1}^N \|c_i - \text{proj}(w_i, K', R', t')\|^2, \quad (6)$$

where $\text{proj}(w_i, K', R', t')$ is the projection of the world point w_i into the image plane specified by K', R' and t' . Instead, the objective function was extended by a term which describes the deviation of the 3-D reconstructed calibration points from the plane which they are lying on. Let \hat{c}_i be the 3-D point reconstructed from c_i specified in world coordinates (of the calibration pattern) using the distance information available from the TOF camera and the extrinsic parameters. Furthermore, ϵ_c denotes the regression plane calculated using all \hat{c}_i , $1 \leq i \leq N$. The extended objective function, which is minimized for a TOF camera in the calibration routine, is

$$\sum_{i=1}^N (\|c_i - \text{proj}(w_i, K', R', t')\| + \alpha \|\hat{c}_i - w_i\| + \beta d(\hat{c}_i, \epsilon_c)), \quad (7)$$

where $d(\hat{c}_i, \epsilon_c)$ is the distance of \hat{c}_i to the regression plane ϵ_c and α, β are scaling parameters. The term $\|\hat{c}_i - w_i\|$ penalizes wrong intrinsic and extrinsic camera parameters which lead to a wrong reconstruction of the calibration points. The term $d(\hat{c}_i, \epsilon_c)$ only penalizes wrong intrinsic camera parameters as only those are relevant for the reconstruction of all \hat{c}_i on a plane (wrong extrinsic parameters only imply a rotation and translation of the plane).

4 Registration

Using the calibration routine described above the extrinsic parameters (R', t', R, t) and intrinsic parameters (K, K') are known for each camera when capturing simultaneously an image of the calibration pattern. This enables the calculation of R_r and t_r as described by equation (5) and (assuming a parallel acquisition of data) a computationally inexpensive assigning of 3-D points to color information: by using formula (4) a 3-D point can be reconstructed which is specified in TOF camera coordinate system and by applying formulas (5) and (2) the 3-D point is projected into the 2-D camera image plane.

5 Surface reconstruction

The registration of consecutively acquired frames of a TOF camera enables the 3-D reconstruction of surfaces greater than the current field of view. Assuming a static scene and considering the framerate of ≥ 12 fps which implies only relatively small camera movement between consecutive frames, two reconstructions r_i and r_j (with TOF camera poses (R'_i, t'_i) and (R'_j, t'_j)) are related via a rotation $R'_{i,j}$ and translation $t'_{i,j}$ of the optical centre of the TOF camera (assuming constant intrinsic parameters). This relative pose between two reconstruction can be estimated by the following steps:

- Initialization:
 1. Acquire the first frame r_1 of the TOF camera.
 2. Detect edges in the amplitude and distance data (number of found points: N_1). The 3-D coordinates q_i , $1 \leq i \leq N_1$ of points detected as lying on an edge are used as world description data $W = \{q_1, \dots, q_{N_1}\}$.
 3. Initialize the TOF camera position with $R'_1 = I$ and $t'_1 = \underline{0}$, where I is the identity matrix and $\underline{0}$ is a 3×1 zero-vector.
- Processing of subsequently acquired frames:
 1. Acquire a frame r_i of the TOF camera.
 2. Detect edges in the amplitude and distance data (number of points N_i). The 3-D coordinates q_i , $1 \leq i \leq N_i$ of points detected as lying on an edge are used as current world description data $W_{cur} = \{q_1, \dots, q_{N_i}\}$.
 3. Set the initial solution of the current camera pose to $R'_i = R'_{i-1}$ and $t'_i = t'_{i-1}$.
 4. The current extrinsic camera parameters are estimated by maximizing the correlation coefficient between edges detected in the current frame and edges already detected in preceding frames. Formally: Apply a Levenberg-Marquardt non-linear optimization on (R'_i, t'_i) to maximize

$$\rho(\text{proj}(W, K', R'_i, t'_i), W_{cur}), \quad (8)$$
 where $\text{proj}(W, K', R'_i, t'_i)$ describes the projection of the world description data W on the image plane whose pose is described by (R'_i, t'_i) and whose intrinsic parameters are given by K' (known from the calibration routine). Furthermore, ρ describes the correlation coefficient according to Neyman-Pearson.
 5. Update W : add the edges found in the current frame (W_{cur}) to W .
 6. The relative camera pose compared to the preceding frame is described by $R'_{i-1,i} = R'_i R'^{-1}_{i-1}$ and $t'_{i-1,i} = t'_i - R'_{i-1,i} t'_{i-1}$.

In each optimization step the world description data is projected into the current image plane. Thus, regions in the current image plane which contain information about parts of the scene which have already been reconstructed can be identified and omitted for an update of the visualization.

Only parts of the scene which have not been seen before are added to the 3-D reconstruction and so the unnecessary accumulation of redundant 3-D information is circumvented.

Clearly, the world description data is growing. And for each optimization step the world description data has to be processed. Consequently, the estimation of the current camera pose gets slower. As the complexity of the estimation task is only depending on the size of the world description data, the world description data might be thinned out when its size exceeds a certain value to meet processing time requirements. This issue is currently out of the scope of this paper.

A global geometry is only available at the 3-D point level. A global triangulation of the scene is not provided by this algorithm. Nevertheless, as stated earlier each frame provides a consistent triangulation of the scene geometry in the current field of view. Each part which is added to the reconstructed scene after a successful estimation of the new extrinsic parameters is consistently triangulated. Thus, by stitching the scene together from consistently triangulated parts, at least the visual effect is that of a closed surface.

6 Results

To evaluate the calibration routine for TOF cameras in terms of its stability the following experiments were done with a SwissRanger 3100 (144×176 pixels). First, the TOF camera was not moved while acquiring images and performing the calibration routine 16 times. Due to the noise in the amplitude information the segmentation of the calibration circles and consequently the input data for the calibration routine do differ. Furthermore, the low lateral resolution and the relatively big dimensions of the TOF sensor elements do hinder a good convergence of the estimation of the camera parameters when minimizing the standard objective function given in equation 6. As the camera was not moved the standard deviation of the calculated intrinsic and extrinsic camera parameters characterize the influence of the effects described. The results are given in table 1.

Objective function		f[mm]	c_x [pix]	c_y [pix]	t_x [mm]	t_y [mm]	t_z [mm]	r_x [rad]	r_y [rad]	r_z [rad]
standard (eq. 6)	μ	8.37	87.855	69.882	-52.69	-55.71	284.40	0.128	0.280	-0.014
	σ	0.057	1.032	0.886	1.87	1.19	1.88	0.003	0.006	0.001
extended (eq. 7)	μ	8.21	86.68	69.33	-53.78	-54.93	279.80	0.126	0.277	-0.014
	σ	0.067	0.382	0.256	1.08	0.34	2.13	0.001	0.003	0.0006

Table 1: Mean and standard deviation of intrinsic and extrinsic camera parameters after 16 calibration routines with a non-moving TOF camera.

The same experiment was repeated but the camera was moved. In addition to the effects described previously, the occurring varying illumination of the calibration pattern leads to a destabilization of the segmentation of the calibration circles. 16 calibration routines were performed. The results are given in table 2. The experiments were repeated with a 2-D camera: a Logitech QuickCam Messenger USB (324× 248 pixel) was used to perform the calibration routine 16 times with non-moving camera. The results are given in table 3

The results indicate that the relative position of both cameras can be estimated with an accuracy of about 5mm in each translation component and an accuracy of 0.014 rad in each rotation component. This accuracy is sufficient to provide an reasonable overlay of 3-D information with color information. Figure 2 shows two simultaneously acquired TOF and Web camera images

Objective function		f[mm]	c_x [pix]	c_y [pix]
standard (eq. 6)	μ	7.95	87.681	70.515
	σ	0.528	0.874	0.830
extended (eq. 7)	μ	8.20	86.19	68.84
	σ	0.168	0.910	0.903

Table 2: Mean and standard deviation of intrinsic and extrinsic camera parameters after 16 calibration routines with a moving TOF camera.

	f[mm]	c_x [pix]	c_y [pix]	t_x [mm]	t_y [mm]	t_z [mm]	r_x [rad]	r_y [rad]	r_z [rad]
μ	3.93	124.43	152.23	-37.06	-72.08	246.95	0.282	-0.421	-0.264
σ	0.027	5.025	0.850	3.086	0.516	1.399	0.006	0.011	0.003

Table 3: Mean and standard deviation of intrinsic and extrinsic camera parameters after 16 calibration routines with a non-moving Web camera.

and the result of projection the 3-D surface reconstruction into the web camera image plane after registering the optical centres of the cameras. Due to the hardware setup and camera characteristics the common field of view does not completely overlap. When no color information could be assigned to a 3-D surface point the corresponding amplitude gray value was used as texture. To illustrate the reconstruction of scenes greater than the current field of view by estimating the current camera pose an image sequence was processed. The scene contained a chair. The initial viewing direction of the camera was to the left of the chair. Then the camera was moved to the left, making the chair move through the field of view from right to left 1.

7 Conclusion and Outlook

Algorithms for the calibration of TOF cameras, the registration of TOF and standard cameras and the reconstruction of surfaces greater than the current field of view were proposed. By extending the standard objective function minimized during calibration a calibration routine especially suitable for TOF cameras was described. Being able to reliably calibrate a TOF camera the registration with standard cameras is enabled as the extrinsic camera parameters for simultaneously acquired images are known. By reducing the data used for estimating the extrinsic parameters for consecutively acquired frames an on-the-fly registration of these frames is possible. The algorithm proposed assumes a static scene.

Considering the registration of standard and TOF cameras the overlay of color and 3-D information may be improved by modelling the mismatch of color and 3-D information as a non-rigid 2-D/2-D multimodal registration problem: The color information has to be aligned with 2-D amplitude/distance data. Several non-linear effects (inaccuracies in distance measurement; lens distortions) motivate this approach. Furthermore, the identification of dynamic parts of the scene will lead to the reconstruction of dynamic scenes which are greater than the current field of view.

References

1. Lange, R.: 3D Time-of-flight distance measurement with custom solid-state image sensors in CMOS/CCD-technology. PhD thesis, University of Siegen (2000)

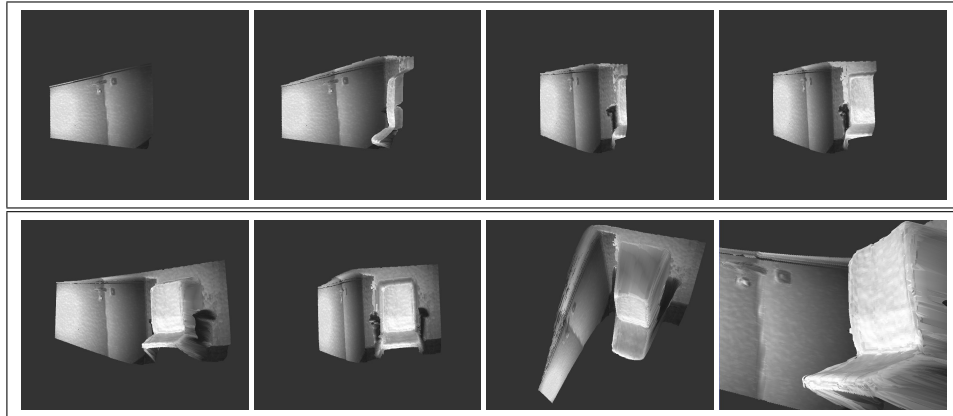


Fig. 1: Reconstructin of a scene containing a chair: the upper row of images shows the consecutive stitching of reconstructed parts of the scene by estimating the camera pose for each acquired frame. The bottom row shows different screenshots of the examination of the scenes. Note that the chair has been stitched together very well.



Fig. 2: Simultaneously acquired TOF and Web camera data (left image). Overlay of color information and 3-D surface reconstruction after registrating TOF and Web camera (right image). Only parts of the reconstruction can be overlaid with color information as the common field of view of both cameras is not 100% overlapping.

2. Schwarte, R., Heinol, H., Buxbaum, B., Ringbeck, T., Xu, Z., Hartmann, K. In: Handbook of Computer Vision and Applications. Volume 1. The Academic Press (1999)
3. Tsai, R.Y.: A Versatile Camera Calibration Technique for High-Accuracy 3D Machine Vision Metrology using Off-the-Shelf TV Cameras and Lenses. IEEE Journal of Robotics and Automation Ra-3(3) (1987) 323–344
4. Dennis, J.E., Schnabel, R.B.: Numerical Methods for Unconstrained Optimization and Non-linear Equations. Prentice Hall, New Jersey (1983)

Author Index

- Adamusiak, Tomasz, 11
Alexandrov, Andrei, 120
Arkushina, E. M., 159
Astapenko, E. M., 197
- Baraniak, Jennifer, 168
Batliner, Anton, 46
Bauernschmitt, Robert, 31, 52
Bechtel, T., 174
Beller, S., 1
Bennewitz, Christian, 92
Bock, Rüdiger, 126
Borsdorf, Anja, 154
Bouattour, Sahla, 41
Brockmann, G., 31
Buck, Andreas, 96
Bugaev, A., 174
Burian, Maria, 96
- Chapursky, V., 174
Couronné, Robert, 37
- D'yachenko, Alexander I., 203
Daghighian, Farhad, 96
Daum, V., 110
Delius, Stefan, 222
Dietrich, Paulus, 41
Doroshenkov, L.G., 18
Douniama, Christian, 37
- Eckardt, K.-U., 110
Efimov, Slawa, 142
Eltner, P., 5
- Fahrig, Rebecca, 131
Feilner, S., 185
Feuerstein, Marco, 87
Feussner, Hubertus, 1, 222, 226, 232
- Ganguly, Arun, 131
Gorbunov, B. B., 76
Gorshkova, V. M., 80
Guggenbichler, J. Peter, 207, 211
Gusev, A. N., 76
- Härtl, Felix, 1
- Höller, Kurt, 1, 226, 232
Hönig, Florian, 46
Han, Jingfeng, 92
Hartl, Alexander, 96
Hauer, Hans, 142, 168
Heining, Sandro M., 87
Helbig, H., 110
Hofmann, Christian, 185
Hornegger, Joachim, 92, 105, 115, 126, 154, 222, 226, 232
Huber, Martin, 115
- Ivashov, S., 174
- Janka, R., 110
- Köstler, Harald, 154
Karlovskiy, D.V., 14
Keck, Benjamin, 131
Khamene, Ali, 105
Kir'yanova, Elena V., 203
Kirpichenko, Y.E., 56, 148
Kobelev, Alexander, 138, 166, 189
Konyshev, V.A., 14, 18
Koplovich, Dmitri, 120
Korenbaum, Vladimir I., 203
Kotin, V. V., 159
Kuwert, Torsten, 92
- László, G. Nyúl, 126
Lange, R., 31
Lasser, Tobias, 96
Leugering, Günter, 168
Luzhnov, P. V., 197
- Maistrou, Aliaksei, 61
Malberg, Hagen, 31, 52
Masloboev, Yury, 24
Mayer, Michael, 154
Meier, Jörg, 126
Meining, Alexander, 222
Michelson, Georg, 126
Morozov, V. V., 70
Mussack, Thomas, 87
- Nöth, Elmar, 46

- Navab, Nassir, 87, 96
Novikova, E. A., 70
- Ohritsky, A. A., 24
Osipova, Antonina A., 203
- Pawliczak, Rafal, 11
Penne, Jochen, 222, 226, 232
Pochekutova, Irina A., 203
Podgaetsky, Vitaly, 217
Pokrovskiy, Andrei, 120
Prümmer, Marcus, 131
Pramatarov, Svetoslav, 180
Prilutsky, D. A., 24
- Rüde, Ulrich, 154
Razevig, V., 174
Retzlaff, Beatrice, 31
Ritt, Philipp, 226
Ryabov, Edward, 142
- Sävransky, V.A., 217
Schaller, Christian, 105
Schneider, Armin, 226
Schookin, Sergey, 138, 166
Schuhmann, Norbert, 168
Schwaiger, Markus, 96
Selishchev, Sergey, 24, 76, 217
Sergeev, Igor, 138, 166, 189
- Shamkina, L. A., 197
Sheyko, A., 174
Shulagin, Yury A., 203
Simunin, M.M., 217
Struck, Matthias, 180
- Tereshchenko, Sergey, 101
Thull, R., 5
Timohin, D.P., 56, 148
Titkova, D.A., 217
Traub, Jörg, 96
- Uhl, C., 31
Umnyashkin, Sergei, 120
- Vasilyev, I., 174
- Wärntges, Simone, 126
Wanninger, W., 211
Weigand, Christian, 180
Wels, Michael, 115
Wendler, Thomas, 96
Wessel, Niels, 31, 52
Wilhelm, Dirk, 222, 232
- Zeltner, R., 110
Zhdanov, A. V., 70
Ziegler, Sybille I., 96

www.biomed07.uni-erlangen.de

